

INFRARED EMISSIONS MODELING

Part 1

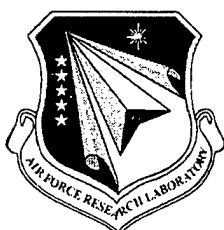
B.D. Green	B.L. Upschulte
W.T. Rawlins	P.A. Mulhall
L.G. Piper	J.F. Cronin
G.E. Caledonia	R.H. Krech
M.E. Fraser	D.B. Oakes
K.W. Holzclaw	

Physical Sciences, Inc.
20 New England Business Center
Andover, MA 01810

September 1998

Final Report

APPROVED FOR PUBLIC RELEASE; DISTRIBUTION IS UNLIMITED.



20001023 032

**AIR FORCE RESEARCH LABORATORY
Space Vehicles Directorate
29 Randolph Rd
AIR FORCE MATERIEL COMMAND
Hanscom AFB, MA 01731-3010**

"This technical report has been reviewed and is approved for publication."

Dean F. Kimball
DEAN F. KIMBALL
Contract Manager
Background Clutter Mitigation Branch

Harold A. B. Gardiner
HAROLD A. GARDINER
Acting Branch Chief
Background Clutter Mitigation Branch

This report has been reviewed by the ESC Public Affairs Office (PA) and is releasable to the National Technical Information Service (NTIS).

Qualified requestors may obtain additional copies from the Defense Technical Information Center (DTIC). All others should apply to the National Technical Information Service (NTIS).

If your address has changed, if you wish to be removed from the mailing list, or if the addressee is no longer employed by your organization, please notify AFRL/VSIM, 29 Randolph Road, Hanscom AFB, MA 01731-3010. This will assist us in maintaining a current mailing list.

Do not return copies of this report unless contractual obligations or notices on a specific document require that it be returned.

REPORT DOCUMENTATION PAGE

Form Approved
OMB No. 0704-0188

Public reporting burden for this collection of information is estimated to average 1 hour per response, including the time for reviewing instructions, searching existing data sources, gathering and maintaining the data needed, and completing and reviewing the collection of information. Send comments regarding this burden estimate or any other aspect of this collection of information, including suggestions for reducing this burden, to Washington Headquarters Services, Directorate for Information Operations and Reports, 1215 Jefferson Davis Highway, Suite 1204, Arlington, VA 22202-4302, and to the Office of Management and Budget, Paperwork Reduction Project (0704-0188), Washington, DC 20503.

1. AGENCY USE ONLY (Leave blank)			2. REPORT DATE	3. REPORT TYPE AND DATES COVERED
			September 1998	Scientific, Final, Sep 1993-Aug 1998
4. TITLE AND SUBTITLE			5. FUNDING NUMBERS	
Infrared Emissions Modeling Part 1 of 2			Contract F19628-93-C-0046 PR S322 TA GD WU AB	
6. AUTHOR(S)			8. PERFORMING ORGANIZATION REPORT NUMBER	
B.D. Green, W.T. Rawlins, L.G. Piper, G.E. Caledonia, M.E. Fraser, K.W. Holzclaw, B.L. Upschulte, P.A. Mulhall, J.F. Cronin, R.H. Krech, and D.B. Oakes			PSI-1179/TR-1580	
7. PERFORMING ORGANIZATION NAME(S) AND ADDRESS(ES)			10. SPONSORING/MONITORING AGENCY REPORT NUMBER	
Physical Sciences, Inc. 20 New England Business Center Andover, MA 01810			AFRL-VS-HA-TR-98-0105	
9. SPONSORING/MONITORING AGENCY NAME(S) AND ADDRESS(ES)				
Air Force Research Laboratory/VSBM 29 Randolph Rd Hanscom AFB, MA 01731-3010 Contract Manager: Dean Kimball				
11. SUPPLEMENTARY NOTES				
12a. DISTRIBUTION AVAILABILITY STATEMENT			12b. DISTRIBUTION CODE	
Approved for Public Release; Distribution Unlimited				
13. ABSTRACT (Maximum 200 words)				
This report summarizes a multi-year program to analyze upper atmospheric radiance data to deduce product distributions, extract the operative kinetic mechanisms, and quantitatively determine local conditions in the emission volume. Spectral and kinetic models were used to analyze emissions from several molecules including NO, NO+, ozone, and excited nitrogen. Radiances from the mesosphere both under equilibrium and non-equilibrium conditions were analyzed. The radiance changes produced by non-equilibrium excitation mechanisms such as electrons, kinetic energy from fast atoms, and solar-induced transients at terminator were all addressed by multiple analyses during this program.				
14. SUBJECT TERMS			15. NUMBER OF PAGES	
Infrared emission Electron excitation Mesospheric chemistry Nitric oxide Ozone Nitrogen				
16. PRICE CODE				
17. SECURITY CLASSIFICATION OF REPORT		18. SECURITY CLASSIFICATION OF THIS PAGE	19. SECURITY CLASSIFICATION OF ABSTRACT	20. LIMITATION OF ABSTRACT
UNCLASSIFIED		UNCLASSIFIED	UNCLASSIFIED	UNL

CONTENTS

<u>Section</u>	<u>Page</u>
1. INTRODUCTION	1
2. ELECTRON INDUCED FLUORESCENCE OBSERVED DURING THE EXCEDE 3 MISSION	3
3. VIBRATIONALLY EXCITED NO ION EMISSION FROM THE AURORALLY DISTURBED THERMOSPHERE AS OBSERVED DURING THE ELIAS MISSION	5
4. LABORATORY STUDIES IN SUPPORT OF FIELD OBSERVATIONS	6
5. OZONE VARIABILITY NEAR THE MESOPAUSE FROM THE CIRRIS 1A DATA BASE	10
6. SPECTRAL ANALYSIS OF THE EMISSION FROM RED SPRITES	14
7. DIURNAL VARIABILITY OF INFRARED ATMOSPHERIC OXYGEN EMISSIONS AS OBSERVED FROM THE DELTA 181 MISSION	17
8. MSX EARTHLIMB ANALYSES AND SUPPORT	18
9. REFERENCES	20

LIST OF APPENDICES:

Appendix 1	- Dosing, Altitude Dependence, and Excitation Mechanisms of NO Vibraluminescence Observed in the EXCEDE III Mission	21
Appendix 2	- Kinetics and Mechanisms for the Formation of Rovibrationally-Excited Nitric Oxide in the EXCEDE III Rocket Experiment	39
Appendix 3	- Excitation of O ₃ (v ₃) by Electron Bombardment in the EXCEDE III Rocket Experiment - Presentation	73
Appendix 4	- Excitation of O ₃ (v ₃) by Electron Bombardment in the EXCEDE III Rocket Experiment - Journal Article	109
Appendix 5	- Hypersonic Beam Facility for Rarefied Flow Studies	

TABLE OF CONTENTS (Continued)

<u>Section</u>		<u>Page</u>
LIST OF APPENDICES (Continued)		
Appendix 6	- Laboratory Studies of Fast Oxygen Atom Interactions with Materials	197
Appendix 7	- Experimental Determination of the Einstein Coefficient for the N(² P-4 ^S) Transition	205
Appendix 8	- Observations on the O/NO Air Afterglow	219
Appendix 9	- CIRRIS 1A Ozone Airglow Analysis	243
Appendix 10	- Analysis of CIRRIS 1A O ₃ (V) Spectra in the 9.6 μ m Region	267
Appendix 11	- Ozone Variability Near the Mesopause from the CIRRIS 1A data ..	291
Appendix 12	- Molecular Excitation in Sprites	313
Appendix 13	- Molecular Excitation from Sprite Emission Spectra	319
Appendix 14	- Spectral and Kinetic Analysis	341
Appendix 15	- Spectroscopy and Chemical Kinetics of Sprites	383
Appendix 16	- Electron Distributions Responsible for Red Sprites	419
Appendix 17	- Diurnal Variability of Infrared Atmospheric Emissions Diagnostic of Odd Oxygen as Observed in the Delta 181 Mission	437
Appendix 18	- Midcourse Space Experiment (MSX): The Aurora of 10 November 1996 Observed Over Scandinavia	447
Appendix 19	- Midcourse Space Experiment (MSX): Auroral MWIR and LWIR Backgrounds, Observations, and Analysis	465

1. INTRODUCTION

This report summarizes a multi-year program to analyze upper atmospheric radiance data to deduce product distributions, extract the operative kinetic mechanisms, and quantitatively determine local conditions in the emission volume. Spectral and kinetic models were used to analyze emissions from several molecules including NO, NO⁺, ozone, and excited nitrogen. Radiances from the mesosphere both under equilibrium and non-equilibrium conditions were analyzed. The radiance changes produced by non-equilibrium excitation mechanisms such as electrons, kinetic energy from fast atoms, and solar-induced transients at terminator were all addressed by multiple analyses during this program. Effects of electron excitation were isolated via the analysis of data from an artificial injection experiment and in the aurorally disturbed and sprite-disturbed mesosphere. The EXCEDE III electron beam injection experiment produced enhanced emissions from NO and Ozone. Our findings are presented in Section 2. Mechanisms responsible for auroral production of NO⁺ are presented in Section 3. Because fast atoms produced in photolytic decomposition and electron impact/recombination apparently contribute to observed radiance enhancements, we performed laboratory simulation experiments to quantify fast atom product distributions and confirm radiometric calibrations. These efforts are described in Section 4. Ozone radiance variability on global spatial scales and at terminators was derived from analysis of the data from the CIRRIS 1A shuttle-based experiment and reported in Section 5. We participated in the spectral analysis of field data observing the transient red sprites phenomenon placing constraints on the excitation electron distribution based on prior laboratory investigations at the Research Laboratory at Hanscom. Our efforts are summarized in Section 6. The CIRRIS 1A mission acquired the first high quality infrared atmospheric emissions global data base from space - the precursor for many other orbital missions. In Section 7 we report a brief investigation of IR radiances acquired during the Delta 181 mission providing simultaneous observation of several oxygen emission features - providing the ability to constrain and improve global radiance models. In Section 8 we present a summary of our participation in the analysis of the MSX satellite data base observing a strong auroral event.

Although the results of several of these analyses should be viewed as preliminary, taken together they represent several significant steps forward in our understanding of the non-equilibrium upper atmosphere.

2. ELECTRON INDUCED FLUORESCENCE OBSERVED DURING THE EXCEDE 3 MISSION

The EXCEDE III rocket experiment bombarded the nighttime lower thermosphere with energetic electrons at high dosing rates and observed the resulting infrared fluorescence with a suite of instruments including a cryogenic interferometer.¹ Nitric oxide fluorescence from the electron dosed upper atmosphere was analyzed to extract excitation mechanisms. A large beam-induced NO production was observed. Vibrational / rotational distributions from previous COCHISE laboratory measurements helped in mechanism investigation. Across the altitude region covered by EXCEDE III, different classes of processes will contribute to the fluorescence. The rotationally hot component appears likely to arise from the reaction of metastable nitrogen atoms with O₂. Production of this component decreases as dose rate increases due to precursor quenching. The interim findings of this study were reported at the Spring AGU Meeting in May 1993. The viewgraphs of that presentation are included as Appendix 1 to this report.

Carrying this effort further, we quantified the relative contributions of the vibrational state populations with both excited and extremely rotationally excited states. The role of metastable and translationally excited atoms were discussed. A poster presentation entitled "Kinetics and Mechanisms for the Fragmentation of Ro vibrationally Excited Nitric Oxide in the EXCEDE III Rocket Experiment" by Fraser, Rawlins, Green, Paulsen, Armstrong, Lipson, Blumberg, and Murphy was given at the 1993 Fall AGU Meeting and is included as Appendix 2 to this report. In addition we supported the companion paper on this topic led by Air Force Research Laboratory researchers.

Fourier transform spectra in the 9 to 11 μm spectral region above the mesopause exhibit the presence of vibrationally excited O₃(v₃) excited both by quiescent and electron initiated processes. We analyzed the fluorescence near 10 μm to extract electron-initiated processes from the natural background chemiluminescence. Populations of ozone v₃,v=1-4 were observed to be enhanced by electron bombardment. Secondary electron excitation of ozone seems to be occurring in agreement with laboratory measurements. The poster presentation at the 1993 Fall

AGU Meeting "Excitation of O₃(v₃) by Electron Bombardment in the EXCEDE III Rocket Experiment" by Rawlins, Green, Paulsen, Blumberg, and Murphy is included as Appendix 3.

As other analyses of the EXCEDE III rocket profile, dosing rates, and atmospheric concentrations arose from other analyses of the EXCEDE III mission, a coherent picture of the ozone production emerged. When the electron beam is on, ozone emission from the irradiated volume is more intense than that from the entire ambient atmospheric column, with excitation into at least four vibrational quanta identified. Direct excitation of ozone vibration by secondary electron impact plays a significant role. In addition, during the period with the most intense dosing, ozone is formed via a bi-molecular reaction of beam-excited metastable precursors. The kinetic behavior favors the O₂(A³Σ_u,v) + O₂ reaction to form O₃ either in excited states or in ground state subsequently efficiently excited by electron impact. A journal article on the beam-produced excitation of ozone as observed in the EXCEDE III rocket experiment is included as Appendix 4.

3. VIBRATIONALLY EXCITED NO ION MISSION FROM THE AURORALLY DISTURBED THERMOSPHERE AS OBSERVED DURING THE ELIAS MISSION

The Earth Limb Infrared Atmospheric Structure (ELIAS) experiment successfully acquired data on the infrared spatial and temporal structure created by an aurora in the polar upper atmosphere. The sub-orbital mission conducted in Alaska on 19 March 1983 was fortunate to observe the emissions from an IBC III⁺ aurora for several hundred seconds. Measurements of the atmospheric radiances from well defined spatial volumes were acquired with bandpass radiometers alternately staring at a spatial position and with the radiometers scanned over the spatial scene. Ultraviolet, and short- and mid-wave infrared emissions were analyzed and correlated to extract auroral excitation of vibrationally excited NO and NO⁺. Through modeling we determined that NO^{+(v)} is produced in aurora from three potential sources: the reactions of N⁺ with O₂, of N₂⁺ with O, and of N^{2P} with O. Modeling indicates that the N₂⁺ channel dominates NO⁺ production. The auroral production efficiency for the NO⁺ fundamental band was predicted to be 1.35 photons per ion pair with the N₂⁺ + O reaction being the dominant contributor. The modeling indicated that about 1% of the deposited auroral energy appears as NO⁺ as opposed to 4% for NO. A nonlinear scaling with dose rate is predicted by the model.

4. LABORATORY STUDIES IN SUPPORT OF FIELD OBSERVATIONS

While field observations provide the fundamental observations of key atmospheric processes, controlled laboratory experiments permit hypotheses to be tested and parameters to be systematically varied. As part of this program we performed several investigations to aid in the understanding of field data observations.

Atoms moving with significant energies (of several eV) can be produced in the natural atmosphere by photolysis, in the aurorally disturbed atmosphere by electron-impact followed by dissociative recombination, and as an artifact of space based observatories arising from the interaction of outgassed or reflected species with the residual natural atmosphere. The role of high velocity (hyperthermal) atoms in enhancing rate coefficients, opening new reaction pathways, and altering vibrational distributions produced by chemiluminescent reactions was investigated using the Physical Sciences Inc. (PSI) fast atom source. In particular, the role of fast atomic oxygen colliding with NO to produce emission from highly excited NO(v, J) states in the thermosphere is explored via controlled laboratory experiments.

SWIR measurements were performed under single collision conditions representative of those encountered by molecules outgassed or produced on or above spacecraft surfaces in low earth orbit interacting with the residual, atomic oxygen dominated atmosphere. The reaction of O with N₂ to produce vibrationally and rotationally excited NO and O was of particular interest for both spacecraft interactions as a precursor for "shuttle glow", and as a potential contributor to NO(v) production in the disturbed atmosphere. The O + N₂ reaction is endothermic by 3.26 eV at room temperature. The center of mass energy with O moving at 8 km/s (orbital velocity) is just comparable to this endothermicity. Thus surrounding spacecraft, the kinetic energy has the potential for overcoming the reaction endothermicity. No theoretical predictions were available for this reaction cross-section. The experiments revealed that the cross-section for NO(v) production begins to rise significantly at 10 km/s with the overtone to fundamental intensity ratio indicating significant vibrational excitation. Spectrally-resolved emission that was obtained using a circularly variable filter substantiates the presence of highly vibrationally excited NO.

Comparisons with field data were performed. The cross-section for this reaction produces sufficient NO in this gas-phase reaction to explain the shuttle glow intensities via gas phase NO production, followed by surface adsorption, and catalytic recombination with O. This cross-section also produces NO(v) in good agreement with the SKIRT mission CVF spectrally resolved NO(v) observations (also on STS-39).² Near field NO(v) radiances were also observed within the CIRRIS 1A data set at radiance levels comparable to the SKIRT radiances and predictions based on the laboratory data. The spectral distribution observed in the CIRRIS 1A data matches the laboratory distribution within their overlap region including clear indications of rotationally hot NO in a non-Boltzmann distribution are produced in the fast O + N₂ reaction.

The reaction of O with CO₂ was also investigated to determine the cross-section as a function of velocity and the favored reaction pathway at 8 km/s: vibrational excitation of CO₂(v₃) or reaction to form CO(v). The cross-section favored the theoretical prediction of Schatz and Redmon.

The ability to measure cross-sections for these hypervelocity collisions required accurate knowledge of the atomic oxygen flux. A description of the atomic oxygen measurement technique and the fast atom apparatus producing a high flux of 5 to 12 km/s velocity atomic oxygen and its performance characteristics is given in Appendix 5. While total flux can be estimated by inlet oxygen mass consumption and flow modeling, the spatial distribution in the test (collision) region needs to be accurately measured to permit absolute cross-section determination. Silver oxidizes very efficiently upon atomic oxygen impact: gaining mass through oxidation; changing from a reflector to optically transmissive; and changing from a conductor to an insulator. Space-based and ground experiments have used resistance and optical changes of thin silver films to monitor atomic oxygen flux. We describe in Appendices 5 and 6 measurements of atomic oxygen fluence using a thin silver film's resistance change (using an actinometer) and mass gain (using a Quartz Crystal Microbalance). The temperature dependence of the silver reaction rate was measured. Diffusion of O into the silver film was determined to produce non-linear responses at film thicknesses greater than 25 nm. Correlating silver with carbon coated QCMs permitted absolute fluence determination. We also report of lower velocity

(2 to 4 km/s) beams created to study the interactions and signatures of plume exhaust species. Beams of CO₂, CO, and H₂O and mixtures were successfully formed.

Metastable nitrogen atoms in the ²P and ²D states are important precursors to NO chemiluminescence in the electron dosed upper atmosphere, as observed in auroral field missions and in artificial auroral experiments such as EXCEDE. Remote measurement of N (²P) concentrations relies upon knowledge of the Einstein coefficient for radiative decay to turn radiances into absolute column densities. Metastable N ²P atoms have transitions that emit brightly in the ultraviolet at 347 nm to the ground state and in the near infrared at 1040 nm to the ²D state. The relative brightness of the ²P emission relative to N₂⁺ B-X First Negative and N₂ B-A First Positive transitions has been used to gauge the depth of auroral penetration and electron energy. The N ²P- ⁴S transition probability has only been estimated in two theoretical calculations. We performed laboratory measurements in a discharge-flow reactor. Metastables were generated in a microwave discharge, and N ²P detected via emission at 346.6 nm, and via VUV resonance absorption at 174 nm using monochromators. The visible monochromator was calibrated for absolute photon emission rate measurements by observing the intensity of the O/NO air afterglow. The N ²P number densities were determined by analysis of the fractional absorption at 174 nm. The 346 nm absolute emission from the same volume was determined to scale linearly with N ²P concentration, permitting determination of an Einstein coefficient of 0.0054 s⁻¹ with a statistical uncertainty from all sources of $\pm 26\%$. This agrees with both theoretical estimates within our experimental determination error bounds. These measurements are described more fully in Appendix 7.

Laboratory measurements of absolute emission rates often rely upon a standard well-characterized reaction to account for optical collection efficiencies, optical element transmissions, and geometric factors, and to determine the spectral responsivity variation with wavelength. The O/NO air afterglow is probably the most widely used such calibration standard. We have used it to determine many absolute decay rates and reaction efficiencies (such as for N ²P presented above). Upon critically reviewing the literature for the O/NO spectral distribution

(and converting them to comparable units), we discovered significant variations at wavelengths longer than 700 nm.

We performed careful measurements of the O/NO intensity distribution over the 400 to 1750 nm spectral region. We generated the precursors using multiple independent techniques, and calibrated the spectral response of the spectrometer/photomultiplier using several different radiation standards with calibrations traceable to NIST. We find the peak of the distribution to be around 670 nm. Detailed comparison with the distributions determined by eight other groups is presented in Appendix 8 along with our tabulated determination. Although the agreement is often excellent, significant discrepancies occur.

We also provide a re-analysis of their data to interpret the differences. Again comparison of the absolute rate coefficient reported by the eight groups is confounded by inconsistent reporting. Careful reanalysis and explanation of their data produces a consistent value for five of the groups. We recommend a value of $(1.17 \pm 0.11) \times 10^{-19} \text{ cm}^3 \text{ molecule}^{-1} \text{ s}^{-1} \text{ nm}^{-1}$ at 580 nm, with a value integrated over all wavelengths of $9 \times 10^{-17} \text{ cm}^3 \text{ molecule}^{-1} \text{ s}^{-1}$.

5. OZONE VARIABILITY NEAR THE MESOPAUSE FROM THE CIRRIS 1A DATA BASE

The CIRRIS 1A mission acquired the first global infrared atmospheric emissions data base during a several day mission in 1991.³ They successfully obtained over 30 hours of observation time of emissions from the daytime and nighttime quiescent and aurorally disturbed mesosphere and thermosphere using a cryogenically-cooled, telescoped interferometer and radiometers. In earlier work we quantified the optical contamination of CIRRIS data by near field particles and high-velocity gas phase interactions. As part of this program we investigated upper atmospheric ozone radiant signatures obtained with the CIRRIS 1A interferometer.

First data from a few high quality observations were thoroughly analyzed to identify ozone vibrational states contributing to the observed emission signatures. Limb emission spectra from three tangent point altitudes of 71, 86, and 98 km were selected to span the altitude regions of most interest. The spectroscopic constants and radiative lifetimes were acquired under previous laboratory investigations in the COCHISE Facility at the Research Laboratory at Hanscom.⁴ Both spectral smoothing and baseline corrections were applied before spectral fitting. We attempted to fit the LWIR ozone emission between 820 and 1060 cm⁻¹ via three approaches: including seven excited states with only v₃ quanta excited; including seven v₁,v₃ coupled dyads (101,002; 102,003;...); and including twelve v₁,v₃ and v₂,v₃ coupled dyad states (101,002; 012,111; ...) in the analysis. We determined that the spectral signature was well described by including the v₁,v₃ and v₂,v₃ dyads in the spectral fitting. Because addition of v₂,v₃ dyad emission does not improve the quality of the least-squares agreement with the data, we feel its inclusion is not required.

Hot band emission and spectral structure from ozone excited states was detected out to beyond 12 μm, demonstrating the excellent quality of the data base. The vibrational population distribution observed agreed well with modeling predictions and the distribution derived from the earlier SPIRE mission data. The ozone spectral distribution changed with altitude indicating vibrational level dependent quenching occurs. The preliminary quenching coefficients for v ≤ 7

agree with both LABCEDE laboratory⁵ and SPIRE⁶ field observations. A preliminary examination of ozone $4.8 \mu\text{m}$ emission supported these conclusions. These findings were summarized at the CIRRIS 1A Program Review on September 9, 1993, and appeared in the Proceedings of that meeting. The viewgraph presentation material is given in Appendix 9.

Spectral fitting of additional selected high resolution data from the wider CIRRIS 1A data base permitted internal distributions to be extracted. Emission from (v_1, v_3) and v_3 states were observed in the data. The CIRRIS 1A data was of excellent quality, however, emission did not extend beyond the laboratory data base. No new spectroscopic information on ozone highly excited vibrational states could be derived. The observed distributions are consistent with three-body recombination as the source of ozone chemiluminescence. While the CIRRIS data agreed well with SPIRE and EXCEDE III background radiances, it highlighted the need for improved ozone photochemical models

Armed with this knowledge of the ozone excited states contributing to the observed radiant signatures, we next undertook a screening of the entire CIRRIS 1A data base to extract variabilities due to spatial, latitudinal, and solar effects. With the assistance of data base screening tools developed by coworkers at the Air Force Research Laboratory, we retrieved the LWIR ozone data "scans" at three spectral resolutions for all observations with tangent point altitudes from 70 to 110 km and transferred the data to PSI for analysis.

Initial batch processing of the data sets was performed to produce radiance altitude profiles. These profiles did not follow a smooth altitude scaling. The profiles exhibited wide scatter between the data with radiances from many scans an order-of-magnitude larger than expected. Upon visual inspection, LWIR spectra in the 9 to $12 \mu\text{m}$ region of the outlying data points were observed to be not ozone, nor even resemble molecular emission. We performed the arduous task of visually reviewing each of 4000 spectra in the entire data base to identify and remove spectral scans containing artifacts. These are likely to arise from either interferometer scanning anomalies or from shuttle environmental perturbations (such as thruster firings required to maintain pointing accuracy) affecting the ability to observe the far-field atmospheric signature.

Over 32% of the spectra were eliminated via this screening process, most for containing excess noise. These removed spectra had the wrong spectral shape, high or low frequency oscillations running across the spectra, baseline offsets, or other clear indications that the spectra were corrupted and not representative of remote mesospheric emissions. Due to the regular periodicity of the "noisy" spectra, we feel these are contaminated radiance from the shuttle thrusters rather than interferometer scan anomalies.

The remaining 2740 spectra were too numerous to permit detailed spectral fitting. To characterize the large data base, we integrated the spectra over ten bandpasses within the ozone feature to permit trends in $v_3, v=1$, hotband, and CO₂ radiances to be extracted. The bandpass wavelengths were selected based on our spectral fitting analysis to isolate the ozone $v=1$ R branch, $v=2$, and other ozone hotbands emissions, while carefully accounting for baseline shifts and ramps and spectral interferences from mesospheric CO₂ emission under sunlit conditions. The integrals were used to correlate ozone relative excited state densities. The integrals from the 2740 spectral scans were incorporated into a single spreadsheet and manipulated to display profiles as a function of altitude, latitude, solar zenith angle, and longitude.

Our review of this data base indicates that the global variability is large compared to the local variability. Over an order-of-magnitude variability was observed in the ozone $v_3, v=1$ radiances (column densities) at altitudes above 100 km even after background correction. Ozone fundamental band radiance was observable above the noise for tangent point altitudes up to 109 km. Excellent quality terminator series were obtained after correction for shuttle pointing jitter. Both 1-quanta states (proportional to total ozone concentration) and 3-quanta states (proportional to atomic oxygen concentration) showed clear terminator effects even up to 100 km tangent point altitudes. The atmospheric CO₂ radiances were used to discriminate local concentration variances from larger scale atmospheric transport (heave). Ozone variability was far in excess of CO₂ variability. The ozone variability does not seem to be due to kinetic rate uncertainties but rather due to dynamic processes. A very significant local enhancement in ozone and atomic oxygen was observed later in time and equatorward of an intense auroral arc, suggesting large scale atmospheric air parcel transport. Ozone variability was observed to be

greatest during high K_p periods. There were no clear trends with latitude or solar zenith angle within the day and nightside data sets, but substantial scatter existed between the values from different data collection times. The transition from day to night distributions appears to occur rather rapidly. Crude temperatures were obtained from bandpass ratios. These results were presented at the 21st IUGG Meeting in July 1995 using the material in Appendix 10. A preliminary draft of a journal article summarizing these analysis efforts is presented in Appendix 11.

6. SPECTRAL ANALYSIS OF THE EMISSION FROM RED SPRITES

During the course of this program a new class of atmospheric phenomena was first systematically observed: sprites. These transient spatially structured radiant columns connect the tops of intense thunderstorms to the bottom of ionosphere and thus are felt to play a significant role in the global electrical circuit. The first spectrally resolved observations of sprites exhibited a visible spectra dominated by nitrogen First Positive emission. PSI has extensive experience in the analysis of radiance from the N₂ B-A system to extract the excited state populations present in the excited volume. Using PSI internal funding we supported meetings sponsored by AFRL and performed a spectral fitting analysis on the first spectrally resolved sprite spectrum to determine the B state distribution in the red sprite field observations. Emission from 570 to 820 nm exhibited N₂ B-A in the $\Delta v=2,3,4$ sequences from vibrational levels up to v=11. N₂⁺ A-X Meinel band emission was not observed, only an upper bound on its column density could be set. Assumption of a Boltzmann distribution for the electron energy permitted the B-state vibrational distribution to be predicted as a function of electron temperature based on previous laboratory measurements. We deduced that electrons with a characteristic temperature of 1 eV were producing the observed sprite distribution, and that no ion state emission was expected (nor observed) at these electron energies. This work was completed under AFRL sponsorship and the complete text of a Geophysics Research Letters article is included as Appendix 12.

As part of this program we undertook a more systematic fitting of sprite data acquired by the University of Alaska group during the 1995 summer campaign. We determined the internal vibrational and electronic state energy distributions of the large spectrometric observations data base to explore red sprite variability. This data set exhibited a very large signal to noise dynamic range of over 1000. Only small variations in the spectral distributions were obtained for all sprites analyzed. The derived B-state distribution agreed with that extracted from the earlier analysis of the first sprite spectrum. These findings were summarized in a presentation at the Fall AGU Meeting which is included as Appendix 13.

This analysis was extended to predict the likely infrared radiances within the red sprite column. We considered several classes of processes that could produce IR emission. Electron impact excitation of Nitrogen electronic states can directly produce W-B emission as observed in EXCEDE⁵ and COCHISE⁷ experiments. Based on observed 600 kR B-state radiances, emission from the nested W state can be accurately predicted as only 1 kR around 3 μ m. Electron impact dissociative excitation of N atom metastable states to produce NO is predicted to yield small MWIR radiances except for long-lived sprite columns. Electron impact efficiently produces vibrationally excited N₂. In the mesosphere vibra-luminescent near-resonant energy transfer from N₂(v) to CO₂(v₃) is the only significant relaxation mechanism. We presented these findings at a Sprites Workshop at Research Laboratory, Hanscom in April 1997. The viewgraphs from this presentation are included as Appendix 14 of this report.

We next undertook more detailed modeling of the electron distribution including all excitation pathways to predict absolute excitation rate as a function of atmospheric field strength E/N. Energy-dependent cross-sections for vibrational levels in all related nitrogen electronic states were assembled as input into the ELENDIF Boltzmann transport model.⁸ Excitation into each excited state of nitrogen and oxygen was computed as a function of E/N. We learned that the observed sprites N₂B state distribution favors E/N in the 3 to 5×10^{-16} V/cm range. Moreover the ion states are predicted to be formed at completely negligible levels. UV emissions from the long-lived sprite component are expected small and due to N₂ C fluorescence. Any UV ion emissions must arise from the short lived (< 1 ms) precursor pulse.

The calculated rates from the code permit the required electron density to be estimated from the observed sprite intensities as a function of E/N. E/N of 3 to 5×10^{-16} require electron densities in the range of 10⁴/cc, a value in agreement with measurements. Thus, we feel the physical regime where sprites can exist are tightly bounded by the current visible observational data. This material was presented at a Sprites Meeting at Air Force Research Laboratory at Hanscom in June 1998 and is included as Appendix 15.

We feel these observations should help constrain sprite mechanisms and provide guidance into formation processes. Based on these conclusions, we feel the emphasis for future measurements should be on performing IR measurements. A draft journal article describing these results is has been prepared for journal submission and is included as Appendix 16 of this report.

7. DIURNAL VARIABILITY OF INFRARED ATMOSPHERIC OXYGEN EMISSIONS AS OBSERVED FROM THE DELTA 181 MISSION

The Delta 181 satellite was a quick response multipurpose mission that operated for several days in a low inclination orbit at about 300 km altitude. Two cryogenically cooled CVF spectrometers providing continuous spectral coverage from 700 to 22000 nm (visible to LWIR) were part of the instrumentation package. Several observations of earthlimb emissions were successfully completed during the brief mission. Daytime, nighttime and dawn and dusk terminator emissions were observed with full spectral coverage. Although the CVF spectrometers had poor off-axis rejection and a large footprint at the tangent point, this data base offers the unique opportunity to understand oxygen chemistry near the mesopause. The Delta 181 data base provides a simultaneous observation of ozone ν_3 LWIR emission (proportional to ozone density), of $O_2 ^1\Delta$ emission at $1.58 \mu m$ (proportional to ozone during the day), and OH vibrational bands (proportional to H and ozone). Surprisingly, neither CIRRIS 1A nor MSX have instrumentation with the ability to perform these observations. Although we had reduced and analyzed the data as part of a previous program, we undertook comparison to photochemical models and previous field radiance observations as part of this program. The Delta 181 data again emphasizes that atmospheric ozone photochemical models appear unable to accurately predict nighttime ozone concentrations. This brief effort is summarized in a draft article for journal submission and included as Appendix 17.

8. MSX EARTHLIMB ANALYSES AND SUPPORT

The Midcourse Space Experiment provided an excellent multispectral earthlimb data base during the one year long cryogenic phase of its mission. Calibrated spectrometers and imagers/radiometers provided nearly continuous spectral coverage over the 110 to 26000 nm region.⁹ PSI provided technical assistance to the MSX Earthlimb team during the course of this program. The work involved coordinating and analyzing data from several Earthlimb experiments. Particular attention was paid to interpreting the results of the aurora of 10 November 1996 that was observed over Scandinavia. Aurora are important upper atmospheric excitation phenomena with critical systems implications. The Midcourse Space Experiment provided the first space-based observations of this phenomena with co-aligned and time synchronized instruments covering wavelengths from the hard ultraviolet into the long-wave infrared.

The aurora was bright, measuring in excess of 200 kR in the 3914 Å band, and was observed for a total of 19 minutes. The field-of-view of the sensors was maintained at a constant tangent height of 105 km. The UVISI ultraviolet and visible imagers acquired both narrow and wide-field data at a rate of two frames per second. SPIRIT III acquired data in all five IR bands with the mirror scan on creating 3 degree images. All five of the UVISI spectrographic imagers were employed as was the space-based visible camera.

Substantial auroral enhancements were observed in the ultraviolet and visible wavelengths. Auroral effects were also observed in three of the SPIRIT III infrared radiometer bands. SPIRIT III observed a strong 4.3 μ m enhancement of 10-20 times the ambient background above 100 km with smaller enhancements at lower altitudes (a fourfold enhancement at 95 km and a two-fold enhancement at 90 km). The strongest dosing regions in the UV and IR appear to coincide. A video presentation from all primary sensors [SBV (visible), SPIRIT III (IR radiometer), and UVISI (images and spectral resolved images)] clearly displayed this correlation.

A preliminary modeling evaluation determined that the strong CO₂ enhancements at lower altitudes requires 300 to 500 seconds pre-dosing (confirmed in late time observations). Preliminary AARC model comparisons produce a consistent altitude profile with the enhanced CO₂ data. The 4.3 μm enhancement is consistent with known sources and excitation mechanisms. The principal contributor is believed to be v-v transfer from vibrationally excited N₂. Another contributor to this wavelength region is NO⁺ emissions arising from ion-molecule reactions.

The enhancement in Band A (6 to 10.9 μm) is attributed to NO radiance above ambient levels produced from N(²D) + O₂. The IR enhancements are dynamic with rapid temporal variations and strong gradients.

This work was presented at the Spring AGU Conference in May 1997 and at the 1997 Meeting of the MSX Interim Results Review (IRR) in June 1997. The viewgraphs from these presentations are included as Appendices 18 and 19 respectively. Future analyses will rely upon insights gathered from sub-orbital and early orbital data bases, but the depth and spatial/temporal coverage of MSX data will supply the most useful data sets for model refinement and validation for many years to come.

9. REFERENCES

1. Paulsen, D. E., EXCEDE III Flight Report, Phillips Laboratory, Geophysics Directorate, Hanscom AFB 1993.
2. Ahmadjian, M., D. Jennings, M. Mumma, B.D. Green, B. Dix, R. Russell, "SKIRT Space Shuttle Glow Experiment," *J. Spacecraft and Rockets*, **29** (1), 102 (1992).
3. Ahmadjian, M., J. Wise, R. Nadile, B. Bartschi, "CIRRIS-1A Space Shuttle Experiment," *J. Spacecraft and Rockets* **27** (6), 669 (1990).
4. Rawlins, W.T., R. Armstrong, "Dynamics of vibrationally excited ozone formed by three-body recombination, I Spectroscopy," *J. Chem. Phys.* **87**, 5202 (1987); and Rawlins, W. T., G. E. Caledonia, and R. Armstrong, "Dynamics of vibrationally excited ozone formed by three-body recombination, II. Kinetics and mechanism," *J. Chem. Phys.* **87**, 5209 (1987).
5. Green, B.D., B.L. Upschulte, K. W. Holtzclaw, G. E. Caledonia, D. B. Oakes, M. E. Fraser, W. T. Rawlins, K. L. Carlton, D. M. Sonnenfroh, D. C. Rossi, H. C. Murphy, W. J. Marinelli, W. J. Kessler, J. C. Person, H. Du, C. L. Goldey, M. F. Hinds, P. A. Mulhall, "Infrared Excitation Efficiencies," PL-TR-94-2015, 3 Volumes, PSI-TR-1283 (1993).
6. Green, B. D., W. T. Rawlins, and R. M. Nadile, "Diurnal variability of vibrationally excited mesospheric ozone as observed during the SPIRE mission," *J. Geophys. Res.* **91**, 311 (1986).
7. Rawlins, W. T., M. E. Fraser, K. W. Holtzclaw, W. J. Marinelli, H. C. Murphy, L. G. Piper, "Ultrasensitive Infrared Chemiluminescence Detection," PL-TR-93-2266, PSI-TR-1277 (1993).
8. Morgan, W. L. and Penetrante, B.M., "ELENDIF: A Time-Dependent Boltzmann Solver for Partially Ionized Plasmas," UCRL-100820, Lawrence Livermore National Laboratory, 1989.
9. Mill, J. D., R. R. O'Neil, S. Price, G. J. Romick, O.M. Uy, E. M. Gaposchkin, G. C. Light, W. W. Moore Jr., T. L. Murdock, and A. T. Stair, Jr., "Midcourse Space Experiment: Introduction to the Spacecraft, Instruments, and Scientific Objectives," *J. Spacecraft and Rockets* **31**(5), 900 (1994).

APPENDIX 1

Dosing, Altitude Dependence, and Excitation Mechanisms of NO Vibraluminescence Observed in the EXCEDE III Mission

**DOSING, ALTITUDE DEPENDENCE, AND EXCITATION
MECHANISMS OF NO VIBRALUMINESCENCE
OBSERVED IN THE EXCDE III MISSION**

**Mark Fraser, Terry Rawlins, and B.D. Green
Physical Sciences Inc.**

**Duane Paulsen, Pete Armstrong,
Steve Lipson, and Bill Blumberg
Phillips Laboratory**

**Randall Murphy
Research Sciences Corporation**

**Presented at the Spring AGU Meeting
May 1993**

Sponsored by the Defense Nuclear Agency

EXCÉDE III NITRIC OXIDE ANALYSIS PLAN

T-16741

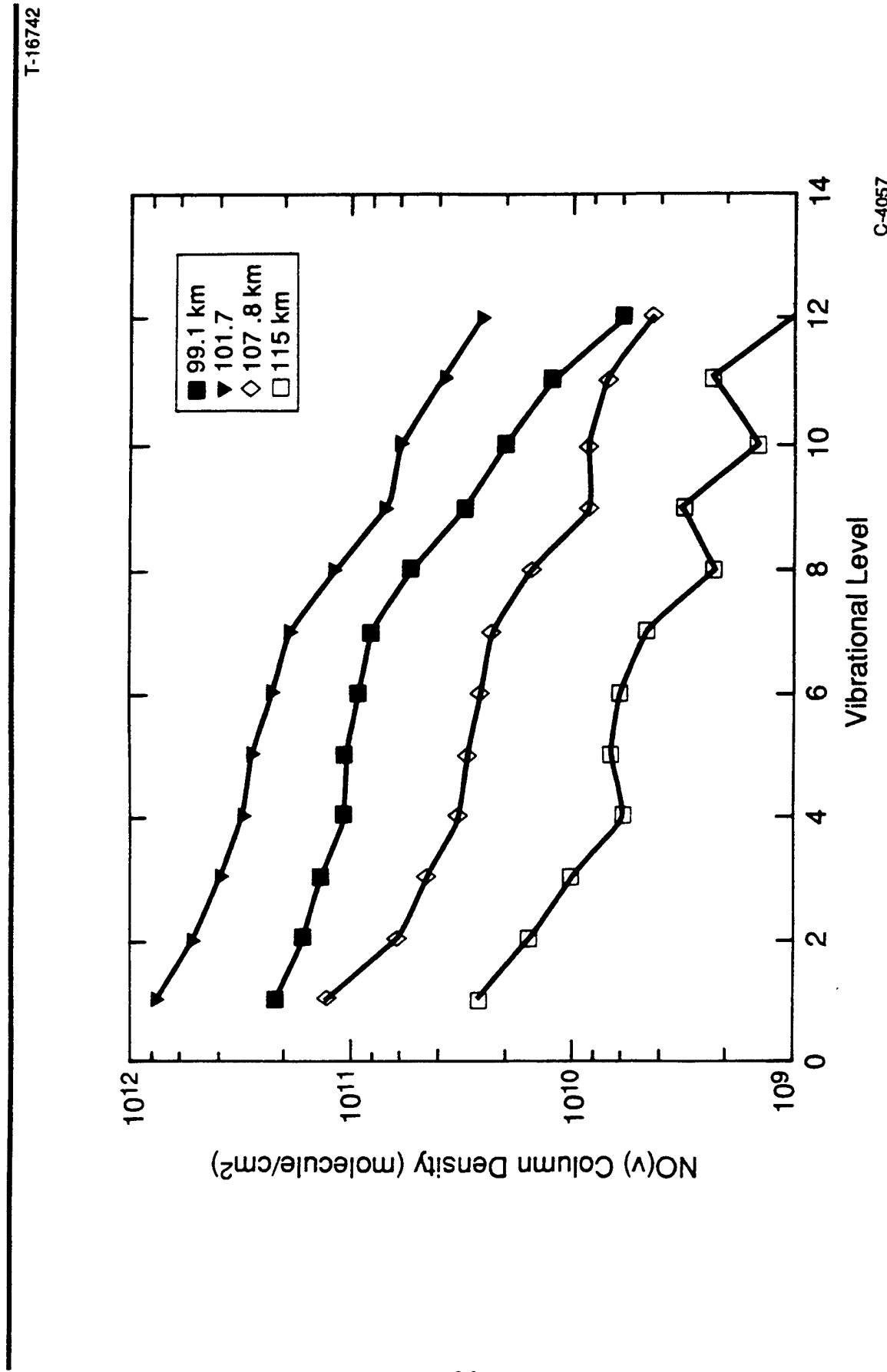
- Electron guns locally deposit energy into lower thermosphere
 - $[e] \sim 10^9 \text{ cm}^{-3}$ in a 10m wide beam
 - $[e] \sim 10^3$ times higher than IBC III aurora
 - Accentuate non-linear processes
- Beam induced NO vibrational emission observed over 95 to 115 km altitudes
- Detailed spectroscopic analyses permit isolation of emitting NO_v, J levels
 - Agree with previous laboratory determinations
 - At least two rotational distributions (quasi-continuum?)
- Observe altitude scaling of radiances, ro-vibrational distributions, and densities
- Scalings provide insight into excitation mechanisms and precursor fates

NO EXCITATION MECHANISMS

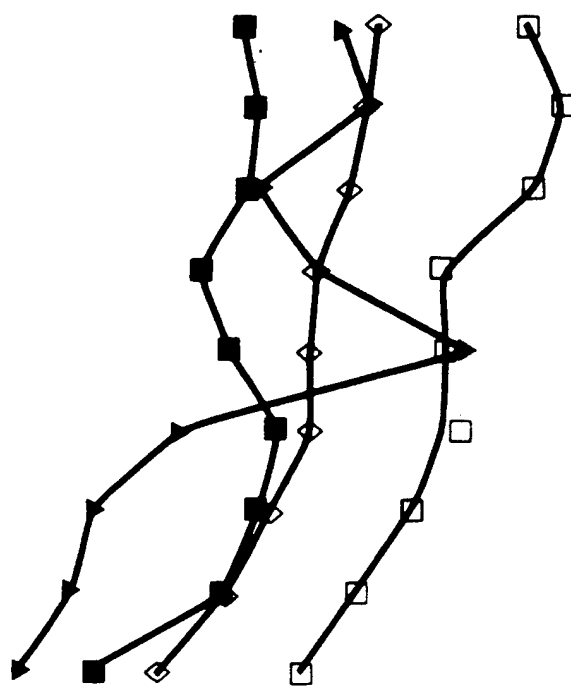
T-12518

- COCHISE mechanism
 - $N(^2P) + O_2 \rightarrow NO(X) + O(3P)$ 4.956 eV
 - $\rightarrow NO(X) + O(1D)$ 2.988 eV
 - $\rightarrow NO(X) + O(1S)$ 0.766 eV
 - $\rightarrow NO(4\Pi) + O(3P)$ 0.143 eV
- $N(^2D) + O_2 \rightarrow NO(X) + O(3P)$ 3.76 eV
- $\rightarrow NO(X) + O(1D)$ 1.8 eV
- Energetics acceptable, hot band source term crucial
- Energy transfer
 - $N^*, N_2^* + NO$
 - Observed in COCHISE but vibrational distributions dissimilar to EXC EDE
 - $O + N_2^*$
 - Possible but never observed
 - $O(\text{fast}) + NO, N_2$
 - Experiments in progress

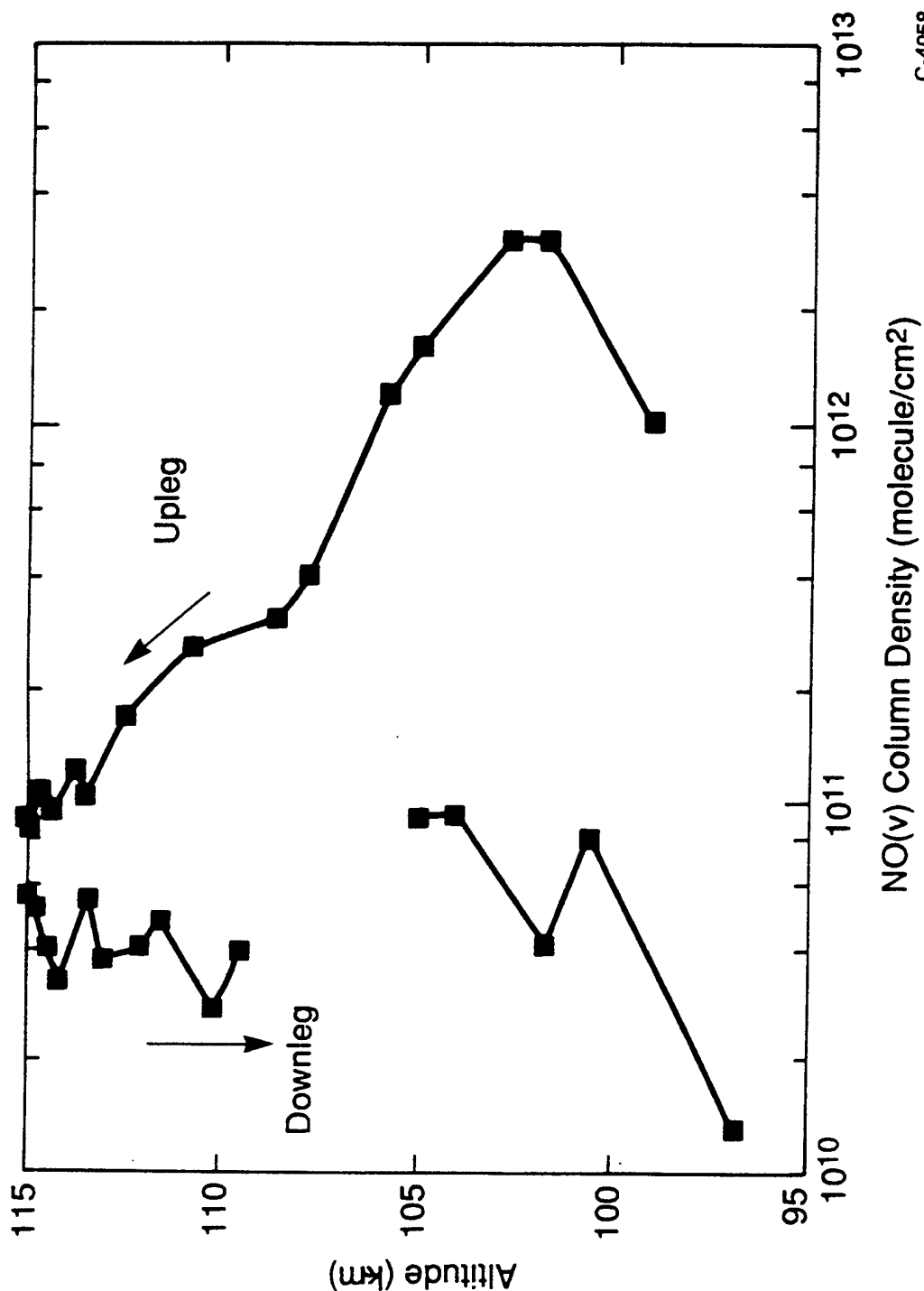
NO VIBRATIONAL DISTRIBUTIONS: UPLEG LOW-J



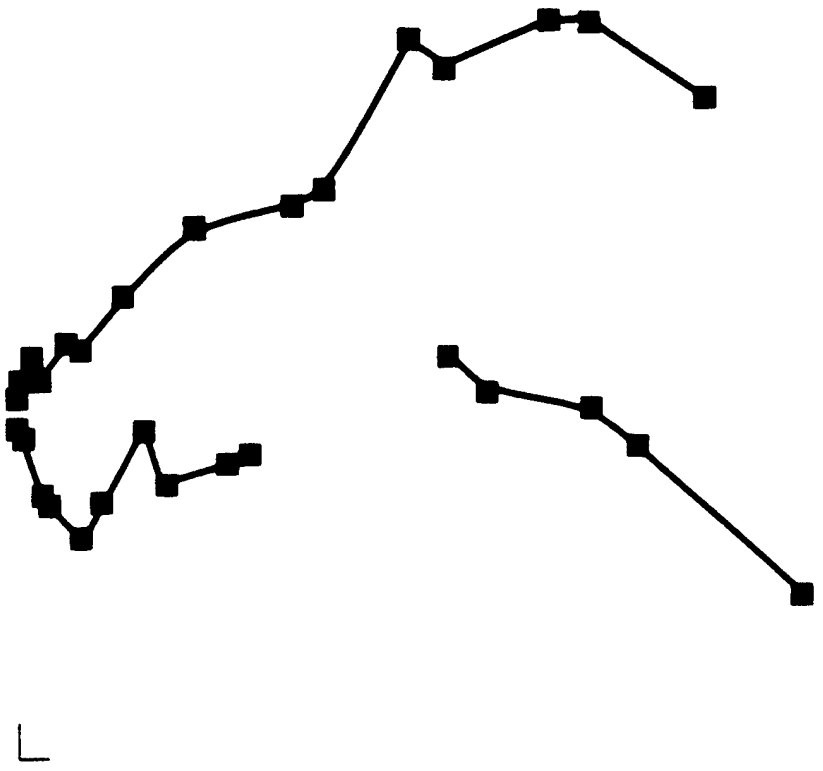
HIGH-J



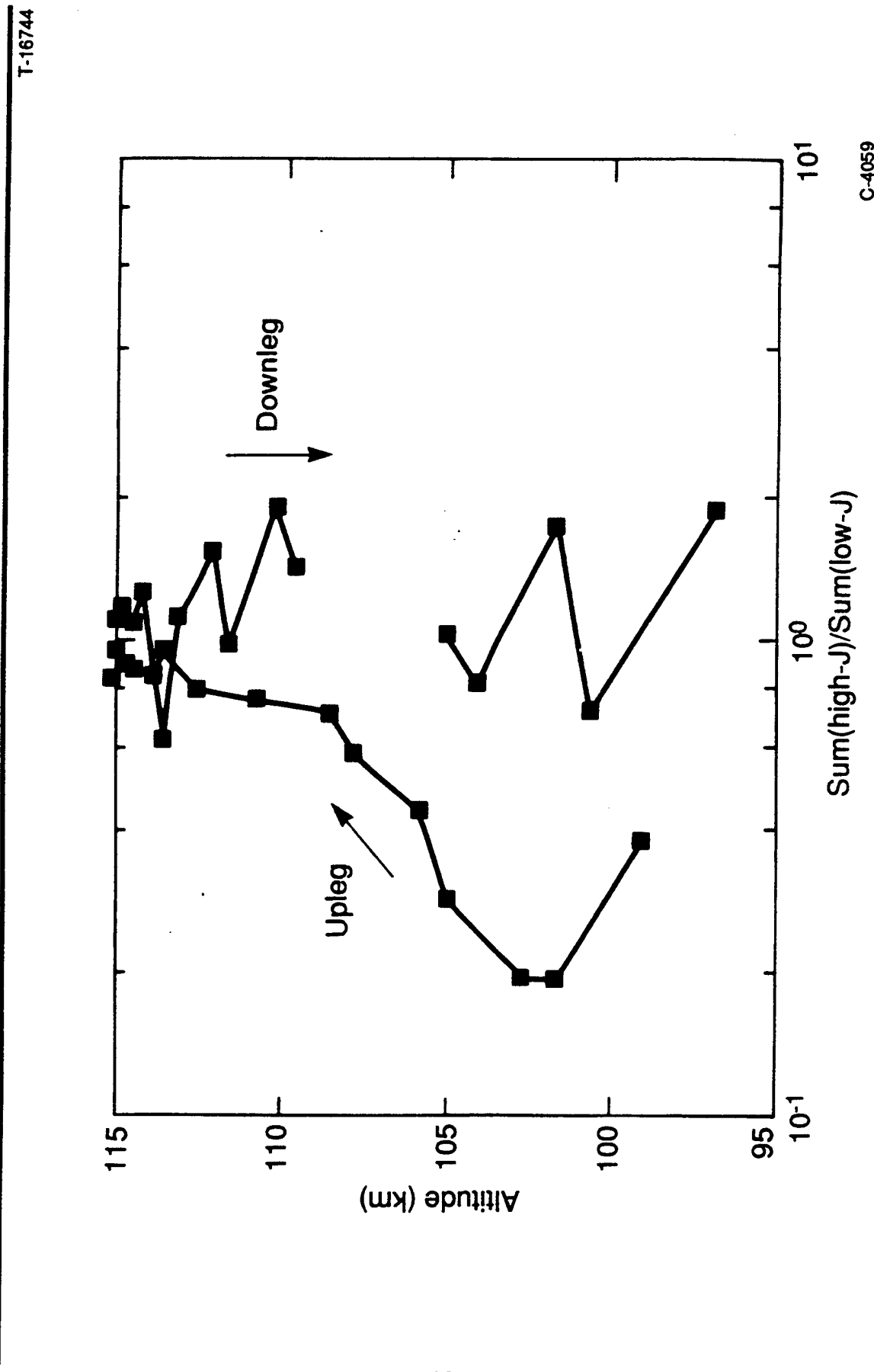
TOTAL NO_x DENSITY LOW-J COMPONENT



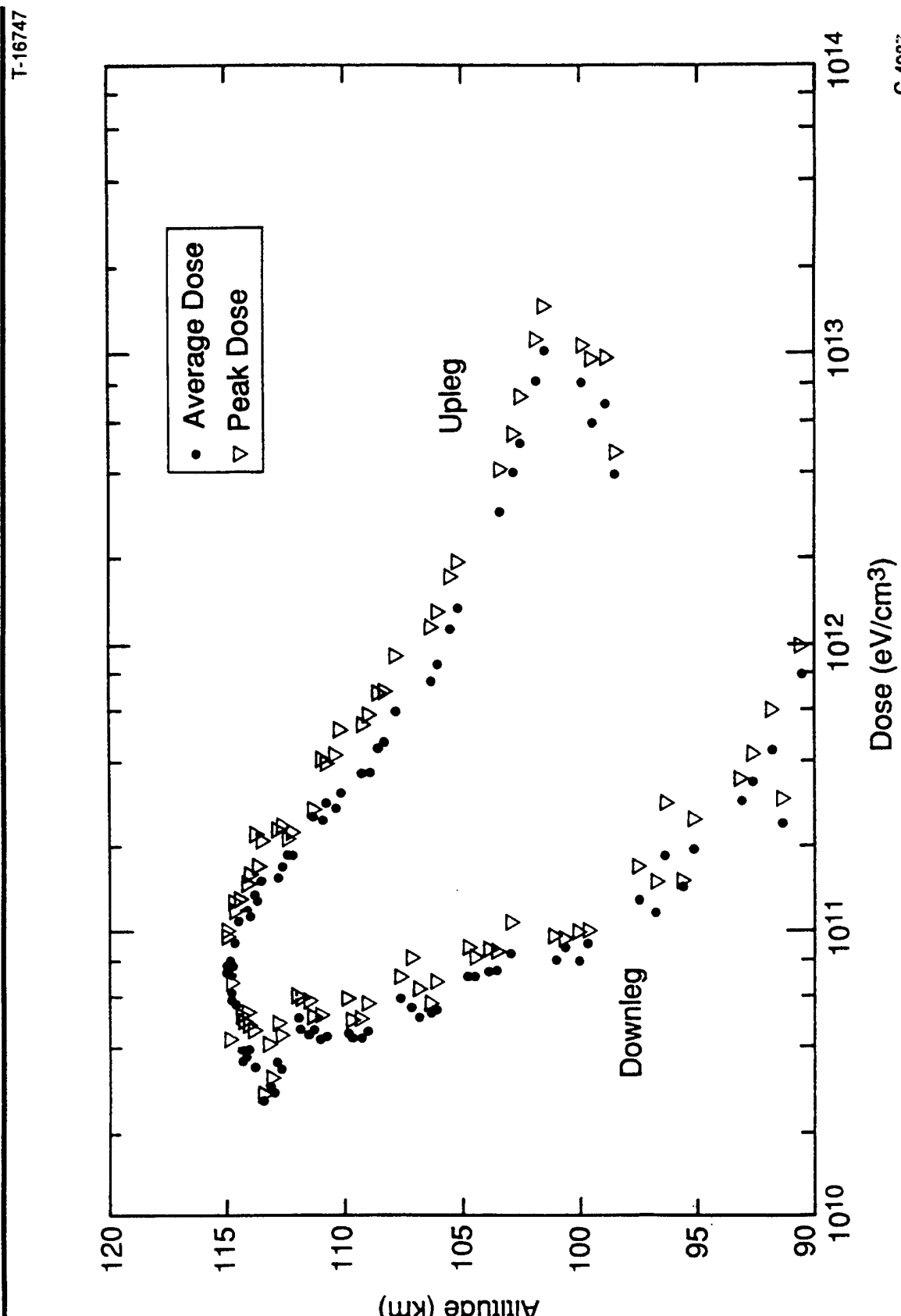
HIGH-J COMPONENT



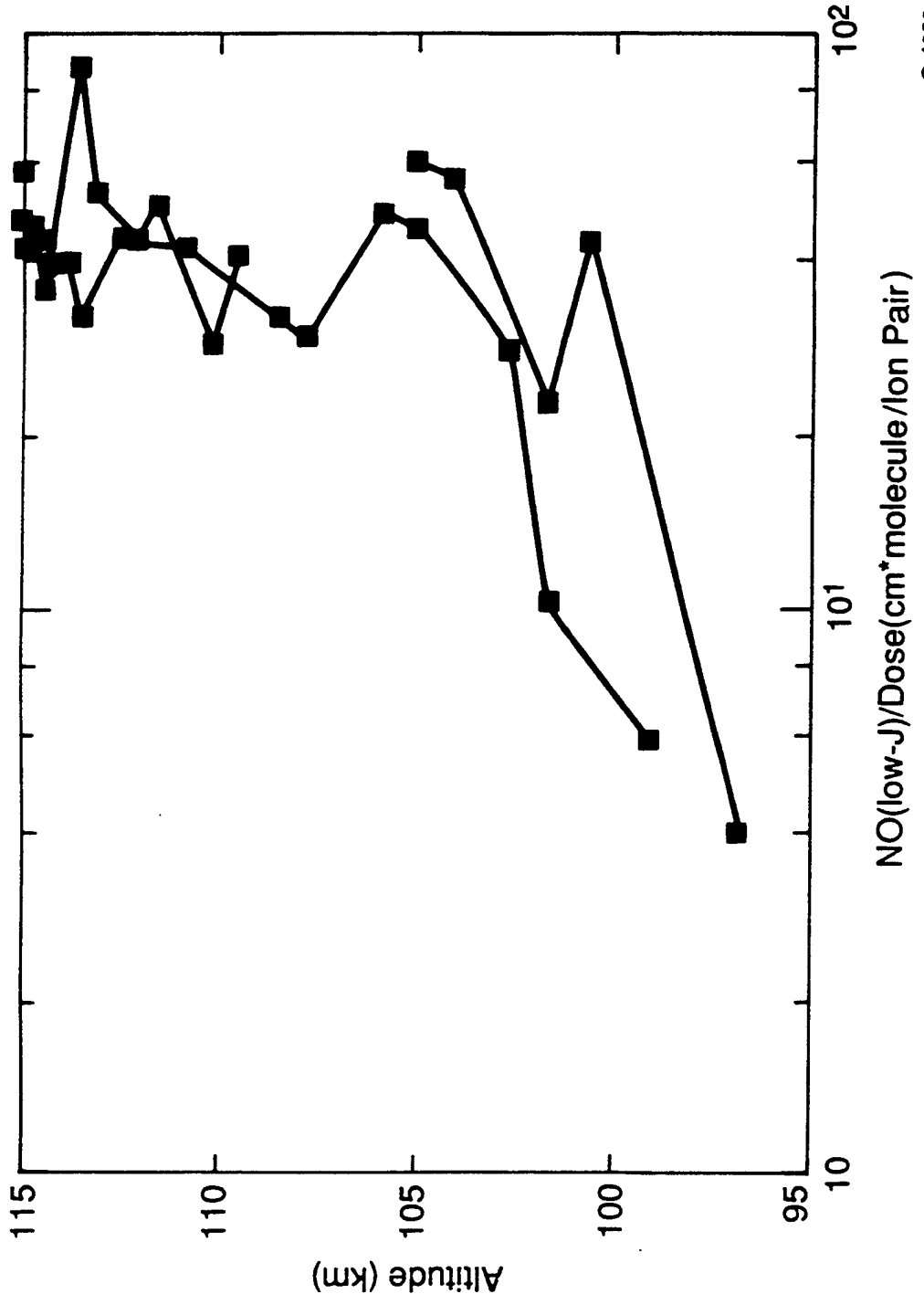
RATIO: HIGH-J/ THERMAL COMPONENTS OF NO



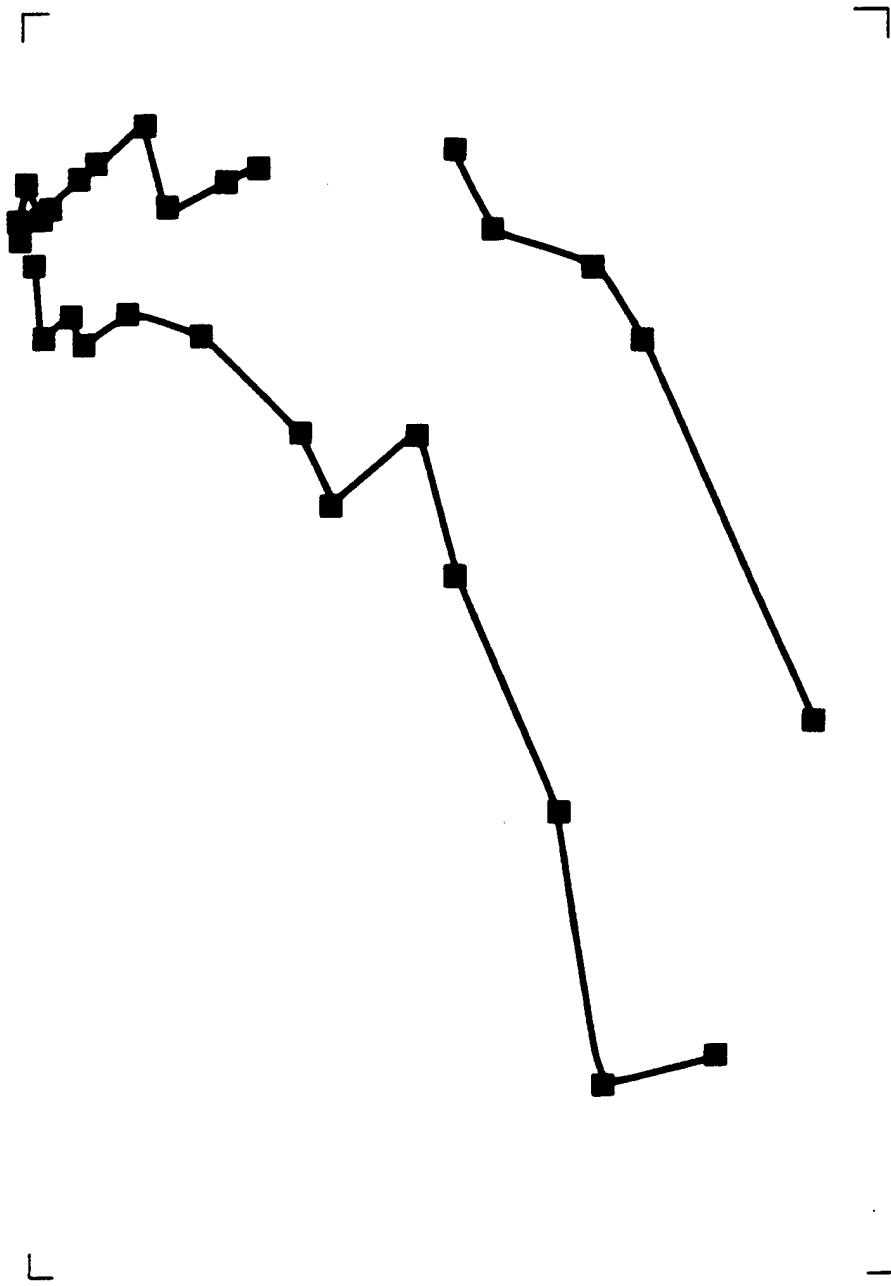
EXC EDE III ENERGY DEPOSITION



DOSING EFFICIENCY: THERMAL COMPONENT



HIGH-J COMPONENT



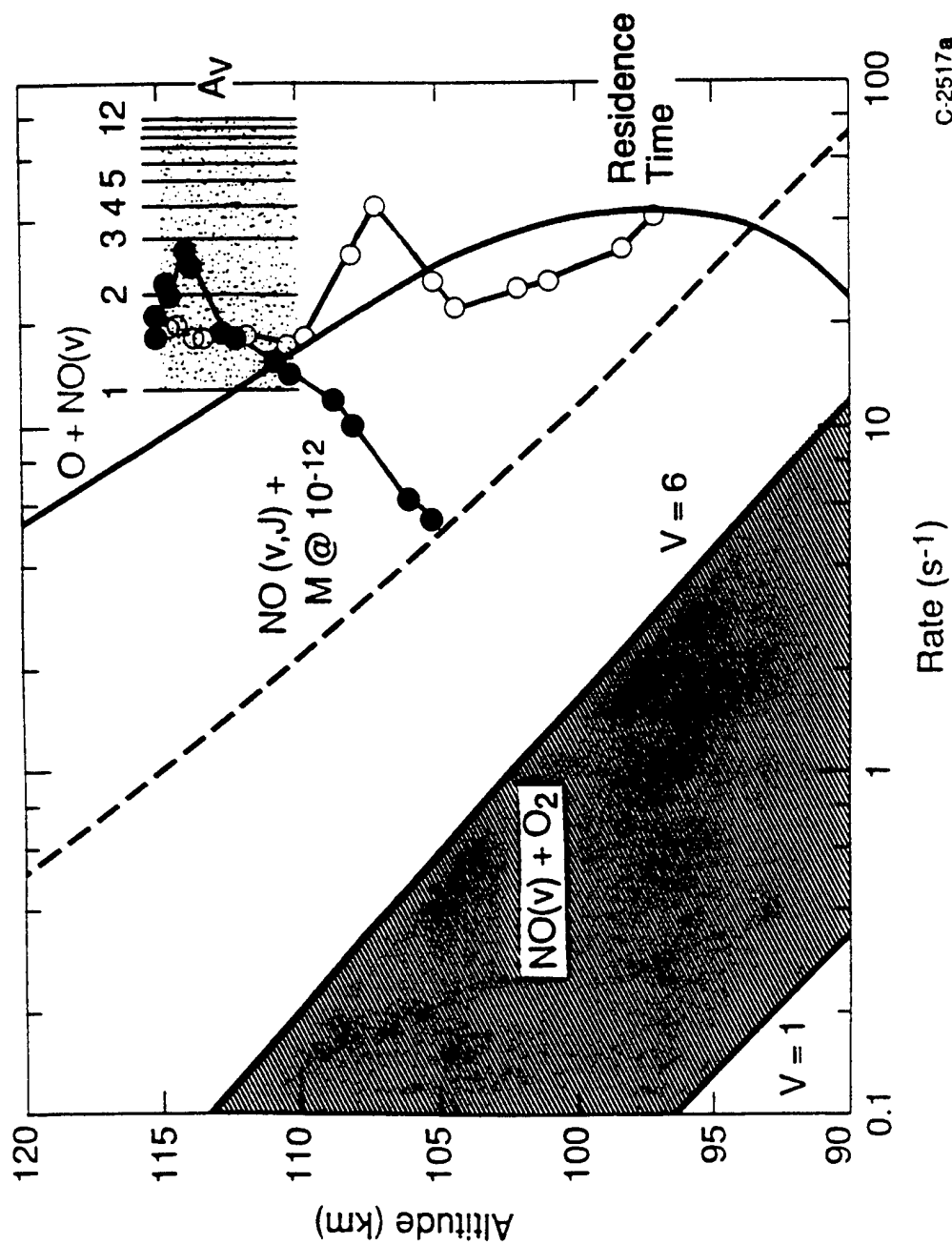
KEY PROCESSES FOR EXCDE

T-12853

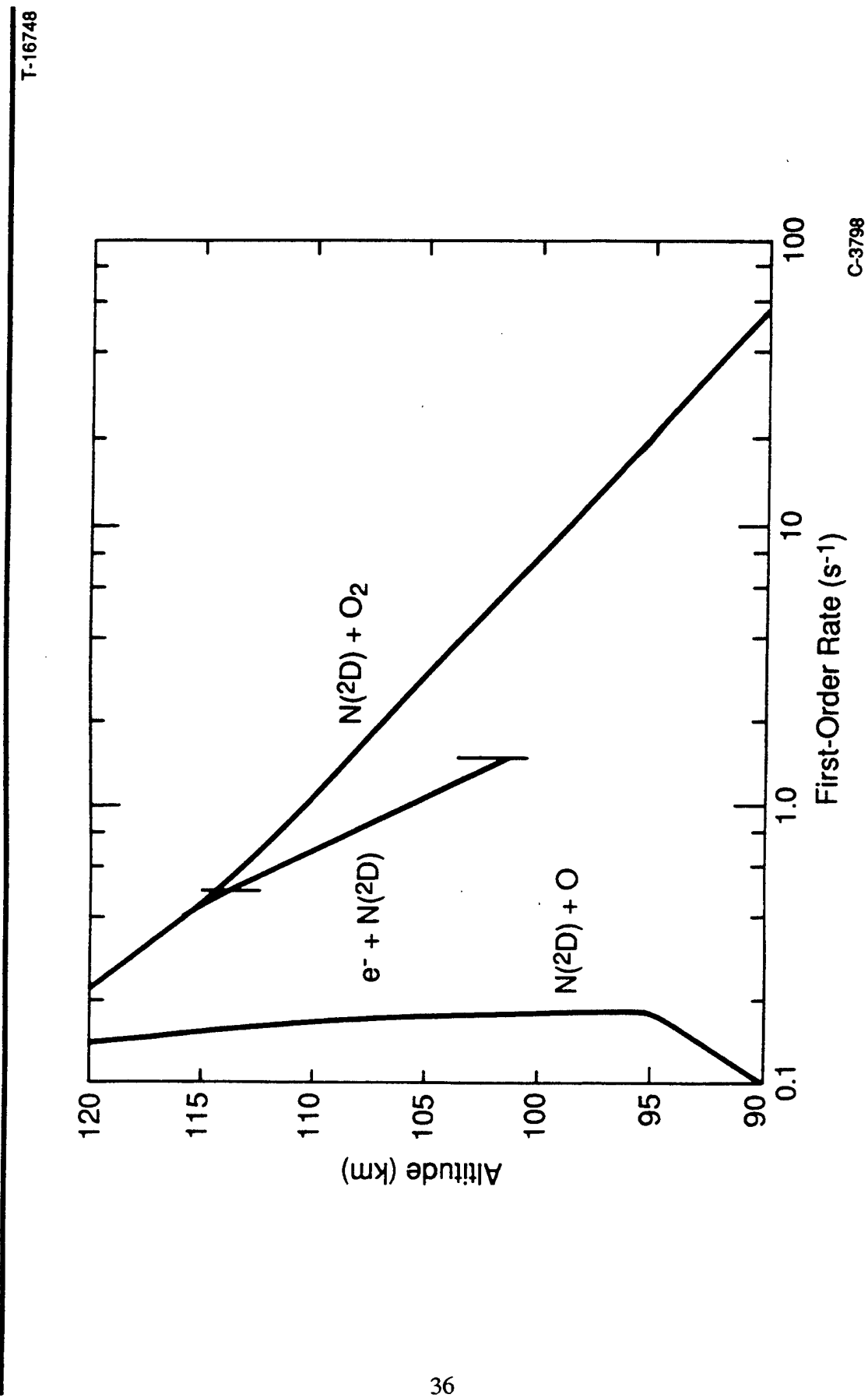
- N^{*} sources
 $e^- + \{N_2, N_2^+, NO^+\}$
 $e^- + N^2P \rightarrow N^2D + e^- \quad (\underline{\text{upleg}})$
~1 to 2 N^{*} per ion pair
- N^{*} losses / reactions
 $N(^2D, ^2P) + O_2$
 $N^2P + e^- \quad (\underline{\text{upleg}})$
 $N^2P + O \quad (\underline{\text{upleg}}, \text{ minor})$
- NO(v, J) deactivation
 $O + NO(v) \quad (\underline{\text{upleg}}, \text{ minor?})$
 $NO(v, J) + M \quad J \text{ cooling}, J \rightarrow V?$
Radiative cascade
- Transport controls yield, distributions for apogee and downleg

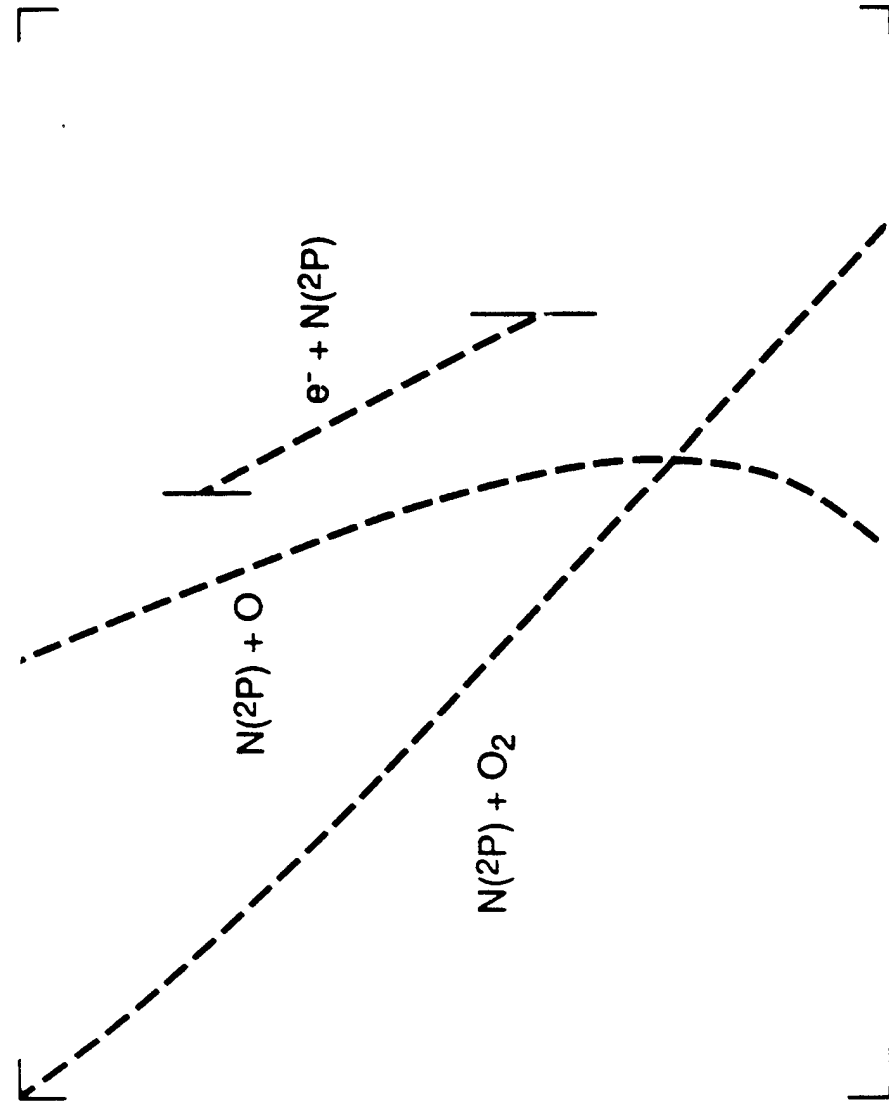
EXCEED III (NO)V LOSS RATES

T-16746



N* PRECURSOR REACTION RATES





CONCLUSIONS AND REMAINING ISSUES

T-16749

- Large beam induced NO production observed
 - Verifies previous observations of laboratory and auroral enhancements
- EXCDE NO(v, J) spectra are consistent with $N^* + O_2$ source as in COCHISE
- Emission efficiency of hot J production drops as dose increases
(precursor quenching)
- Does N(2P) play a role?
 - Spectral features suggest 4 eV internal energies
 - Long wavelength cutoff also indicates 3.9 eV states
 - Max dose behavior consistent with $e^- + N^2P$ quenching.
- Hot N* may affect distributions, production rates

APPENDIX 2

Kinetics and Mechanisms for the Formation of Rovibrationally-Excited
Nitric Oxide in the EXCEDE III Rocket Experiment

**KINETICS AND MECHANISMS FOR THE FORMATION
OF ROVIBRATIONALLY-EXCITED NITRIC OXIDE
IN THE EXCÈDE III ROCKET EXPERIMENT**

**M.E. Fraser, W.T. Rawlins, and B.D. Green
Physical Sciences Inc.**

**D.E. Paulsen, P.S. Armstrong, S.J. Lipson, and W.A.M. Blumberg
Phillips Laboratory/GPOS**

**R.E. Murphy
Research Sciences Corp.**

**1993 Fall Meeting
American Geophysical Union**

Sponsored by the Defense Nuclear Agency

December 1993

The EXCIDE III rocket experiment observed UV, visible, and infrared fluorescence from the lower thermosphere excited by an electron beam. High resolution Fourier transform spectra obtained by a cryogenic interferometer show the presence of highly rotationally and vibrationally excited NO($X^2\Pi$) over a wide range of dosing conditions and altitudes. We examine these variations in terms of the kinetics of the known or expected excitation and deactivation processes for NO(v,J) in the upper atmosphere. Candidate excitation processes include:



These reactions appear to be responsible for much of the observed excited NO at the lower altitudes and higher dosing levels. However, additional, previously unidentified processes are clearly important, especially near apogee. Kinetic modeling calculations suggest that rotationally/vibrationally excited NO(v,J) is rapidly formed at high altitudes by reactions(s) of translationally hot N(2D and/or $4S$) with O₂. We discuss the possible excitation reactions in terms of the kinetic constraints imposed by the spectral measurements

INTRODUCTION AND BACKGROUND

T-18882

- Previous observations of NO(v,J)
 - Laboratory (*J. Phys. Chem.* 93, 1097 (1989))
 - $\text{N}^{\text{2D}} + \text{O}_2 \rightarrow \text{NO}(\nu) + \text{O}$, $\nu=1$ to 14, rotationally thermal
 - $\text{N}^{\text{2P}} + \text{O}_2 \rightarrow \text{NO}(\nu, J) + \text{O}$, $\nu=1$ to 9, $J \geq 80$ band heads
 - Rocketborne (Picard et al., 1987): bandheads in overhead aurora
 - CIRRISS 1A: aurora and dayglow (See Poster SA42C-6)
 - Additional high-J excitation mechanisms are suspected
- EXCEDE III measurements
 - Electron-irradiated lower thermosphere
 - 2 cm^{-1} cryogenic interferometer views excitation volume
 - Copious NO(v,J) excitation 95 to 115 km

EXCÉDE III NITRIC OXIDE ANALYSIS

T-18883

- Electron guns locally deposit energy into lower thermosphere
 - $[e] \sim 10^9 \text{ cm}^{-3}$ in a 10m wide beam
 - $[e] \sim 10^3$ times higher than IBC III aurora
 - Accentuate non-linear processes
- Beam-induced NO vibrational emission observed over 95 to 115 km altitudes;
 $J \geq 80$ band heads clearly evident throughout
- Detailed spectroscopic analyses permit isolation of emitting NO(v, J) levels
 - Similar to previous laboratory determinations
 - At least two rotational distributions (quasi-continuum?):
thermal (200 to 300 K) and "high- J " (6000 to 8000 K)
- Observe altitude scaling of radiances, rovibrational distributions,
and densities
- Scalings provide insight into excitation mechanisms and precursor kinetics

REGIMES AND PROCESSES SAMPLED BY EXCÉDE INTERFEROMETER

T-18884

Altitude

- High-J collisional cooling
- Missing chemistry

Dosing

- Precursor production rates
- Electron quenching
- Non-linear effects

Residence Time

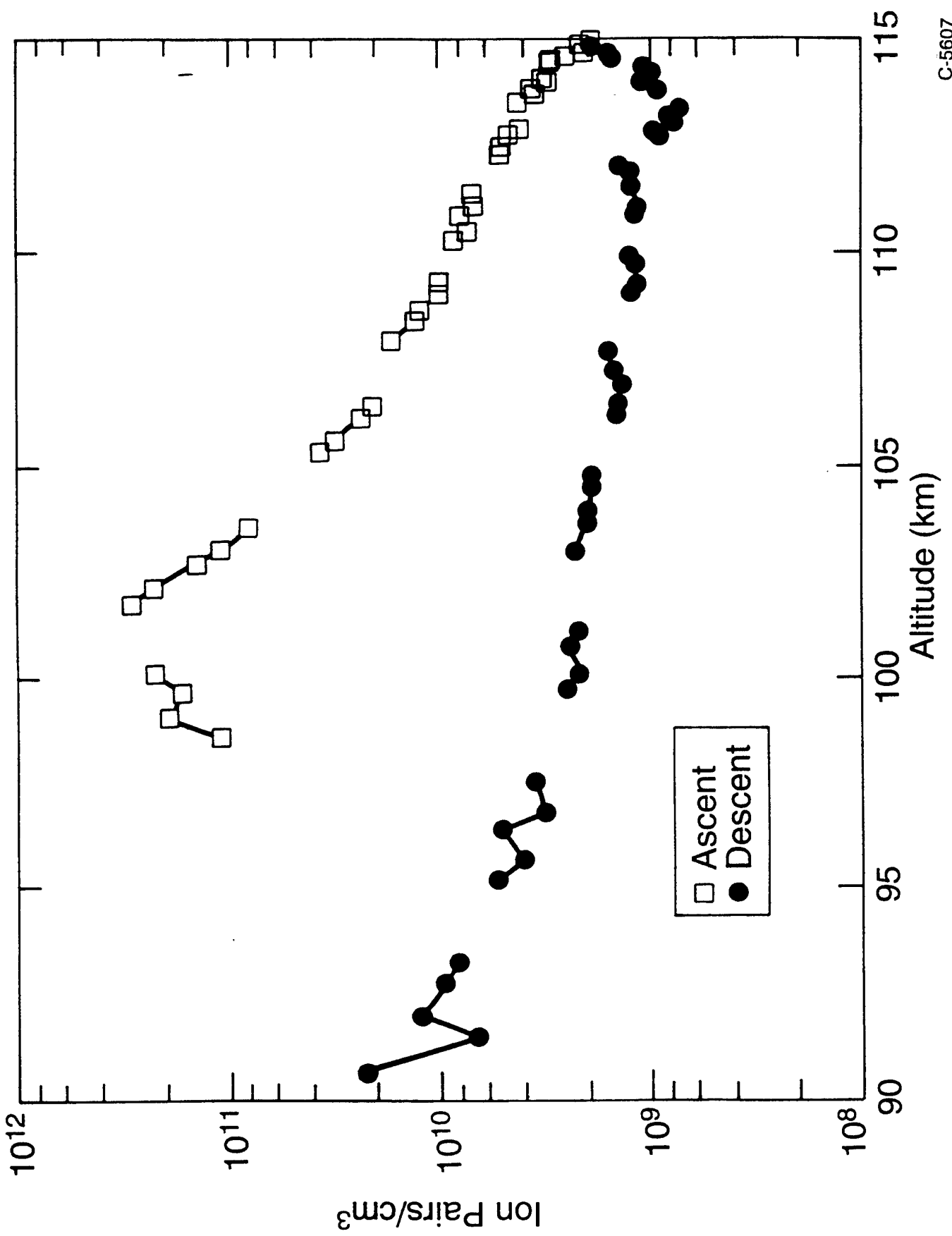
- Collisional quenching
- Steady state versus initial rates

TITLE

T-18

This figure shows the time-integrated number density of ion pairs created in the viewed beam volume for each electron beam cycle, taking account of the gas residence time in the viewed beam volume. The altitude of maximum dosing is between 100 and 105 km on ascent. Much weaker dosing levels are observed near apogee and on descent, owing primarily to shorter residence times. (See Posters SA42C-2, -3 for more discussion of viewing geometry and dosing.)

TOTAL ION PAIRS CREATED PER cm³



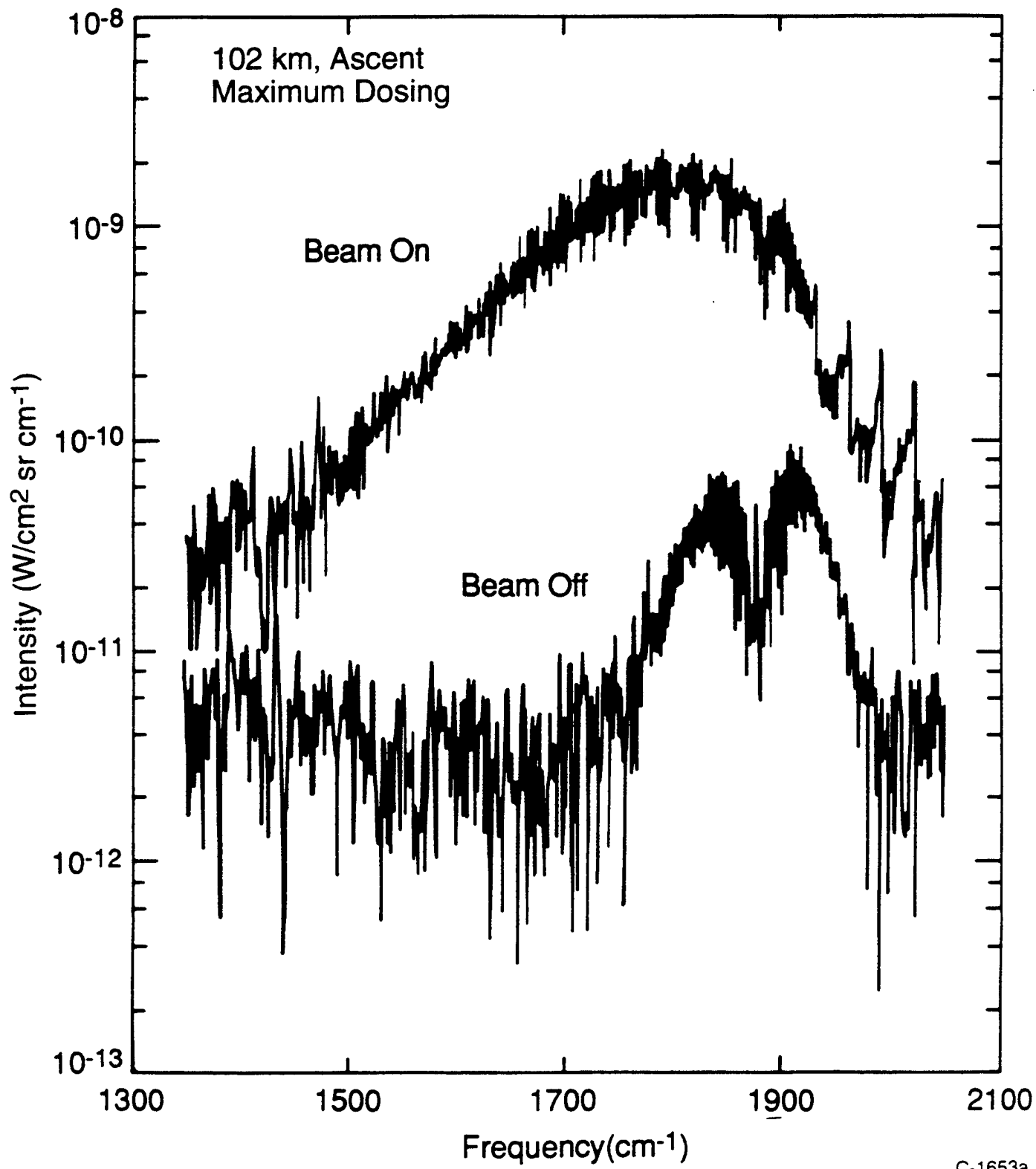
TITLE

T-18885-
T-18890

This figure shows nitric oxide spectra observed near the maximum dosing altitude with the beam on and with the beam off. Both the intensity and the spectral (rotational and vibrational) distribution of the fluorescence are governed by processes initiated by the electron bombardment. We have used a linear least squares spectral fitting analysis to determine the vibrational state populations. The wide variation in rotational state populations was approximated by a bimodal distribution containing rotationally thermal and rotationally hot ($T_{\text{rot}} = 8000 \text{ K}$) components, each with a separate vibrational population distribution determined by the fitting procedure. (See Poster SA42C-5 for additional discussion of the spectral analysis.)

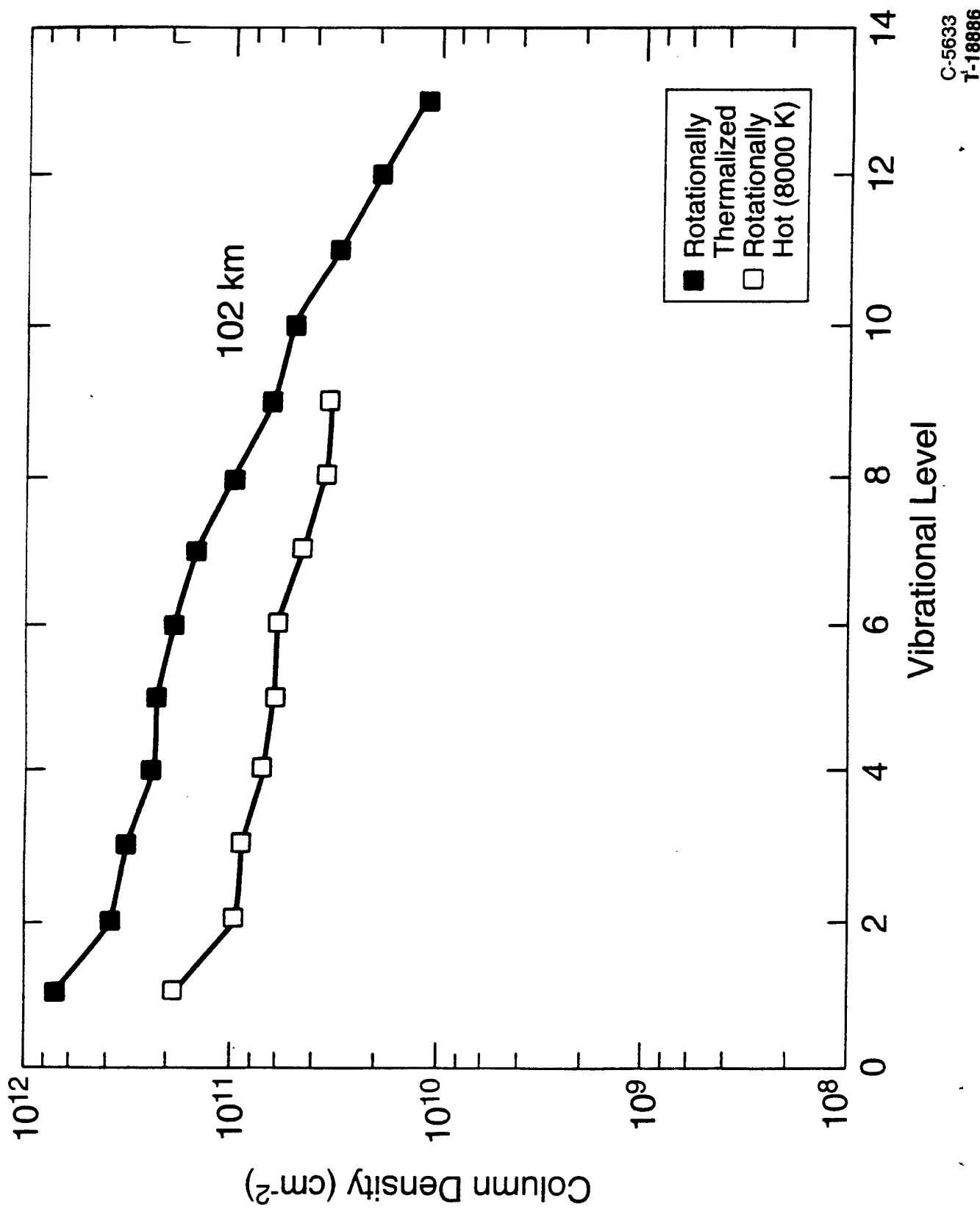
The following figures show vibrational distributions, excited state number densities, and formation efficiencies determined via the spectral fitting analysis.

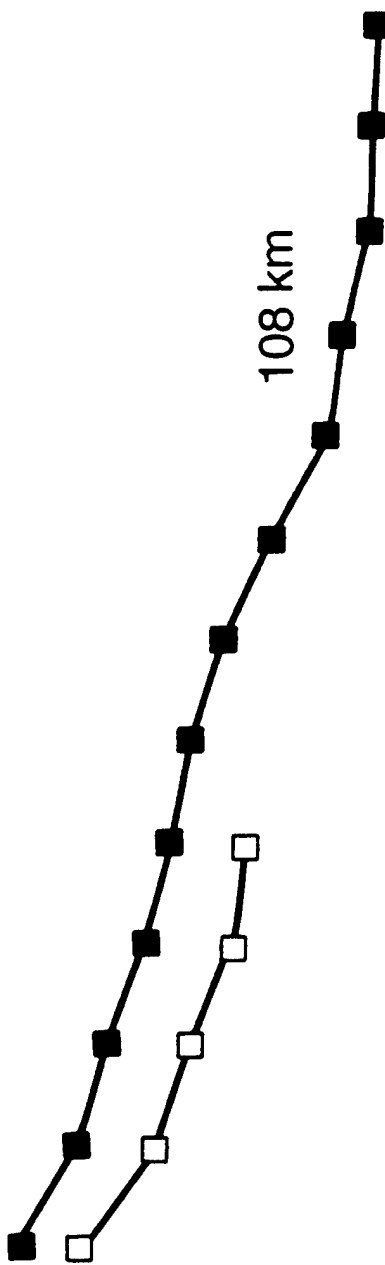
EXCEDE III NO(v,J) SPECTRA

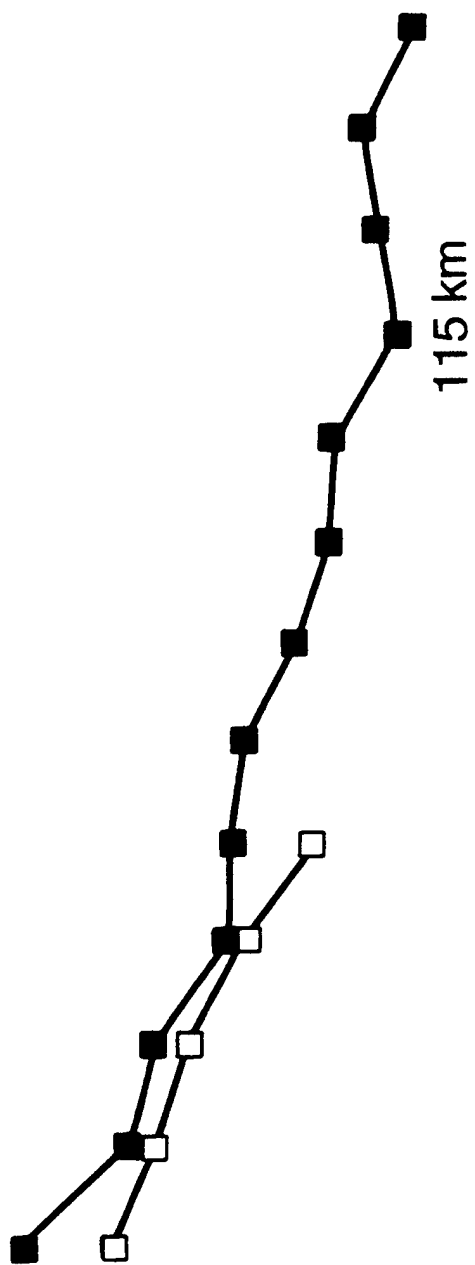


C-1653a
T-18885

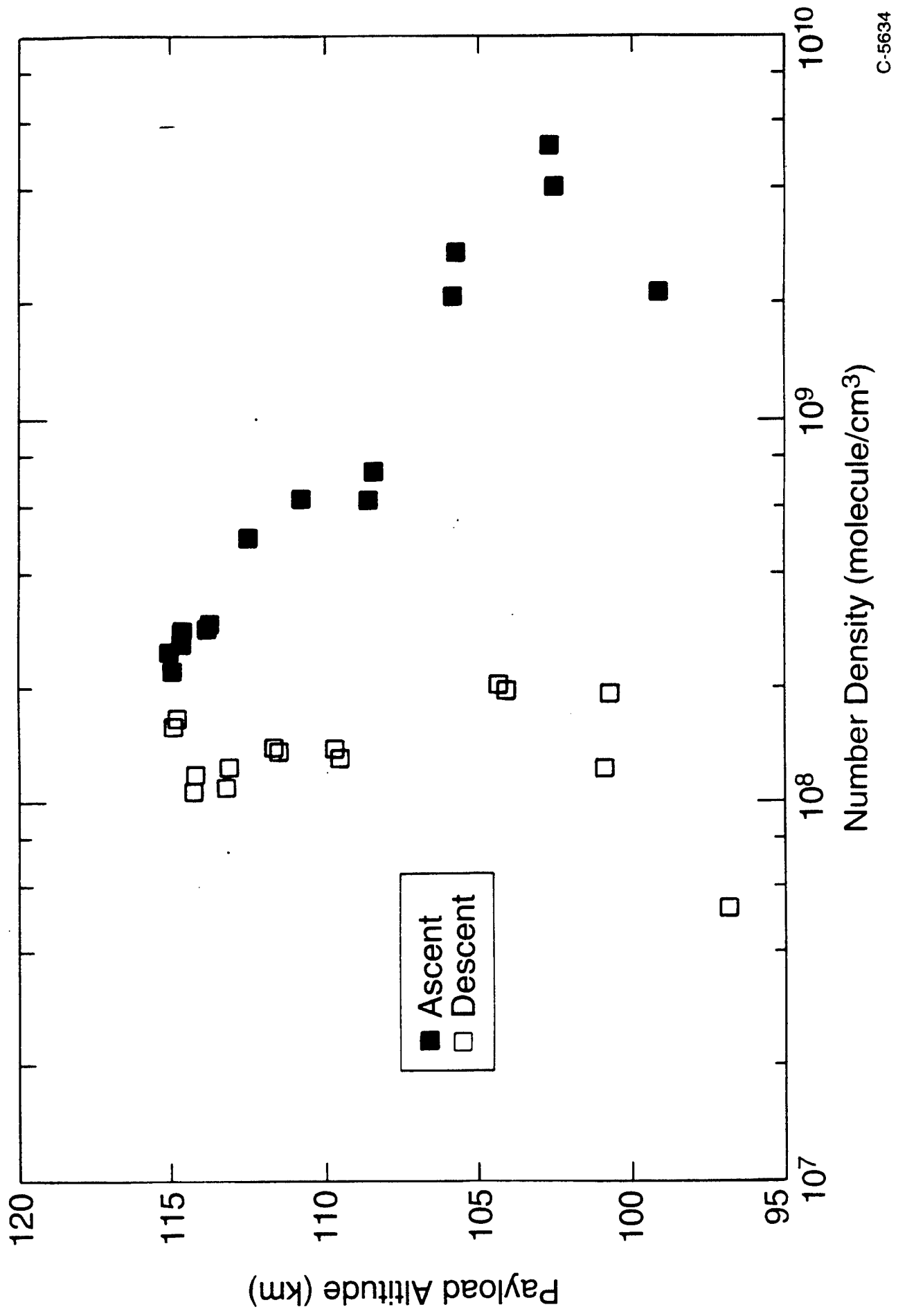
OBSERVED VIBRATIONAL DISTRIBUTIONS: ASCENT





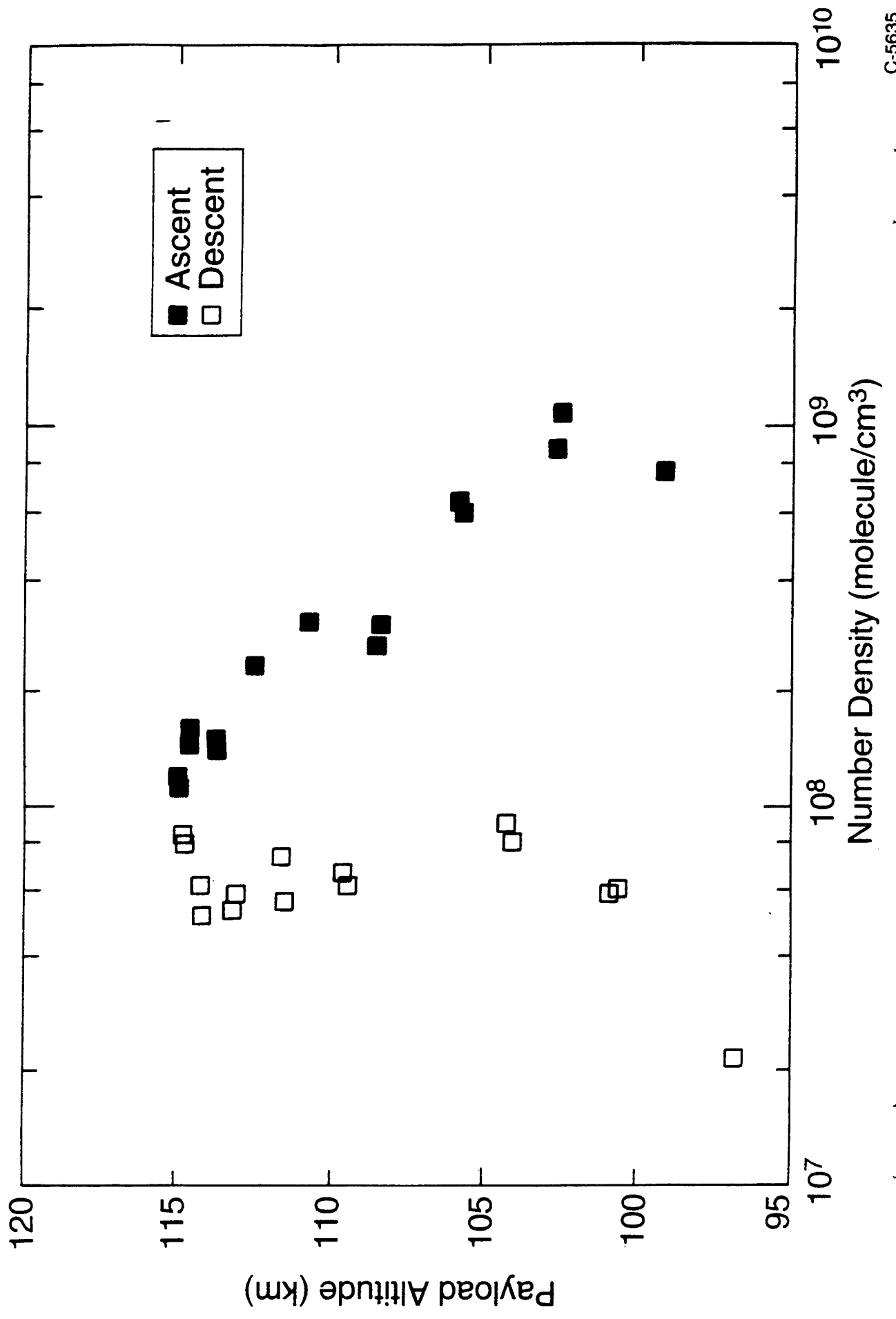


NO(v) NUMBER DENSITIES: LOW-J COMPONENT

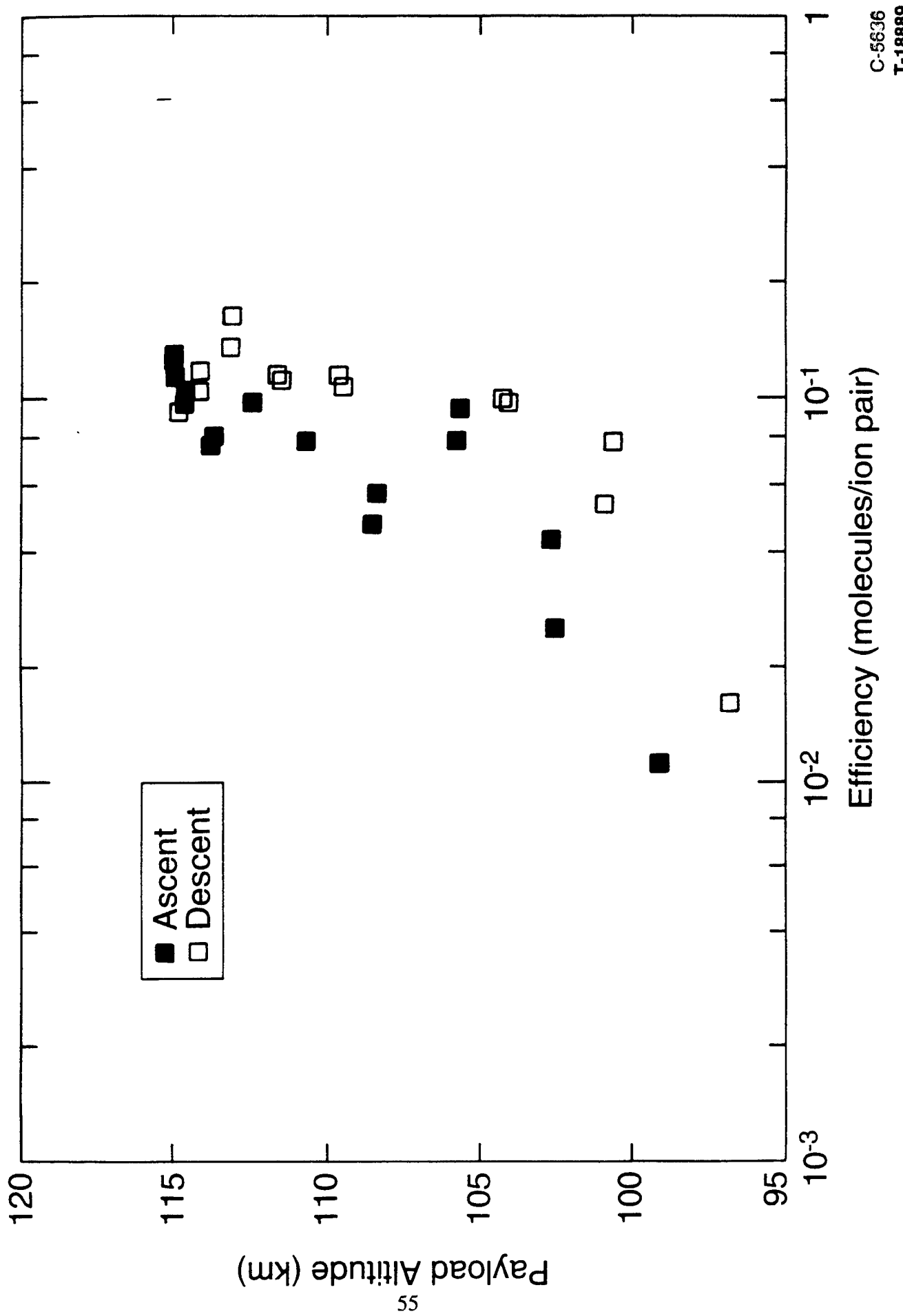


C-5634
T-18887

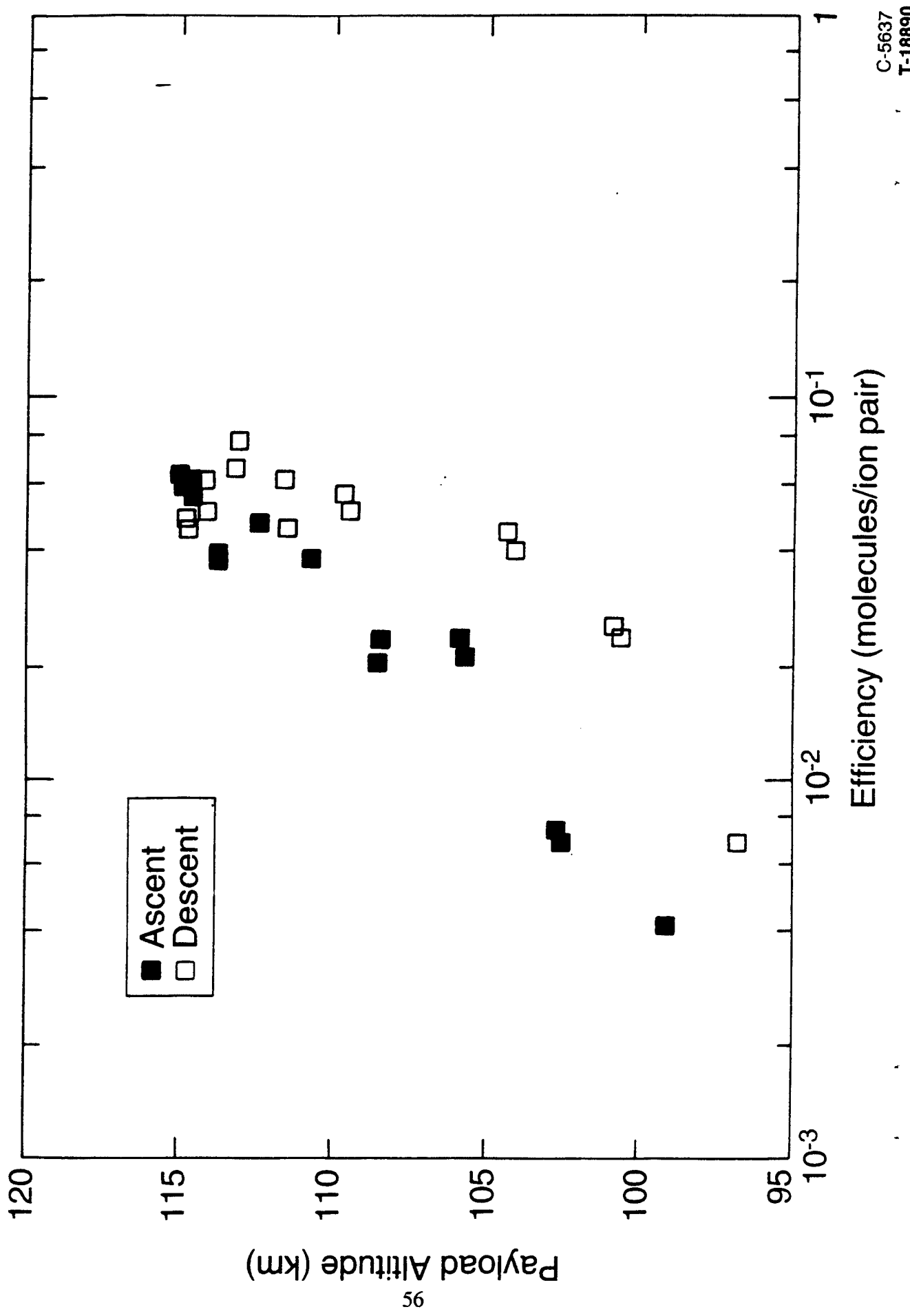
NO(v,j) NUMBER DENSITIES: HIGH-j COMPONENT



NO(v) PRODUCTION EFFICIENCIES: LOW-J



NO(v,J) PRODUCTION EFFICIENCIES: HIGH-J



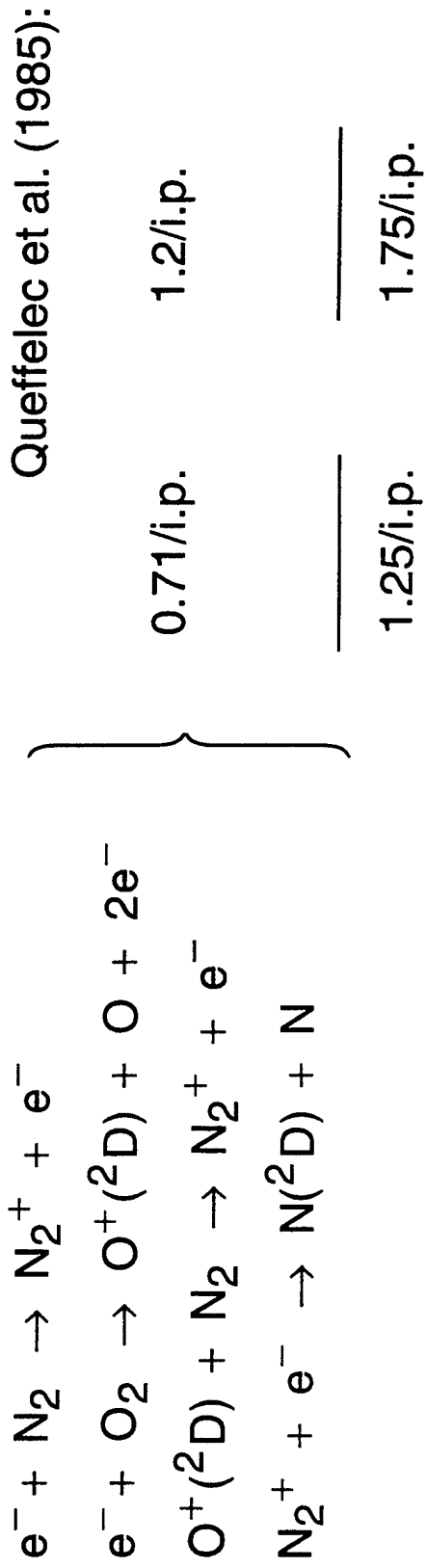
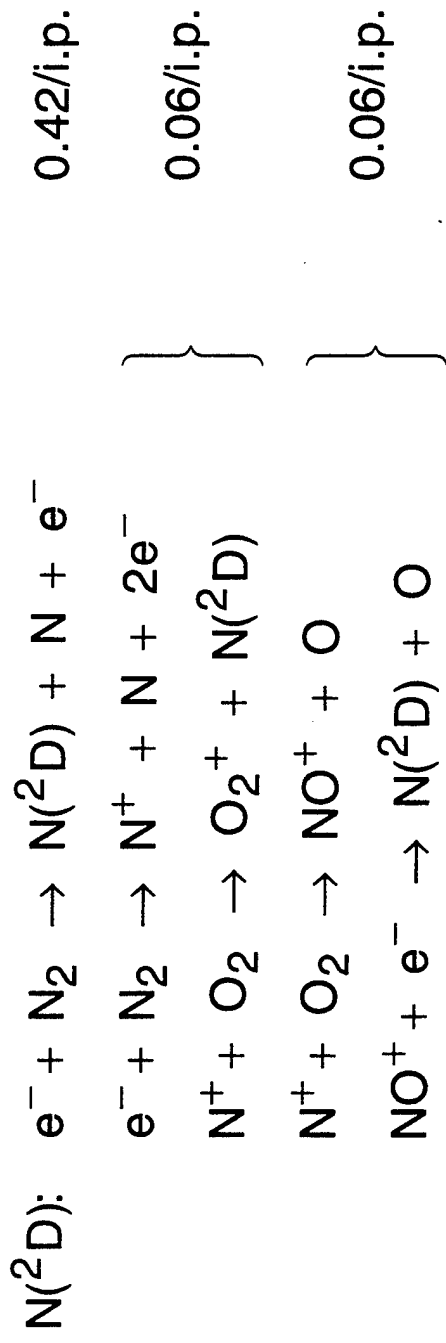
KEY PROCESSES FOR EXCDE

T-18891

- N^{*} sources
 - e⁻ + {N₂, N₂⁺, NO⁺}
 - e⁻ + N^{2P} $\xleftrightarrow{*}$ N^{2D} + e⁻
 - ~1 to 2 N^{*} per ion pair
- N^{*} losses/reactions
 - N(^{2D}, ^{2P}) + O₂ \rightarrow NO(v, J) + O
 - N^{2P} + e⁻
 - N^{2P} + O
- NO(v, J) deactivation
 - O + NO(v) (minor)
 - NO(v, J) + M
 - Radiative cascade
- Short residence time controls yield, distributions for apogee and descent

N* PRODUCTION (Gilmore, 1985)

T-18892

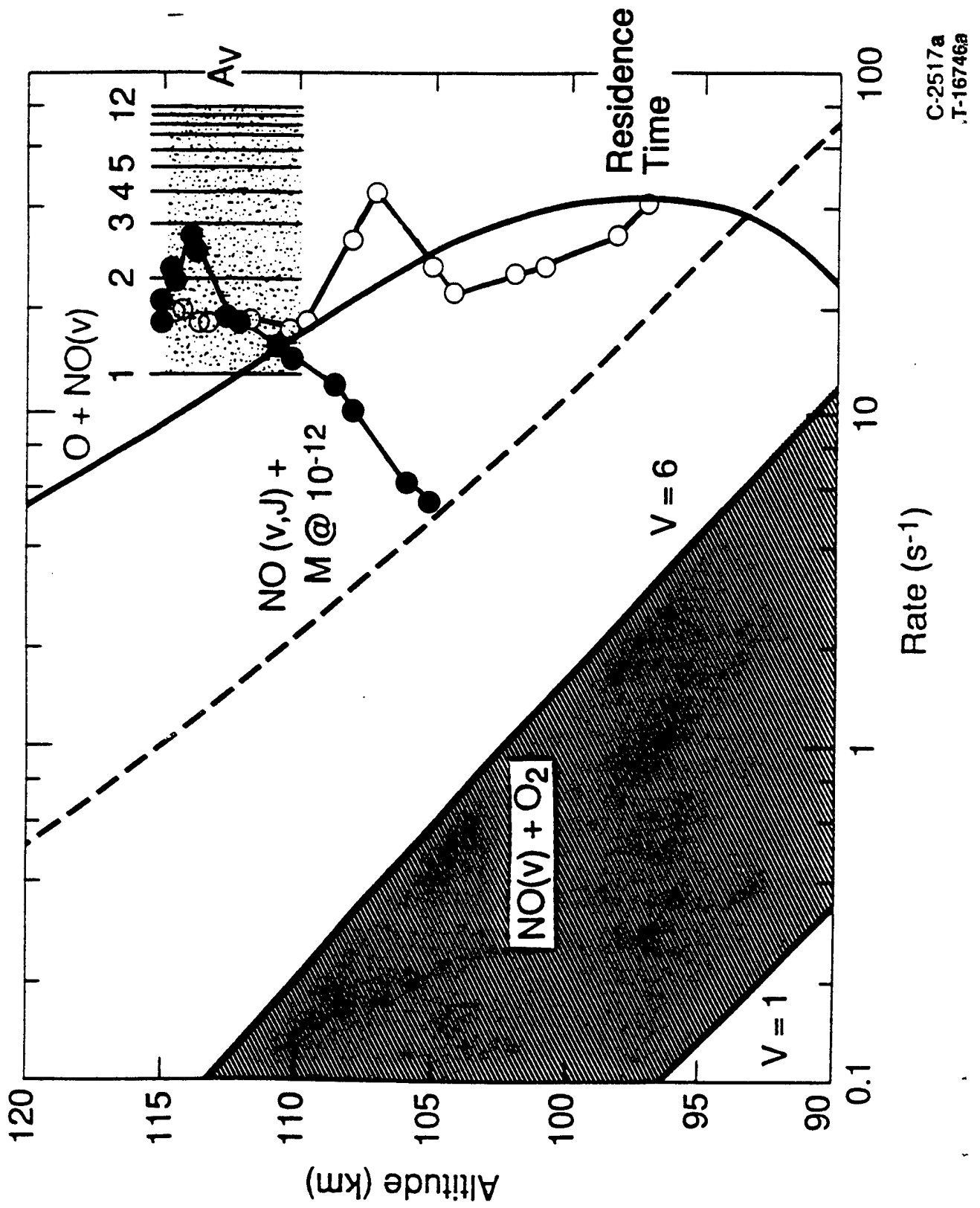


TITLE

T-18

This figure compares the first-order loss rates for $\text{NO}(\nu, J)$ as encountered during the EXC EDE III flight. The short residence times on apogee and downleg prevent the attainment of steady state kinetic conditions; however these conditions are nearly achieved for the longer residence times near maximum dose (upleg).

EXCEEDE III NO(v) LOSS RATES

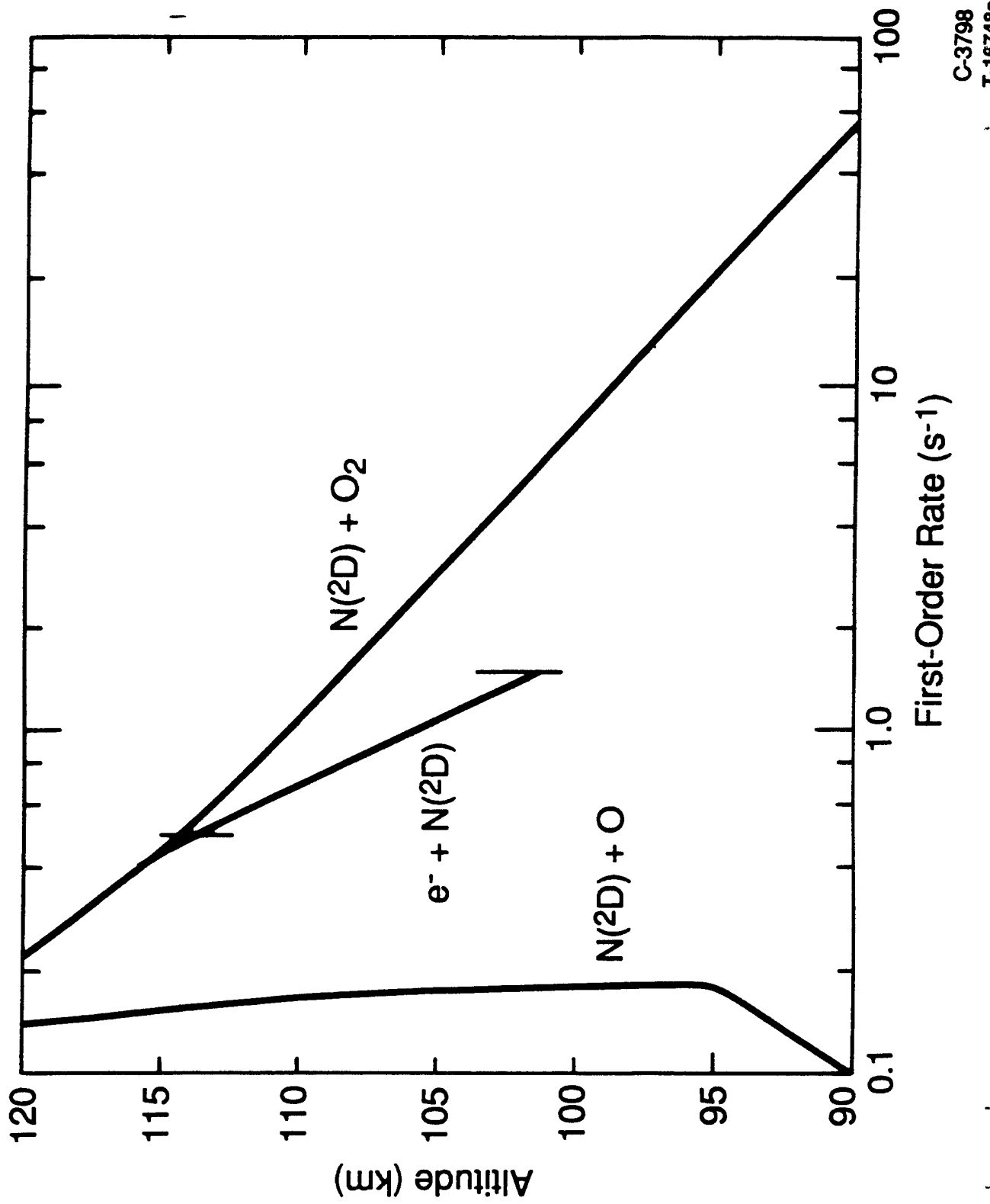


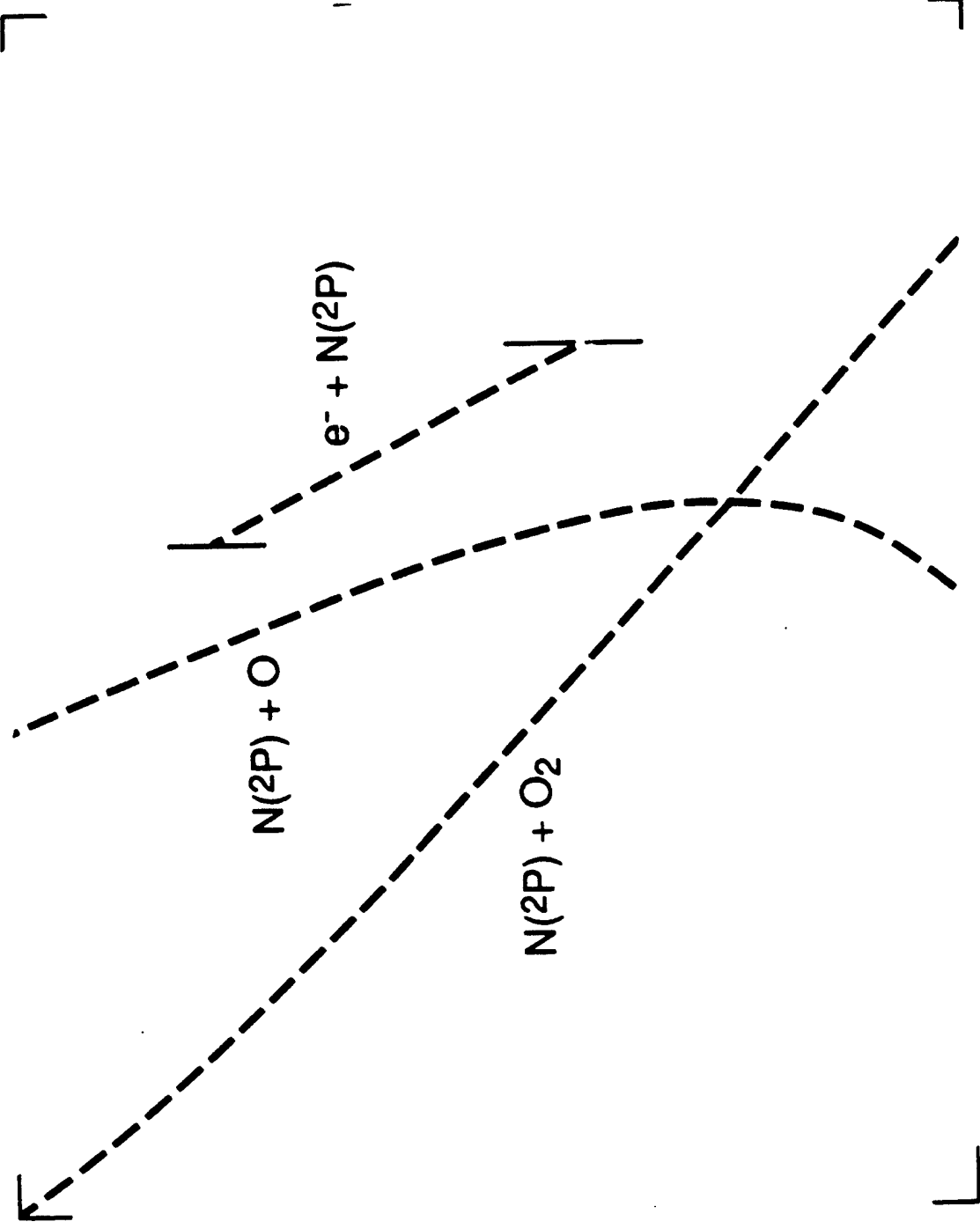
TITLE

T-18

This figure compares the predicted first-order loss rates of N(²D) and N(²P), which are likely precursors to NO(v,J) via reaction with O₂. Quenching of N(²D) by non-reactive processes is relatively unimportant. Quenching by electrons is the dominant loss process for N(²P).

N* PRECURSOR REACTION RATES





KINETIC MODELING OF NO(v, J) PRODUCTION

T-18893

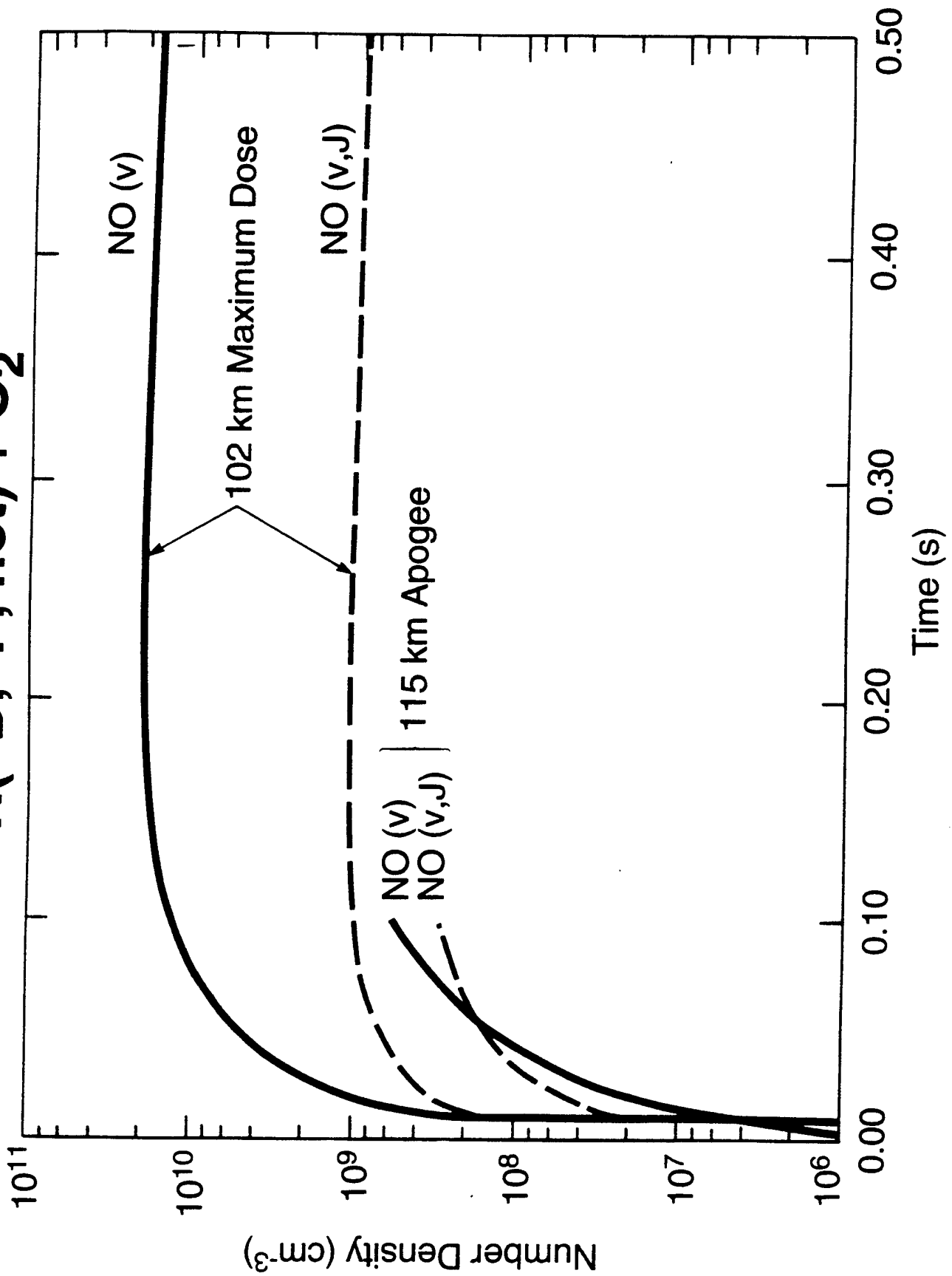
- Maximum dose results roughly consistent with N(2D, 2P) + O₂ chemistry
 - More NO($v, \text{high-}J$) than expected for likely N(2P) production
 - Observe NO(v, J) states up to ~ 4 eV
- Apogee results clearly require an additional source of NO($v, \text{high-}J$)
 - Mystery NO($v, \text{high-}J$) production rate
 $\sim 3 \times 10^9 \text{ cm}^{-3} \text{ s}^{-1}$ at 115 km

POSSIBLE MISSING CHEMISTRY

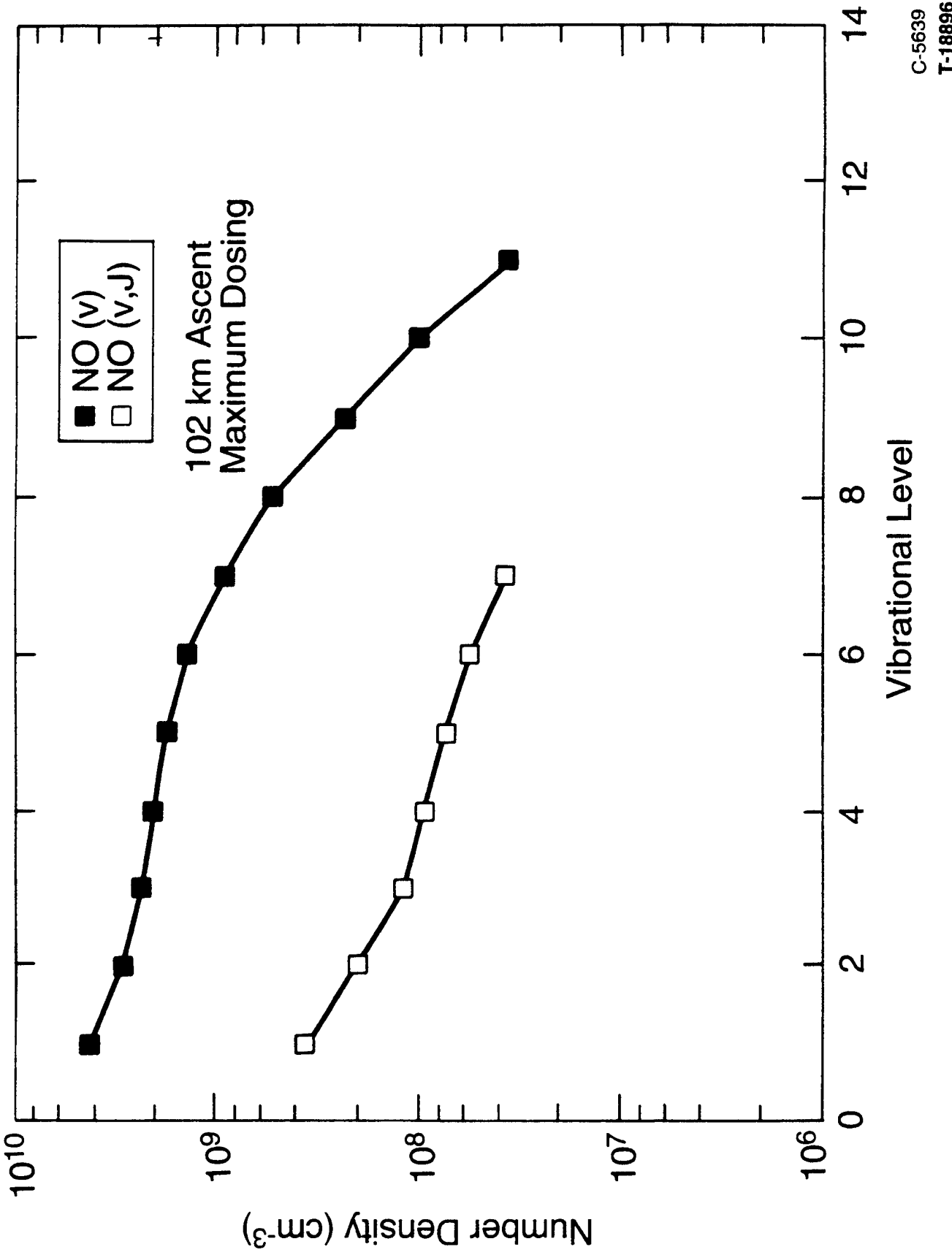
T-16894

- Translationally "hot" $\vec{N} + O_2 \rightarrow NO(v, J) + O$
- \vec{N} could be in 2D or 4S states, formed from $e^- + N_2^+$
- ~10X more reactive than thermal $N(^2D, ^2P)$, enough energy to access observed NO states
- Collisions reduce role for lower altitudes and longer residence times

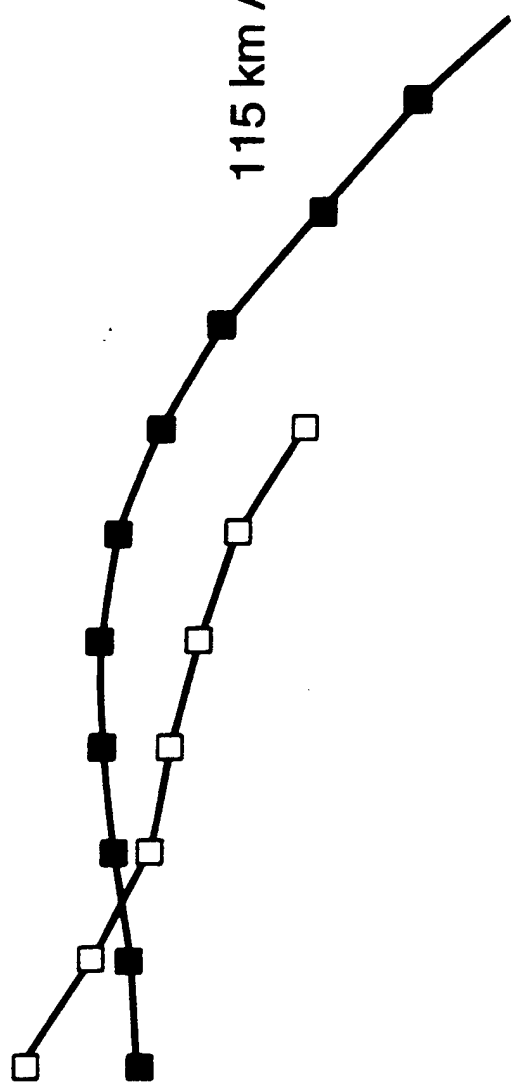
PREDICTED NO(v, J) PRODUCTION $N(^2D, ^2P, \text{hot}) + O_2$



PREDICTED VIBRATIONAL DISTRIBUTIONS $N(^2D, ^2P, \text{hot}) + O_2$

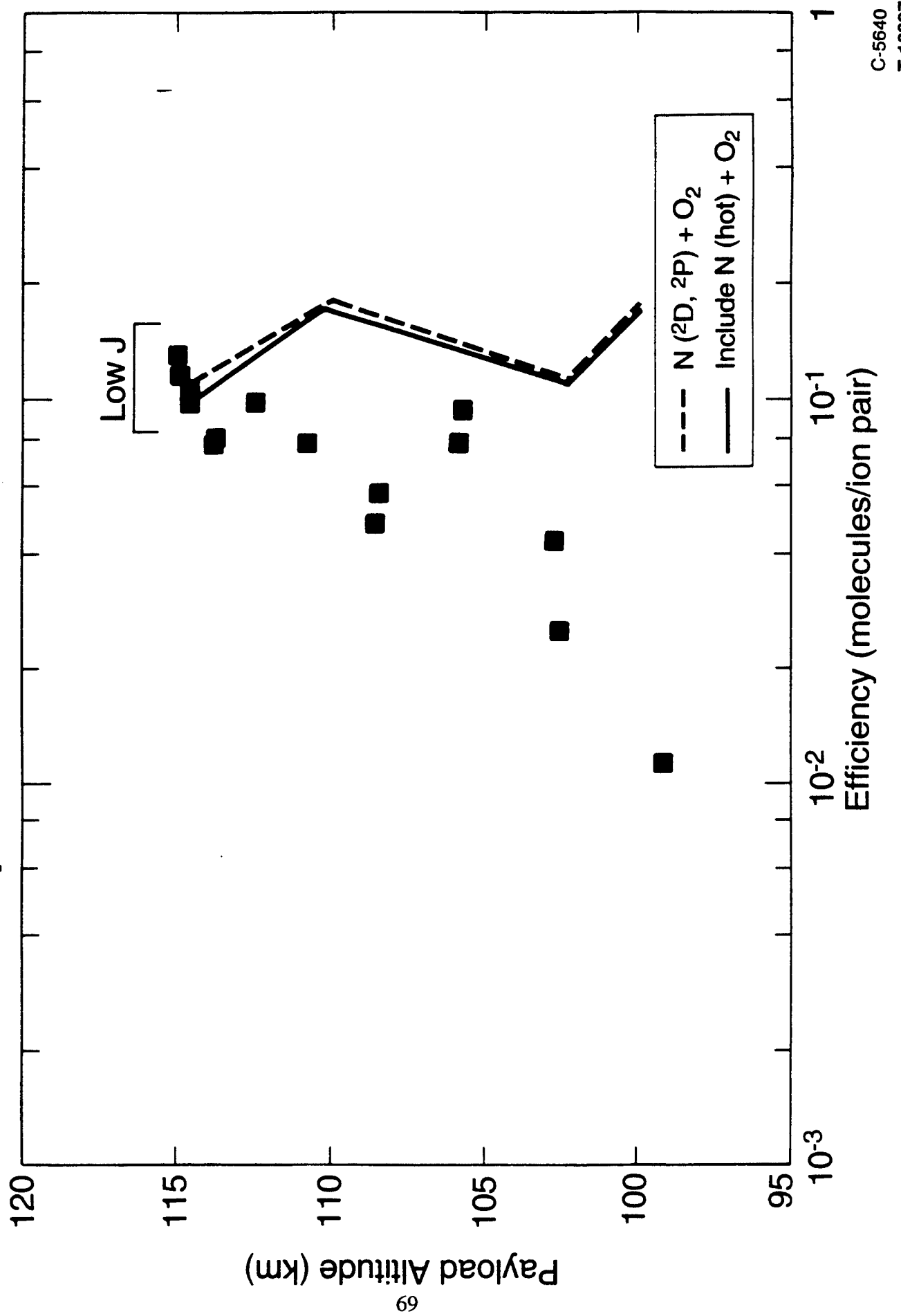


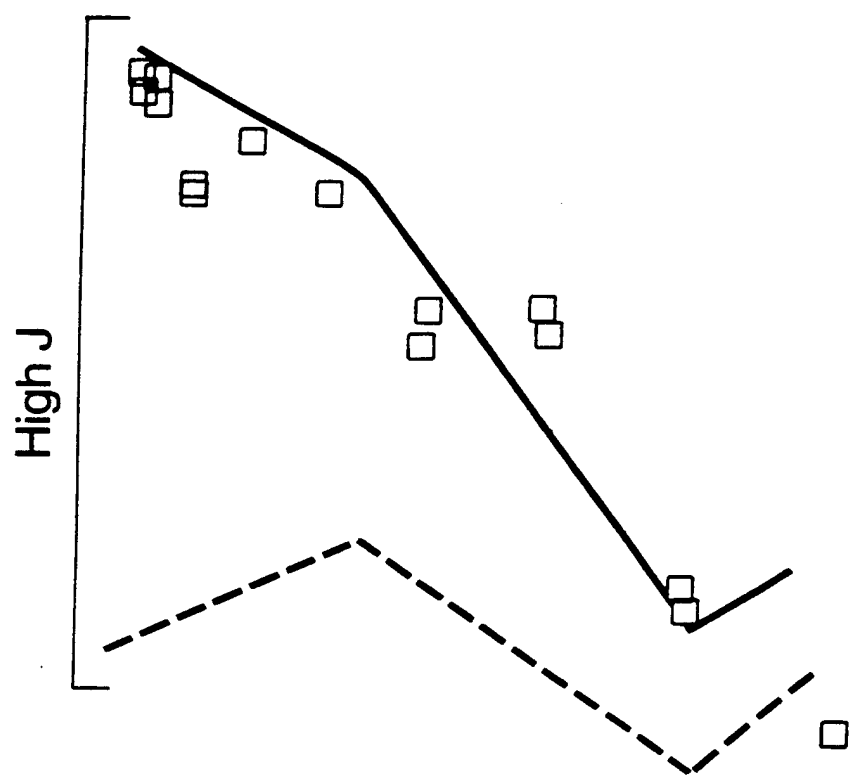
115 km Apogee



NO(v) PRODUCTION EFFICIENCIES: ASCENT

Comparison To Model Predictions

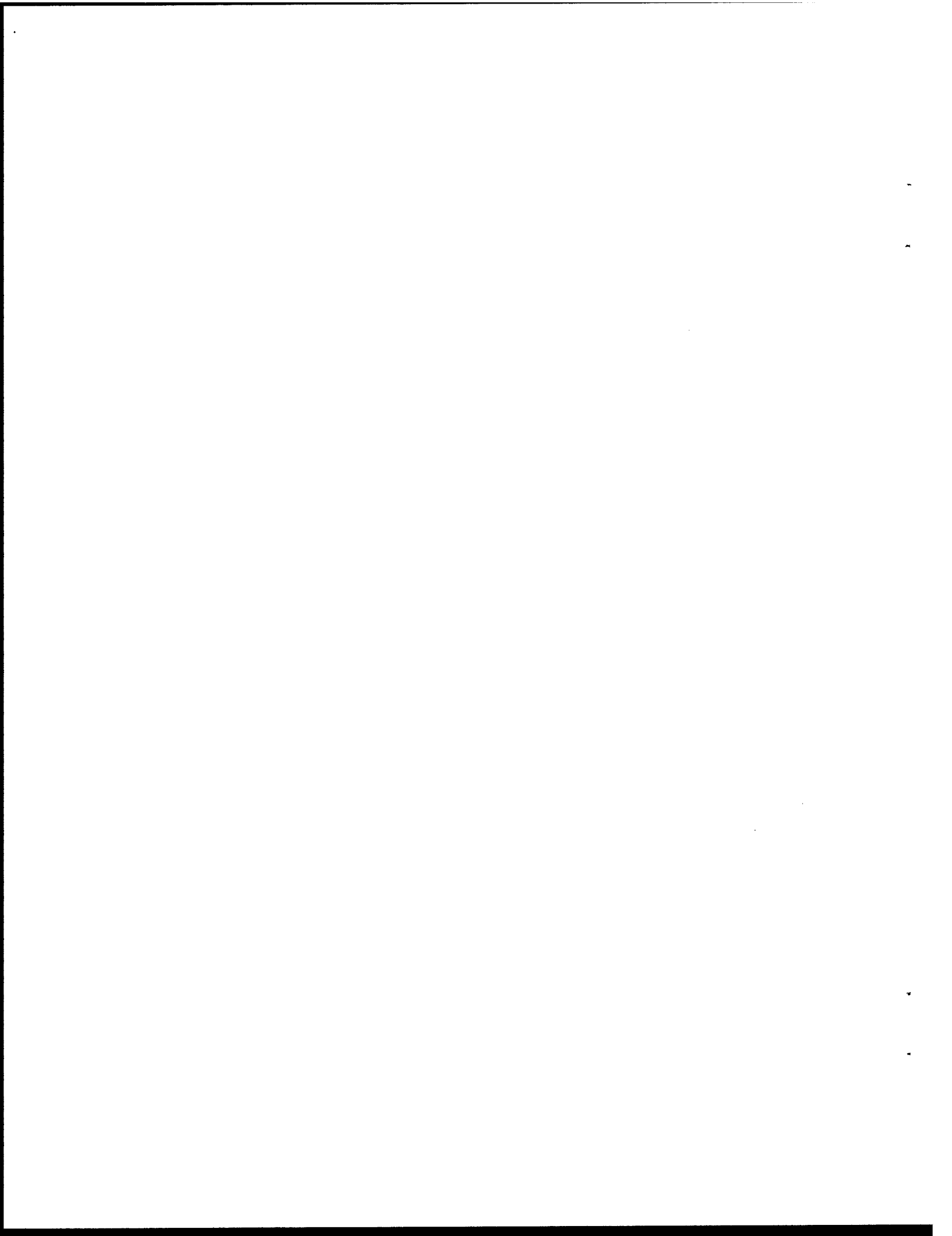




CONCLUSIONS

T-18898

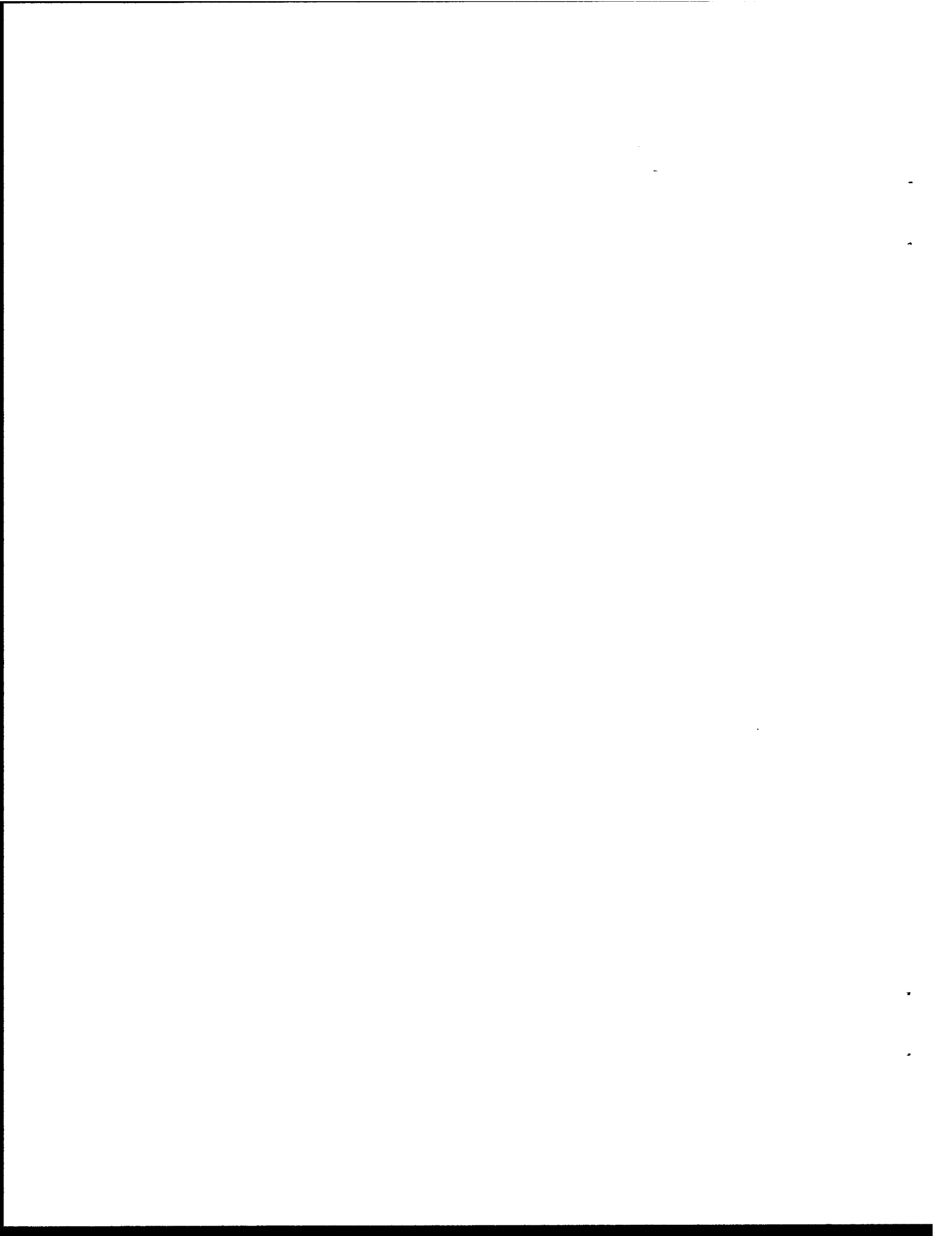
- Excitation reactions for NO(v,J):
 - (1) $N(^2D) + O_2 \rightarrow NO(v) + O$
 - (2) $N(^2P) + O_2 \rightarrow NO(v,J) + O$
 - (3) $\vec{N}(^2D, ^4S) + O_2 \rightarrow NO(v,J) + O$
- Overprediction of NO(v) production at lower altitudes (ascent):
 - Suggests k_1 decreases markedly for lower T (~ 200 K)
 - Pre-dosing may alter branching of N^* production
 - $\vec{N}(^2P)$ contributes to NO(v,J) only for lower altitudes, long residence times
 - relevant to auroras near 100 km
- $N(^2D, ^4S)$ dominates NO(v,J) production at high altitudes
 - relevant to dayglow, auroras above 120 km



APPENDIX 3

Excitation of O₃(v₃) by Electron Bombardment in the EXCEDE III Rocket Experiment

Presentation



**EXCITATION OF O₃(v₃) BY ELECTRON BOMBARDMENT
IN THE EXCIDE III ROCKET EXPERIMENT**

**W.T. Rawlins and B.D. Green
Physical Sciences Inc.**

**D.E. Paulsen and W.A.M. Blumberg
Phillips Laboratory/GPOSS**

**R.E. Murphy
Research Sciences Corp.**

1993 Fall Meeting: American Geophysical Union

Sponsored by the Defense Nuclear Agency

December 1993

The EXCIDE III rocket experiment bombarded the nighttime lower thermosphere with energetic electrons at high dosing rates and observed the resulting infrared fluorescence with a cryogenic interferometer. Fourier transform spectra in the 900 to 1100 cm⁻¹ spectral region, obtained at altitudes between 85 and 105 km, show the presence of vibrationally excited O₃(v) excited by both quiescent and electron-initiated processes. When the electron beam is on, O₃ (v=1) emission from the irradiated volume is much more intense than that from the ambient background, and the excitation of higher vibrational levels can also be observed. Least squares spectral fitting analysis determines the vibrational state column densities for both the quiescent and beam-excited components and their dependencies on altitude and dosing. Systematic kinetic analysis of these results yields new information on the processes responsible for electron-initiated ozone excitation. Direct excitation of O₃(v) by secondary electron impact on ground state ozone clearly plays a key role, however, the possibility of formation and/or excitation of ozone through bimolecular reactions involving beam-excited metastable precursors must also be considered. We discuss the kinetics of the likely excitation processes in comparison with the EXCIDE III data.

ELECTRON EXCITATION OF O₃(v)

T-18796

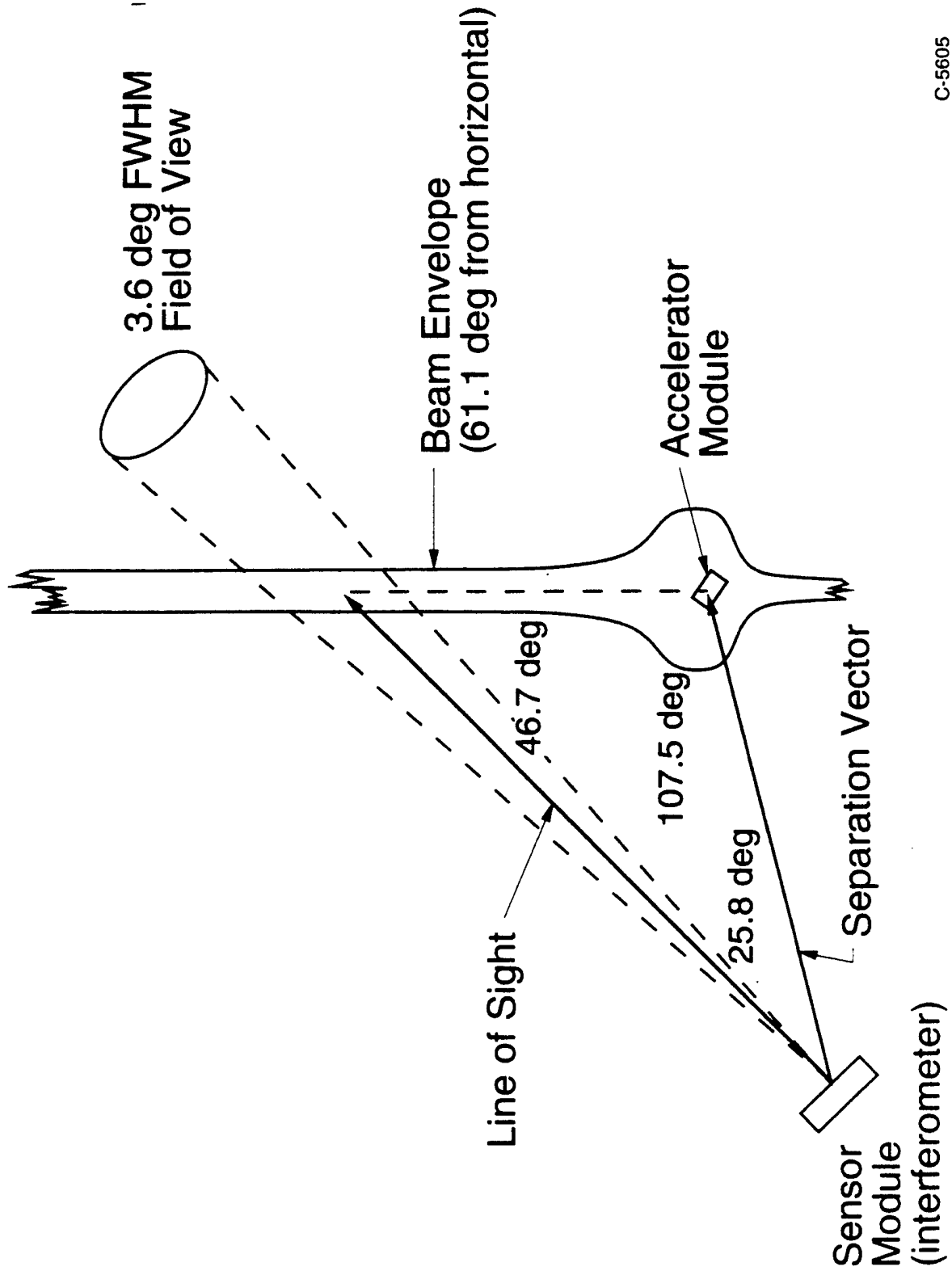
- Summary of previous observations
 - Auroral excitation via rocketborne measurements: HIRIS (1976), SPIRIT I (1986) - not definitive
 - Laboratory experiments (B.D. Green et al., 1990)
 - $e^- + O_3 \rightarrow O_3(v) + e^-$ is efficient, $\sigma \geq 10^{-16} \text{ cm}^2$, modeling \Rightarrow large effect in IBC III auroras near 100 km
 - Possible two-body chemical process: $O_2(A) + O_2(v) \rightarrow O_3(v) + O$
- New results: EXCIDE III electron beam rocket experiment
 - Launched 27 April 1990, White Sands, NM
 - 2.5 keV, 18-Amp electron beam
 - Fluorescence measurements via 2-cm⁻¹ cryogenic interferometer plus radiometers, photometers, UV spectrometer, CVF IR spectrometers
 - Altitudes 85 to 115 km
 - Maximum $\approx 6 \times 10^{11}$ ion pairs cm⁻³ s⁻¹, $[e^-] \approx 10^9 \text{ cm}^{-3}$
 - Beam residence times 20 to 200 ms
 - O₃(v) fluorescence spectra 85 to 105 km, ascent and descent, beam off versus beam on
 - Apparent beam-induced enhancement near 100 km

Title

T-18797

Illustration of the viewing geometry for beam-excited atmospheric fluorescence. The electron beam is directed along the Earth's magnetic field lines. The velocity vector determines the gas flow residence time in the beam irradiation volume. Early in ascent, the velocity vector is towards the beam axis, resulting in long residence (dosing) times. For the remainder of the flight, the velocity vector is transverse to the beam, resulting in short residence times.

VIEWING GEOMETRY

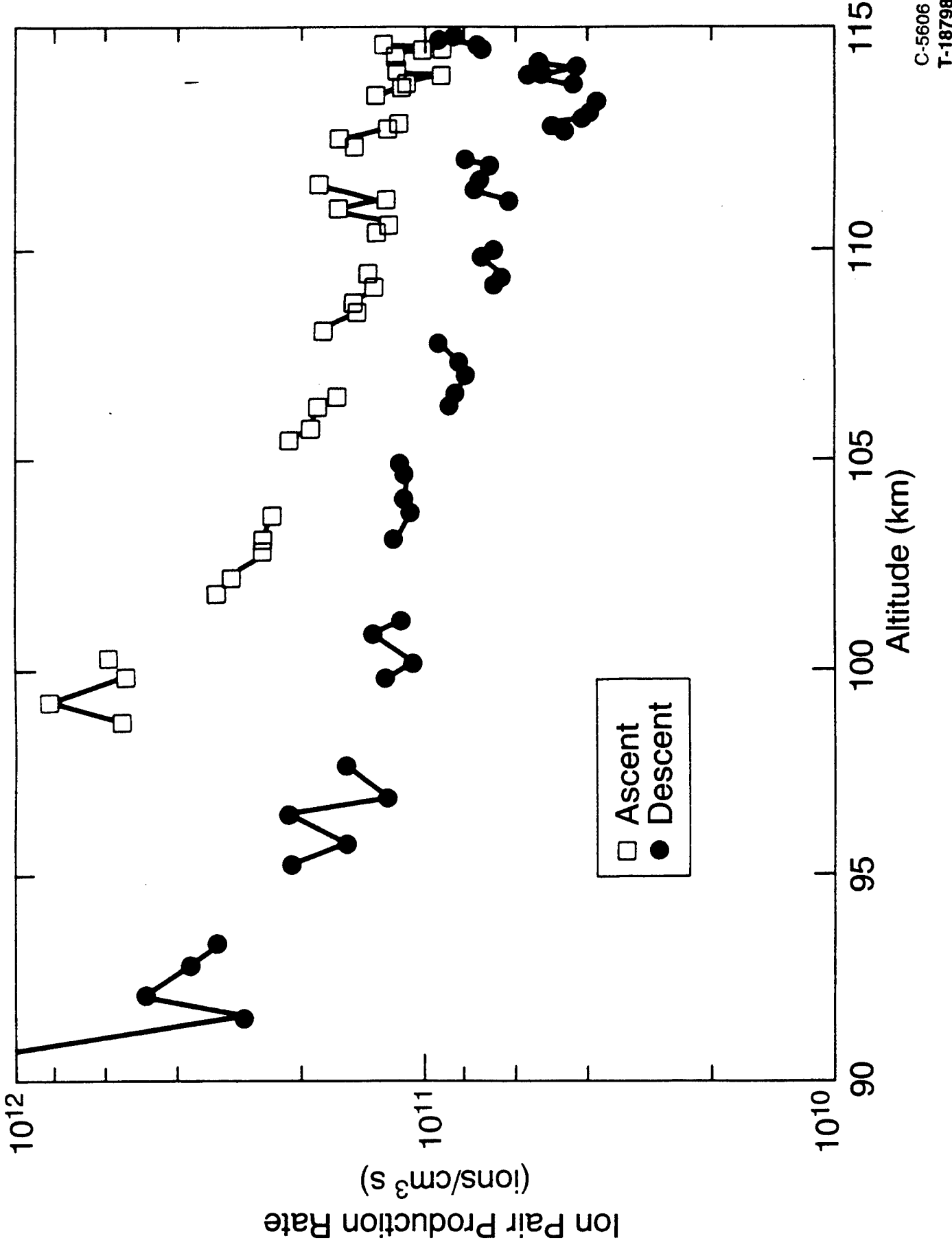


Title

T-18798

The ion pair production rates achieved during the EXCERDE III flight were determined from a spatially scanning 391.4 nm photometer (R.J. Rieder et al., 1993). These rates are related to the excitation rates of precursors to IR fluorescence.

ION PAIR PRODUCTION RATE (VOLUME)



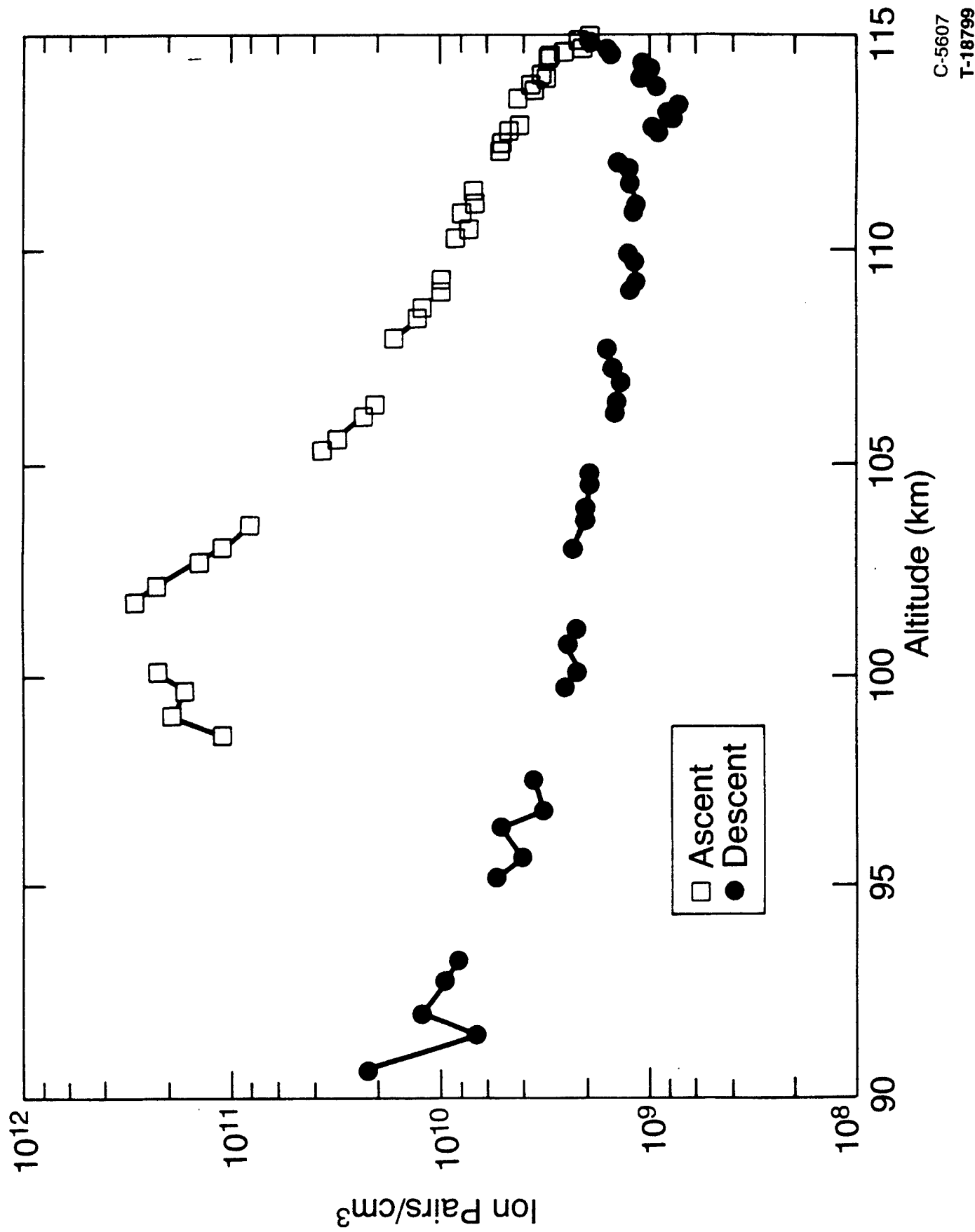
C-5606
T-18798

Title

T-18799

This figure shows the total number of ion pairs created per unit volume during each beam pulse, taking into account the residence time in the portion of the electron beam viewed by the interferometer. The most favorable dosing conditions for observing O₃(v) excitation occur on ascent between 100 and 105 km.

TOTAL ION PAIRS CREATED PER cm³

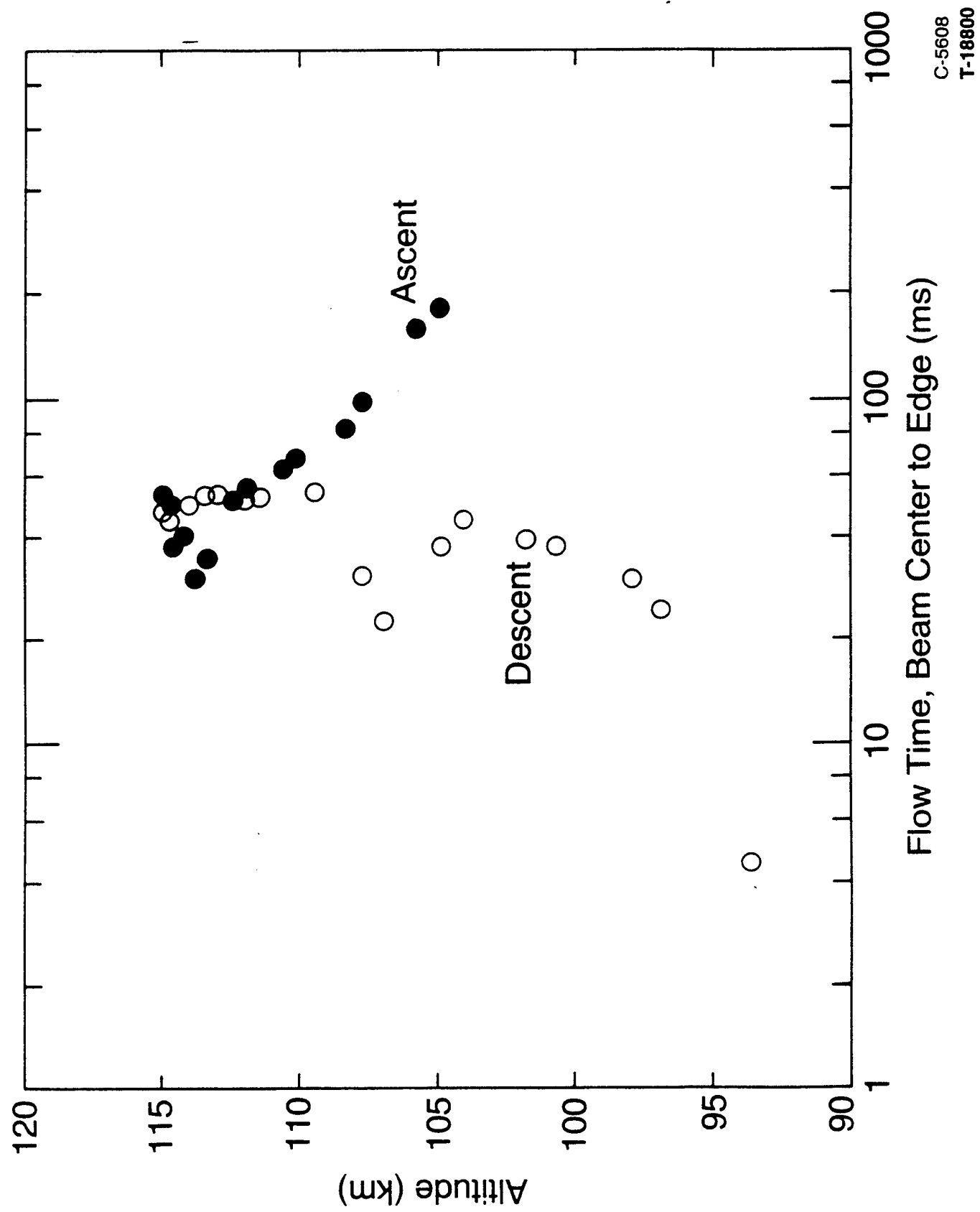


Title

T-18800

The gas flow residence times in the irradiated volume bound the kinetics of the excitation and deactivation processes. The long times early in ascent permit near-steady-state conditions; the short times for apogee and descent sample the initial excitation rates.

FLOW TIME THROUGH VIEWED EXCITATION VOLUME



EXCÉDE III O₃(v) DATA

T-168801

- Beam off, 2 cm⁻¹: 7 scans
4 scans upleg 93 to 105 km
3 scans downleg 84 to 102 km

- Beam off, 11 cm⁻¹ : 4 scans
2 ascent 94 to 98 km
2 descent 94 to 98 km

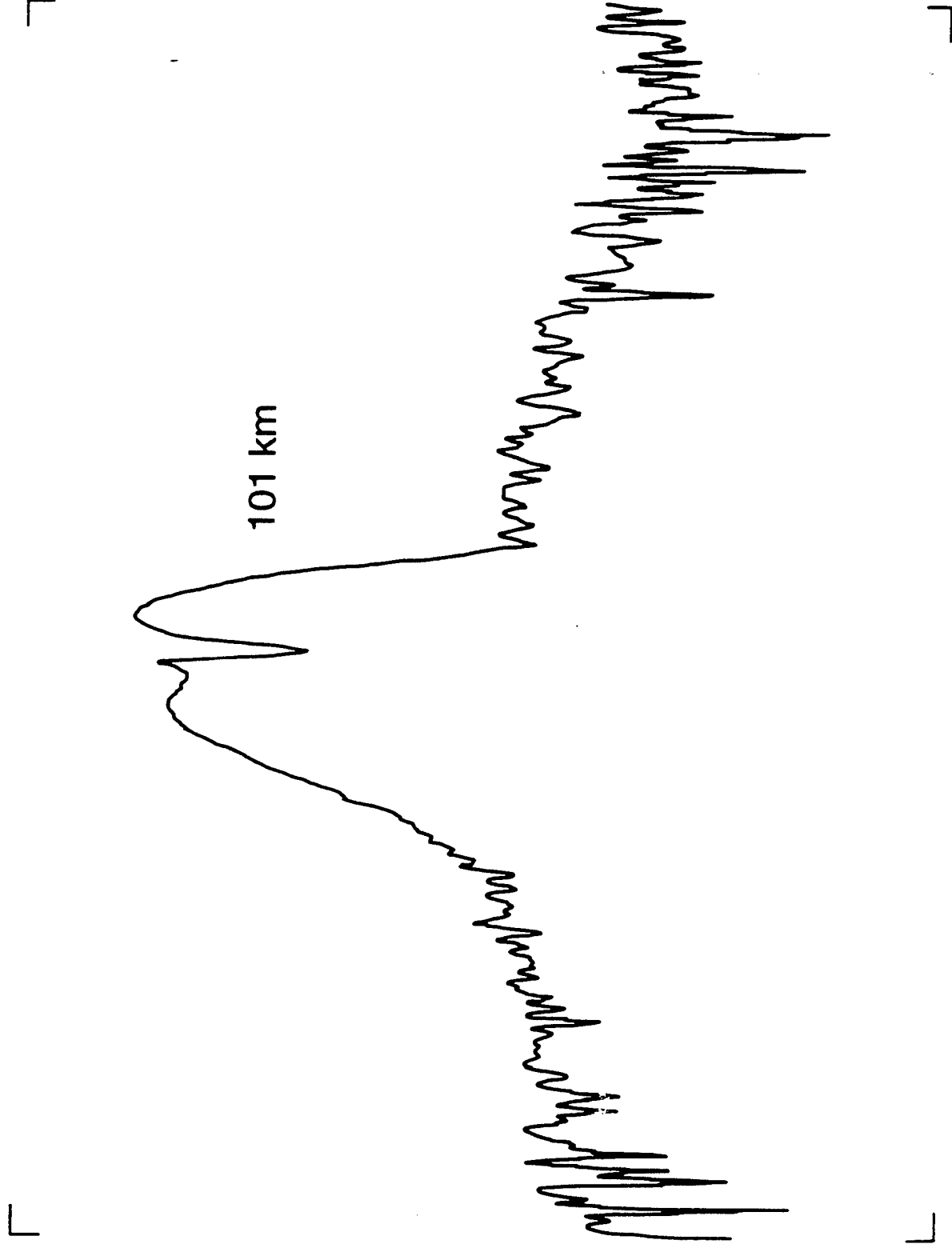
- Beam on, 2 cm⁻¹: 15 scans
6 ascent 95 to 104 km
9 descent 87 to 104 km

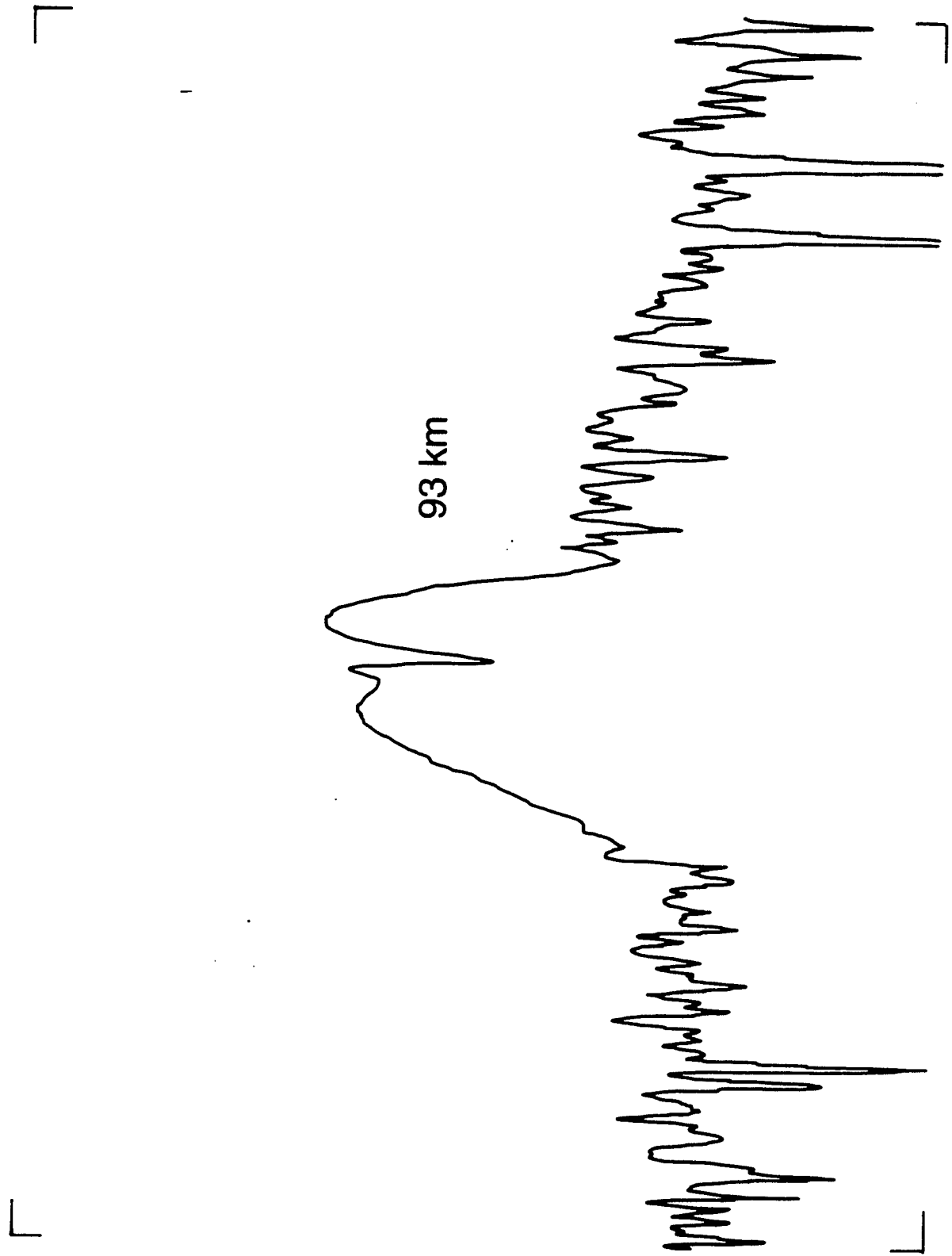
- Total 26 spectra

Title

T-18802

Observed spectra of O₃ (v) fluorescence with the electron beam off consist of an intense (001→000) feature between 1000 and 1060 cm⁻¹ and vibrational "hot band" emission below 1000 cm⁻¹. The observed emission is from O₃(v) excited by the normal, quiescent atmospheric processes of radiative up-pumping (001 only) and three-body recombination (all v). No O₃ emission is observable above 105 km. The weak fluorescence beyond 1040 cm⁻¹ is invariant with altitude and is probably due to an off-gassed contaminant (e.g., a silicon oxide). The observed signal level of ≈10⁻¹² W/(cm² sr cm⁻¹) is an instrumental background which is present in all the spectra.



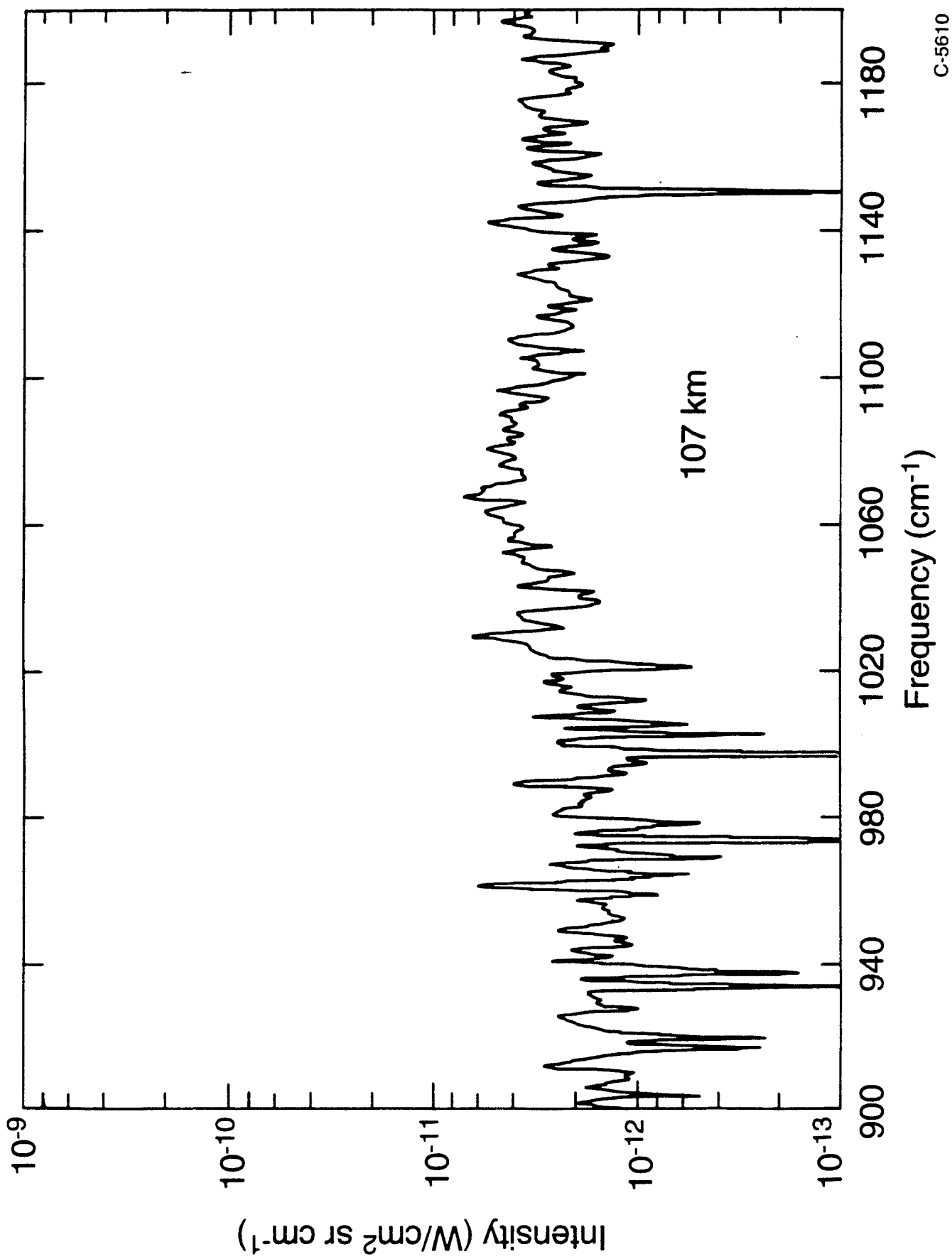


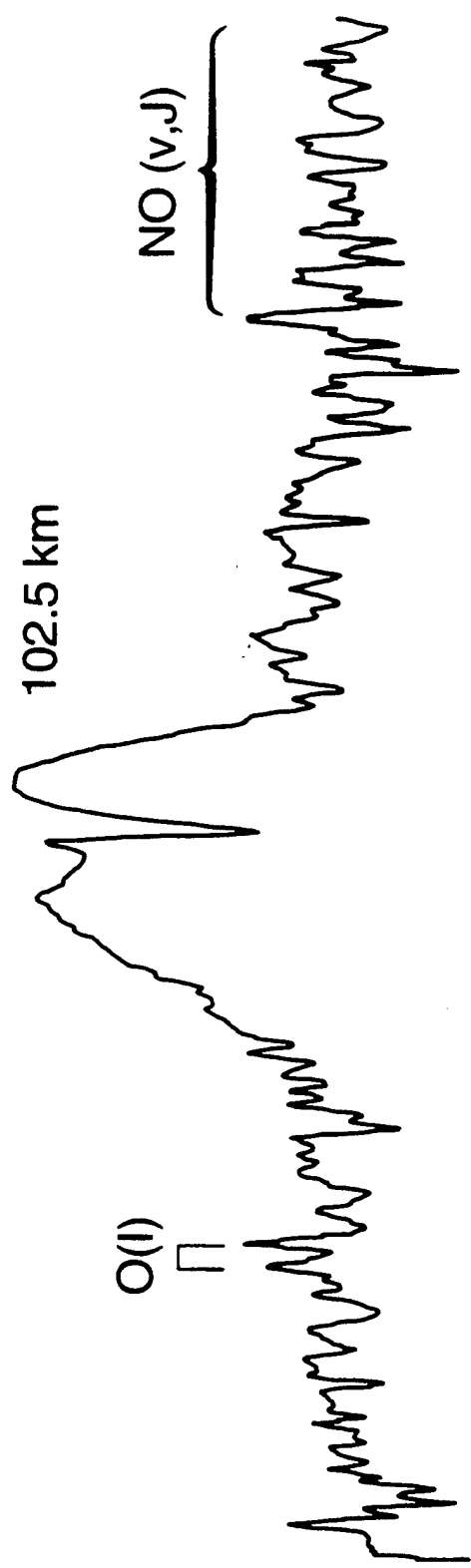
Title

T-18803

This figure shows spectra observed from 102.5 and 107 km (ascent) with the beam on, near the maximum dosing regime of the flight. The intensities of the $(001 \rightarrow 000)$ and higher vibrational state emissions at 103.5 km are significantly larger than we would expect by extrapolation of the beam-off data from lower altitudes. O(ℓ) Rydberg and NO(v, J) features are also present.

$O_3(v)$ FLUORESCENCE, BEAM ON





DATA ANALYSIS SEQUENCE

T-18804

- Linear least squares spectral fitting $\rightarrow [O_3(v)]$ column densities versus payload altitude
- Isolate background atmosphere
 - Curve fit beam-off $[O_3(v)]$ column densities
 - Differentiate \rightarrow ambient $[O_3(v)]$
- Use ambient $[O_3(v)] + MSI90$ to infer $[O]$, $[O_3]$, $[H]$ via quiescent model
(cf., *JGR* 98, 3677 (1993))
- Beam enhancement: subtract curve fit column densities, apply beam diameter $\rightarrow [O_3(v)]$ excited in beam

SPECTRAL ANALYSIS

T-18805

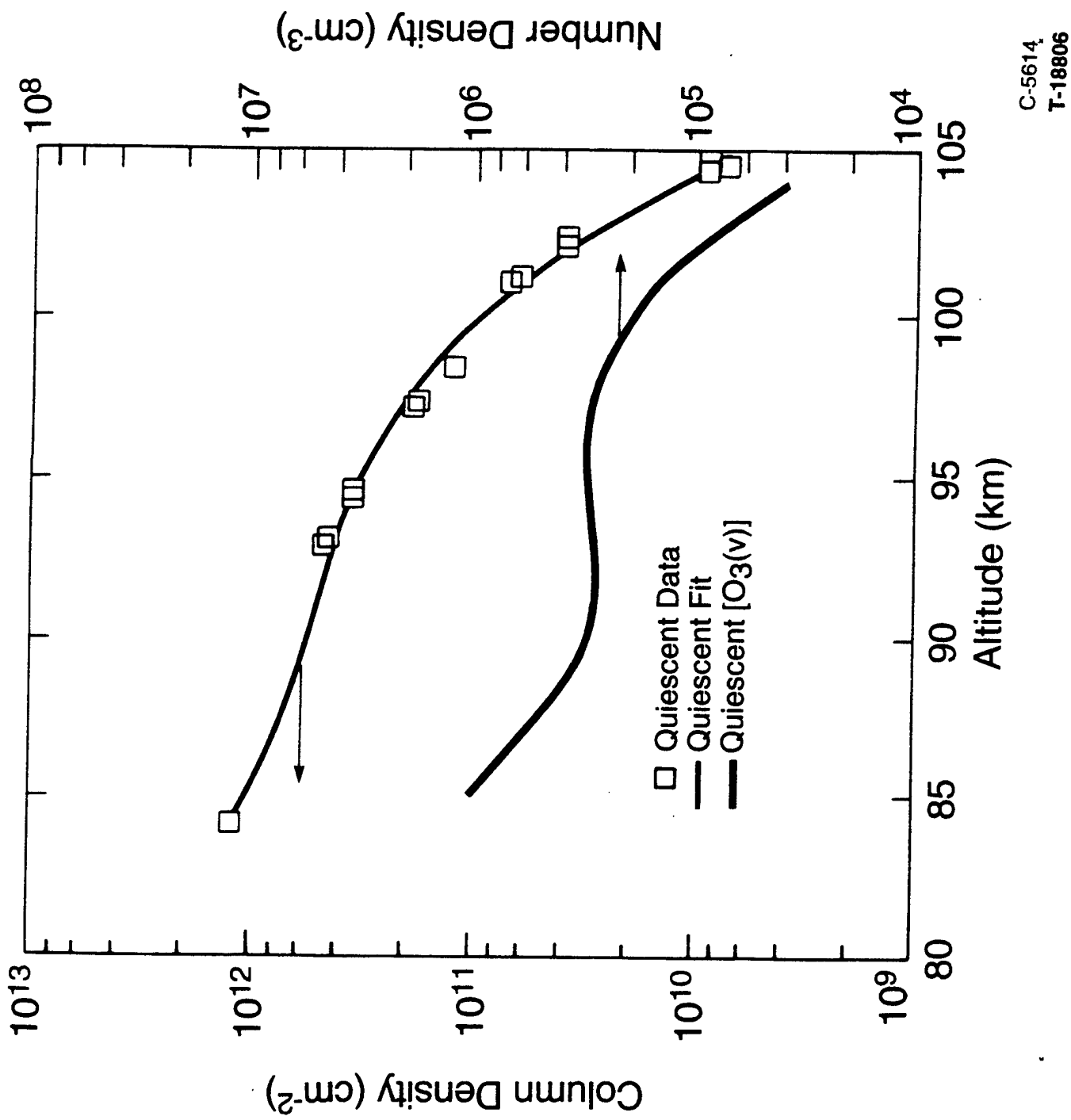
- Darling-Dennison $\nu_{ov'}$ + harmonic $A_{\nu'\nu''}$
- 9-band model: $(00\nu_3 + 10\nu_3)$ in thermal equilibrium
- 18-band model: $(00\nu_3 + 10\nu_3)$, $(01\nu_3 + 11\nu_3)$
 - Slightly better spectral fit
 - Population distributions equivalent to 9-band
- 9-band fits used throughout
- Relevant references
 - *JGR*, 98, 3677 (1993)
 - *J. Chem. Physics*, 87, 5202 (1987)

Title

T-18806
T-18807

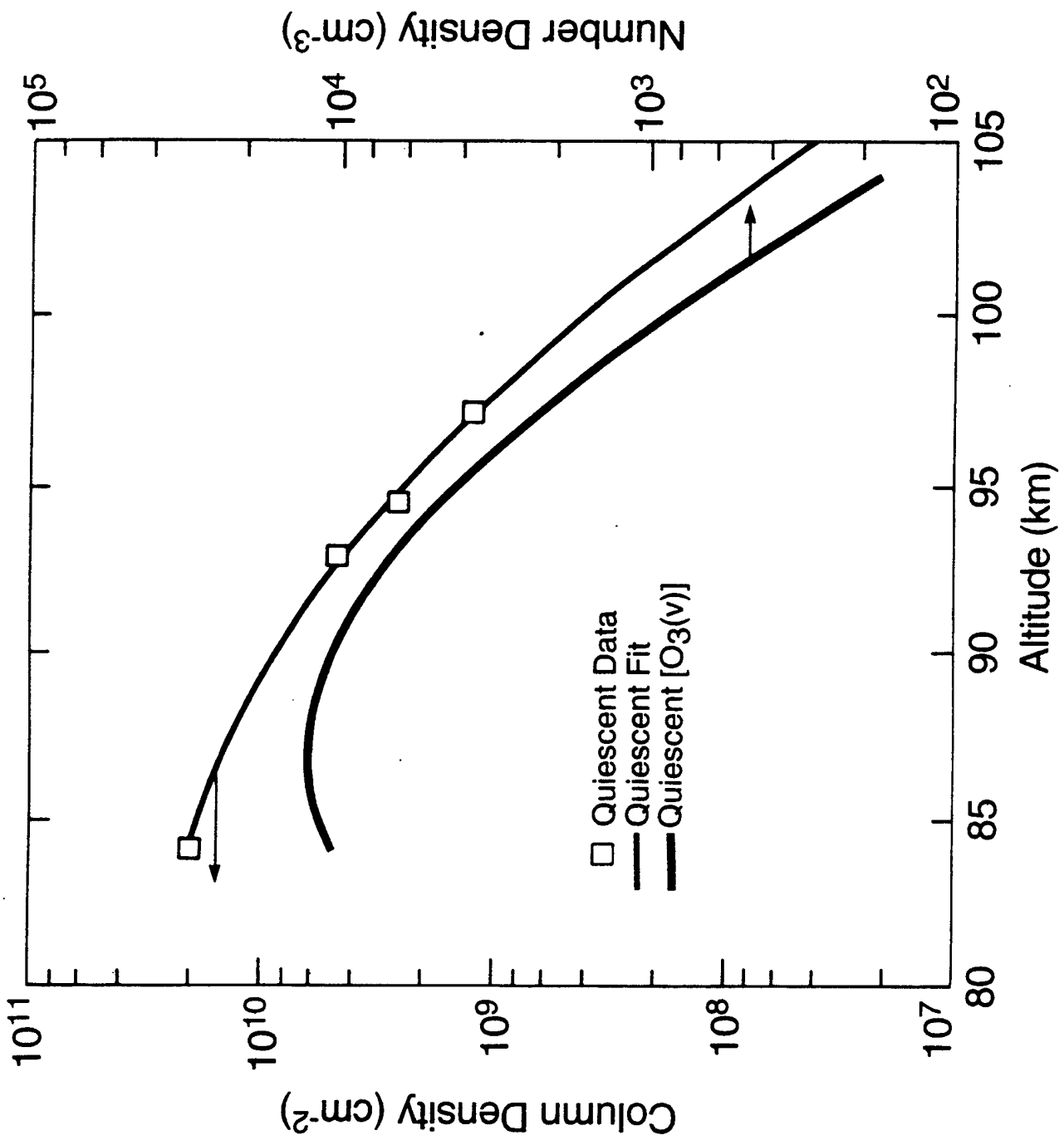
These figures show column densities determined for O_3 ($v=1,3$) versus altitude. The quiescent (beam-off) data were fit to a polynomial function as shown. The departure of the beam-on column densities from the curve indicates the enhancement produced by the electron beam. Beam enhancements are clearly observed between 99 and 104 km but are not significant below 100 km (descent). The fitted quiescent curve was corrected to zenith and differentiated to give the ambient O_3 ($v=1$) number density profile (plotted against the right-hand axis).

$O_3(v = 1)$ COLUMN DENSITIES



- Beam On, Descent
- Beam On Ascent

$O_3(v = 3)$ COLUMN DENSITIES



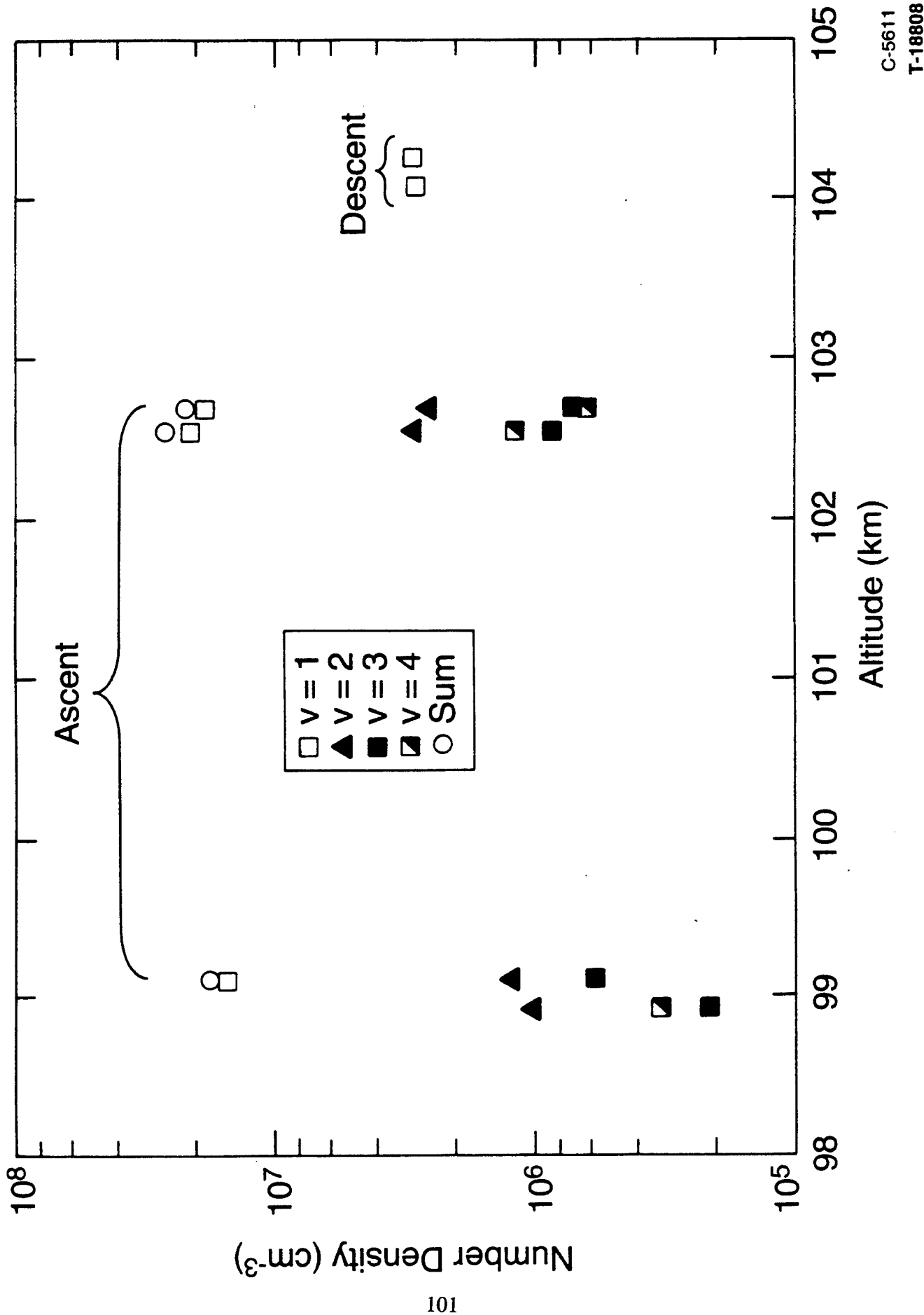
Beam On, Descent
 Beam On Ascent

Title

T-18808

The $O_3(v)$ number densities excited in the viewed electron beam volume are two to three orders of magnitude larger than ambient $O_3(v \geq 1)$ number densities and are large fractions of the expected ambient $[O_3]$.

$[O_3(v)]$ EXCITED IN E-BEAM

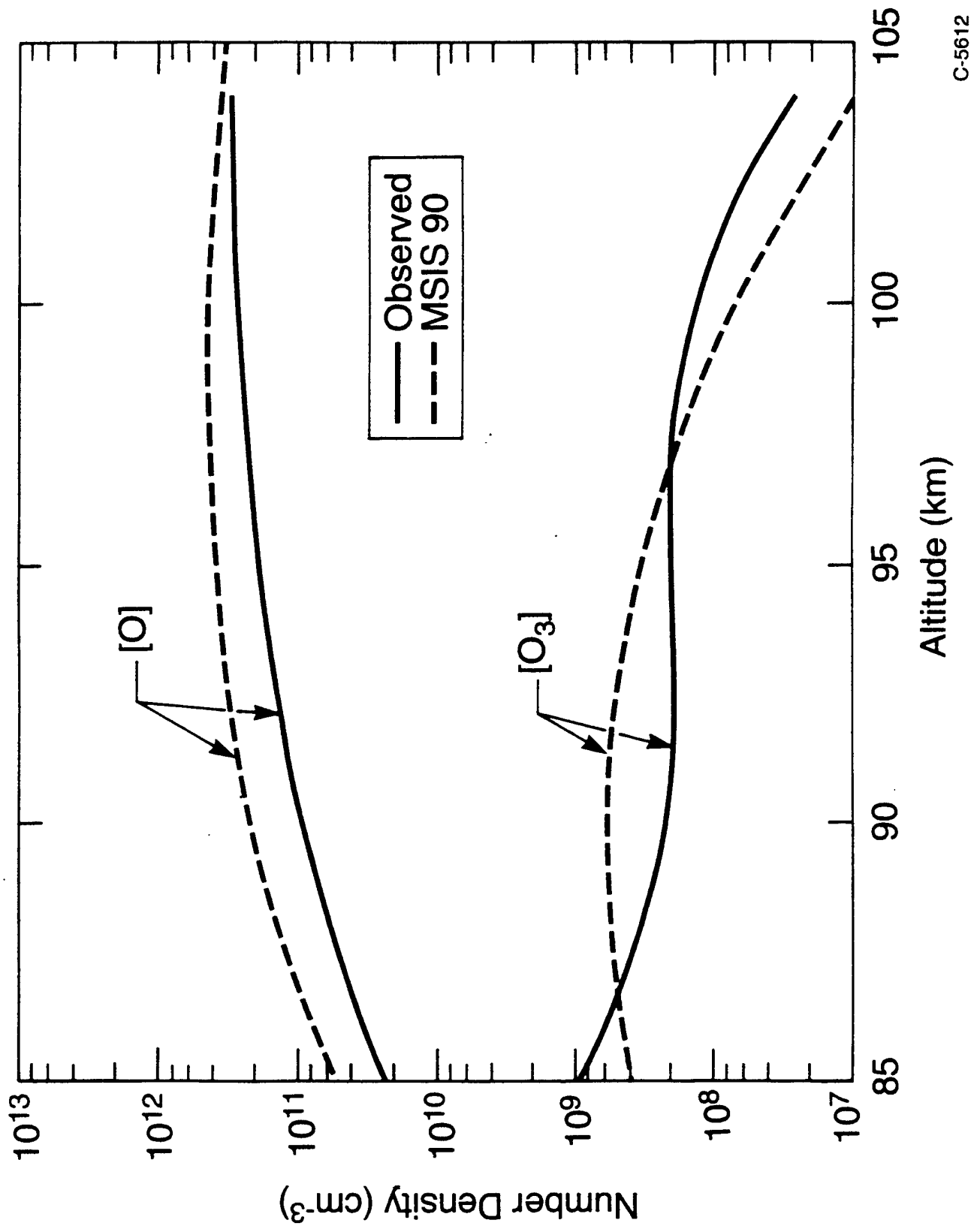


Title

T-18809

The ambient (beam-off) $O_3(v)$ number densities provide estimates of the local ambient $[O_3]$ and $[O]$ profiles through a simple kinetic analysis (*JGR*, 98, 3677 (1993)). The observed $[O_3(v)]$ values are incompatible with MSIS90 predictions and suggest a +5 km upward displacement of the MSIS90 density profile, apparently due to dynamic perturbations. Note that $[O_3]$ values above 100 km are two to three times larger than the expected values.

ESTIMATED AMBIENT O₃, O NUMBER DENSITIES



KINETIC INTERPRETATIONS

T-18810

- Direct excitation: $e^- + O_3 \rightarrow O(v) + e^-$
- Laboratory-estimated cross section ($\approx 10^{-15} \text{ cm}^2$) can account for observed $O_3(v)$ excitation rates at maximum dosing
- BUT cross section must be $\approx 10^{-16} \text{ cm}^2$ to agree with absence of beam enhancement on descent
- Analysis indicates requirement for additional source of O_3 production in beam volume at maximum dosing: two-body reaction?
- Two-body process: $O_2(A) + O_2(v \geq 0) \rightarrow O_3(v \geq 0) + O$
- " $O_2(A)$ " is generic term for the three highest metastable states of O_2 :
 $A^3\Sigma_u^+, A'^3\Delta_u, C^1\Sigma_u^-$; could be vibrationally excited
- Generates enough total O_3 to sustain $e^- + O_3$ process during maximum dosing scans (beam/FOV residence times $\approx 200 \text{ ms}$)
- Too slow to generate O_3 in descent scans (residence times $\leq 50 \text{ ms}$); accounts for absence of enhancement on descent
- Required O_3 production rate $\approx 3 \times 10^8 \text{ cm}^{-3} \text{ s}^{-1}$
- $k \approx 10^{-12} \text{ cm}^3 \text{ s}^{-1}$ if reaction with $O_2(v=0)$
- $k \approx 10^{-11} \text{ cm}^3 \text{ s}^{-1}$ if reaction with $O_2(v \geq 1)$

CONCLUSIONS

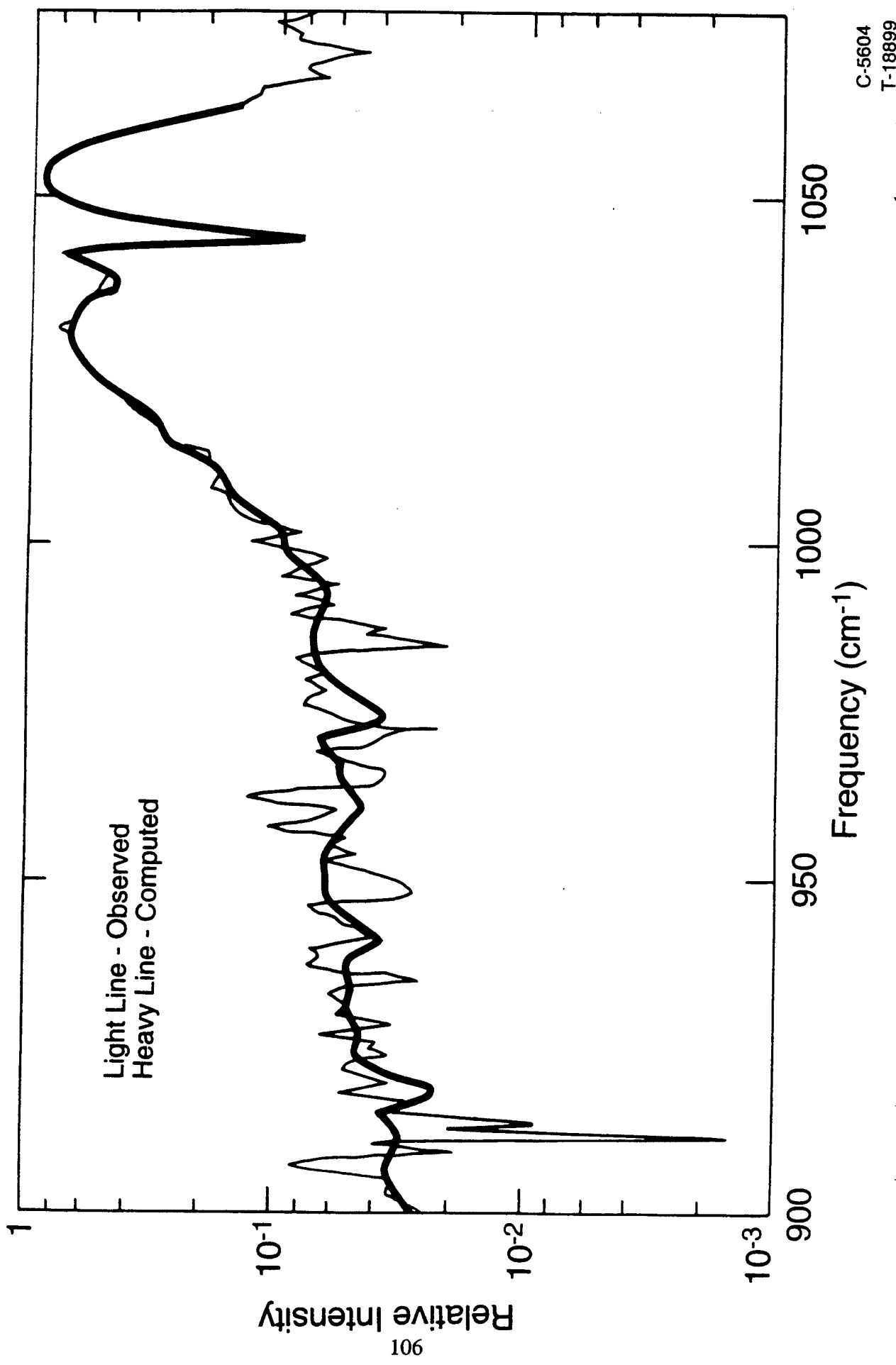
● O₃(v=1 to 4) populations and fluorescence (900 to 1100 cm⁻¹) are enhanced by energetic electron bombardment of the atmosphere near 100 km

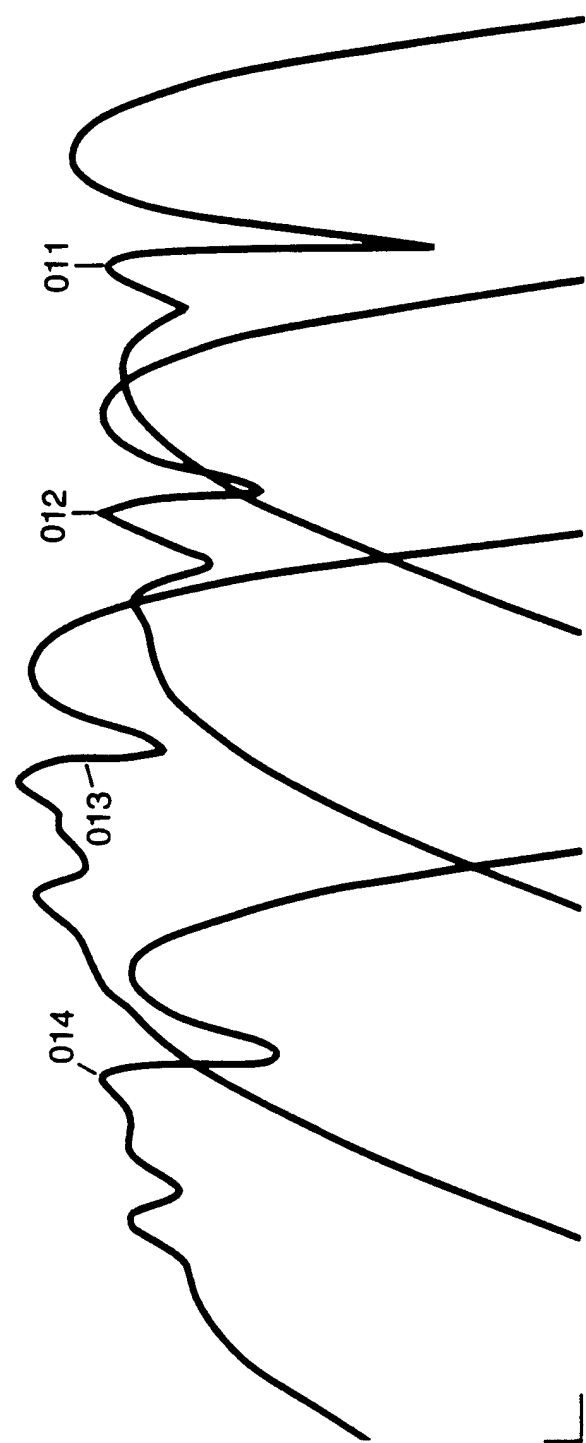
● Likely excitation processes

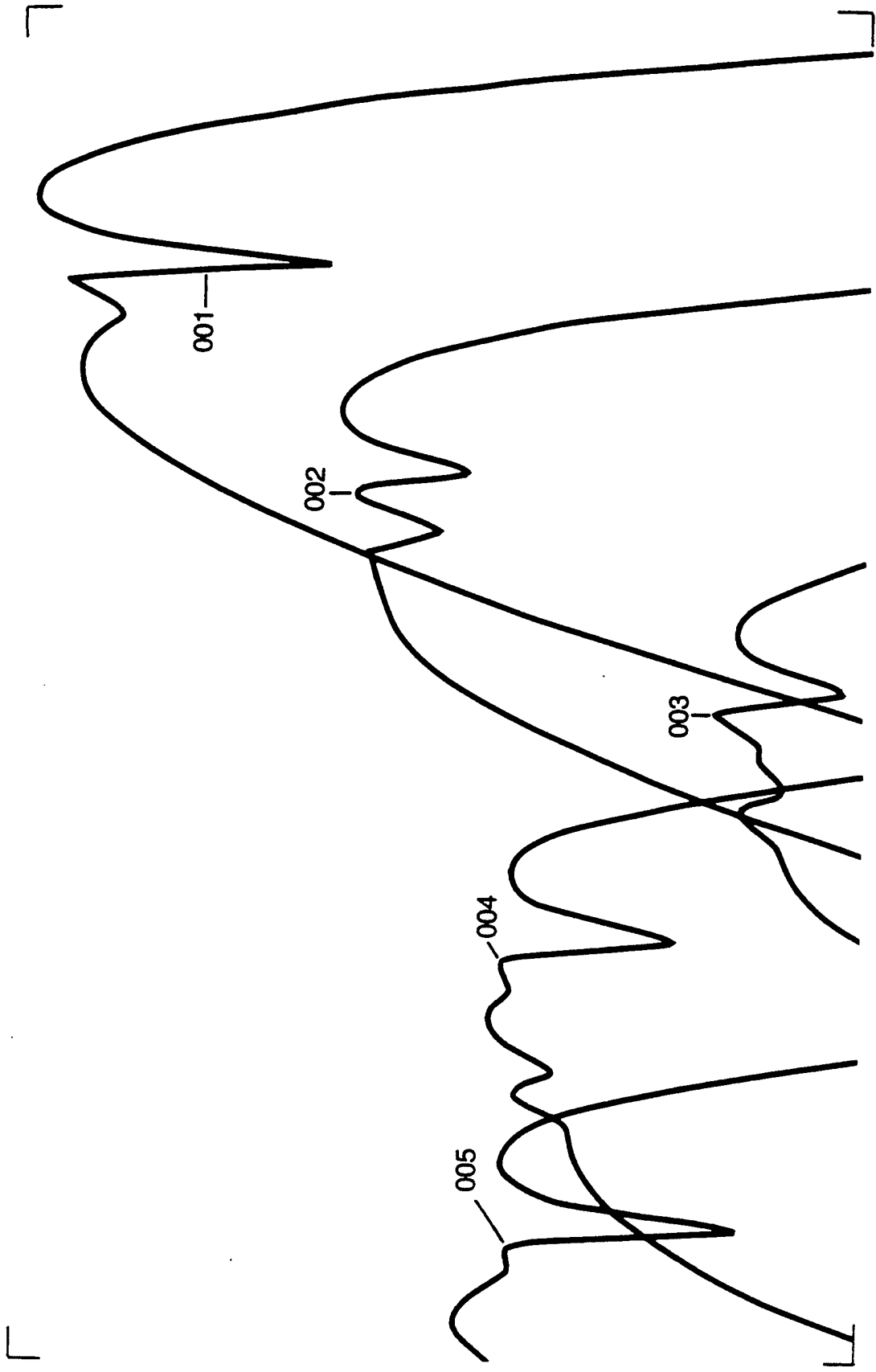
- (1) e⁻ + O₃(v=0) → O₃(v≥1) + e⁻
Well-studied in laboratory: fast process
Forms primarily O₃(v=1)
Quantitative predictions possible
- (2) e⁻ + O₃(v=1) → O₃(v≥2) + e⁻
Efficiency unknown; probably as fast as (1)
Product v distribution unknown
- (3) O₂(A) + O₂(v=0) → O₃(v) + O
Known slow quenching, O₃ yield unknown
Replenishes O₃ in beam volume
- (4) O₂(A) + O₂(v) → O₃(v) + O
Unknown; O₂(v) may accelerate reaction
May contribute to high-v O₃(v) excitation
Implicated in laboratory e⁻ + O₂ experiments
Partner could be O₂(a¹Δ u) instead of O₂(v)

● Results can be applied to model predictions of O₃(v) excitation and O₃ formation in auroras, oxygen/air discharges

**EXAMPLE 18-BAND FIT ($00v_3 + 10v_3$), ($01v_3 + 11v_3$)
Ascent 102.5 km, Beam On**







APPENDIX 4

Excitation of O₃(v₃) by Electron Bombardment in the EXCEDE III Rocket Experiment

Submitted to the Journal of Geophysical Research

Excitation of O₃(v₃) by electron bombardment in the EXCEDE III rocket experiment

W. T. Rawlins and B. D. Green

Physical Sciences Inc., 20 New England Business Center, Andover, MA 01810

D. E. Paulsen and W. A. M. Blumberg

Air Force Research Laboratory, Hanscom Air Force Base, MA 01731

R. E. Murphy

Research Sciences Corp., Ft. Myers, FL 33908

Abstract

The EXCEDE III rocket experiment bombarded the nighttime lower thermosphere with energetic electrons at high dosing rates and observed the resulting infrared fluorescence with a suite of instruments including a cryogenic interferometer. Fourier transform spectra in the 900 to 1100 cm⁻¹ (9 to 11 μm) spectral region, obtained at altitudes between 85 and 105 km, show the presence of vibrationally excited O₃(v₃) excited by both quiescent (ambient) and electron-initiated processes. When the electron beam is on, O₃(v) emission from the irradiated volume is more intense than that from the ambient background, and the excitation of at least four vibrational quanta can be identified. Least squares spectral fitting analysis determines the vibrational state column densities for both the ambient and beam-excited components, and their dependencies on altitude and dosing. Systematic kinetic analysis of these results yields new information on the processes responsible for electron-initiated ozone excitation. Direct excitation of O₃(v) by secondary electron impact on ground state ozone clearly plays a key role. In addition, the observations at the highest dosing levels (~102 km) indicate the formation of additional ozone in the beam through bimolecular reactions involving beam-excited metastable precursors. The observations match well with the expected kinetics of the reaction

of beam-created $O_2(A^3\Sigma_u^+, v)$ with O_2 to produce O_3 , which is either formed in vibrationally excited states or subsequently excited by electron impact.

1. Introduction

The EXCEDE III upper atmospheric rocket experiment observed spectrally resolved atmospheric infrared fluorescence excited in the lower thermosphere (85 to 115 km) by a pulsed, 2.5 kV, 18 A electron beam generated by a rocketborne accelerator module. A separate, extensively instrumented sensor module included a cryogenic scanning Michelson interferometer which produced Fourier transform spectra of the ambient and beam-created fluorescence over the 2.4 to 21 μm (4200 to 475 cm^{-1}) spectral region with $\approx 2 \text{ cm}^{-1}$ spectral resolution. The spectra reveal a rich assortment of beam-created excited state species, including NO, NO^+ , CO_2 , and O_3 . This paper describes the observations and analysis of beam-created fluorescence from the asymmetric stretching fundamental (v_3) of vibrationally excited $O_3(v)$ near 10 μm , observed at altitudes near 100 km.

The kinetics and mechanisms of non-equilibrium $O_3(v)$ excitation in the quiescent upper mesosphere and lower thermosphere are fairly well understood [Rawlins, 1985; Solomon et al, 1986]. However, the question of auroral excitation or enhancement of ozone is still unresolved. This issue is also relevant to mechanisms for electrical and photochemical production of ozone in the middle and lower atmosphere. In the quiescent upper atmosphere, $O_3(001)$ is populated by thermalizing collisions and by resonant absorption of upwelling 10 μm Earth and atmospheric radiation, and $O_3(v_3 \geq 1)$ is generated by three-body recombination of O and O_2 . Additional

processes for excitation of O₃(v) in electron-bombarded air have been suggested, but the available auroral data base has not clearly demonstrated their occurrence. Potential O₃(v) formation/excitation mechanisms include direct electron impact excitation of O₃, energy transfer to O₃ from metastable electronically or vibrationally excited species, and chemiexcitation reactions of the type O₂⁺ + O₂ → O₃(v) + O; these mechanisms were discussed by Rawlins [1985].

Because of the low precursor concentrations for these processes, their effects are likely to be observable above ambient only for relatively strong dosings at low altitudes, e.g., an IBC III or III⁺ aurora near 90 to 100 km. These conditions are rarely encountered by auroral rocketborne flight measurements, and the limited existing data are qualitative and inconclusive. The HIRIS rocketborne interferometer spectrometer observed a very intense IBC III to IV arc [Stair et al, 1983; Rawlins et al, 1985], with an apparently large O₃(v) excitation efficiency of 2 to 5 vibrational quanta per ion pair near 100 km. Unfortunately, this cannot be taken to be a definitive result, since tumbling motion of the payload introduced a large uncertainty in the altitude of the aurorally excited O₃(v) emission. A more recent measurement by the SPIRIT 1 rocketborne interferometer [Rawlins et al, 1993] observed O₃(v) emission near 100 km in the vicinity of an IBC III arc, however the instrument did not get a sufficiently direct view of the arc to conclusively distinguish the observed O₃(v) emission as auroral rather than intervening ambient fluorescence. These observations resulted in an upper bound of 0.8 to 2.3 quanta per ion pair, which is consistent with HIRIS but nevertheless inconclusive. In order to clearly assess the possible excitation kinetics and scalings with dosing conditions, it is essential to obtain quantitative observations of O₃(v) emission from a dosed volume at a well determined altitude.

A recent series of laboratory electron-beam dosing experiments provides considerable insight into the excitation of O₃(v) fluorescence in the bombardment of atmospheric species by energetic electrons [Upschulte et al., 1989; Holtzclaw et al, 1992]. These experiments, performed in the cryogenic LABCEDE facility [Upschulte et al, 1994a] at the Phillips Laboratory/Geophysics Directorate, observed infrared O₃(v) fluorescence from electron-irradiated O₃/Ar, O₃/N₂, O₂/Ar, and O₂/N₂ mixtures at pressures of 0.1 to 80 mtorr and temperatures near 90 K. The measurements demonstrated the following:

- (1) Excitation of O₃(v) by secondary electron impact on O₃ is highly efficient, with a cross section approximately 10 times larger than that of the analogous excitation of CO₂(v₃);
- (2) O₃ is formed from electron irradiation of O₂ at low pressures, apparently by a two-body reaction involving beam-created metastable oxygen precursors.

The results from the e⁻ + O₃ excitation measurements indicate an auroral excitation rate which scales with secondary electron number density rather than with dosing strength (ion pair production rate), and which should be readily observable in zenith or limb views of IBC III or greater auroras at \approx 100 km [Blumberg et al, 1990].

Recent laboratory kinetics investigations reported by Copeland and coworkers [Copeland, 1994; Copeland et al, 1994; Knutson et al, 1994] have determined room-temperature rate coefficients for the quenching of the metastable O₂(A³ Σ_u^+ , 6 \leq v \leq 9) by O₂. These investigators

find the quenching rate coefficients to be orders of magnitude faster than previously believed [Kenner and Ogryzlo, 1980], and observe substantial production of atomic oxygen, suggesting a high probability for reactive formation of ozone. Thus both the electron impact excitation and the two-body reactive production of ozone now appear to be considerably more efficient than previously suggested by Rawlins [1985], and one can expect that these reactions should contribute to O₃(v) excitation in the electron-irradiated upper atmosphere.

In the present paper, we report observations from a high-altitude, rocketborne electron irradiation experiment in which spectrally resolved infrared fluorescence was observed from the bombardment of the ambient atmosphere by a pulsed electron beam at altitudes of 85 to 115 km. This bombardment produced a maximum dosing level of 6×10^{11} ion pairs/(cm³s) near 103 km and electron number densities as high as 1.5×10^9 cm⁻³, with gas residence times of 20 to 600 ms in the irradiated volume. These measurements provide the first conclusive and quantitative atmospheric observations of O₃(v) excitation by electron-initiated processes. The results are consistent with the recent laboratory observations of efficient e⁻ + O₃ excitation and rapid reaction of beam-created O₂^{*} metastables with O₂ to form O₃.

2. Summary of Flight Measurements

The instrumentation and flight of EXCEDE III are described elsewhere. The payload was launched aboard an Aries booster on 27 April, 1990, at White Sands, NM, 01:00:59 MDT (07:00:59 GMT), and achieved an apogee of 115 km. The booster was separated from the payload at 68 km. At 82.7 km on ascent, the payload separated into two modules, one containing

the electron beam accelerator system and supporting instrumentation, and one containing a suite of optical spectrometers and photometers for viewing the beam-excited volume. The accelerator system generated pulses of nominally 2.6 kV and 18 A in a series of 7.1-second cycles (4.73 s on, 2.37 s off). Eighteen usable electron beam cycles occurred between \approx 95 km on ascent, 115 km apogee, and 87 km on descent.

For the present analysis, the primary instrument aboard the sensor module was a cryogenic infrared interferometric spectrometer (2.4 to 21 μm), which was used to obtain high-resolution (\approx 2 cm^{-1}) fluorescence spectra of the excited $\text{O}_3(v_3)$ band between 9 and 12 μm . Additional sensors included three circular-variable-filter spectrometers (2.4 to 21 μm), a visible grating monochromator (300 to 800 nm), an ultraviolet grating spectrometer (180 to 300 nm), two X-ray proportional counters [Rappaport et al, 1993], four spatially scanning filter photometers centered at 391.4, 380.4, 557.7, and 276.1 nm, additional fixed filter photometers at 391.4, 520.0, and 522.8 nm, an atomic oxygen resonance fluorescence light source and detection system, and video and film cameras. For the ozone excitation analysis described here, the key supporting sensors were the scanning 391.4 nm photometer, which determined the local ion pair production rate in the interferometer's field of view for each beam pulse, and the vacuum-ultraviolet (130 nm) resonance fluorescence diagnostic, which provided estimates of the ambient atomic oxygen number densities [Nelson et al, 1992].

The interferometer was a cryogenic, telescoped, scanning Michelson interferometer with dual optical channels [Thurgood and Huppi, 1989]. The instrument was configured to operate simultaneously in four spectral bandpasses: 2.4 to 4.0 μm , 4.0 to 7.5 μm , 7.0 to 12.5 μm , and

12.5 to 21 μ m. Careful selection of the cut-on and cut-off wavelengths of the bandpass filters allowed sensitive observations of the principal high-altitude radiators (NO, O₃, and CO₂) without interferences from detector non-linearity or dynamic range limitations. The interferometer's scanning cycle and the electron beam cycle were synchronized such that, in each beam cycle, there were two complete interferometer scans with the beam on and a third complete scan and rapid retrace with the beam off. The instrument produced single-sided interferograms, which were detrended, phase-corrected, and transformed using triangular apodization. Typical spectral resolutions of the Fourier transform spectra were 1.7 to 1.9 cm⁻¹, depending on the number of data points in the interferogram.

The field of view of the interferometer was 3.6 deg x 3.6 deg along an upward-looking line of sight as illustrated in Figure 1. The beam elevation was 61.1 deg, constrained by the local magnetic field lines. Throughout most of the measurements, the included angle between the beam and the line of sight was \approx 47 deg; however this angle increased late in the descent as the sensor scanned back toward the accelerator module. The spatially scanning 391.4 nm photometer provided determinations of the energy deposition within the observed beam volume throughout the flight. The volumetric ion pair production rates were determined from the photometric data assuming 14.1 N₂⁺ ions per 391.4 nm photon [Borst and Zipf, 1970] and 0.62 N₂⁺ ion per total ion [Rees and Jones, 1973], and using the observed beam widths from generalized Gaussian fits to the spatial distributions. Typical beam diameters were \approx 8 m. The local volumetric ion pair production rates are plotted for ascent and descent in Figure 2.

Figure 1 and Figure 2

During the early stage of the ascent, the velocity vector of the accelerator module was directed along the direction of beam propagation, resulting in longer gas residence times in the irradiated volume for altitudes up to about 110 km. As the module approached apogee and subsequently descended, the flow direction became more nearly orthogonal to the beam, and the residence times were correspondingly shorter. Flow times through the viewed dosed volume were determined from the velocities and beam dimensions, and are plotted in Figure 3. The characteristic flow times on ascent up to 105 km were well in excess of 100 ms, in contrast to values of \approx 30 ms or less near apogee and throughout the descent. The long residence times on ascent resulted in the largest energy depositions of the flight, in excess of 10^{12} eV/cm³ below 105 km and peaking at \approx 10^{13} eV/cm³ near 101 km. The difference in residence times between the maximum dosing on ascent below 105 km and the remainder of the flight is a key element in the kinetic interpretation of the observed excitation phenomena. As discussed further below, the residence times near maximum dose are long enough for the beam excitation processes to closely approach steady state kinetics conditions, while the shorter times near apogee and throughout descent more closely sample the initial excitation rates.

Figure 3

3. O₃ Spectral Data and Analysis

The spectral analysis centered on the asymmetric stretch (v_3) band of O₃ near 1000 cm⁻¹ (10 μ m). Example spectra of O₃(v) fluorescence, observed on ascent with the beam off, are shown in Figure 4a. At altitudes below \approx 105 km, the (001) - (000) band, centered at 1042 cm⁻¹,

is clearly identifiable by its characteristic R, Q, and P branch rotational structure. The vibrational "hot bands", resulting from $\Delta v_3=1$ transitions from upper-state vibrational levels at higher energy than (001), are discernible at transition frequencies below about 1000 cm^{-1} . Fluorescence from these states is detectable at altitudes below $\approx 97\text{ km}$, and is below the instrument noise-equivalent signal radiance (NESR) above that altitude. The fluorescence from the (001) and higher states follows the spectral and altitude behavior expected for ambient nighttime atmospheric O₃ fluorescence [Green et al, 1986; Rawlins et al, 1993]. The spectra also show a weak, broad feature centered near 1070 cm^{-1} . The intensity of this feature is essentially independent of altitude up to 115 km , a behavior signifying a rocketborne contaminant species. Based on prior experience with rocketborne infrared spectrometer measurements, this feature is probably due to earthshine-pumped, near-field fluorescence from outgassing products of silicon oxide sealants used on the payload [Smith, 1988]. The presence of this feature does not significantly affect the analysis of the O₃(v) fluorescence. As shown by the 107 km spectrum in Figure 4a, the spectral scans for altitudes above 105 km show a constant baseline radiance of $\approx 10^{-12}\text{ W}/(\text{cm}^2\text{ sr cm}^{-1})$ between 900 and 1040 cm^{-1} , signifying the effective detection limit of the instrument in this spectral region.

Figure 4

Fluorescence spectra observed during ascent with the electron beam on are shown in Figure 4b, illustrating the behavior above and below the altitude threshold for detectable O₃(v) emission. The 107 km "baseline" spectrum exhibits the same noise floor between 900 and 1040 cm^{-1} as with the beam off, with the addition of a few sharp atomic lines due to O(I) Rydberg transitions. The contamination feature centered near 1070 cm^{-1} remains unchanged, however the

intensity above 1100 cm^{-1} is enhanced by the electron beam. This fluorescence has been identified as high- J' transitions of rovibrationally excited $\text{NO}(v,J)$ formed by beam-initiated chemical processes [Fraser et al., 1993; Lipson et al., 1993; Armstrong et al., 1995]. The majority of the fluorescence from this band system lies at higher frequencies (roughly 1600 to 2000 cm^{-1}), and will not be discussed further here. The $\text{NO}(v,J)$ fluorescence does not appear to be significant below $\approx 1100\text{ cm}^{-1}$, and thus does not impact the analysis of the $\text{O}_3(v)$ system. As shown by the 102.5 km spectrum in Fig. 4b, the $\text{O}_3(v)$ fluorescence spectra with the beam on appear qualitatively similar to those observed from the ambient atmosphere with the beam off. However, the beam-on spectra show significantly more fluorescence from the higher ozone vibrational levels (900 to 1000 cm^{-1}) than the ambient spectra at similar altitudes, as illustrated by comparison of the 102.5 km spectrum in Fig. 4b with the 101 km spectrum in Figure 4a.

The spectral data were subjected to more detailed analysis in order to determine systematic trends in $\text{O}_3(v)$ formation with altitude and dosing. After subtracting the instrumental baseline, the spectra were analyzed by a least squares spectral fitting method developed for the analysis of $\text{O}_3(v)$ spectra by Rawlins and Armstrong (1987) and improved by Rawlins et al. (1993). The $\text{O}_3(v)$ spectrum was simulated using two models, one incorporating nine vibrational bands and one incorporating eighteen. The 9-band model includes transitions from the $(00v_3)$ and $(10(v_3-1))$ vibrational states, $1 \leq v_3 \leq 5$, with the relative populations of each $(00v_3)/(10(v_3-1))$ dyad set to local thermodynamic equilibrium values. This accounts for the likely excitation of the v_1 mode through near-resonant vibrational energy transfer, and reduces the complexity due to spectral overlap between neighboring bands. The least squares fitting procedure then gives the total column density for each dyad required to minimize the variance

between the computed and observed spectra. The 18-band model is similar and includes additional transitions from $(01v_3)/(11(v_3-1))$ dyads, thus including the possibility of excitation in the v_2 (bending) mode. Typical spectral fitting results are illustrated in Figure 5 for the 18-band model.

Figure 5

In general, the two spectral models give very similar results. The beam-off spectra tend to be more consistent with the 9-band model, and the beam-on spectra are equally consistent with both models. However, it is not possible to distinguish clearly whether any v_2 combination states other than (011) are significantly populated in the ambient atmosphere or in the beam-irradiated volume. Nevertheless, as in previous analyses of laboratory [Rawlins and Armstrong, 1987] and atmospheric [Rawlins et al, 1993] $O_3(v)$ spectra, it is clear from the EXCEDE III spectra that population of at least the $(00v_3)$ and $(10(v_3-1))$ states is required to account for the nearly continuous, unstructured spectral distributions in the "hot band" region. When the populations are lumped into a common upper state $v = v_1 + v_2 + v_3$, the values for the beam-off condition agree well with the relative population distributions predicted by the steady-state kinetic model of Rawlins (1985) for $2 \leq v \leq 5$. Similar agreement was found for SPIRIT 1 $O_3(v)$ spectra [Rawlins et al, 1993]. In contrast, the lumped populations for the beam-on case indicate greater excitation at the higher levels, as discussed further below.

4. $O_3(v)$ Altitude Profiles

In order to quantify the $O_3(v)$ component excited in the electron beam, it was first necessary to determine the contribution from the ambient, quiescent atmosphere. The beam-off $O_3(v)$ column densities for ascent and descent were fit to parametric expressions for altitudes from 84 to 105 km. These expressions were then used to correct the beam-on quantities for the ambient component. The residuals from these corrections give a measure of the amount of $O_3(v)$ produced by beam-initiated processes.

The observed column densities for ambient $O_3(v)$ on ascent and descent are plotted in Figure 6. The $O_3(v=1)$ column densities are fairly well ($\pm 10\%$ or better) determined, especially above 92 km. However, only four beam-off spectra had sufficient signal/noise ratio to permit determination of the $O_3(v \geq 2)$ column densities, and values above 97 km were below the detection limit. The solid curves in Figure 6 represent polynomial fits to the data points. The $O_3(v=1)$ data were fit to a cubic polynomial in $\log(\text{column density})$ vs altitude, and the $O_3(v \geq 2)$ data were fit to quadratic polynomials. The $O_3(v=5)$ column densities are highly uncertain, especially above 95 km; however the $O_3(v=2-4)$ values are well determined and exhibit an altitude dependence characteristic of quiescent nighttime $O_3(v)$.

Figure 6

The $O_3(v=1-3)$ column densities observed on ascent and descent with the beam on are shown in Figure 7, overlaid with the curvefits to the ambient values from Figure 6. This

comparison illustrates the departure from the ambient vibrational distributions and altitude dependencies observed with the electron beam on, especially during ascent between 95 and 103 km when the dosing residence times are longest. In particular, the beam-induced enhancement in $O_3(v \geq 2)$ above 98 km is readily apparent. Figure 8 shows the beam-on column densities for $v=1,3$ plotted as ratios to the corresponding beam-off values interpolated from the curvefits. This figure shows that the apparent enhancement above 95 km is as large as a factor of 2 for $v=1$ and a factor of ≈ 9 for $v=3$. Since the optical path through the electron beam is much shorter than the viewed ambient atmospheric column, these observations indicate dramatic enhancement in the $O_3(v)$ number densities within the beam-irradiated volume.

Figure 7 and Figure 8

The path-averaged $O_3(v)$ number densities excited by the electron beam between 98 and 105 km are shown in Figure 9. These values were determined by subtracting the curvefit ambient column density at each altitude from the observed beam-on column density, and dividing the result by the viewed path length across the beam. Total $O_3(v)$ number densities of $\approx 2 \times 10^7 \text{ cm}^{-3}$ were generated by the electron beam in the maximum-dose configuration on ascent, and $\approx 3 \times 10^6 \text{ cm}^{-3}$ were produced near 104 km for short dosing time on descent. As can be seen from Figs. 7 and 8, there is no clear indication for any beam-enhanced $O_3(v)$ on descent for altitudes between 85 and 100 km, i.e. the column densities observed with the beam on are within $\pm 20\%$ of the curvefit ambient values. The final descent spectrum, at 84 km, appears to indicate observable $O_3(v)$ enhancement above the ambient level, however the field of view through the beam-dosed region is large and highly uncertain, precluding quantitative analysis for that case.

Figure 9

5. Excitation Kinetics and Mechanisms

The beam-produced $O_3(v)$ number densities shown in Figure 9 are extremely large. Based on MSIS90 [Hedin, 1991] atmospheric profiles and the $O_3(v)$ kinetics discussed by Rawlins et al. (1993), the ambient $O_3(v)$ number densities at 103 km should be $\approx 2 \times 10^4 \text{ cm}^{-3}$ for $v=1$ and $\leq 80 \text{ cm}^{-3}$ for $v \geq 2$. Thus $O_3(v=1)$ in the dosed volume is enhanced by up to three orders of magnitude, and $O_3(v \geq 2)$ is enhanced by more than four orders of magnitude. Indeed, the total $O_3(v)$ number density produced by the beam in the maximum-dose configuration at 103 km is comparable to the *total* O_3 number density expected for that altitude for normal quiescent conditions. Clearly, this cannot occur unless chemical processes initiated by the electron beam are *generating* new ozone at a substantial rate. It is also obvious that three-body recombination of O and O_2 cannot account for this observation. We present here a simple kinetic analysis to identify the $O_3(v)$ formation mechanisms, focussed on the data for 103 km on ascent and 104 km on descent.

We summarize our analysis first and then present a more detailed discussion. To first order, the primary deactivation process for $O_3(v=1)$ at 103-104 km is radiative decay at $\approx 11 \text{ s}^{-1}$. As discussed further below, superelastic deactivation by electrons contributes another $\approx 5 \text{ s}^{-1}$. At 104 km on descent, the gas residence time in the beam is only $\approx 20 \text{ ms}$ (cf. Figure 3), which is substantially less than the kinetic lifetime of $O_3(v=1)$. Under these conditions, the chemical losses during the residence time are relatively small, and the data provide a measure of the initial

production rate of $O_3(v=1)$. This rate is then $\approx 2 \times 10^8 \text{ cm}^{-3}\text{s}^{-1}$, and is likely due to vibrational excitation by secondary electron impact on ambient ozone. In contrast, for 103 km on ascent, the gas residence time substantially exceeds the chemical lifetime, so the system is approaching steady state. From the steady state approximation, the apparent $O_3(v)$ production rate at 103 km on ascent is then $\approx 3 \times 10^8 \text{ cm}^{-3}\text{s}^{-1}$, comparable to the value estimated from the initial rate. However, excitation of ozone at this rate will deplete $O_3(v=0)$ on the 100 ms time scale, such that the actual excitation rate would have to be significantly larger to achieve the observed $O_3(v=1)$ number densities. Indeed, most or all of the ambient O_3 in the beam would have to be vibrationally excited, a condition that cannot be achieved because of radiative and superelastic deactivation from $v=1$ back to $v=0$. Thus either the ambient ozone number density is much larger than inferred from the ambient radiance data, or a beam-initiated chemical process makes more ozone in the dosed volume. Based on obvious kinetic considerations, such a beam-initiated process would likely be a two-body reaction involving at least one beam-created metastable precursor, e.g. $O_2^+ + O_2$.

Electron Impact Excitation

We have modeled the kinetics of the electron beam excitation process using model-derived species profiles, secondary electron distributions, and the reaction mechanisms listed in Table 1. Concentration profiles for O_3 and O were derived from the ambient $O_3(v)$ data using the density and temperature profiles given by MSIS90 together with the kinetic analysis described by Rawlins et al. (1993). For this purpose, the ambient $O_3(v)$ curvefit column densities were corrected to zenith values and were differentiated with respect to altitude to give local

number density profiles. $O_3(v=1)$ number densities were used to compute $O_3(v=0)$ number densities via radiative/collisional steady state, and $O_3(v \geq 2)$ number densities were used to estimate three-body recombination rates and hence O number densities. The inferred O and O_3 number density profiles are compared to those obtained from MSIS90 in Figure 10. Here the "MSIS" O_3 number densities were computed from the MSIS O, H, T, and density profiles assuming steady-state formation of O_3 by three-body recombination and loss of O_3 by reaction with H and O. The atomic oxygen profile derived from $O_3(v)$ is intermediate between that of MSIS and that determined by resonance fluorescence measurements on board the sensor module [Nelson et al, 1992]. The resonance fluorescence measurements indicate a peak O number density near 10^{11} cm^{-3} between 100 and 105 km, and $\approx 2.5 \times 10^{10} \text{ cm}^{-3}$ at 85 km, with factor-of-two estimated uncertainty. The derived O_3 profile is significantly different from the MSIS expectation, and suggests an elevated density profile due to a dynamic perturbation. In particular, the apparent O_3 number density near 103 km is roughly twice that of the MSIS estimate.

Table 1 and Figure 10

Estimates of the electron number densities at apogee and maximum dose and a computed secondary electron energy distribution for apogee were provided by F. Bien and J. Duff (private communication, 1993), based on detailed modeling of the degradation of the primary electron energy and flux through inelastic collisions in the atmosphere. The modeled secondary electron energy distribution for apogee (115 km) was non-Boltzmann, with a peak between 0.05 and 0.5 eV and a tail extending to 10^7 of the peak at 100 eV. The low-energy portion of this

distribution is similar to that for an electron "temperature" of ≈ 0.5 eV. We expect the secondary electron "temperatures" at lower altitudes to be "cooler" due to increased collision rates.

Using these results and the approximation of steady state between ion pair production and electron-ion recombination, we estimated electron densities for the remaining beam-on cases. The estimated values ranged from 4×10^8 cm $^{-3}$ at apogee (115 km) to 1.5×10^9 cm $^{-3}$ at maximum dose (103 km ascent). However, we note that, for these values, the e-folding time for electron-ion recombination is about 10 to 20 ms, which is a substantial fraction of the beam residence times for the apogee and descent cases (see Figure 3). Hence the electron-ion steady state approximation is less accurate for these cases, and provides an overestimate of the mean electron number density during the beam pulse. However, for present purposes of rough kinetic estimates, this approximation is adequate, introducing negligible error at maximum dosing (103 km ascent) and less than 30% error for 104 km descent.

To model the electron impact excitation process, we require the first 30 reactions listed in Table 1, which describe the excitation, deactivation, and dissociation of O₃ by secondary electrons, and vibrational deactivation of O₃(v) by radiative and collisional processes. To describe the electron impact excitation (Reactions 1 to 5), the total rate coefficient was varied to match the observed total vibrational excitation, and the partitioning by vibrational level was taken from the laboratory measurements [Holtzclaw et al., 1991, 1992]. The rate coefficients for superelastic deactivation (Reactions 6 to 9) were then obtained from microscopic reversibility using 0.5 eV as an approximation for the secondary electron "temperature." Rate coefficients for the dissociation of O₃(v) (Reactions 10 to 15) were estimated by convolving the modeled

secondary electron energy distribution with the cross section of Keto (1981) for dissociation of $O_3(v=0)$, where the values for $O_3(v \geq 1)$ were determined by adjusting the cross section's threshold by an amount corresponding to the vibrational energy of the molecule.

The radiative rates and collisional deactivation rate coefficients were taken from laboratory determinations as cited. The collisional deactivation processes were included for completeness, however their rates are too slow to contribute significantly to $O_3(v)$ losses on the time scale of the measurements. The total first-order loss rates in the beam for $O_3(v=1)$ and $O_3(v=0)$ between 95 and 105 km are estimated to be ≈ 20 and $3-8 \text{ s}^{-1}$ respectively. These values are too slow compared to the beam processing rates to permit the steady-state approximation on these species except near maximum dosing, so it was necessary to numerically integrate the coupled rate equations.

The results of the model calculations were compared to the observations of beam-excited $O_3(v)$ at maximum dosing (103 km ascent) and descent (104 km), as well as to the absence of observable $O_3(v)$ excitation on descent below 100 km. The total $O_3(v)$ number density observed at maximum dosing is consistent with a total rate coefficient of $\approx 5 \times 10^{-8} \text{ cm}^3/\text{s}$ for electron impact excitation of $O_3(v)$; the excitation is accompanied by dissociation of about 2/3 of the ambient O_3 in the beam volume. However, this model predicts essentially no difference between the beam-enhanced $O_3(v)$ number densities on ascent and descent, with a predicted enhancement at 100 km of a factor of 4 in excess of the detection limit. In order to accommodate the excitation observed at 104 km (descent) and the absence of observable excitation on descent below that altitude, it is necessary to use a total electron impact excitation rate coefficient an

order of magnitude smaller, $\approx 5 \times 10^{-9} \text{ cm}^3/\text{s}$. This then results in a substantial underprediction of the excitation observed at maximum dosing, suggesting that another reaction must be generating O_3 in the beam volume. Assuming that we have accounted for all the loss processes, the additional O_3 production rate required to account for the excitation at 103 km (ascent) is $\approx 3 \times 10^8 \text{ cm}^{-3}\text{s}^{-1}$.

Metastable Oxygen Chemistry

The O_3 production rate deduced from the maximum dose data is consistent with a moderately efficient ($\geq 10\%$ collision efficiency) bimolecular reaction between a major ambient atmospheric species and a beam-created trace species, most likely metastable. Bimolecular reactions which could potentially contribute to O_3 formation and/or $\text{O}_3(v)$ excitation in electron-bombarded oxygen or air have been reviewed in previous papers [Rawlins et al, 1985; Rawlins, 1985; Rawlins et al, 1987]. Of these reactions, the one most likely to be responsible for the EXCEDE III observations at high altitude is the process of the form



Here $\text{O}_2(\text{A})$ is a generic representation of any or all of the three nested metastable states $\text{A}^3\Sigma$, $\text{A}'^3\Pi$, and $\text{c}^1\Sigma$, which lie at energies above 4 eV. Due to the high energy of $\text{O}_2(\text{A})$, this process is exoergic, and has been previously suggested for both the auroral [Rawlins et al, 1985; Rawlins, 1985] and quiescent [Allen, 1986] thermosphere. Since the reverse reaction provides adiabatic, statistically favored pathways for the well-known reaction of O with O_3 , it is reasonable to expect

that the forward reaction can occur. However, very little is known about the kinetics of $O_2(A)$ or its production in electron-disturbed air. In addition, previous measurements [Kenner and Ogryzlo, 1980] of the rate coefficients for quenching of $O_2(A^3\Sigma)$ by O_2 indicated that the reaction was too slow to account for significant O_3 production in the upper atmosphere, given the likelihood for relatively low $O_2(A)$ number densities even in auroral conditions. However, recently reported laboratory measurements now show that the reactions of $O_2(A^3\Sigma, v)$ with O_2 are indeed highly efficient, and are likely to form O_3 [Copeland, 1994; Copeland et al., 1994; Knutson et al., 1994; Yang et al., 1993].

To test the potential of Reaction (R1) as the missing O_3 production step, we examine its kinetics in steady state at maximum dose (103 km, 0.5 s). Based on Knutson et al. (1994), a suitably conservative estimate for the rate coefficient for Reaction (R1) is $\approx 3 \times 10^{-11} \text{ cm}^3/\text{s}$. Given the O_2 number density at 103 km ($3.4 \times 10^{12} \text{ cm}^{-3}$) and the apparent bimolecular O_3 production rate of $3 \times 10^8 \text{ cm}^{-3}\text{s}^{-1}$, the $O_2(A)$ number density would have to be about $3 \times 10^6 \text{ cm}^{-3}$ in the beam-irradiated volume. At this altitude, the total $O_2(A^3\Sigma)$ loss rate due to radiation and quenching by N_2 , O_2 , and O (see Table 1) is $\approx 400 \text{ s}^{-1}$, compared to the characteristic flow loss of $\approx 2 \text{ s}^{-1}$ (cf. Fig. 3). Thus the required $O_2(A)$ production rate in the beam would have to be $\approx 1.2 \times 10^9 \text{ cm}^{-3}\text{s}^{-1}$ or 5×10^{-3} molecules per ion pair.

This value is consistent with the expected production rate of $O_2(A^3\Sigma)$ in electron-irradiated air. Based on detailed modeling of energetic electron deposition in air and the excitation cross section given by Keto (1981) has determined an $O_2(A^3\Sigma)$ excitation rate of 0.02 molecules per ion pair. (We note that Keto (1981) quoted this cross section for excitation of the

$c^1\Sigma$ state, but the same cross section was reported earlier for excitation of the $A^3\Sigma$ state by Watson et al. (1967).) Vertical excitation from $O_2(X^3\Sigma, v=0)$ populates the A-state on its repulsive wall above the dissociation limit, resulting in a high dissociation probability. Based on Franck-Condon considerations, only about 5 to 10% of the direct excitation events will result in bound $O_2(A^3\Sigma)$, with initial population in high vibrational levels. This suggests a molecular excitation rate of ≈ 0.002 molecules per ion pair.

The excitation of $O_2(A^3\Sigma)$ can be significantly augmented by the presence of vibrationally excited $O_2(v \geq 1)$, which has high Franck-Condon overlap with bound vibrational levels of $O_2(A^3\Sigma, v)$. Using the Keto (1981) cross section and the computed secondary electron energy distribution described above, we estimate an effective rate coefficient of $5 \times 10^{-12} \text{ cm}^3/\text{s}$ for electron-impact excitation of $O_2(X^3\Sigma, v=1)$ to $O_2(A^3\Sigma, v \approx 6-8)$. If we assume an excitation rate for $O_2(v)$ of 3 quanta per ion pair. The main collisional loss for $O_2(v)$ is deactivation by atomic oxygen. Based on the measured rate coefficients for the high-pressure limit of $O + O_2$ recombination [Hippler et al, 1990] and for $O + O_2$ isotope exchange [Anderson et al, 1985], this rate coefficient is probably no larger than $\approx 6 \times 10^{-12} \text{ cm}^3/\text{s}$. This corresponds to high-altitude loss rates of less than 2 s^{-1} , i.e. less than the flow loss even for maximum dose conditions. Thus $O_2(v)$ does not reach steady state in the irradiated volume. For the maximum dose, a time-averaged median number density for $O_2(v=1)$ is $\approx 1 \times 10^{11} \text{ cm}^{-3}$. This gives an $O_2(A, v)$ production rate of $7.5 \times 10^8 \text{ cm}^{-3}\text{s}^{-1}$ or 0.003 molecules per ion pair. The total estimated $O_2(A)$ production rate from direct electron impact on $O_2(v=0,1)$ is then 0.005 molecules per ion pair, in excellent agreement with the value required to account for the maximum dose observations.

More detailed kinetic calculations, performed by numerical integration of the coupled differential equations represented by the reaction mechanism of Table 1, confirm the above analysis. Example time-dependent calculations for the maximum dose and descent conditions are illustrated in Figure 11, showing the effect of including and omitting the O₂(A) chemistry. In this case we have assumed that O₂(A) reacts with O₂ to form O₃(v=0), and that all the vibrational excitation of O₃(v) comes from electron impact according to the laboratory [Holtzclaw et al., 1991, 1992] vibrational distribution. The maximum-dose case is shown in Figure 11a. In the absence of the O₂(A) contribution, total ozone in the beam-irradiated gas is depleted by a factor of two, and O₃(v) levels are less than half the measured values. When production of O₃(v=0) by O₂(A) is included, total ozone decreases at early times and then increases substantially as the O₂(A) number density increases beyond a certain level. The effect of the O₂(A) chemistry appears only after about 100 ms of reaction time, owing to the relatively slow production rate of O₂(A). Thus the effect should not be observable in spectral scans with shorter beam residence times, as on descent. As shown in Figure 11b, the 104 km (descent) scan has only a factor of two smaller ion pair production rate than the maximum dose case, but the beam residence time of less than 20 ms prevents O₂(A) chemistry from contributing to the observed O₃(v) excitation. In this case, the O₃(v) enhancement reflects only the initial excitation rate of O₃(v) by secondary electron impact.

Figure 11

The vibrational distributions predicted for maximum dose are compared to the observed ones in Figure 12. The calculated distributions, which are essentially those observed in the

laboratory for secondary electron impact, agree with the observations below $v=3$, but greatly underpredict the excitation for $v=4,5$. This suggests the possibility of direct formation of $O_3(v \geq 3)$ via $O_2(A)$, or possibly the energy transfer process



as postulated to account for similar vibrational distributions observed in laboratory microwave discharges [Rawlins et al, 1987].

Figure 12

We have also considered other possible beam-initiated reactions for formation of O_3 . The reactions of $O_2(A)$ with vibrationally excited $O_2(v)$ and/or the metastable $O_2(a^1\Delta)$,



have the necessary energetics, and both $O_2(v=1)$ and $O_2(a^1\Delta)$ are formed efficiently and quenched slowly in electron-bombarded air. However, even at maximum dose these species can only reach number densities approximately 1/10 and 1/100 of the ambient O_2 number density, so Reactions (R3) and (R4) would require rate coefficients near or in excess of the gas kinetic limit in order to be responsible for all the observed $O_3(v)$ excitation. While Reaction (R3) could

possibly contribute, Reaction (R4) is unlikely to play a role. The associative detachment reaction,



requires $\text{O}_2(v \geq 3)$ to be exoergic. O^- is produced at 0.015 molecules per ion pair, and is rapidly destroyed by associative detachment with O. Thus O^- and $\text{O}_2(v \geq 3)$ are not likely to be formed in sufficient abundance to produce O_3 with a reasonable rate coefficient. The reaction



has recently been shown not to occur with a significant rate coefficient [Upschulte et al. 1994b].

6. Discussion and Conclusions

In summary, the EXCEDE III flight experiment obtained high-altitude data under well-controlled dosing and measurement conditions; the data clearly indicate a mechanism for the excitation of $\text{O}_3(v)$ in electron-bombarded air. Most of the excitation is caused by inelastic collisions of secondary electrons with ozone molecules. Furthermore, it is likely that additional O_3 is formed in the dosed volume by reactions of electron-excited, metastable molecular oxygen with ambient O_2 . This interpretation of the EXCEDE III flight results is quantitatively consistent with laboratory kinetic measurements of the excitation processes.

To further test the comparison between the flight and laboratory results, we have examined the relative $O_3(v_3)$ and $CO_2(v_3)$ excitation observed by EXCEDE III. Comparisons of the O_3 radiances near $10 \mu m$ and the CO_2 radiances at $4.3 \mu m$, accounting for the differences in the ambient O_3 and CO_2 number densities, clearly indicate that O_3 excitation by electron impact is roughly an order of magnitude more efficient than CO_2 excitation. From inspection of the beam-excited $CO_2(v_3)$ radiances near $100 km$, we estimate the ratio of the O_3 and CO_2 excitation rate coefficients to lie in the range

$$7 \leq k_{e+O_3}/k_{e+CO_2} \leq 20.$$

This is quite consistent with the laboratory value for this ratio of 12 ± 6 , determined in the LABCEDE electron beam facility at ≈ 1 mtorr and $100 K$ [Holtzclaw et al, 1992]. Since the $CO_2(v_3)$ excitation cross section peaks at $\approx 10^{-16} cm^2$ near $1 eV$ [Lowke et al, 1973], this ratio indicates a peak $O_3(v_3)$ excitation cross section near $\approx 10^{-15} cm^2$. Thus the electron-impact excitation of ozone is a highly efficient collisional process, perhaps owing to the propensity of ozone to attach low-energy electrons.

The high excitation efficiency of $O_3(v_3)$ applies directly to the auroral excitation scenario. For an IBC III⁺ aurora of the type observed in the HIRIS rocket flight [Rawlins et al, 1985; Blumberg et al., 1990], i.e. ≈ 600 kR at $391.4 nm$ near $110 \pm 10 km$, the local ion pair production rate exceeds $10^6 cm^{-3}s^{-1}$, and the electron number density exceeds $10^6 cm^{-3}$. Under these conditions, the excitation of $O_3(v)$ by electron impact will proceed at a rate near $10^5 cm^{-3}s^{-1}$, or perhaps faster if the auroral secondary electron distribution is more energetic than that produced

by the EXCEDE III electron beam. This excitation rate is comparable in magnitude to that observed for the unusually intense auroral arc in the HIRIS flight above 100 km [Rawlins et al, 1985]. This excitation rate is also comparable in magnitude to the production rate of $O_3(v=1)$ by radiative excitation near 100 km, and is well in excess of the production rate of $O_3(v \geq 1)$ by three-body recombination above 100 km [Rawlins, 1985; Rawlins et al, 1993]. Although more detailed modeling of the auroral excitation process is warranted, it appears that direct excitation of $O_3(v)$ by secondary electron impact should give rise to observable auroral enhancements, especially for strong auroras at altitudes between 100 and 110 km.

The two-body reaction (R1) can contribute to O_3 formation in both the auroral and the quiescent upper atmosphere. In auroras, $O_2(A,A',c)$ is produced by electron impact excitation of ambient O_2 and aurorally generated $O_2(v)$ as outlined above for the electron beam. (However, due to moderately efficient quenching of $O_2(v)$ by O, the $O_2(v)$ pathway may be less significant at auroral dosing levels and electron number densities.) $O_2(A,A',c)$ is also formed by three-body recombination of atomic oxygen, a process which occurs in both quiescent and auroral conditions. Ambient $O_2(A,A',c)$ number densities maintained by O-atom recombination are typically 10^2 to 10^3 cm $^{-3}$ near 100 km [Allen, 1986; Murtagh et al, 1986]. Using the rate coefficient for Reaction (R1) discussed above, these number densities will give two-body O_3 production rates of roughly 10^4 to 10^5 cm $^{-3}s^{-1}$ at 100-105 km. These values are comparable to the three-body (O + O₂ + M) recombination rate at this altitude [Rawlins, 1985; Rawlins et al, 1993]. Thus it appears likely that metastable O_2 via Reaction (R1) contributes significantly to the production of ozone near 100 km, and may be partly responsible for the unexpectedly large ozone number densities observed at these altitudes as suggested by Allen (1986). Clearly, more detailed modeling of this

complex process is warranted, in order to re-examine the prevailing views of odd-oxygen chemistry in the lower thermosphere.

Acknowledgements

The authors acknowledge many useful discussions with M. Fraser, G. Caledonia, F. Bien, J. Duff, and R. Rieder. This effort was supported by the Defense Nuclear Agency under a contract with the Geophysics Laboratory.

References

Allen, M., A new source of ozone in the terrestrial upper atmosphere?, *J. Geophys. Res.* 91, 2844, 1986.

Anderson, S.M., F.S. Klein, and F. Kaufman, Kinetics of the isotope exchange reaction of ^{18}O with NO and O_2 at 298 K, *J. Chem. Phys.* 83, 1648, 1985.

Armstrong, P.S., J.A. Dodd, S.J. Lipson, W.A.M. Blumberg, R.B. Lockwood, J.R. Lowell, R.M. Nadile, D.E. Paulsen, R.E. Murphy, W.T. Rawlins, M.E. Fraser, and B.D. Green, High rotational and vibrational excitation of thermospheric nitric oxide in natural and artificial auroras, *EOS* 76 (46), F439, 1995.

Blumberg, W.A.M., B.D. Green, and W.T. Rawlins, Auroral excitation of LWIR fluorescence in the lower thermosphere (abstract), *Eos Trans. AGU* 71, 577, 1990.

Borst, W.L. and E.C. Zipf, Cross section for electron-impact excitation of the (0,0) first negative band of N_2^+ from threshold to 3 keV, *Phys. Rev. A* 1, 834, 1970.

Copeland, R.A., Laser double resonance study of collisional removal of O₂(A³Σ_u⁺, v=7) with O₂, *J. Chem. Phys.* 100, 744, 1994.

Copeland, R.A., K. Knutsen, and T.G. Slanger, Using laser-induced fluorescence to study molecules of atmospheric importance, *Proc. of the Conference on Lasers '93*, Society for Optical and Quantum Electronics, McLean VA, 1994.

Fraser, M.E., W.T. Rawlins, B.D. Green, D.E. Paulsen, P.S. Armstrong, S.J. Lipson, W.A.M. Blumberg, and R.E. Murphy, Kinetics and mechanisms for the formation of rovibrationally excited nitric oxide in the EXCEDE III rocket experiment, *EOS* 74 (43), 469, 1993.

Green, B.D., W.T. Rawlins, and R.M. Nadile, Diurnal variability of vibrationally excited mesospheric ozone as observed during the SPIRE mission, *J. Geophys. Res.* 91, 311, 1986.

Hedin, A.E., Neutral atmosphere empirical model from the surface to the lower exosphere. MSIS90, *J. Geophys. Res.* 96, 1159, 1991.

Hippler, H., R. Rahn, and J. Troe, Temperature and pressure dependence of ozone formation rates in the range 1-1000 bar and 90-370 K, *J. Chem. Phys.* 93, 6560, 1990.

Holtzclaw, K.W., B.D. Green, and W.A.M. Blumberg, Electron excitation efficiencies of infrared radiances, *EOS* 72 (44), 361, 1991.

Holtzclaw, K.W., K.L. Carleton, B.L. Upschulte, B.D. Green, S.J. Lipson, and W.A.M. Blumberg, Relative electron excitation efficiencies for vibrations of O₃, CO₂, and N₂O, Paper CA-5 at the 45th Annual Gaseous Electronics Conference, 1992. *Bulletin Am. Phys. Soc.* 37.

Lipson, S.J., P.S. Armstrong, J.R. Lowell, W.A.M. Blumberg, D.E. Paulsen, M.E. Fraser,

W.T. Rawlins, B.D. Green, and R.E. Murphy, EXCEDE III nitric oxide

rovibrational distribution analysis, *EOS* 74 (43), 469, 1993.

Lowke, J.J., A.V. Phelps, and B.W. Irwin, Predicted electron transport coefficients and operating characteristics of CO₂-N₂-He mixtures, *J. Applied Physics* 44, 4664, 1973.

Kenner, R.D., and E.A. Ogryzlo, Deactivation of O₂(A³Σ_u⁺) by O₂, O, and Ar, *Int. J. Chem. Kin.* 12, 501, 1980.

Keto, J.W., Electron beam excited mixtures of O₂ in argon. II. Electron distributions and excitation rates, *J. Chem. Phys.* 74, 4445, 1981.

Knutsen, K., M.J. Dyer, and R.A. Copeland, Laser double-resonance study of the collisional removal of O₂(A³Σ_u⁺, v=6,7,9) with O₂, N₂, CO₂, Ar and He, *J. Chem. Phys.* 101 (9), 7415-7422, 1994.

Murtagh, D.P., G. Witt, and J. Stegman, O₂-triplet emissions in the nightglow, *Can. J. Phys.* 64, 1587, 1986.

Nelson, D.D., M.S. Zahniser, P. Espy, W. Pendleton, J. Ulwick, and D. Paulsen, Atomic oxygen measurements during EXCEDE III (abstract), *Eos Trans. AGU* 73, 218, 1992.

Rappaport, S.A., R.J. Rieder, W.P. Reidy, R.L. McNutt, Jr., J.J. Atkinson, and D.E. Paulsen, Remote X ray measurements of the electron beam from the EXCEDE III experiment, *J. Geophys. Res.* 98, 19,093, 1993.

Rawlins, W.T., Chemistry of vibrationally excited ozone in the upper atmosphere, *J. Geophys. Res.* 90, 12283, 1985.

Rawlins, W.T. and R.A. Armstrong, Dynamics of vibrationally excited ozone formed by three-body recombination. I. Spectroscopy, *J. Chem. Phys.* 87, 5202, 1987.

Rawlins, W.T., G.E. Caledonia, and R.A. Armstrong, Dynamics of vibrationally excited ozone formed by three-body recombination. II. Kinetics and mechanism, *J. Chem. Phys.* 87, 5209, 1987.

Rawlins, W.T., G.E. Caledonia, J.J. Gibson, and A.T. Stair, Jr., HIRIS rocketborne spectra of infrared fluorescence in the O₃(v₃) band near 100 km, *J. Geophys. Res.* 90, 2896, 1985.

Rawlins, W.T., Woodward, A.M., and Smith, D.R., Aeronomy of infrared ozone fluorescence measured during an aurora by the SPIRIT 1 rocketborne interferometer, *J. Geophys. Res.* 98, 3677, 1993.

Rees, M.H., and R.A. Jones, Time-dependent studies of the aurora - II: spectroscopic morphology, *Planet. Space Sci.* 21, 1213, 1973.

Saxon, R.P. and T.G. Slanger, Molecular absorption continua at 195-300 nm and O₂ radiative lifetimes, *J. Geophys. Res.* 91, 9877, 1986.

Smith, D.R., Evidence for off-axis leakage radiance in high-altitude IR rocketborne measurements, *Proc. Soc. Photo-Opt. Instrum. Eng.* 967, 30, 1988.

Solomon, S., J.T. Kiehl, B.J. Kerridge, E.E. Remsberg, and J.M. Russell III, Evidence for non-local thermodynamic equilibrium in the v₃ mode of mesospheric ozone, *J. Geophys. Res.* 91, 9865, 1986.

Stair, A.T. Jr., J. Pritchard, I. Coleman, C. Bohne, W. Williamson, J. Rogers, and W. T. Rawlins, The rocketborne cryogenic (10 K) high resolution interferometer spectrometer flight - HIRIS: Atmospheric and auroral infrared emission spectra, *Appl. Opt.* 22, 1056, 1983.

Thurgood, V.A. and R.J. Huppi, A cryogenic infrared optical channel interferometer spectrometer for upper atmospheric measurements, *Proc. Soc. Photo-Opt. Instrum. Eng.* 1145, 591, 1989.

Upschulte, B.L., B.D. Green, K.W. Holtzclaw, T. Quagraro, S.J. Lipson, and
W.A.M. Blumberg, Vibrational excitation and relaxation of ozone, *EOS* 70, 408,
1989.

Upschulte, B.L., B.D. Green, W.A.M. Blumberg, and S.J. Lipson, Vibrational relaxation and
radiative rates of ozone, *J. Phys. Chem.* 98, 2328, 1994a.

Upschulte, B.L., W.J. Marinelli, and B.D. Green, Reactions of $O_2(a^1\Delta_g)$ with O^- and O_2^- , *J. Phys. Chem.* 98, 837, 1994b.

Watson, C.E., V.A. Dulock, Jr., R.S. Stolarski, and A.E.S. Green, Electron impact cross sections
for atmospheric species. 3. Molecular oxygen, *J. Geophys. Res.* 72, 3961, 1967.

Yang, X., J.M. Price, J.A. Mack, C.G. Morgan, C.A. Rogaski, D. McGuire, E.H. Kim, and A.M.
Wodtke, Stimulated emission pumping studies of energy transfer in highly vibrationally
excited molecules, *J. Phys. Chem.* 97, 3944, 1993.

Table 1. List of Reactions and Rate Coefficients

Reaction	Rate Coefficient	Source
O₃(v) excitation: electron impact		
1 e ⁻ + O ₃ (0) = O ₃ (1) + e ⁻	4.0 x 10 ⁻⁹ cm ³ /s	See text; LABCEDE v-distribution
2 e ⁻ + O ₃ (0) = O ₃ (2) + e ⁻	9.0 x 10 ⁻¹⁰ cm ³ /s	
3 e ⁻ + O ₃ (0) = O ₃ (3) + e ⁻	1.7 x 10 ⁻¹⁰ cm ³ /s	
4 e ⁻ + O ₃ (0) = O ₃ (4) + e ⁻	3.5 x 10 ⁻¹¹ cm ³ /s	
5 e ⁻ + O ₃ (0) = O ₃ (5) + e ⁻	7.5 x 10 ⁻¹² cm ³ /s	
O₃(v) deactivation: superelastic		
6 e ⁻ + O ₃ (1) = O ₃ (0) + e ⁻	5.2 x 10 ⁻⁹ cm ³ /s	Reverse of excitation; T _e = 0.5 eV
7 e ⁻ + O ₃ (2) = O ₃ (0) + e ⁻	1.5 x 10 ⁻⁹ cm ³ /s	
8 e ⁻ + O ₃ (3) = O ₃ (0) + e ⁻	3.5 x 10 ⁻¹⁰ cm ³ /s	
9 e ⁻ + O ₃ (4) = O ₃ (0) + e ⁻	9.4 x 10 ⁻¹¹ cm ³ /s	
O₃(v) dissociation: electron impact		
10 e ⁻ + O ₃ (0) = e ⁻ + O + O ₂	2.8 x 10 ⁻¹⁰ cm ³ /s	Cross section: Keto (1981)
11 e ⁻ + O ₃ (1) = e ⁻ + O + O ₂	4.1 x 10 ⁻¹⁰ cm ³ /s	
12 e ⁻ + O ₃ (2) = e ⁻ + O + O ₂	6.0 x 10 ⁻¹⁰ cm ³ /s	
13 e ⁻ + O ₃ (3) = e ⁻ + O + O ₂	9.0 x 10 ⁻¹⁰ cm ³ /s	
14 e ⁻ + O ₃ (4) = e ⁻ + O + O ₂	1.4 x 10 ⁻⁹ cm ³ /s	
15 e ⁻ + O ₃ (5) = e ⁻ + O + O ₂	2.1 x 10 ⁻⁹ cm ³ /s	
O₃(v) deactivation: radiative cascade		
16 O ₃ (5) = O ₃ (4) + hv	41.4 s ⁻¹	Rawlins et al. (1987)
17 O ₃ (4) = O ₃ (3) + hv	35.8 s ⁻¹	
18 O ₃ (3) = O ₃ (2) + hv	28.9 s ⁻¹	
19 O ₃ (2) = O ₃ (1) + hv	20.7 s ⁻¹	
20 O ₃ (1) = O ₃ (0) + hv	11.2 s ⁻¹	
O₃(v) deactivation: collisions with O		
21 O ₃ (5) + O = O ₂ + O ₂	3.6 x 10 ⁻¹¹ cm ³ /s	Rawlins et al. (1987)
22 O ₃ (4) + O = O ₂ + O ₂	2.7 x 10 ⁻¹¹ cm ³ /s	
23 O ₃ (3) + O = O ₂ + O ₂	2.0 x 10 ⁻¹¹ cm ³ /s	
24 O ₃ (2) + O = O ₂ + O ₂	1.4 x 10 ⁻¹¹ cm ³ /s	
25 O ₃ (1) + O = O ₃ (0) + O	8.0 x 10 ⁻¹² cm ³ /s	
O₃(v) Deactivation: N₂, O₂ collisions		
26 O ₃ (5) + M = O ₃ (4) + M	1.0 x 10 ⁻¹³ cm ³ /s	Upschulte et al. (1994a)
27 O ₃ (4) + M = O ₃ (3) + M	8.0 x 10 ⁻¹⁴ cm ³ /s	
28 O ₃ (3) + M = O ₃ (2) + M	6.0 x 10 ⁻¹⁴ cm ³ /s	
29 O ₃ (2) + M = O ₃ (1) + M	4.0 x 10 ⁻¹⁴ cm ³ /s	
30 O ₃ (1) + M = O ₃ (0) + M	2.0 x 10 ⁻¹⁴ cm ³ /s	

Table 1. List of Reactions and Rate Coefficients (Continued)

Reaction	Rate Coefficient	Source
O₂(v), O₂(A) processes		
31 e ⁻ + O ₂ (0) = O ₂ (v) + e ⁻	3 (ion pair) ⁻¹	Gilmore (1987); v=1
32 e ⁻ + O ₂ (0) = O ₂ (A) + e ⁻	0.002 (ion pair) ⁻¹	Gilmore (1987); likely very high v
33 e ⁻ + O ₂ (v) = O ₂ (A) + e ⁻	5.0 x 10 ⁻¹² cm ³ /s	see text; likely v=6-8
34 O + O ₂ (v) = O + O ₂	6.0 x 10 ⁻¹² cm ³ /s	see text
35 O ₂ (A) + N ₂ = O ₂ + N ₂	2.4 x 10 ⁻¹¹ cm ³ /s	Knutsen et al. (1994)
36 O ₂ (A) + O = O ₂ + O	9.0 x 10 ⁻¹² cm ³ /s	Kenner and Ogryzlo (1980)
37 O ₂ (A) + O ₂ = O ₃ (0)+ O	2.8 x 10 ⁻¹¹ cm ³ /s	Knutsen et al. (1994)
38 O ₂ (A) = O ₂ + hν	6.67 s ⁻¹	Saxon and Slanger (1986)

Figure 1. Electron beam viewing geometry (85 to 115 km).

Figure 2. Volumetric ion pair production rates.

Figure 3. Gas residence times in viewed electron beam volume.

Figure 4. Observed $O_3(v)$ fluorescence spectra. (a) electron beam off; (b) electron beam on.

Figure 5. Example of spectral fitting analysis. Observed spectrum: ascent, 102.5 km, electron beam on. Computed spectrum: $(00v_3 + 10v_3)$, $(01v_3 + 11v_3)$, 18-band model.

Figure 6. $O_3(v)$ column densities, electron beam off.

Figure 7. $O_3(v)$ column densities, electron beam on, $v=1-3$. Filled symbols: ascent; open symbols: descent. Curves are curvefits to beam-off data (Fig. 6).

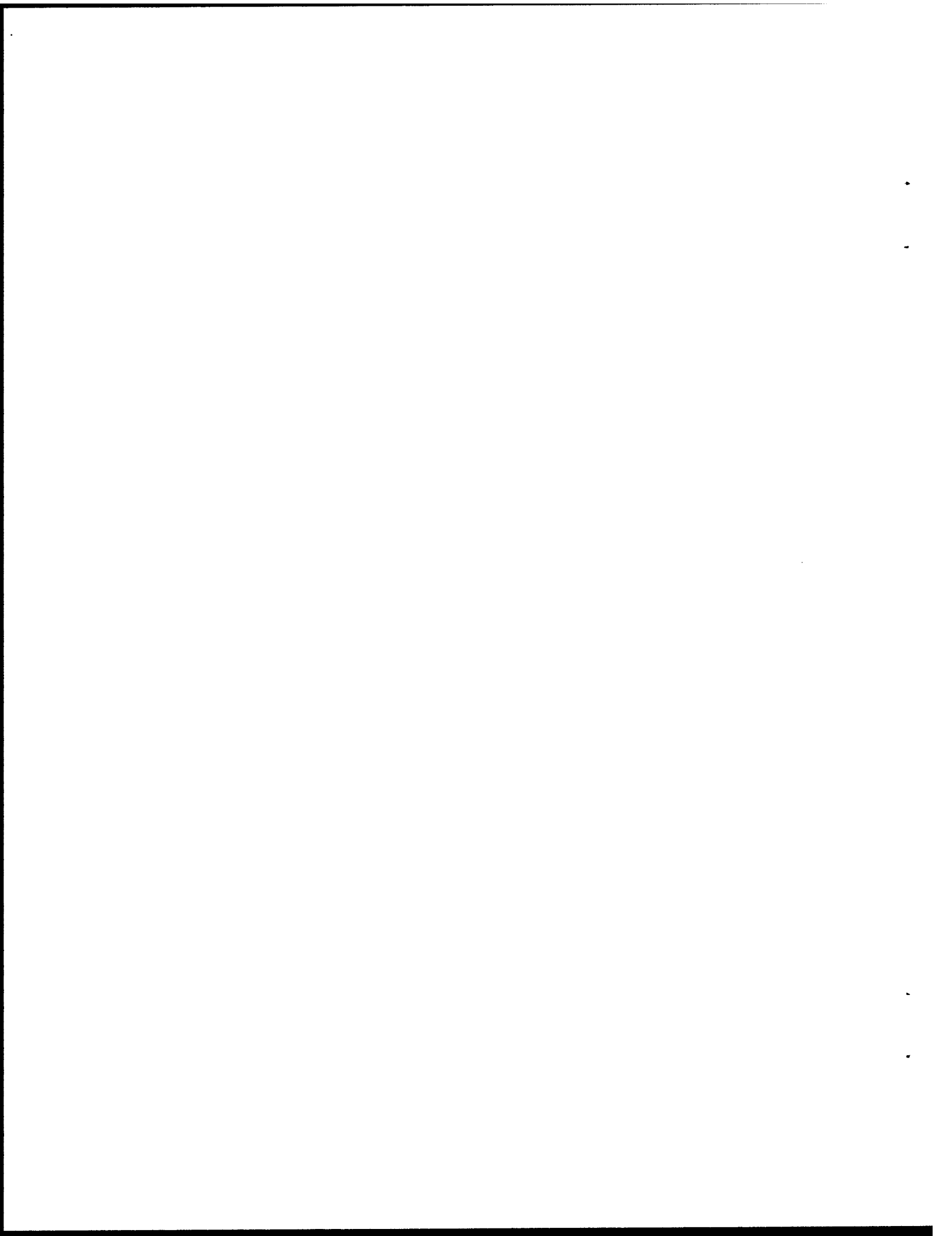
Figure 8. $O_3(v)$ column enhancement by electron beam.

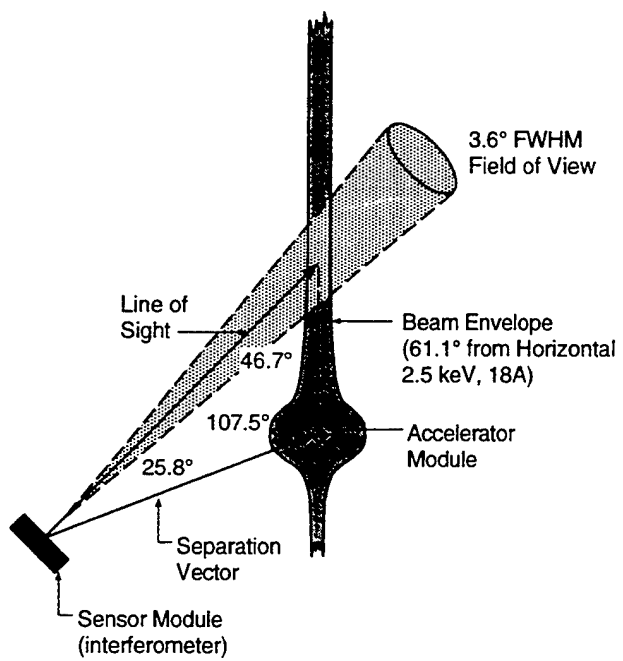
Figure 9. $O_3(v)$ number densities excited by electron beam in viewed beam volume.

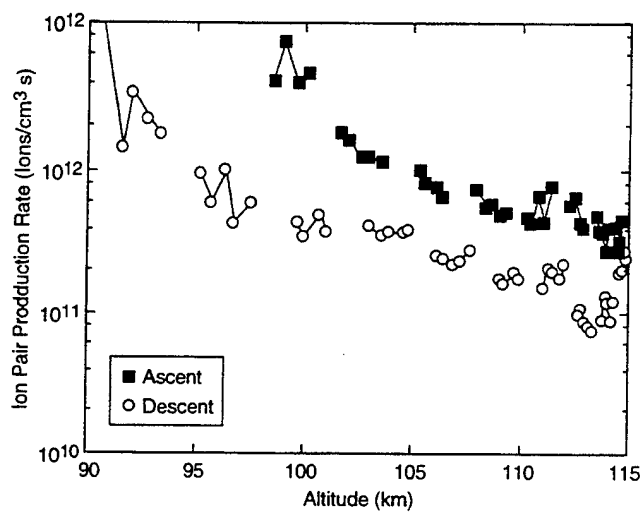
Figure 10. Estimated ambient O_3 and O number densities, compared to MSIS90 predictions.

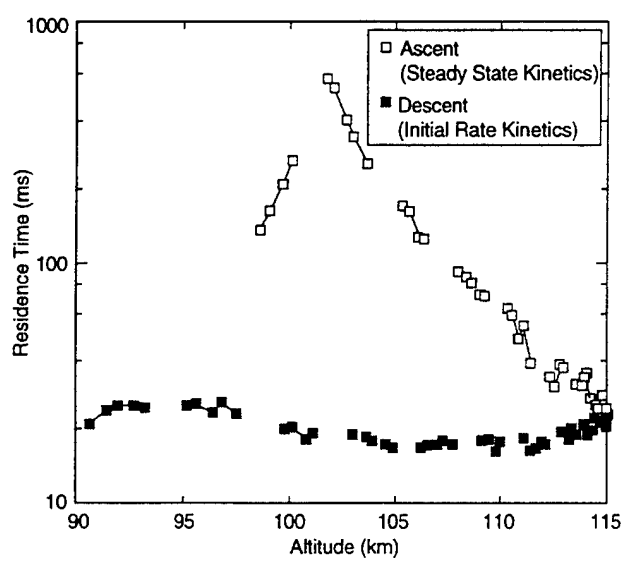
Figure 11. Predictions of kinetic model for time-dependent beam excitation. (a) 103 km ascent; (b) 104 km descent. The solid lines indicate predictions including formation of O_3 by $O_2(A) + O_2$; the dashed lines show the effects of omitting that reaction from the kinetic scheme. The observed, time-integrated $O_3(v \geq 1)$ number densities are also indicated.

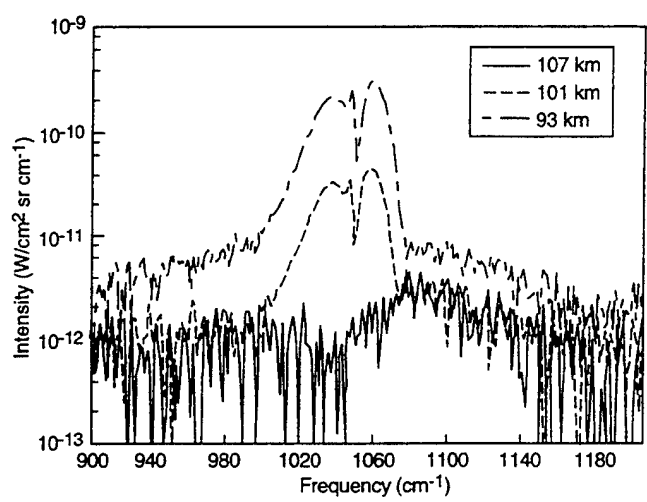
Figure 12. Vibrational distributions of $O_3(v)$ excited in electron beam at maximum dose. The solid and dashed lines indicate the model predictions for electron impact excitation with and without formation of additional O_3 by the $O_2(A) + O_2$ reaction.

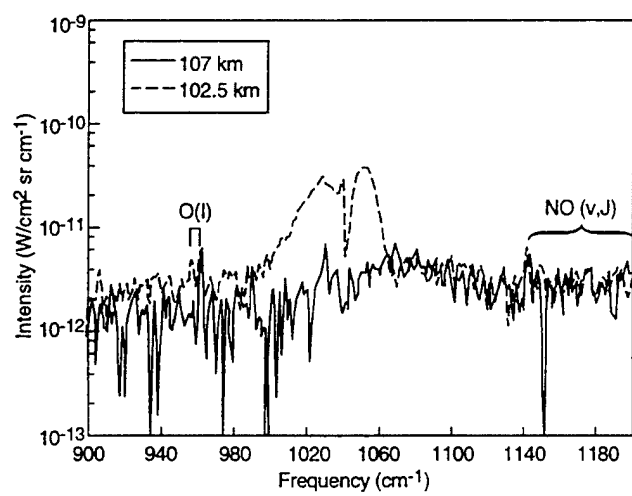


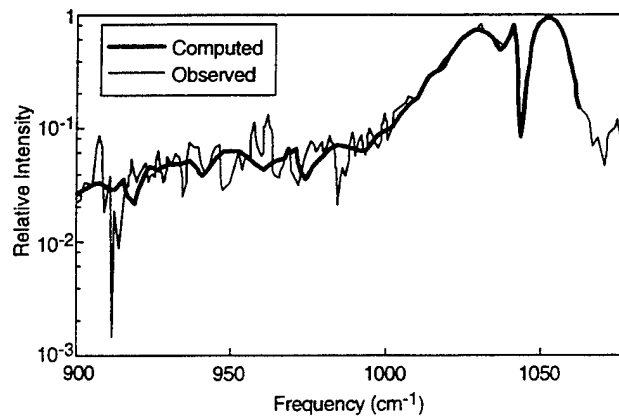


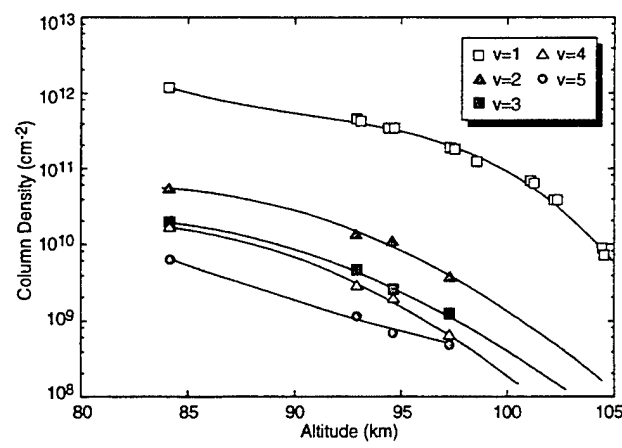


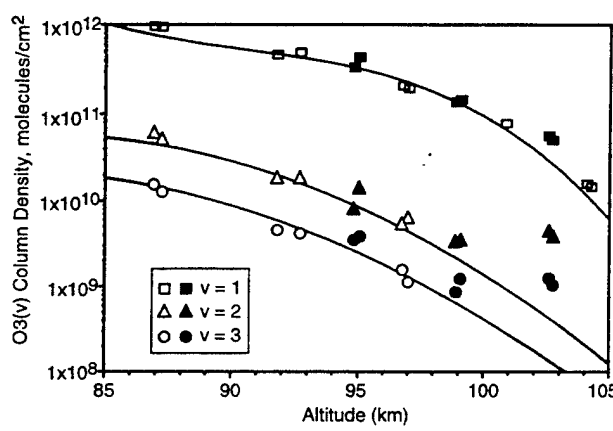


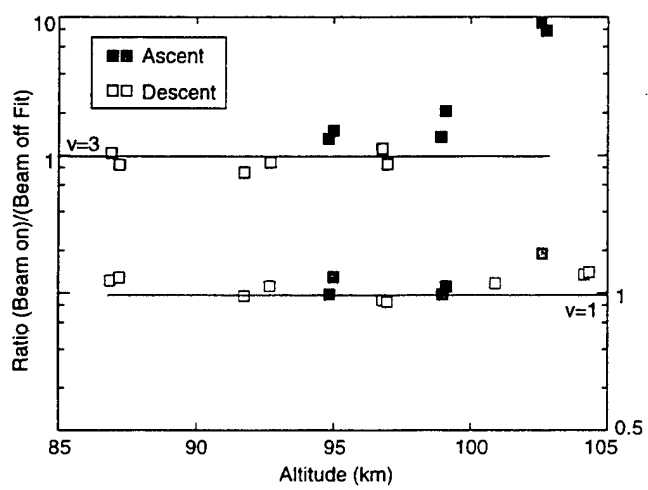


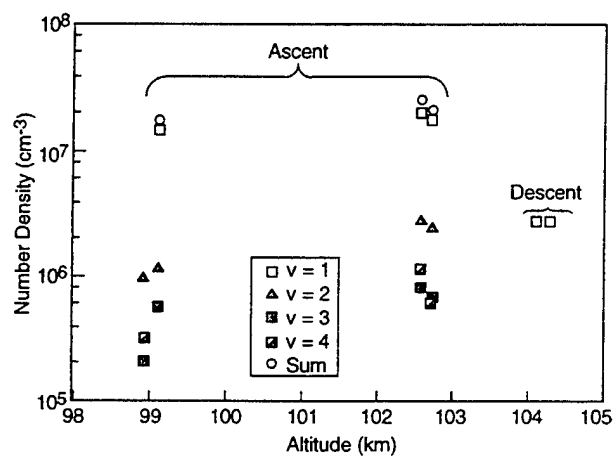


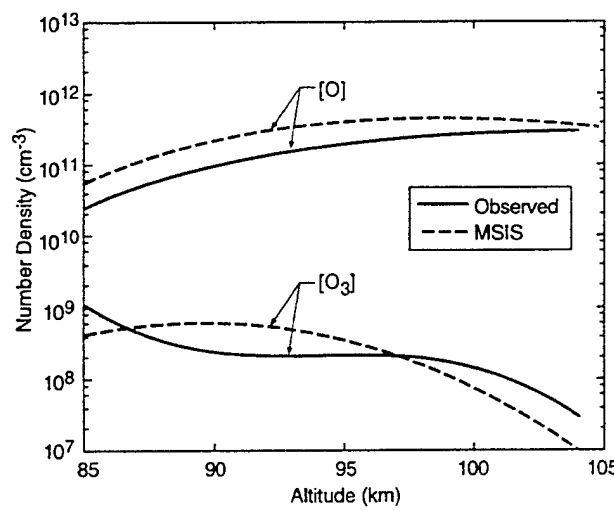


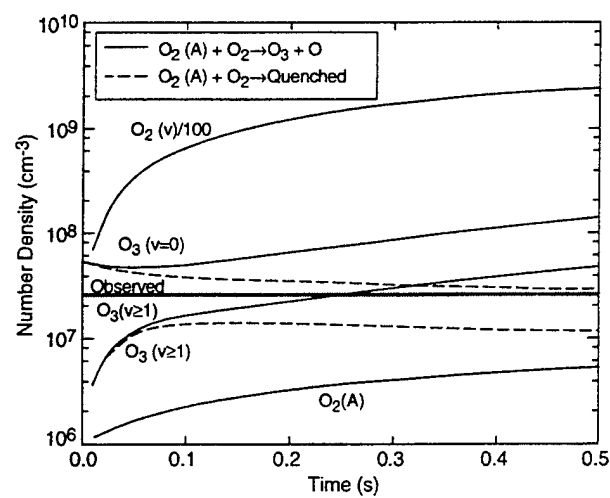


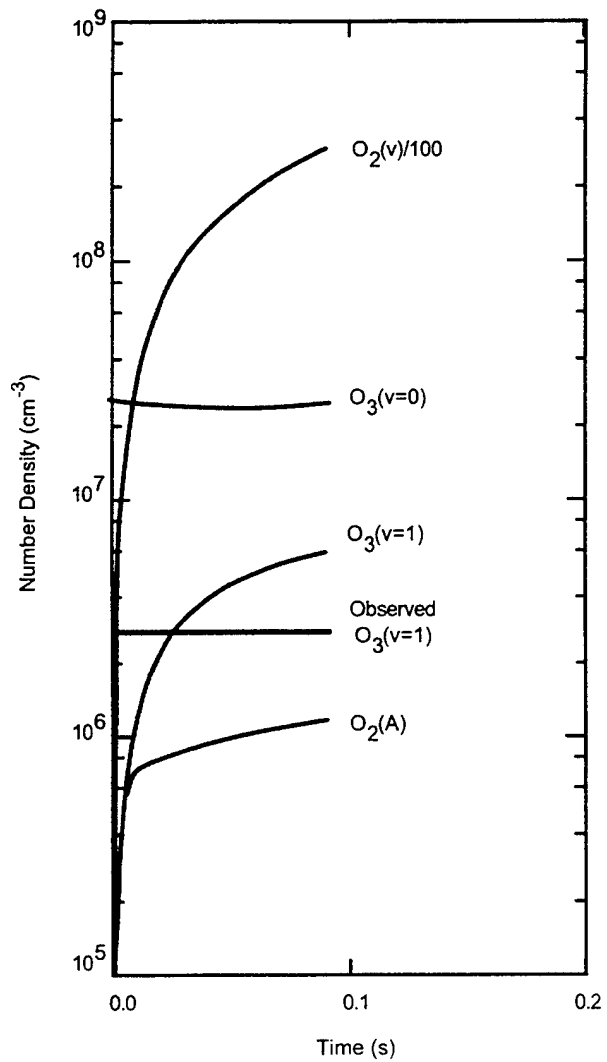


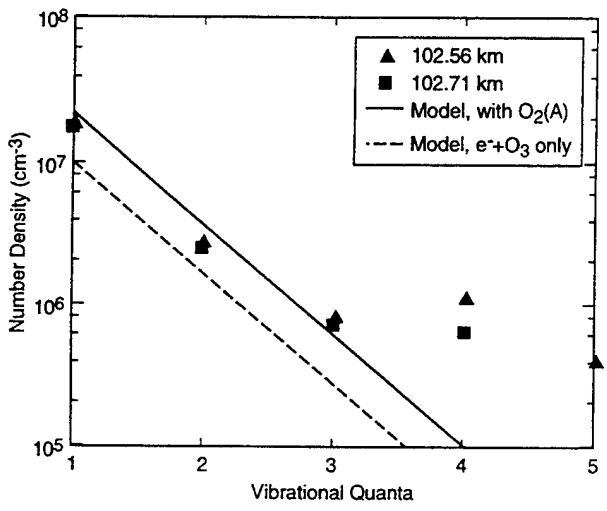












APPENDIX 5

Hypersonic Beam Facility for Rarefied Flow Studies



AIAA 94-2638

**HYPersonic BEAM FACILITY FOR
RAREfied FLOW STUDIES**

G.E. Caledonia, R.H. Krech, B.L. Upschulte,

K.W. Holtzclaw, and D.B. Oakes

Physical Sciences Inc.

20 New England Business Center

Andover, MA 01810-1077

**18th AIAA Aerospace Ground Testing
Conference**

June 20-23, 1994 / Colorado Springs, CO

HYPersonic BEAM FACILITY FOR RAREfied FLOW STUDIES

G.E. Caledonia*, R.H. Krech, B.L. Upschulte, K.W. Holtzclaw, and D.B. Oakes

Physical Sciences Inc.

20 New England Business Center

Andover, MA 01810-1077

Abstract

A high flux, wide area pulsed hypersonic molecular beam facility has been developed for the study and simulation of rarefied flow phenomenology. The beam source operates via the use of laser-induced breakdown in a confined volume of cold gas. The device is small scale, housed in a 40 cm stainless steel vacuum chamber, however the beam area can be as large as 1000 cm². The facility can be used to study gas-surface and gas-gas interactions under free molecular or transition flow regime conditions.

The device was designed initially for the production of an oxygen atom beam, tunable over the velocity range of 5 to 12 km/s. This beam has been successfully used to study material erosion, momentum and energy accommodation on surfaces, contaminant cleanup, surface glows and collisional excitation of gases. The source has recently been extended to produce beams of species such as N₂, CO₂ and H₂O in the velocity range of 2 to 3.6 km/s. This extended capability significantly broadens the range of applications for the facility, for example, it can be applied to exhaust plume impingement evaluations.

The operating principles and characteristics of the facility will be presented. Key facility diagnostics, such as a time of flight mass spectrometer, quartz crystal microbalances, and silver film scatterometers will be described, and representative data applicable to various rarefied flow phenomena will be presented.

Introduction

We developed a pulsed fast oxygen atom beam in the late 1980's¹ to provide a ground test facility to qualify materials to be used in low earth orbit (LEO). This was in response to a number of early space shuttle observations²⁻⁵ of material erosion and property change resulting from interactions with the LEO ambient atmosphere, which is dominantly atomic oxygen. These interactions occur at orbital velocities, ~8 km/s, and for

a while there was a frenzied activity to develop atomic oxygen beams which operate at this velocity. The manifold of such sources has been reviewed previously⁶ and to our knowledge our source is the only system that provides a neutral oxygen atom beam with sustained high flux and wide area operating capability at the desired velocity of 8 km/s. Indeed, in several tests groups of materials having dimensions of 2.5 x 2.5 cm have been simultaneously irradiated to 8 km/s oxygen atom fluences of 10²² cm⁻².

Over the years this fast beam technology has found many applications beyond material testing. For example, the O-atom beam has been used to study and simulate the visible shuttle glow,⁷⁻⁹ demonstrating this glow results from the interaction of ambient oxygen atoms with surface-adsorbed NO. Erosion induced infrared glows have also been measured.¹⁰ The O-atom beam has also been used to study LEO ambient atmosphere scouring of surface contaminants¹¹ and to measure fast oxygen atom surface accommodation coefficients¹² and scattering distributions. Lastly, the O-atom beam has been used in a crossed beam configuration to study gas-gas interactions which lead to ultraviolet, visible, and infrared emissions.¹³⁻¹⁶

The basic fast beam technology has been extended to other atomic systems: rare gases for contaminant cleaning applications; nitrogen atoms for kinetic studies; and chlorine and fluorine atoms for semiconductor etching applications. Most recently the technique has been extended to form wide area beams of molecular species for plume impingement simulation.

Several of these activities have been reviewed recently¹⁷ and others are in the development stage. In this paper we will provide an overview of the fast beam technology, including a review of diagnostic capabilities, then discuss new work on thin silver film oxidation and O-atom scattering distributions. Lastly, we will present preliminary results on the formation of lower velocity molecular beams.

*Associate Fellow, AIAA. Copyright 1994 by George Caledonia. Published by the American Institute of Aeronautics and Astronautics Inc. with permission.

The Fast Atom Source

The hyperthermal oxygen atom source and experimental configuration have been described in detail previously^{1,17} and will be discussed only briefly here. A schematic of the experimental system is shown in Fig. 1. It is comprised of two stainless steel six-way crosses, including an 8 in. cross source chamber housing a pulsed oxygen valve/nozzle assembly, connected to a 16 in. cross expansion chamber. The system is pumped by a cryopump (CVI, TM250) attached to the large cross which maintains a base pressure of 3×10^{-7} Torr.

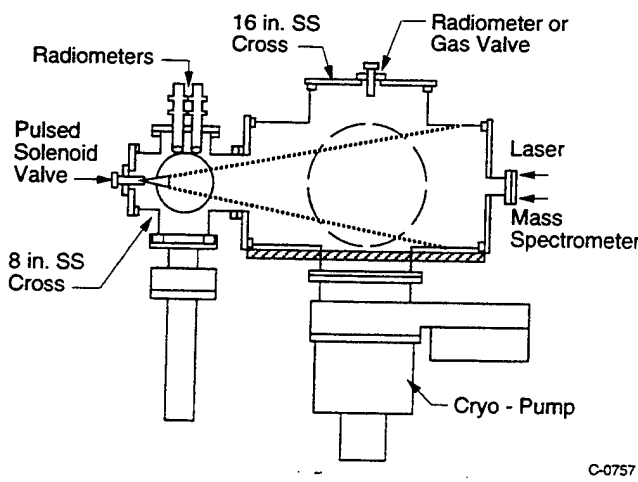


Fig. 1. Schematic of the Fast-2 system.

The oxygen atoms are generated in a pulsed laser discharge of pure O₂ as described by Caledonia et al.¹ A 10 J/pulse CO₂ laser is focused with a 100 cm focal length BaF₂ lens into the throat of a 20-deg full angle, 12.5 cm long conical expansion nozzle which has been partially filled with O₂ by a pulsed beam valve (General Valve). The plasma, ignited at the throat, expands out the nozzle dissociating the molecular oxygen in front of it. The nozzle was designed to allow ion and electron recombination while the slower kinetics of atom/atom recombination maintains a highly dissociated beam. The result, at 8 km/s, is an approximately 50 μ s pulse of highly dissociated oxygen (> 80% atoms) with less than 1% ion content (the beam is charge neutral). The general beam properties are provided in Table 1 while the diagnostics used in evaluating these properties are summarized in Table 2.

The beam velocity (5 to 12 km/s) is selected by varying the time delay between the pulsing of the O₂ valve and the triggering of the CO₂ laser. The delay determines the mass of O₂ processed by the pulsed discharge which is inversely related to the beam velocity. The velocity is determined by measuring the time of

Table 1. Fast O-Beam Properties

Velocity	8 km/s \pm 15% (5 to 12 km/s range)
Fluence	$\sim 10^{18}$ O-atoms/pulse, 3 Hz
Composition	> 80% oxygen atoms
Size	Expandable to > 1000 cm ² area
Charge content	< 1% ions (controllable by pseudo-Helmholtz coils)
Metastable content	O(¹ D) concentration < 0.4%
Temperature	T \approx 300 K

flight of the pulse between two radiometers attached to the source chamber, mounted along the beam axis and separated by 7.6 cm, and filtered to monitor the ⁵S-⁵P oxygen atom line (777 nm) (see Fig. 1).

Table 2. O-Beam Diagnostics

Velocity, temporal pulse shape	Radiometers Mass spectrometer (standard quadrupole and TOF)
Pulse fluence	Mass flow meter Thin silver film actinometer
Beam composition	Mass spectrometer
Excited state concentrations	spectrometer Bandpass filters
Charge content (beam is charge neutral)	Langmuir probe
Beam shape	Erosive witness samples Positionable Langmuir probe 2D visible imaging
Beam translational temperature	Slitted thin silver film target chamber

We have estimated the flux of oxygen atoms generated per pulse by measuring the mass of O₂ processed per pulse. This was determined by using the known time delay between the pulsing of the oxygen valve and the firing of the laser, monitoring the flow of oxygen with a mass flow meter and measuring the temporal profile of the molecular oxygen pulse (laser off) with a pressure transducer aligned along the beam axis. With this measure of the O₂ processed per pulse, the flux at any point down stream can be estimated if the

expansion characteristics of the beam are known. The expansion properties have been determined previously^{13,17} by measuring the fast O-atom erosive mass loss of polyethylene samples mounted 75 cm downstream from the nozzle throat as a function of radial position. The expansion half angle (to 1/e times the on-axis flux) was found to be 14 deg. These calibrations have been cross checked by measuring the absolute oxidation rates of materials and comparing them with equivalent space flight measurements. More recently, as discussed in the next section, the oxidation rate of thin silver films has been used as a calibration standard.

Although the beam is charge neutral, it does have a small but finite ion content. The charge concentration can be decreased by up to a factor of eight using a pair of pseudo-Helmholz coils as shown in Fig. 2. Thus any effects due to charged rather than neutral species can be delineated. The local charge concentration can be measured through use of a retractable Langmuir probe, Fig. 2. The probe is positionable both horizontally and vertically and it has been found that the spatial and temporal shape of the ion distribution matches that of the neutral distribution.¹⁷

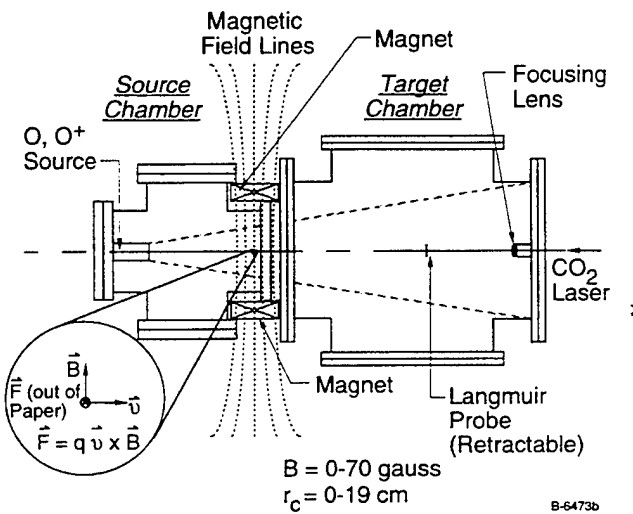


Fig. 2. Schematic of beam ion control system.

We have recently measured the O(¹D) concentration of the beam by monitoring the emission from the forbidden O(¹D \rightarrow ³P) transition using a specially constructed bank of narrow-band interference filters. The O(¹D) concentration was found to be $\leq 0.4\%$ for a beam velocity of 8 km/s and to increase monotonically with beam velocity over the velocity range of 6 to 12 km/s. This concentration is sufficiently low as to render metastable effects negligible in the various studies mentioned above.

We have also evaluated the translational temperature of the beam. This was done by passing the O-beam through a 0.15 cm diameter circular aperture and measuring the oxidation pattern on a thin silver film witness plate placed 5 cm behind the aperture. Any growth in the beam beyond the slit width is due to the Maxwellian motion of the O atoms and can be related to an effective temperature for an 8 km/s velocity beam. This temperature was deduced to be ~ 300 K at a distance of 85 cm from the nozzle throat. The beam temperature will be higher closer to the throat and is calculated to be ~ 1000 K at the nozzle exit plane.

Thin Silver Film O-Atom Diagnostic

There has been a need for some time for a general purpose monitor for the flux of atomic oxygen. Thin silver films were a prime candidate because they have the virtue of being oxidized efficiently by oxygen atoms but not by oxygen molecules. A number of the film properties change upon oxidation. Specifically, the film goes from being electrically conductive to insulative, the film transmission characteristics for visible light go from opaque to transparent and, of course, the film gains mass. Each of these properties may be exploited to evaluate the flux of oxygen atoms impinging the film surface. Early uses of this diagnostic as an in-situ ambient O-atom diagnostic¹⁸⁻²² relied upon a temporal monitor of the resistivity (conductivity) of the films although recently the use of silver-coated quartz crystal monitors (QCM) have been discussed.²³

Thin silver films have also been used in recent years for LEO applications. Gregory and Peters²⁴ have flown scatterometers designed to monitor the angular distribution of ambient oxygen atoms scattered off of targets in LEO. These scatterometers use a thin silver film witness plate with the oxide thickness diagnosed by visible light transmission measurements. Cross and Blais²⁵ have developed silver actinometers to monitor erosion rates and to calibrate their laboratory fast oxygen atom beam (2 to 3 eV). As in the earlier work, these actinometers use the change in resistance in a thin silver film to deduce impinging oxygen atom fluxes.

Prior to our work, there does not appear to have been any systematic study of the phenomenology of the interaction between energetic oxygen atoms and thin silver films. In particular, for high velocity interaction, we could locate no information on the oxidation mechanism, its efficiency and velocity and temperature dependence, and on the effects of surface contamination

and film thickness. We, therefore, undertook such investigations using our fast oxygen atom source. The results of this study are described in detail elsewhere²⁶ and summarized briefly below.

We have employed our fast O-atom beam to study oxidation rates of thin silver films vacuum deposited on crystals (various thicknesses of up to 1 μm) and on kapton sheets (600 Å Ag films). The resistance method was used to monitor the oxidation rate of the latter films but the data scatter was so large that our analysis was confined to the QCM results.

Oxidation of the silver QCM crystal results in a mass gain and a corresponding decrease in the oscillator frequency. The QCM used in this work (from Sycon Instruments) incorporates a 6 MHz quartz crystal with a sensitivity of $1.25 \times 10^{-8} \text{ g/cm}^2/\text{Hz}$. A frequency shift of 1 Hz therefore corresponds to the oxidation of 0.8 Å of silver to AgO . The mass gain during oxidation was monitored by sending the output of the QCM controller (voltage proportional to mass loading) to a Data Translations D/A board for collection and monitoring in real time with a personal computer.

The QCM was mounted directly onto a temperature-controlled aluminum block and thus the quartz crystal, which is in intimate thermal contact with the QCM base, was maintained to $\pm 0.5^\circ\text{C}$. Temperature regulation of the QCM was necessary since the oscillator frequency is temperature dependent. Therefore, a change in temperature could be erroneously interpreted as a mass gain or loss. Near 20°C , the temperature dependence results in a frequency shift of +0.2 Hz/deg for the AT-cut of this QCM crystal (35 deg, 11 min), but at 60°C , the sensitivity is +6 Hz/deg.

Typical oxidation histories for irradiation by 8 km/s oxygen atoms at room temperature are shown in Fig. 3. Shown is oxidation depth versus the number of impinging O-atom pulses as determined by the measured mass increase for two film thicknesses. Two important features can be seen. First, no oxidation occurs during the first two hundred pulses. This is typically observed and we relate it to the required removal of a contamination layer on the silver film. Indeed, if we first irradiate the film with several hundred pulses of a fast argon beam and then shortly thereafter impinge it with fast oxygen atoms, we find that oxidation initiation is immediate. Second, after oxidation initiation, the oxidation depth increases linearly with O-atom fluence for approximately the first 250 Å of the silver film and then

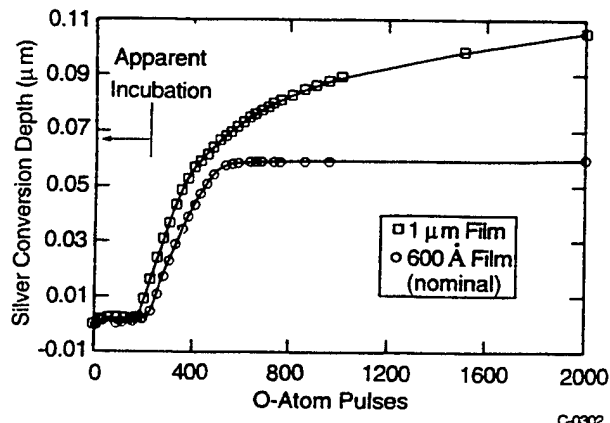


Fig. 3. Oxidation behavior of thin silver films coated on QCM crystals (O-atom velocity = 8 km/s, room temperature).

the oxidation rate slows down. We believe the oxidation rate becomes diffusion controlled at these thicknesses and thus only very thin films are useful as a linear calibration source. Note that the observed oxidation rate continues to decrease very dramatically in the case of the 1 μm thick film.

Note that in the interpretation of the QCM data it is important to understand the oxidation process. During the course of our work we realized that the polycrystalline silver oxidized to the peroxide, AgO , rather than Ag_2O . This was determined by measuring the mass uptake of a totally oxidized film with known silver loading, and verified both by heating the film to 200°C to form Ag_2O and by X-ray diffraction analysis of the film.

We also examined the temperature dependence of the silver oxidation rate over the range of 0° to 85°C . These results are shown in Fig. 4, contrasted with simultaneous measurements performed on a polycrystalline carbon film also coated on a QCM crystal (for convenience, all results are normalized to a silver reactivity of unity at 273 K). Although there is some scatter in the data, the silver oxidation rate is independent of temperature, unlike that for carbon. Thus, we believe that these silver films will provide a good standard for relative investigation of high velocity oxidation behavior of materials. Indeed, we have found that the silver film oxidation efficiency is also independent of O-atom velocity over the velocity range of 8 to 12 km/s.

We now have developed a clear understanding of the behavior of thin silver films subjected to high velocity oxygen atom irradiation and believe that they will prove a valuable diagnostic tool within their demonstrated

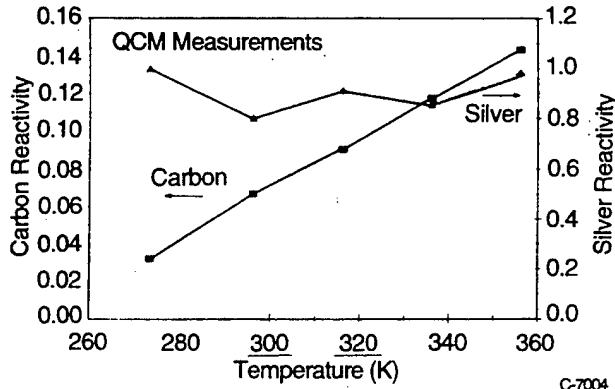


Fig. 4. Measured silver and carbon reactivity vs temperature (O-Atom velocity 8 km/s).

surfaces. In this device the beam passes through a small slit into a chamber containing the target material. The O-atoms scattered from the target ultimately interact with a silver film "witness plate" positioned at the front of the chamber (around the slit). The distance between target and slit must be large enough to allow sufficient spread of the scattered beam to provide good measurement resolution on the witness plate for the scattered angular distribution. This measurement is complicated however, in that the beam does grow in extent between the slit and the target because of its random or Maxwellian velocity component. The ratio between the thermal and directed velocities defines a beam spread angle which must be known in order to interpret the witness plate data. All this information is available for our device as described previously.

limitations. One such diagnostic application, the measurement of the scattering distribution for high velocity oxygen atoms impinging on selected surfaces, is described in the next section.

O-Atom/Surface Scattering Experiments

Knowledge of the scattering behavior of ambient oxygen atoms striking spacecraft surfaces in LEO is important for two reasons: 1) the degree of elasticity of the collisions affects spacecraft lift and drag; and 2) the scattered atoms can cause deleterious effects to materials not impinged by the ram flow.

Silver film scatterometers designed to measure the atomic oxygen scattering distribution off various materials have been flown on-orbit in shuttle experiments by John Gregory²⁴ and other investigators. These on-orbit measurements show that the atomic oxygen scattering is non-specular. Our laboratory measurements represent the first attempt to confirm these observations in the laboratory in an 8 km/s atomic oxygen flow. The representative materials chosen for this study are clear and black anodized aluminums provided by NASA/Johnson Space Center, and microscope slide glass. These materials are relevant as most spacecraft are constructed from aluminum to minimize mass, and the largest exposed area on a spacecraft are the glass covered solar arrays. We observed that scattering off all three materials is non-specular. The details of the scatterometer design, silver film cleaning procedures, and atomic oxygen scattering measurements are described briefly below.

We used a modified version of Gregory's scatterometer in our laboratory experiments to measure the oxygen atom angular scattering distributions from

We have designed and built silver film scatterometers specific to our experiment. Two scatterometers were constructed from 6061-T6 aluminum to hold up to three samples in individual compartments at either a 90 or 45 deg angle of incidence to the 8 km/s atomic oxygen flow. The 90 deg scatterometer is shown in Fig. 5. The silver film to be oxidized by the scattered atomic oxygen was attached to the 2.222 cm radius surface by adhesive which securely held the film flat, and yet permitted easy removal. A 0.25 cm wide by 1.25 cm long slit was cut in the film prior to mounting to restrict the atomic oxygen flow into the scatterometer. The glass and aluminum samples were cut to fit the individual sample chambers and attached to the silver coated kapton covered rear surface with double faced tape. A key feature of our scatterometers not found in other designs is the addition of a hinged cover to permit cleanup via argon atom bombardment of both the sample and silver film surfaces to remove the surface contamination layers in the chamber immediately prior to the oxygen scattering measurement. We have

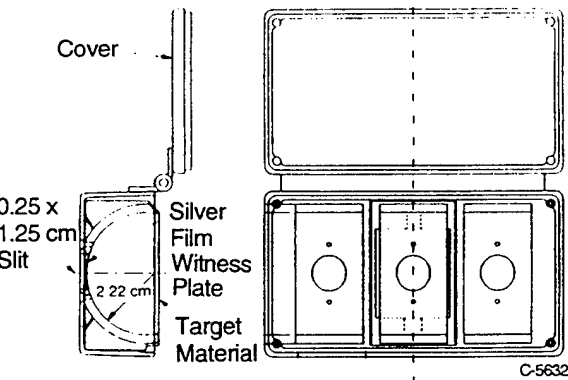


Fig. 5. Normal incidence spectrometer used to measure distribution of fast oxygen atoms scattered off of selected materials.

found that this was a key feature for successful accomplishment of the experiments.

Our witness samples, 500Å silver film on 2 mil mylar, were prepared by Sheldahl. In this application, the films were analyzed for oxidation by measuring optical transmission with a computer page scanner equipped with a transmission attachment. As mentioned earlier, silver oxide is transparent although silver is opaque. The fast O-atom beam was used to calibrate the film transparency, e.g., optical thickness versus atomic oxygen fluence, and the scattering measurement experiment duration was limited to ensure that $\leq 250\text{\AA}$ depth of the film was oxidized, i.e., to the range of linear oxidation behavior.

The resulting measured scattered oxygen atom distributions versus angle from the slit are shown in Figs. 6 and 7 for normal and 45 deg incidence respectively. The results are averaged over the width of the witness film and are presented as a percentage of the incident flux per degree. The angular resolution of the data is about 2.5 deg. The absolute calibration for this data is uncertain to about a factor of two but this uncertainty can be greatly reduced in future work by simultaneously monitoring the O-atom flux during the scattering measurement.

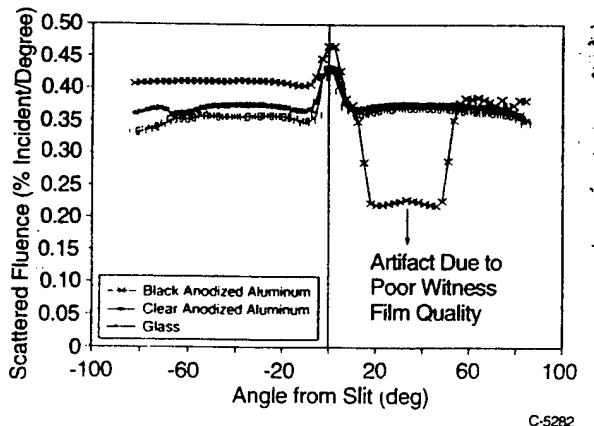


Fig. 6. Oxygen scattering distribution at 0 deg angle of incidence for three materials. O-atom velocity is 8 km/s. Low measurements at positive angles on black anodized aluminum are due to improper witness film cleaning.

The scattering distribution is quite flat, suggesting isotropic scattering for all three materials. No strong specular regions are apparent. The central spike that is seen in the figures should be ignored. It is due to the presence of a slit in the silver film and the fluence indicated is an artifact of the analysis technique.

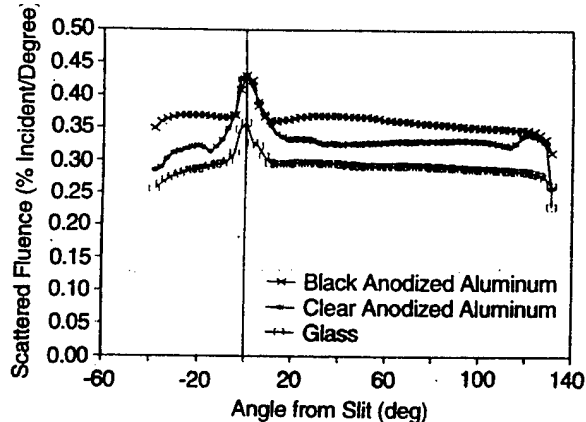


Fig. 7. Oxygen scattering distribution at 45 deg angle of incidence for three materials. V = 8 km/s. C-5280

The importance of working with clean films was accidentally demonstrated in the data for black anodized aluminum shown in Fig. 6. It turns out that the door of the scatterometer opened too far during the exposure of the black anodized sample and one side of the silver was not scoured by the atom beam. Thus, the anomalously low apparent scattered fluence.

There is one interesting observation on the data presented in Figs. 6 and 7 which can only be treated as a conjecture at present. That is that the apparent fractional scattering of oxygen atoms is largest for black anodized aluminum, smaller for clear anodized aluminum and smallest for glass. The difference is small in the case of normal incidence but the scattered fluences differ by 20% in the 45 deg incidence measurements. These measurements were taken to evaluate the scattering distribution, not the magnitude of the scattered fluence, and thus the incident fluence was not highly controlled ($\sim 10\%$). Nevertheless, considering the order the data was taken in, it would be highly coincidental that the apparent scattering efficiency of the three materials would be artificially preserved at two different impingement angles. If this is a true variation, it could imply a higher efficiency of O-atom recombination on glass than on aluminum.

We note that an isotropic scattering distribution need not imply high surface accommodation. The roughness of the surfaces tested could provide for specular scattering over a wide range of effective angles of incidence. The nature of the scattering is best deduced by measuring the velocity of the scattered atoms using a time-of-flight mass spectrometer (TOFMS).

Our approach was to mount a Comstock system EII mass spectrometer onto a rotating ISO 400 flange on the

top of our FAST-2 test chamber. The experiment was configured to provide sufficient ion signal based upon expected scattering densities compared to the operating background pressure of 3×10^{-7} Torr.

Experiments were performed to observe scattered atomic oxygen after impact with a sample of clear-anodized aluminum as provided by NASA Johnson. The experimental setup is shown in Fig. 8. The TOFMS was mounted on the top-most flange of a 40.6 cm diameter six-way cross which comprises the target chamber in the FAST-2 atomic oxygen test facility. The TOFMS ionization region, flight tube, and detection region were differentially pumped with a turbo-molecular pump to pressures of $\approx 3 \times 10^{-7}$ Torr (ultimately determined by the background pressure in the FAST-2 facility). The TOFMS was mounted 13.3 cm off centerline on a flange modified to allow 360-deg rotation around the vertical centerline of the six-way cross. Two apertures in the shroud surrounding the ionization region of the TOFMS were aligned to define an axis through the center of the chamber. The use of two apertures, one on either side of the ionization region, allows passage of incoming species through the mass spectrometer. This reduces the likelihood of a density gradient occurring in the region around the ionizer as would almost certainly occur in the absence of a second aperture.

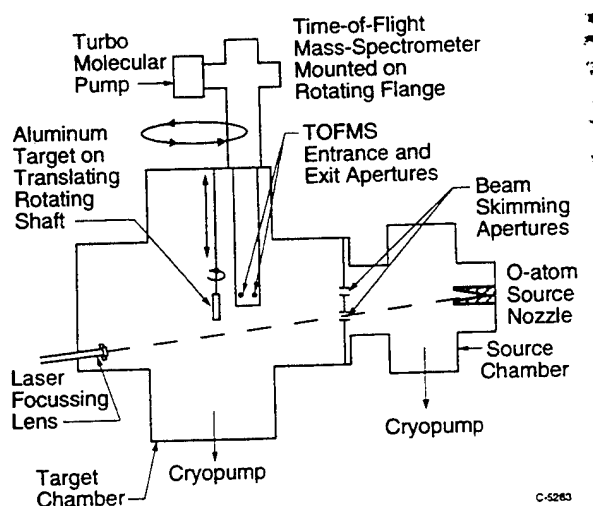


Fig. 8. Experimental arrangement for measurement of O-atom scattering with a time-of-flight mass spectrometer.

The target was mounted 75 cm from the O-atom source in the center of the chamber on a shaft which could be translated along the vertical axis and rotated with respect to the O-atom beam. Consequently, the target could be removed from the O-atom beam for

measurement of background mass spectra. The angle of impact for the atomic oxygen could be varied from 0 to 90 deg by rotation of the target. Since the TOFMS was always aligned with a path through the center of the chamber, the center of the target was always observed by the TOFMS regardless of target rotation or placement of the TOFMS with respect to the O-atom beam centerline. The target was oversized at 5 x 7.5 cm to provide ease in aligning the spectrometer. The center of the TOFMS ionizer was positioned 12.5 cm from the target.

To minimize contamination from test chamber-scattered oxygen atoms, an aluminum plate with two apertures 3.2 cm in diameter was placed 42 cm downstream from the throat of the O-atom source. These apertures served to limit oxygen flow into the target chamber and thus limit background signal. One aperture was placed directly on centerline to allow oxygen to impact the target, the second was placed to allow laser access to the nozzle throat. The O-atom source chamber was equipped with a second cryopump to allow for efficient removal of the bulk of the oxygen between laser shots.

Since the ionization efficiency in any mass spectrometer is small, the minor ion content of the O-atom beam can completely obscure any signal generated by ionization of atomic oxygen neutrals. Ions were prevented from entering the mass spectrometer by placing a 90% transmitting tungsten mesh screen (~ 0.3 mm mesh pitch) in front of each aperture. A bias of +20V was found to be sufficient to eliminate the ion signal from the beam.

Two sets of experiments have been performed. In the first, the target was oriented perpendicular to the O-atom source and the TOFMS was positioned 40 deg off-axis from the beam. The second experiment was performed with the target tilted 45 deg and the TOFMS oriented 90 deg with respect to the O-atom beam. Consequently, to the extent that surface roughness does not blur the angular scattering of the O-atoms, the second experiment was arranged to maximize the probability of detecting "specularly" scattered atoms.

The results from the first experiment described above are shown in Fig. 9 where both the mass 16 and mass 32 (O and O₂) signals are displayed. For mass 16, the indicated maximum number density occurs at a delay of ≈ 300 μ s after the laser fires or approximately 210 μ s after the oxygen impacts the target. This

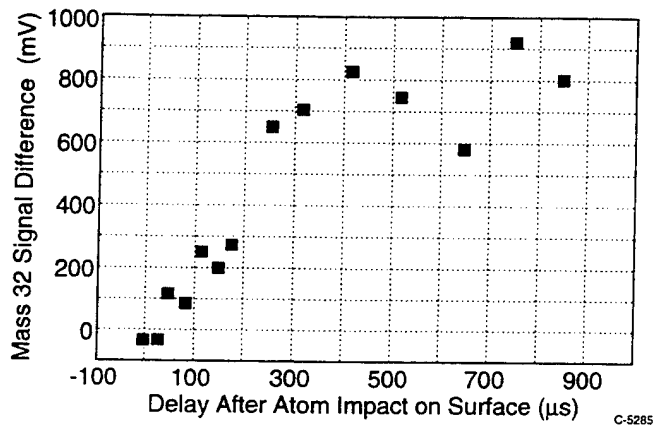
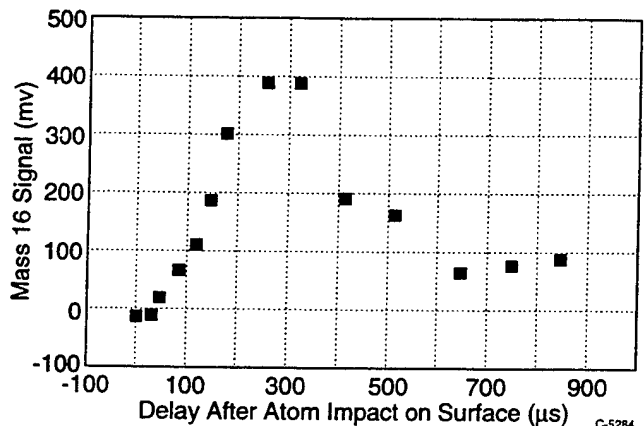


Fig. 9. Temporally resolved signals from atomic oxygen and molecular oxygen. The target was positioned normal to the O-atom pulse and the TOFMS was placed 40 deg off-normal with respect to the target. The O-atom nominal velocity was 8 km/s corresponding to a time-of-arrival of 95 μ s after the laser shot.

corresponds to a most probable O-atom velocity of 7×10^4 cm/s or a kinetic energy of ≈ 0.04 eV. It should be noted that the mass 16 signal was quite prominent at its maximum being ≈ 5 times larger than the signal present with the target retracted. The corresponding mass 32 data show a most probable time-of-arrival of ≥ 300 μ s although this is less well defined.

These data are consistent with the hypothesis that the incoming O-atom kinetic energy is largely accommodated by the aluminum surface and that the atoms leave the surface at near thermal velocities. The large mass 32 signal, which indicates a similar maximum number density of O_2 when the larger O_2 ionization cross-section is accounted for (a factor of ~ 1.6), further suggests a significant probability for surface-assisted O-atom recombination on the aluminum since the O_2 content in the incident beam is $\leq 20\%$.

Similar results are observed for signals generated with the target tilted 45 deg and the mass spectrometer collection axis normal with respect to the O-atom beam. In neither experiment was a prominent signal for mass 16 observed at the short times consistent with elastic scattering from the aluminum. These experiments do suggest that a small fraction of the atoms scattered from the surface leave with velocities consistent with near-elastic scattering. For example, a signal for mass 16, significantly above that observed with the target recessed, was observed only 45 μ s after the nominal time of O-atom impact. This corresponds to a leading velocity of 3×10^5 cm/s.

In summary, these experiments suggest that: 1) the great majority of atomic oxygen impacting the aluminum was accommodated by this surface; 2) there is a substantial range in the extent to which the O-atom kinetic energy is accommodated (based on the wide range of indicated leaving velocities); and 3) there is substantial O-atom recombination occurring on the aluminum surface as indicated by the prominent mass 32 signals.

While these data suggest the preceding conclusions, they are by no means definitive and they must be viewed as preliminary. There are several uncertainties in the experiment which could greatly influence their interpretation. First, the extent to which species leaving the surface are detained in the mass spectrometer (i.e., the extent to which they "rattle around" before being ionized) is not presently known. The layout of the experiment allows this possibility since the target was large enough ($\approx 5 \times 8$ cm) to produce scattered species with an angle of incidence sufficiently oblique onto the TOFMS to preclude clean passage on one pass through the instrument. This "piling up" in the TOFMS would have the effect of lengthening the duration of the O-atom pulse. A second effect would be an apparent increase in the O_2 content since collisions with the interior TOFMS surfaces would promote O-atom recombination into O_2 . These uncertainties will be evaluated in future work.

In any event, the scatterometer and TOFMS measurements are consistent with each other both in terms of the clear inelasticity/isotropicity of the scattering and also in terms of the evidence for significant surface induced atomic recombination in these high velocity gas surface interactions. It is clear that the combination of these two diagnostics provides a powerful tool for the investigation of such scattering phenomena.

Lower Velocity Molecular Beams

The last topic in this paper is a preliminary study of the extension of our laser breakdown technique to form beams of molecular species at lower velocities, e.g., 2 to 4 km/s. This effort was originally driven by the desire to simulate exhaust plume impingement effects. The effect of exhaust plume impingement on spacecraft surfaces has been an issue for many years. The need to evaluate these effects at relatively large plume expansion distances and low pressures has required the use of costly test facilities with high pumping capacity. In this work, we have investigated the potential of using the laser breakdown technique to develop a small-scale facility which provides beams of exhaust species that can be directed onto surfaces. This beam can be operated over a range of density/velocity to study plume impingement effects.

Our effort was directed towards the design, construction, implementation, and testing of a system that would generate a pulsed beam/jet that simulates the 3.5 km/s exhaust of a hypergolic bipropellant thruster. Our ultimate goal would be to obtain a velocity controlled beam with the mole fractions of species listed in Table 3.⁵ Single species simulation is critical for plume impingement model evaluation and development and this was investigated first.

Table 3. Example Shuttle Thruster Exhaust Species

Species	Mole Fraction
H ₂ O	0.33
N ₂	0.31
H ₂	0.17
CO	0.13
CO ₂	0.036
H	0.015
O ₂	0.0004

A design modification of our usual breakdown nozzle was required for a multi-component, slow velocity beam. The existing nozzle allows injection of only one gas stream. This severely restricts synthesis of the proper gas mixture by requiring sources of premixed gases for the injector. We therefore modified the usual nozzle to accept a second pulsed valve and gas injector as shown in Fig. 10. This allowed us to controllably mix gases in the

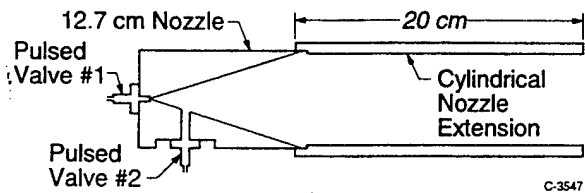


Fig. 10. Schematic of modified nozzle.

nozzle. The relative fraction of the two gas streams could be controlled on a pulse-to-pulse basis for testing of exhaust beam relative mole fractions. This design is not optimum for good gas mixing as discussed later. A more appropriate design would have both valves inletting into the nozzle throat area.

Our usual nozzle length, and laser power in conjunction with the maximum operating pressure of the pulsed valve restricts the minimum operating velocity of the breakdown source to about 5 km/s. In order to slow the exhaust beam even further it is necessary to add more gas or reduce the laser power. Reducing the laser power translates into a reduced flux and density of the exhaust beam. We chose to keep the laser power high to generate the maximum exhaust density for plume impingement studies, and thus lengthened the existing nozzle so as to add more gas to the breakdown. A cylindrical nozzle extension, 20 cm long was added to the 12.7 cm long 10 deg half angle nozzle to confine the longer gas pulses. The modified nozzle is shown schematically in Fig. 10.

The standard velocity diagnostic for the fast O beam source is a pair of radiometers viewing the exhaust at known distances downstream of the nozzle exit plane. Visible emission arising from the ion-electron recombination of residual charge is observed as the exhaust beam passes the radiometer's narrow field of view. A simple timing analysis of the emission arising in the radiometers in combination with a known separation between the radiometers allows the beam velocity to be measured. This technique lacks the sensitivity required to detect the beam passage in the current configuration. First, slower beams produce less ionization in the beam exhaust, which translates into weaker visible emissions, and second, the nozzle extension quenches some of the ions and electrons, which further reduces the intensity of the visible emissions.

For the velocities of interest in this work, we found that piezo-electric dynamic pressure transducers are the preferred diagnostic. The velocity evaluated in this

manner was cross-checked through measurements of the time of arrival of the pulse at the mass spectrometer positioned at the end of the test chamber.

We concentrated on generating 3 to 4 km s⁻¹ exhaust plumes containing the relevant species in approximately the ratio predicted by equilibrium calculations of the combustion products in a hypergolic bi-propellant thruster. Beams containing individual constituents were also generated. A quadrupole mass spectrometer (Balzers) was used to evaluate the species components of the beam. Experiments were performed with single and double gas injection into the breakdown nozzle, and with liquid water injection at the nozzle throat. Pure gas experiments using N₂ and CO₂ exhibited more than 88 % molecular species in the plume at velocities around 3.0 to 3.6 km s⁻¹. A typical mass spectrometric scan for the CO₂ beam is shown in Fig. 11. The beam width is seen to be several hundred μ s. This result is typical for the pure gas experiments. Injection of liquid water at the nozzle throat also proved to be an excellent means of generating a fast beam of molecular H₂O at 3 km s⁻¹,

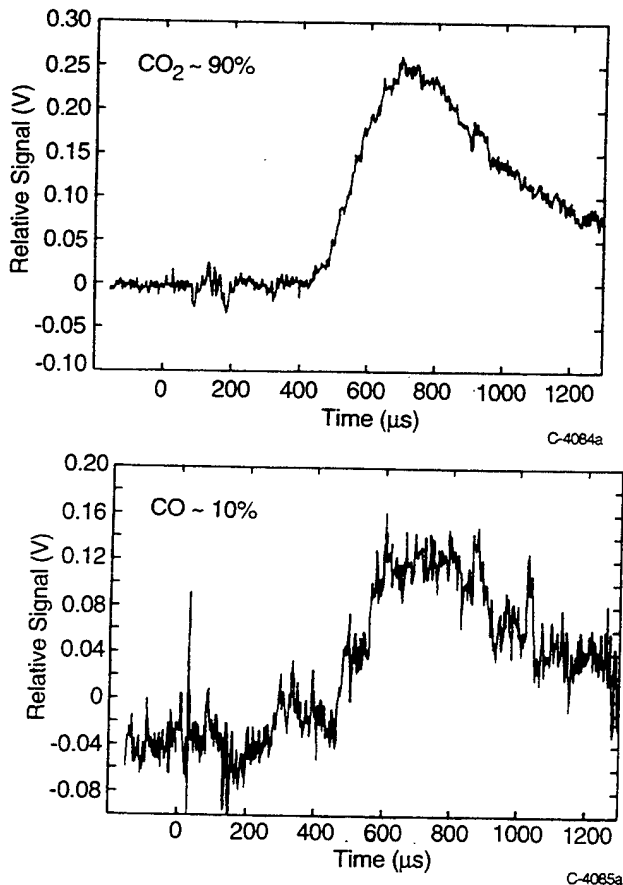


Fig. 11. Mass spectrometer signal for CO₂ and CO observed for a 3.6 km/s beam formed by laser breakdown in pure CO₂. The CO signal has been corrected for the CO₂ cracking fraction.

i.e., with greater than 75 % H₂O in the beam. Several experiments using gas mixtures and mixtures of liquid water with gases were also performed in an attempt to generate the exact mole fractions of exhaust species. The run matrix is summarized in Table 4. The results indicate that the generation of an exact simulation of all the species at the correct velocity may be possible. However, the matrix of gases, liquids, and setup parameters are so broad that the experiments to perfect such a simulation were beyond the scope of this preliminary effort. Interestingly, we found out that the mixture species remained largely undissociated in the fast beam. This observation is likely due to the large fraction of the gas pulse that is not processed by the laser breakdown, but by the blast wave. This observation further reinforces the belief that the whole exhaust plume can ultimately be simulated. The beam velocity in these multi-injection experiments was easily tuned but we observed some temporal separation of species in the exhaust pulse. We attribute this to poor mixing in the nozzle and believe that an improved design can eliminate this problem.

Simulations of exhaust plumes using fast molecular beams of a single or pure gas are more valuable to our understanding of plume impingement effects than a simulation of the exact exhaust composition. The exact beam composition will determine the final surface heating and momentum accommodation information for the experimental conditions, but such a measurement is too complex to provide insights to the mechanisms or key components involved. On the other hand, the single component beams provide the laboratory tool to evaluate plume impingement heating, momentum transfer, and even surface chemical effects under controlled conditions with straightforward interpretation. Most importantly, the individual species beams can be used to evaluate the angular dependent momentum accommodation coefficients.

In this preliminary work, we have demonstrated the ability to create 2 to 4 km/s velocity pulsed beams of a variety of molecule species. These beams have not yet been fully calibrated in terms of both flux and spatial dimensions, however, we have performed a "plume impingement heating" experiment to demonstrate their utility. Specifically, we have experimentally measured the heating due to the impingement of 3.6 km/s carbon dioxide and nitrogen plumes on a thin thermally isolated nickel foil using a previously developed technique¹² that is illustrated in Fig. 12. The plume gases carry kinetic energy (and possibly chemical and/or thermal enthalpy

Table 4. Gas Mixture Experiments

Gas - 1%	Gas - 2%	Gas - 3%	Gas - 4%
Nozzle Throat Valve		Side Valve	
N ₂ -50	O ₂ -50		
O ₂ -100		H ₂ -52	N ₂ -38
N ₂ -50	O ₂ -50	Monomethylamine-100	
H ₂ O (Liq)-100		H ₂ -50	N ₂ -50
H ₂ O (Liq)-100		H ₂ -80	N ₂ -20

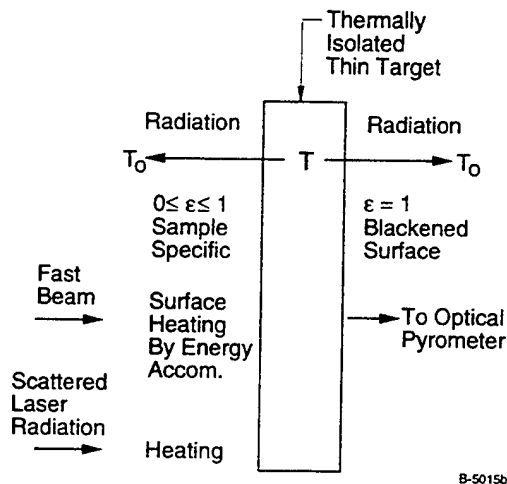


Fig. 12. Schematic of the plume impingement heating experiment.

but these are negligible in comparison to the kinetic energy under the test conditions). Upon striking a surface these gases will deposit some fraction of this energy into the surface as sensible heat. This fractional deposition is defined as the energy accommodation coefficient. For normal incidence, without chemical heating, this quantity can be directly related to the momentum accommodation coefficient. The purpose of this study was to demonstrate that the pulsed beams were sufficiently intense to allow employment of this diagnostic.

A thermally isolated foil in vacuum can only lose heat by radiation. It must ultimately reach a steady state temperature that reflects a balance between plume energy accommodation and radiative cooling. Our experimental procedure involves the repetitive exposure of the front surface of a nickel foil to the simulated plume, and recording the black painted back surface foil temperature rise due to the plume impingement heating. The temperature was measured with an Omega Model OS-602

optical pyrometer. The details of our approach and the relationship between temperature increase and accommodation coefficient are provided in Ref. 12.

We performed heating studies on a nickel foil with both N₂ and CO₂ beams. A 0.6° to 0.7°C temperature rise was observed in the foil temperature when it was exposed to a 3 Hz 3.6 km/s beam of either CO₂ or N₂ as shown in Fig. 13. Scattered 10.6 micron CO₂ laser radiation from the nozzle will also contribute to the foil heating, however this effect is small and was measured to be 0.2 C by placing a very thin polyethylene film in front of the foil which allows the scattered laser radiation to heat the foil but prevents beam impingement. The signal to noise of the data is clearly large enough to provide useful data on plume impingement heating once the beams are calibrated.

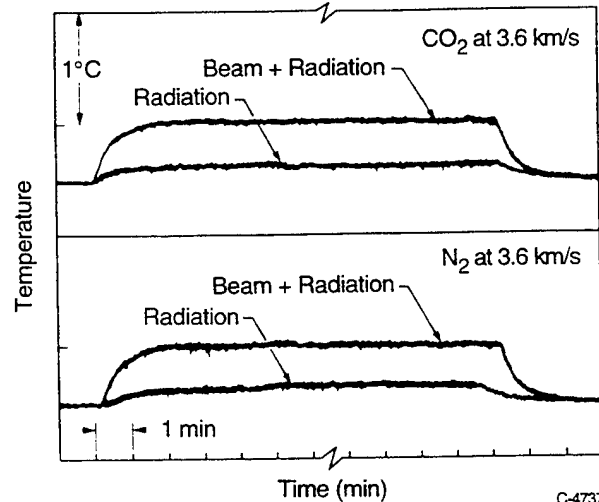


Fig. 13. Typical temperature variation on nickel foil observed during beam impingement experiment.

These individual constituent beams should provide a powerful tool in evaluating plume impingement heating and momentum transfer parameters for various

materials. We have demonstrated that the beams are sufficiently intense to produce measurable temperature changes on isolated targets. This has been done without an optimized system. We fully anticipate that similar measurements of momentum transfer can be achieved in our system.

Conclusions

The fast O-atom beam source has proven to be a very versatile facility for the study and simulation of a wide variety of phenomena of relevance to the interaction of the ambient atmosphere with spacecraft (and their local environment) operating in low earth orbit. The development and phenomenological understanding of thin film silver probes and the implementation of a time-of-flight mass spectrometer within the test facility have significantly enhanced the diagnostic capabilities and measurement domain of the system.

The recent extension of the laser breakdown technique to form lower velocity, 2 to 4 km/s, beams of selected molecular species and mixtures will provide the ability to examine other rarefied flow phenomena, such as exhaust plume impingement effects, in a small-scale laboratory facility.

Acknowledgements

Professor John Gregory of the University of Alabama at Huntsville provided key support in the thin silver film and scatterometer studies. Mr. Charles Goldey provided valuable assistance in the laboratory. The thin silver film phenomenological study was largely supported by the Defense Nuclear Agency under DNA MIPR No. 92-586, Work Unit 2 and monitored by Dr. William Blumberg of the Geophysics Directorate of the USAF Phillips Laboratory. The scatterometer work was supported by the NASA Lyndon B. Johnson Space Center and monitored by Mr. Steve Fitzgerald. The exhaust plume impingement simulation effort was supported by the NASA Marshall Space Flight Center, monitored by Mr. Peter Sulyma.

References

1. Caledonia, G.E., Krech, R.H., and Green, B.D., "A High Flux Source of Energetic Oxygen Atoms for Material Degradation Studies," AIAA J. 25/1, 59 (1987).
2. Leger, L.J., Spiker, I.K., Kuminecz, J.F., and Visentine, J.T., "STS Flight 5 LEO Effects Experiments - Background Description and Thin Film Results," AIAA Paper 83-2631, Oct. 1983.
3. Leger, L.J., Visentine, J.T., and Kuminecz, J.F., "Low Earth Orbit Atomic Oxygen Effects on Surfaces," AIAA Paper 84-0548, Jan. 1984.
4. Visentine, J.T., Leger, L.J., Kuminecz, J.F., and Spiker, I.K., "STS-8 Atomic Oxygen Effects Experiment," AIAA paper 85-0415, Jan. 1985.
5. Green, B.D., Caledonia, G.E., and Wilkerson, T.D., "The Shuttle Environment: Gases, Particulates and Glow," Journal of Spacecraft and Rockets, Vol. 22, Sept.-Oct. 1985, pp. 500-511.
6. Caledonia, G.E., "Laboratory Simulations of Energetic Atom interactions Occurring in Low Earth Orbit," in Rarefied Gas Dynamics: Space Related Studies, eds. E.P. Muntz, D.P. Weaver and D.H. Campbell, Vol. 116, Progress in Astronautics and Aeronautics, AIAA, Washington, D.C., pp. 129-142, 1989.
7. Caledonia, G.E., Holtzclaw, K.W., Green, B.D., Krech, R.H., Leone, A., and Swenson, G.R., "Laboratory Investigation of Shuttle Glow Mechanisms," Geophys. Res. Lett. 17(11), p. 1881-1884, October 1990.
8. Swenson, G.R., Leone, A., Holtzclaw, K.W., and Caledonia, G.E., "Spatial and Spectral Characterization of Laboratory Shuttle Glow Simulations," J. Geophys. Res. 96, 7603 (1991).
9. Caledonia, G.E., Holtzclaw, K.W., Krech, R.H., Sonnenfroh, D.M., Leone, A., and Blumberg, W.A.M., "Mechanistic Investigations of Shuttle Glow," J. Geophys. Res. 98, 3725 (1993).
10. Holtzclaw, K.W., Fraser, M.E., and Gelb, A., "Infrared Emission from the Reaction of High Velocity Atomic Oxygen with Graphite and Polyethylene," J. Geophys. Res. 95, 4147 (1990).
11. Sonnenfroh, D.M. and Caledonia, G.E., "Collisional Desorption of NO by Fast O-Atoms," J. Geophys. Res. 98, 21, 605 (1993).

12. Krech, R.H., Gauthier, M.J., and Caledonia, G.E., "High Velocity Atomic Oxygen/Surface Accommodation Studies," *J. Spacecraft and Rockets* 30, 509 (1993).
13. Upschulte, B.L. and Caledonia, G.E., "Laboratory Measurements of Infrared Excitation Cross Sections of Fast O-Atom Collisions with CO, CO₂ and CH₄," *J. Chem. Phys.*, 96 3, pp. 2205-2033, 1992.
14. Upschulte, B.L., Oakes, D.B., and Caledonia, G.E., "Infrared Emissions Arising from the Reactions of Fast O/O⁺ with N₂," *Geophys. Res. Lett.* 19, 993, 1992.
15. Sonnenfroh, D.M. and Caledonia, G.E., "Emission from OH(A) Produced in the Dissociative Recombination of H₂O⁺ with Electrons," *J. Chem. Phys.* 98, 2872 (1993).
16. Oakes, D.B., Sonnenfroh, D.M., Caledonia, G.E., and Blumberg, W.A.M., "Velocity Dependent O-Atom IR Excitation Cross Sections - Connection with Flight Data," Accepted, *J. Geophys. Res.* (1994).
17. Caledonia, G.E., Krech, R.H., Upschulte, B.L., Sonnenfroh, D.M., Oakes, D.B., and Holtzclaw, K.W., "Fast Oxygen Atom Facility for Studies Related to Low Earth Orbit Activities," AIAA Paper 92-3974, 17th Aerospace Ground Testing Conference, Nashville, TN, July 6-8, 1992.
18. Henderson, W.R. and Schiff, H.I., "A Simple Sensor for the Measurement of Atomic Oxygen Height Profiles in the Upper Atmosphere," *Planet. Space Sci.* 18, 1527 (1970).
19. Henderson, W.R., "O-Region Atomic Oxygen Measurements," *J. Geophys. Res.* 76, 3166 (1971).
20. Thomas, R.J. and Baker, D.J., "Silver Film Atomic Oxygen Sensors," *Can. J. Phys.* 50, 1676 (1972).
21. Henderson, W.R., "Atomic Oxygen Profile Measurements," *J. Geophys. Res.* 79, 3819 (1974).
22. Henderson, W.R., "Silver Film Atomic Oxygen Sensors: Further Evidence for Utility as an Atmospheric Probe," *Can. J. Phys.* 52, 2174 (1974).
23. Matijasevic, V., Garwin, E.L., and Hammond, R.H., "Atomic Oxygen Detection by a Silver-Coated Quartz Deposition Monitor," *Rev. Sci. Instrum.* 61, 1747 (1990).
24. Gregory, J.C. and Peters, P.N., "Measurement of the Angular Distribution of 5 eV Oxygen Scattered Off a Solid Surface in Earth Orbit," in Proc. 15th International Symposium on Rarefied Gas Dynamics, Grado, Italy, 1986, eds. V. Boffi and C. Cerignani, pp. 644-656.
25. Cross, J.B. and Blais, N.C., "High Energy/Intensity CW Atomic Oxygen Beam Source," in Rarefied Gas Dynamics: Space-Related Studies, eds. E.P. Muntz, D.P. Weaver, and D.H. Campbell, Vol. 116, *Progress in Astronautics and Aeronautics*, 1989, pp. 143-155.
26. Oakes, D.B., Krech, R.H., Upschulte, B.L., and Caledonia, G.E., "The Oxidation of Polycrystalline Silver Films by Hyperthermal Oxygen Atoms," submitted to *J. Appl. Phys.*

APPENDIX 6

Laboratory Studies of Fast Oxygen Atom Interactions with Materials

LABORATORY STUDIES OF FAST OXYGEN ATOM INTERACTIONS WITH MATERIALS*

George E. Caledonia, Robert H. Krech and David B. Oakes
Physical Sciences Inc.
Andover, MA 01810

ABSTRACT

We have used Physical Sciences Inc.'s (PSI) pulsed 8 km/s oxygen atom source to perform a number of measurements of material interactions of interest to low earth orbit applications. In particular, we have developed a new system to measure the scattering distribution resulting from 8 km/s oxygen atoms impinging on selected spacecraft materials. We will present data for scattering from glass and black and clear anodized aluminum. We will also present results on: the fast atom oxidation mechanism for thin silver films; the O-atom velocity dependent erosion rates for selected materials; and the oxidation dependence on material temperature.

Key words: oxygen atoms, LEO, Ag, material oxidation

1. INTRODUCTION

In the mid-1980's we developed a pulsed fast oxygen atom beam to provide a ground test facility to qualify materials to be used in low earth orbit (LEO) (Ref. 1). To our knowledge, ours is the only system that provides a high flux neutral oxygen atom beam with wide area operating capability at the desired velocity of 8 km/s. Sets of materials (2.5×2.5 cm samples) have been simultaneously irradiated to 8 km/s oxygen atom fluences of 6×10^{21} cm $^{-2}$ in our facility.

Flight tests of materials are preferable but considerably more expensive than ground evaluation. Furthermore, it is difficult to acquire material aging data from flight tests which, LDEF notwithstanding, are generally limited to less than 2 weeks experiment duration. Lastly, the flight data represent an average over the orbital environmental conditions of the flight. Many materials exhibit an increased rate of oxidative behavior with increased temperature, e.g. Ref. 2. Materials can vary in temperatures between -40°C to +65°C as the surface exposure varies from deep space to solar illumination (pathological materials excluded). Thus a measurement over a short shuttle experiment may not be reliably extended to a longer mission with different orbits, even if the aging effects can be linearly extrapolated.

The use of ground test data has been problematical both because facility definitions have been vague and because standardized measurement techniques have not been applied. The need for a measurement

protocol is clear. Banks et al. have recently discussed this for asher systems (Ref. 3) and Minton (Ref. 4) has recently presented version 1 of a detailed testing protocol.

PSI has performed commercial evaluation of LEO materials since 1987 and has developed a measurement protocol very similar to that outlined by Minton. The first step in such a protocol is the clear definition of the capabilities and operating properties of the fast oxygen atom facility. Since the PSI O-atom beam source has been used for material evaluation for the past 7 years, a significant effort has been dedicated to characterizing its operating properties in detail. The operating principles and characteristics of our device are described below. This discussion is followed by some representative results of material behavior under simulated LEO conditions.

1.1 The fast atom source

The hyperthermal oxygen atom source and experimental configuration have been described previously (Refs. 1,5,6) and will be discussed only briefly here. A schematic of the experimental system is shown in Figure 1. It is comprised of two stainless steel six-way crosses, including an 8 in. cross source chamber housing a pulsed oxygen valve/nozzle assembly, connected to a 16 in. cross expansion chamber. The system is pumped by a cryopump attached to the large cross which maintains a base pressure of 3×10^{-7} Torr.

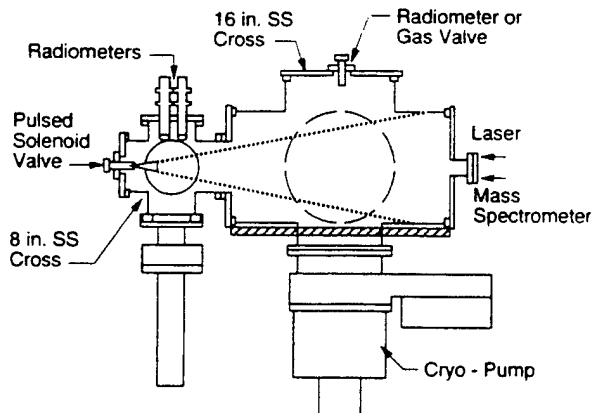


Figure 1. Schematic of the fast-2 system.

*This work was supported in part by the Defense Nuclear Agency, monitored by Dr. William Blumberg of the Geophysics Directorate of the USAF Phillips Laboratory and by the NASA Lyndon B. Johnson Space Center, monitored by Mr. Steve Fitzgerald.

The oxygen atoms are generated in a pulsed laser discharge of pure O₂ as described by Caledonia et al. (Ref. 1). A 12-J/pulse CO₂ laser is focused with a 100 cm focal length BaF₂ lens into the throat of a 20 deg full angle, 12.5 cm long conical expansion nozzle which has been partially filled with O₂ by a pulsed beam valve. The plasma, ignited at the throat, expands out the nozzle dissociating the molecular oxygen in front of it. The nozzle was designed to allow ion and electron recombination while the slower kinetics of atom/atom recombination maintains a highly dissociated beam. The result, at 8 km/s, is an approximately 50 μ s pulse of highly dissociated oxygen (> 80% atoms) with less than 1% ion content (the beam is charge neutral). The general beam properties are provided in Table 1 while the diagnostics used in evaluating these properties are summarized in Table 2.

Table 1. Fast O-beam properties.

Velocity	8 km/s \pm 15% (5 to 12 km/s range)
Fluence	$\sim 10^{18}$ O-atoms/pulse, 3 Hz
Composition	>80% oxygen atoms
Size	Expandable to >1000 cm ² area
Charge content	< 1% ions (controllable by pseudo-Helmholtz coils)
Metastable content	O(¹ D) concentration < 0.4%
Temperature	T = 300 K
VUV/UV content	One photon per 10 ⁴ O atoms (similar to LEO)

The beam velocity (5 to 12 km/s) is selected by varying the time delay between the pulsing of the O₂ valve and the triggering of the CO₂ laser. The delay determines the mass of O₂ processed by the pulsed discharge which is inversely related to the beam velocity. The velocity is determined by measuring the time of flight of the pulse between two radiometers attached to the source chamber, mounted along the beam axis and separated by 7.6 cm, and filtered to monitor the ⁵S-⁵P oxygen atom line (777 nm) (see Figure 1).

We have estimated the flux of oxygen atoms generated per pulse by measuring the mass of O₂ processed per pulse and the expansion characteristics of the beam. The expansion properties have been determined previously (Refs. 5,6) by measuring the fast O-atom erosive mass loss of polyethylene samples mounted 75 cm downstream from the nozzle throat as a function of radial position. The expansion half angle (to 1/e times the on-axis flux) was found to be 14 deg. These calibrations have been cross checked by measuring the absolute oxidation rates of materials and comparing them with equivalent space flight measurements. More recently, as discussed in the next section, the oxidation rate of thin silver films has been used as a calibration standard.

Although the beam is charge neutral, it does have a small but finite ion content. The charge concentration can be decreased by up to a factor of eight using a pair of pseudo-Helmholtz coils. Thus any effects due to charged rather than neutral species can be delineated. Control of the ionic concentration is critical in that some materials are efficiently oxidized by O⁺ and not by O. The local charge concentration can be measured through use of a retractable Langmuir probe. The probe is positionable both horizontally and vertically and it has been found that the spatial and temporal shape of the ion distribution matches that of the neutral distribution (Ref. 6).

Table 2. O-Beam diagnostics

Velocity, temporal pulse shape	Radiometers, mass spectrometer (standard quadrupole and TOF)
Pulse fluence	Mass flow meter, thin silver film actinometer
Beam composition	Mass spectrometer
Excited state concentrations	Spectrometer, bandpass filters
Charge content (beam is charge neutral)	Langmuir probe
Beam shape	Erosive witness samples, positionable Langmuir probe, 2D visible imaging
Beam translational temperature	Slotted thin silver film target chamber

We have recently measured the O(¹D) concentration of the beam by monitoring the emission from the forbidden O(¹D \rightarrow ³P) transition using a specially constructed bank of narrow-band interference filters. The O(¹D) concentration was found to be \leq 0.4% for a beam velocity of 8 km/s and to increase monotonically with beam velocity over the velocity range of 6 to 12 km/s.

We have also evaluated the translational temperature of the beam. This was done by passing the O-beam through a 0.15 cm diameter circular aperture and measuring the oxidation pattern on a thin silver film witness plate placed 5 cm behind the aperture. Any growth in the beam beyond the slit width is due to the Maxwellian motion of the O atoms and can be related to an effective temperature for the 8 km/s velocity

beam. This temperature was deduced to be ~ 300 K at a distance of 85 cm from the nozzle throat. The beam temperature will be higher closer to the throat and is calculated to be ~ 1000 K at the nozzle exit plane.

Lastly, we have measured the VUV/UV content of the beam and find that it is somewhat less than the equivalent LEO value per oxygen atom. Since the beam is pulsed, the VUV radiation can be chopped allowing independent examination of VUV effects on materials.

Our O-beam facility has been employed on several occasions to pre-test materials which were subsequently flown in space experiments. In general, the comparison between flight data and ground test data has been quite good. The most recent large ground test was for the SEE program on materials for the EOIM-3 flight (Ref. 7). We irradiated 84 materials to a fluence of $2 \times 10^{20} \text{ cm}^{-2}$ 8 km/s oxygen atoms and followed a careful protocol of pre- and post-test weighing taking account of water uptake. The Jet Propulsion Laboratory performed subsequent surface analysis. With a few understood exceptions, the comparison between our ground test results for these materials and the flight observations was quite good (Ref. 7), demonstrating our ability to simulate LEO conditions.

2. EXAMPLE MATERIAL STUDIES

Material oxidation rates can be significantly affected both by the test environment and the test system parameters. In this section we will briefly examine the effect of sample temperature and O-atom velocity on two materials, a thin silver film and μ -crystalline carbon. In the case of the thin silver film the effect of two additional parameters, test duration and surface contamination will be addressed.

We have performed investigations of the temperature dependent oxidative behavior of several materials over the temperature range of 0° to 85°C. An example of such studies is our observations of the oxidative behavior of thin films of silver (600 Å) (Ref. 8) and μ -crystalline carbon (1 μm) which were vacuum deposited onto the crystals of quartz crystal monitors (QCM's). QCM's are the diagnostic of choice for monitoring mass change as the measurements are performed continuously in-situ. Unfortunately in many instances the materials to be tested cannot be coated on a crystal. Then weight change is monitored by pre- and post-testing weighing using our Mettler analytical balance and Cahn micro-balance. (Here a careful protocol must be followed to account for moisture uptake).

The silver and carbon films are good examples for consideration in that the silver gains mass upon oxidation while the carbon loses mass. In these experiments, the QCM was mounted directly onto a temperature-controlled aluminum block and thus the quartz crystal, which is in intimate thermal contact with the QCM base, was maintained to $\pm 0.5^\circ\text{C}$ (material coupons can be monitored in the same manner). Temperature regulation of the QCM was necessary since the oscillator frequency is temperature

dependent. Therefore, a change in temperature could be erroneously interpreted as a mass gain or loss.

The silver films are particularly interesting since because of their high oxidation efficiency we feel that they can be used as a standard for laboratory flux calibrations. Furthermore, they have been successfully used in both flight (Ref. 9) and laboratory (Ref. 6) studies to examine the distributions of hyperthermal oxygen atoms scattered off of selected surfaces. The oxidation behavior of these films exhibits several intriguing effects. Our studies in this are described in detail in Ref. 8 and presented briefly below.

Typical thin film silver oxidation histories for irradiation by 8 km/s oxygen atoms at room temperature are shown in Figure 2. Shown is oxidation depth versus the number of impinging O-atom pulses as determined by the measured mass increase for two film thicknesses. Two important features can be seen. First, no oxidation occurs during the first two hundred pulses. This is typically observed and we relate it to the required removal of a contamination layer on the silver film. Indeed, if we first irradiate the film with several hundred pulses of a fast argon beam and then shortly thereafter impinge it with fast oxygen atoms, we find that oxidation initiation is immediate. Second, after oxidation initiation, the oxidation depth increases linearly with O-atom fluence for approximately the first 250 Å of the silver film and then the oxidation rate slows down. We believe the oxidation rate becomes diffusion controlled at these thicknesses and thus only very thin films are useful as a linear calibration source. Note that the observed oxidation rate continues to decrease very dramatically in the case of the 1 μm thick film.

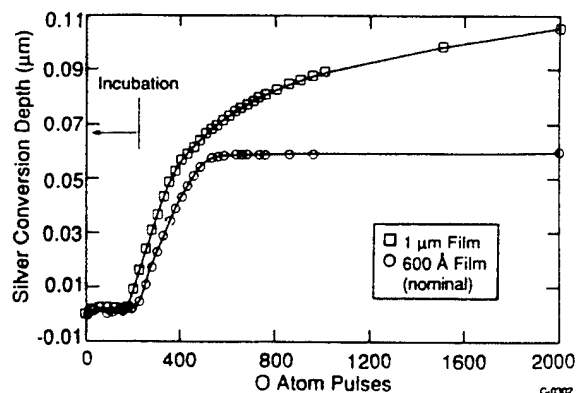


Figure 2. Oxidation behavior of thin silver films coated on QCM crystals (O-atom velocity = 8 km/s, room temperature).

Note that in the interpretation of the QCM data it is important to understand the oxidation process. During the course of our work we realized that the polycrystalline silver oxidized to the peroxide, Ag_2O , rather than Ag_2O . This was determined by measuring the mass uptake of a totally oxidized film with known silver loading, and verified both by heating the film to 200°C to form Ag_2O and by X-ray diffraction analysis of the film.

These limited tests on silver films demonstrate a number of interesting features. From the perspective

of a ground test facility, the two that are most important are the demonstrated role of surface contamination and the observation of the time (thickness) variation in the oxidative behavior.

In further studies we examined the temperature dependence of the silver and carbon oxidation rate over the range of 0° to 85°C. These results are shown in Figure 3. (For convenience, all results are normalized to a silver reactivity of unity at 273 K). Although there is some scatter in the data, the silver oxidation rate is apparently independent of temperature, unlike that for carbon. Thus, we believe that these silver films will provide a good standard for relative investigation of high velocity oxidation behavior of materials. On the other hand, the oxidation rate for this particular form of carbon varies significantly with temperature, a critical effect for predicting lifetime if this material were to be used in an engineering design.

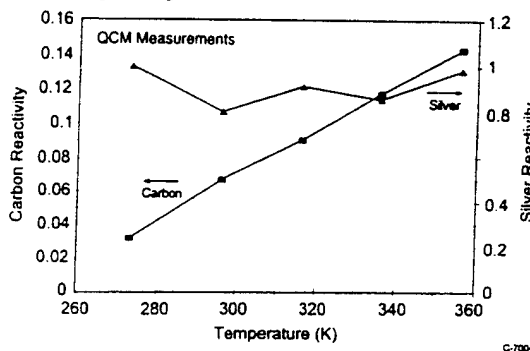


Figure 3. Measured silver and carbon reactivity versus temperature (O-atom velocity 8 km/s).

We have also investigated the effect of O-atom velocity on the oxidation rate. This study is complicated by the fact that the number of oxygen atoms per pulse in our beam decreases as the beam velocity increases. Rather than go into the details of our velocity dependent calibration we will only discuss the relative oxidation behavior of the thin silver film and carbon samples as the beam velocity is varied.

The carbon and silver film samples were irradiated simultaneously at velocities of 8, 10 and 12 km/s at a pulse frequency of 2 Hz. The observed oxidation depth versus time of the thin silver film is shown in Figure 4.

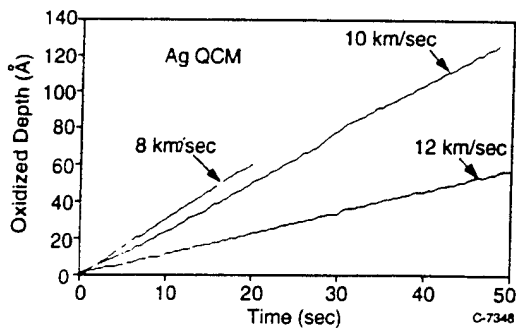


Figure 4. Observed silver oxidation depth versus time for three O-atom velocities. Pulse repetition frequency was 2 Hz.

The decreasing oxidation rate with increasing velocity correlates with the decreased number of oxygen atoms produced per pulse as the velocity is increased. Indeed within the uncertainty of our calibration the silver film oxidation efficiency remained constant over the velocity range. (This is not surprising since the oxidation efficiency is near unity.)

This result is contrasted with the observed etched depth histories in the carbon sample as shown in Figure 5. Here it can be seen that the etch rate increased with velocity even though the O-atom fluence decreased. Thus the carbon sample studied shows a strongly velocity dependent oxidation rate. We have observed a similar trend over the velocity range of 6 to 11 km/s in other materials, such as kapton (Ref. 10).

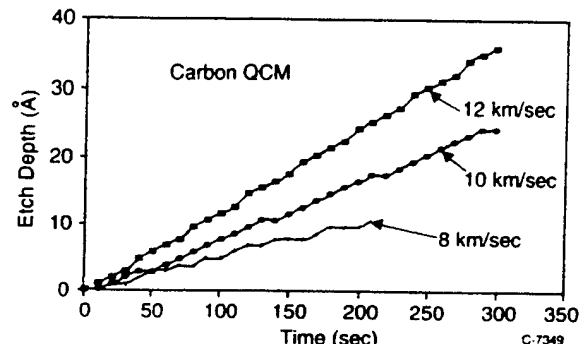


Figure 5. Observed etch depth of carbon versus time for three O-atom velocities. Pulse repetition frequency was 2 Hz.

3. SCATTERING STUDIES

We employed the oxidative behavior of thin silver films to measure the scattering distribution of 8 km/s oxygen atoms impinging selected surfaces. These scattering distributions are of interest to the materials community since non-ram surfaces can be oxidized by scattered ambient oxygen atoms.

Silver film scatterometers designed to measure the atomic oxygen scattering distribution off various materials have been flown on-orbit in shuttle experiments by John Gregory (Ref. 9) and other investigators. These on-orbit measurements show that the atomic oxygen scattering is largely non-specular. Our measurements attempt to confirm these observations in the laboratory in an 8 km/s atomic oxygen flow. The representative materials chosen for this study are clear and black anodized aluminums and glass. As described previously (Ref. 6), we observed that scattering off all three materials is largely non-specular. The details of the scatterometer design atomic oxygen scattering measurements are described briefly below.

We used a modified version of Gregory's scatterometer in our laboratory experiments to measure the oxygen atom angular scattering distributions from surfaces. In this device the beam passes through a small slit into a chamber containing the target material. The O-atoms scattered from the target ultimately interact with a silver film "witness plate" positioned at the front of the

chamber (around the slit). The distance between target and slit must be large enough to allow sufficient spread of the scattered beam to provide good measurement resolution on the witness plate for the scattered angular distribution.

We designed and built silver film scatterometers specific to our experiment. Two scatterometers were constructed to hold up to three samples in individual compartments at either a 90 or 45 deg angle of incidence to the 8 km/s atomic oxygen flow. The 90 deg scatterometer is shown in Figure 6. The silver film to be oxidized by the scattered atomic oxygen was attached to the 2.22 cm radius surface. A 0.25 cm wide by 1.25 cm long slit was cut in the film prior to mounting to restrict the atomic oxygen flow into the scatterometer. The glass and aluminum samples were cut to fit the individual sample chambers and attached to the silver coated kapton covered rear surface. A key feature of our scatterometers not found in other designs is the addition of a hinged cover to permit cleanup via argon atom bombardment of both the sample and silver film surfaces to remove the surface contamination layers in the chamber immediately prior to the oxygen scattering measurement. We have found that this was a key feature for successful accomplishment of the experiments.

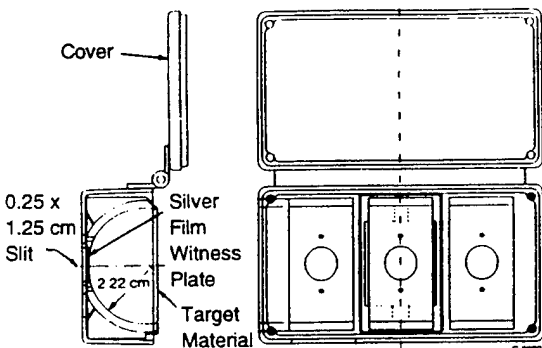


Figure 6. Normal incidence spectrometer used to measure distribution of fast oxygen atoms scattered off of selected materials.

Our witness samples, 500Å silver film on 2 mil mylar, were prepared by Sheldahl. In this application, the films were analyzed for oxidation by measuring changes in film transmission (silver oxide is transparent although silver is opaque). The fast O-atom beam was used to calibrate the film transparency, e.g., optical thickness versus atomic oxygen fluence, and the scattering measurement experiment duration was limited to ensure that $\leq 250\text{\AA}$ depth of the film was oxidized, i.e., to the range of linear oxidation behavior.

The resulting measured scattered oxygen atom distributions versus angle from the slit is shown in Figure 7 for normal incidence. All measurements were taken in the central chamber. The results are averaged over the width of the witness film and are presented as a percentage of the incident flux per degree. The angular resolution of the data is about 2.5 deg. The absolute calibration for this data is uncertain to about

a factor of two but this uncertainty can be greatly reduced in future work by simultaneously monitoring the O-atom flux during the scattering measurement.

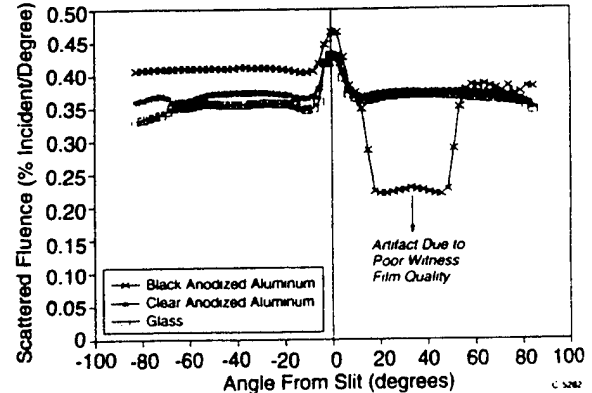


Figure 7. Oxygen scattering distribution at normal incidence for three materials. O-atom velocity is 8 km/s. Low measurements at positive angles on black anodized aluminum are due to improper witness film cleaning.

The scattering distribution is quite flat, suggesting largely isotropic scattering for all three materials. Similar results were observed at 45 deg incidence with no strong specular regions apparent. The central spike that is seen in the figure should be ignored. It is due to the presence of a slit in the silver film and the fluence indicated is an artifact of the analysis technique.

The importance of working with clean films was accidentally demonstrated in the data for black anodized aluminum shown in Figure 7. It turns out that the door of the scatterometer opened too far during the exposure of the black anodized sample and one side of the silver was not scoured by the atom beam. Thus, the anomalously low apparent scattered fluence.

Subsequent measurements made at a few scattering angles with a time-of-flight mass spectrometer showed that, although the velocity spread of the scattered atoms was quite broad, a significant degree of thermalization occurred. The details of these measurements are presented in Ref. 6.

4. SUMMARY

Ground testing provides a critical adjunct to the evaluation and validation of material applicability for low earth orbit operations. Care must be taken, however, to ensure that the ground test facility can provide valid test results. In the case of hypersonic oxygen atom testing, proper material evaluation and data interpretation require both a clear understanding of the characteristics of the test facility as well as a standardized measurement protocol.

Details of the PSI fast oxygen atom source have been provided. This system has been used to evaluate materials since 1987, over 2000 material samples have been tested. Good comparison with space test results has been demonstrated. All major beam parameters,

e.g., VUV, metastable content, beam velocity spread, have been evaluated and a standard measurement protocol has been applied.

Example test data has been presented for 8 km/s oxygen atom beam irradiation of a thin silver film and a sample of micro-crystalline carbon. Typical measurements of the scattering distributions of 8 km/s oxygen atoms impinging representative spacecraft surfaces were also shown. Although these data are of interest in their own right, they also demonstrate the importance of controlling test parameters such as contamination level, sample temperature, and beam velocity.

5. REFERENCES

1. Caledonia GE & al 1987, A high flux source of energetic oxygen atoms for material degradation studies, *AIAA Journal*, 25. 1. 59 p.
2. Kamenetzky RR & al 1993, Effects of atomic oxygen on polymeric materials flown on EOIM-3, AIAA 93-4103, AIAA Space Programs and Technologies Conference and Exhibit, Sect. 21-23, Huntsville, AL.
3. Banks BA & al 1993, Atomic oxygen durability evaluation of protected polymers using thermal energy plasma systems, Int. Conf. on Plasma Synthesis and Processing of Materials, Denver, CO.
4. Minton TK 1994, Protocol for atomic oxygen testing of materials in ground-based facilities, version Number 1, *JPL Publication* 94-02.
5. Caledonia GE & al 1992, Fast oxygen atom facility for studies related to low earth orbit activities, AIAA Paper 92-3974.
6. Caledonia GE & al 1994, Hypersonic beam facility for rarefied flow studies, AIAA 94-2638.
7. Chung SY & al 1993, Flight- and ground-test correlation study of BMDO SDS materials, *JPL Publication* 93-31.
8. Oakes DB & al 1994, The oxidation of polycrystalline silver films by hyperthermal oxygen atoms, accepted for publ. *J. Appl. Phys.*
9. Gregory JC & Peters PN 1986, Measurement of the angular distribution of 5 eV oxygen scattered off a solid surface in earth orbit in *Proc. 15th International Symposium on Rarefied Gas Dynamics*, Grado, Italy, eds. V. Boffi and C. Cerignani, pp. 644-656.
10. Krech RH 1993, Determination of oxygen erosion yield dependencies upon specific LEO environments, Physical Sciences Inc. TR-1178.

APPENDIX 7

Experimental Determination of the Einstein Coefficient for the N(^2P-4S) Transition

EXPERIMENTAL DETERMINATION OF THE EINSTEIN COEFFICIENT FOR THE N(²P-⁴S) TRANSITION

Lawrence G. Piper
Physical Sciences Inc.
20 New England Business Center
Andover, MA, 01810-1022

ABSTRACT

We have measured the Einstein coefficient for the forbidden atomic transition, N(²P-⁴S), at 346.6 nm, by determining absolute photon emission rates at 346.6 nm when known number densities of N(²P) are in the detector field of view. The N(²P) is generated in a discharge-flow reactor and its number density is determined by vacuum ultraviolet resonance absorption at 174 nm. The absolute response of the monochromator is determined from measurements of the O/NO air afterglow. This first experimental determination, $(5.4 \pm 1.4) \times 10^{-3} \text{ s}^{-1}$, agrees well with published theoretical calculations.

Key words: Einstein coefficient, metastable nitrogen atoms, aurora

1. INTRODUCTION

Metastable N(²P) nitrogen atoms are a source of bright auroral radiation at both 346.6 nm in the ultraviolet, from the N(²P-⁴S) transition, and at 1040 nm in the near infrared, from the N(²P-²D) transition.¹⁻³ Observations of N(²P) emission intensities in comparison with intensities of N₂⁺(B-X) or N₂(C-B) transitions have been used to estimate the depth of penetration of auroral electrons² and the altitude profiles of atomic oxygen number densities.³ Both of these measurements rely on the fact that long-lived N(²P) is quenched rather efficiently by atomic oxygen under auroral conditions, whereas the molecular emissions are not because of their short radiative lifetimes.

Proper analysis of N(²P) emission measurements in aurorae require accurate knowledge of the N(²P - ²D, ⁴S) transition probabilities and the rate coefficient for N(²P) quenching by atomic oxygen. We determined the latter experimentally several years ago.⁴ The former, however, is known only through two theoretical calculations published some 30 years apart.^{5,6} Although the two calculations agree within 12%, our observations of N(²P) excitation in the energy transfer reaction between N₂(A) and N(⁴S)⁷ suggested the calculation of the N(²P-⁴S) transition probability could possibly be erroneous, and an experimental determination of that transition probability was warranted.

2. EXPERIMENTAL

The intensity of an electronic transition is given by the product of the number density of species in the emitting state and the Einstein coefficient for spontaneous radiation:

$$I = NA, \quad (1)$$

where I is the absolute photon emission rate in units of photons cm⁻³ s⁻¹, N is the number density in species cm⁻³, and A is the Einstein coefficient in units of s⁻¹. The basis of our measurement, therefore, is to determine absolute photon emission rates and number densities of emitting species simultaneously. The ratio of these two quantities, then, is the Einstein coefficient we seek.

Our experiments used the 5 cm diameter discharge-flow reactor shown schematically in Figure 1. N(²P) was generated in the upstream section of the reactor in a microwave discharge sustained in a flow of N₂ dilute in either helium or argon at total pressures between 0.3 and 1.5 Torr. The N(²P) was then detected in emission at 346.6 nm using a 0.5 m monochromator equipped for photoelectric detection and also by vacuum ultraviolet resonance absorption at 174 nm. The absorption measurements are made across the central diameter of the flow reactor. The source of the resonance radiation was a microwave excited discharge in helium with a trace of added air. On the opposite side of the flow reactor, a 0.2 m vacuum monochromator and solar-blind photomultiplier detected the radiation. Normal to the diameter defined by the resonance absorption system, a 0.6 cm diameter fiber-optic bundle collected 346.6 nm radiation emanating from the center of the flow reactor and transported it to the 0.5 m monochromator.

Fig. 1

The number density of the N(²P) atoms varies radially across the flow reactor, being highest in the center and zero at the walls. The absorption and emission diagnostics, therefore, both sample average number densities in the reactor. Because the system and flows are cylindrically symmetric, however, and because the two diagnostics have similar fields of view across the flow reactor (narrow and collimated), the average number densities they monitor are the same. Thus, the non-uniform N(²P) number densities have no effect on the experimental results.

The 0.5 m monochromator was calibrated for absolute photon emission rate measurements by observing the intensity of the O/NO air afterglow when known amounts of O and NO were added to the reactor. Titrating N atoms with NO, using procedures we have detailed previously,^{8,9} produced the O. Our air afterglow calibrations, made at 580 nm, used a chemiluminescence rate coefficient of $1.17 \times 10^{-19} \text{ cm}^3 \text{ molecule}^{-1} \text{ s}^{-1} \text{ nm}^{-1}$. This value is an average based upon our critical analysis¹⁰ of the published literature¹¹⁻¹⁸ on the air afterglow. We think this value is accurate within $\pm 10\%$.

We established the relative spectral response of the system *in situ* to extrapolate the calibration made at 580 nm to 346.6 nm. We used a branching ratio technique based upon measurements of NO(B ²Π -- X ²Π) band intensities and the NO(B-X) transition probabilities we reported¹⁹ (which were confirmed theoretically by Langhoff, *et al.*²⁰ and experimentally by Luque and Crosley²¹) to determine the response variation between 250 and 500 nm, and O/NO air afterglow intensity measurements to establish the relative spectral response between 400 and 850. The two techniques agreed to within $\pm 5\%$ in the region of spectral overlap.

We have discussed our use of VUV resonance absorption techniques to determine atomic number densities in a discharge-flow reactor previously.^{22,23} The 174.3 nm transition that is absorbed by N(²P) is actually a multiplet consisting of four separate transitions, two doublets separated by about 0.25 nm with a separation between the lines in each doublet of about 0.0008 nm or 0.26 cm⁻¹. The Doppler width of each line is about 0.17 cm⁻¹, small enough that the unresolved multiplet can be treated as a composite of four independent transitions.

Our measurements were made with a resolution of 1 nm to ensure that all lines of the multiplet were transmitted equally through the instrument. The equation describing the fractional absorption, A=(I_o-I)/I_o, then becomes²⁴

$$A = \frac{\sum_i C_i \int_{-\infty}^{\infty} (1 - e^{-k_{oi} e^{-\omega_i^2}}) e^{-(\omega_i/\alpha)^2} d\omega_i}{\sum_i C_i \int_{-\infty}^{\infty} e^{-(\omega_i/\alpha)^2} d\omega_i}, \quad (2)$$

where C_i is the relative intensity of each multiplet component, k_{oi} the absorption coefficient at line center, ω_i, the reduced frequency of the line, α is the ratio of the width of the line from the

resonance lamp to that of the absorption line, and ℓ is the absorption path length. The reduced frequency, ω , is given in terms of the separation from the center-line frequency, v_o , by

$$\omega = \frac{2(v - v_o)}{\Delta v_D} \sqrt{\ln 2} , \quad (3)$$

where Δv_D is the full width at half maximum of the line as determined by Doppler broadening:

$$\Delta v_D(s^{-1}) = \frac{2}{\lambda_o} \sqrt{\frac{2RT \ln 2}{M}} , \quad (4)$$

λ_o being the center wavelength of the transition, R the gas-law constant, T the translational temperature, and M the mass of the atom.

Doppler broadening is the only significant mechanism of line broadening in a low power, low pressure microwave discharge resonance lamp and of the absorption line as well (collision broadening contributes less than 1% to the total linewidth in 3 Torr of helium).²⁵ As a result the ratio of the widths of the lamp line to the absorption line is just the square root of the ratio of translational temperatures in the lamp and the flow reactor. The translational temperature in the flow reactor is equal to the laboratory temperature, 300 K. We determined the translational temperature in the resonance lamp to be 500 K from measurements of the band profiles of N₂(C ³Π_u - B ³Π_g) transitions. Figure 2 shows a comparison between a fit of the observed N₂(C-B) bands and band contours calculated assuming rotational temperatures of 400, 500, and 600 K. The rotational profile calculated from a 500 K temperature best reproduces the data. The uncertainty in this value, ±50 K, contributes to an uncertainty in the overall absorption measurement of only ±3%.

The absorption coefficient at line center is

$$k_o = \frac{2}{\Delta v_D} \sqrt{\frac{\ln 2}{\pi}} \frac{\lambda_o^2 d_u}{8\pi d_l} A_{ul} N , \quad (5)$$

where d_u and d_l are the degeneracies of the upper and lower states in each of the four transitions in the multiplet, A the Einstein coefficient, and N the number density of absorbing atoms. We used transition probabilities based upon the radiative lifetime for the upper state of the multiplet of 1.8 ns as measured by Hutchison.²⁶ Table 1 summarizes the relevant spectroscopic data.

3. RESULTS

Figure 3 shows typical results of measurements of the 346.6 nm intensity as a function of $N(^2P)$ number density. The $N(^2P)$ number densities were determined by measuring the fractional absorption at 174 nm and using the results of a numerical integration of Eq. (2) to relate the fractional absorption to $N(^2P)$ number density. Since the absolute photon emission rate is the product of the number density of emitters and the Einstein coefficient for the transition, the Einstein coefficient for the 346.6 nm transition is just the slope of the line through the data in Figure 3.

719

The average result from several measurements in both Ar and He carrier gas is $5.4 \times 10^{-3} \text{ s}^{-1}$. We estimate the uncertainty in this value to be $\pm 26\%$ based upon the square root of the sum of the squares of the various uncertainties in the experimental parameters: 5% in the raw data (ratio of intensity to number density), 12% in the number density diagnostic (lamp temperature and transition probabilities), 10% in the air afterglow rate coefficient, and 20% in the photometric calibration of the monochromator.

4. DISCUSSION

This Einstein coefficient was first calculated by Garstang to be $5.4 \times 10^{-3} \text{ s}^{-1}$ over 40 years ago.⁵ More recently, Godefroid and Froese-Fischer⁶ calculated a value of $4.8 \times 10^{-3} \text{ s}^{-1}$. Both of these values agree well with our experimental determination. We had speculated these calculated values might be erroneous because we determined a rate coefficient for $N(^2P)$ formation in the energy-transfer reaction between $N_2(A)$ and $N(^4S)$ to be five times larger than the rate coefficient for $N_2(A)$ quenching by $N(^4S)$.⁷ The most likely explanation for this discrepancy seemed to be that the Einstein coefficient used to determine either $N_2(A)$ or $N(^2P)$ number density was in error. We have considered the issue of the $N_2(A)$ Einstein coefficient,²⁷ and determined that previously accepted values are not seriously in error.²⁸ The results of this investigation indicate that the same can be said for the $N(^2P-^4S)$ transition. Thus the discrepancy in our previous measurements must result from an additional metastable in our flow reactor that we have so far been unable to detect. Evidence for this additional metastable has been found in other studies as well.^{29, 30}

ACKNOWLEDGMENTS

We appreciate partial financial support from the Air Force Office of Scientific Research (Task 2310G4) and Defense Nuclear Agency (Project SA, Task SA/SDI, work unit 00175) from a contract with the Phillips Laboratory/Geophysics Directorate under contract no. F19628-88-C-00173 and F19628-93-C-0046.

REFERENCES

1. M.H. Rees and G.J. Romick, *J. Geophys. Res.* **90**, 9781 (1985).
2. A. Vallance Jones and R.L. Gattinger, *J. Geophys. Res.* **84**, 1315 (1979).
3. E. C. Zipf, P. J. Espy, and C. F. Boyle, *J. Geophys. Res.* **85**, 687 (1980).
4. L. G. Piper, *J. Phys. Chem.* **98**, 8560 (1993).
5. R. H. Garstang, *The Airglow and the Aurora*, Armstrong and A. Dalgarno, eds., New York: Pergamon (1956).
6. M. Godefroid and C. Froese Fischer, *J. Phys. B* **17**, 681 (1984).
7. L. G. Piper, *J. Chem. Phys.* **90**, 7087 (1989).
8. L. G. Piper, G. E. Caledonia, and J. P. Kennealy, *J. Chem. Phys.* **75**, 2847 (1981).
9. L. G. Piper and W. T. Rawlins, *J. Phys. Chem.* **90**, 320 (1986).
10. L. G. Piper, *Chem. Phys.*, submitted (1998), in review.
11. A. Fontijn, C. B. Meyer, and H. I. Schiff, *J. Chem. Phys.* **40**, 64 (1964).
12. M. Vanpee, K. C. Hill, and W. R. Kineyko, *AIAA J.* **9**, 135 (1971).
13. M. F. Golde, A. E. Roche, and F. Kaufman, *J. Chem. Phys.* **59**, 3953 (1973).
14. D. Golomb and J. H. Brown, *J. Chem. Phys.* **63**, 5246 (1975).
15. G. A. Woolsey, P. H. Lee, and W. D. Slafer, *J. Chem. Phys.* **67**, 1220 (1977).
16. M. Sutoh, Y. Morioka, and M. Nakamura, *J. Chem. Phys.* **72**, 20 (1980).
17. A. M. Pravilov and L. G. Smirnova, *Kinet. Catal. (USSR)* **19**, 202 (1978).
18. G. Bradburn and H. V. Lilienfeld, *J. Phys. Chem.* **92**, 5266 (1988).
19. L. G. Piper, *J. Chem. Phys.* **94**, 7667 (1991).
20. S. R. Langhoff, H. Partridge, and C. W. Bauschlicher, Jr., *J. Chem. Phys.* **94**, 6638 (1991).
21. J. Luque and D. R. Crosley, *J. Quant. Spectrosc. Radiat. Transfer* **53**, 189 (1995).

22. W. T. Rawlins and L. G. Piper, Proc. Soc. Photo.-Opt. Instrum. Eng. 279, 58 (1981).
23. L. G. Piper, M. E. Donohue, and W. T. Rawlins, J. Phys. Chem. 91, 3883 (1987).
24. M. Mitchell and M. W. Zemansky, Resonance Radiation and Excited Atoms, New York: Academic Press (1971).
25. M. A. A. Clyne and L. G. Piper, JCS Faraday 2 72, 2178 (1976).
26. R. B. Hutchison, J. Quant. Spectrosc. Radiat. Transfer 11, 81 (1971).
27. L. G. Piper, J. Chem. Phys. 99, 3174 (1993).
28. D. E. Shemansky, J. Chem. Phys. 51, 689 (1969).
29. M. E. Fraser, and L. G. Piper. J. Phys. Chem. 93, 1107 (1989).
30. T. D. Dreiling and D. W. Setser, Chem. Phys. Lett., 74, 211 (1980).

Figure Captions

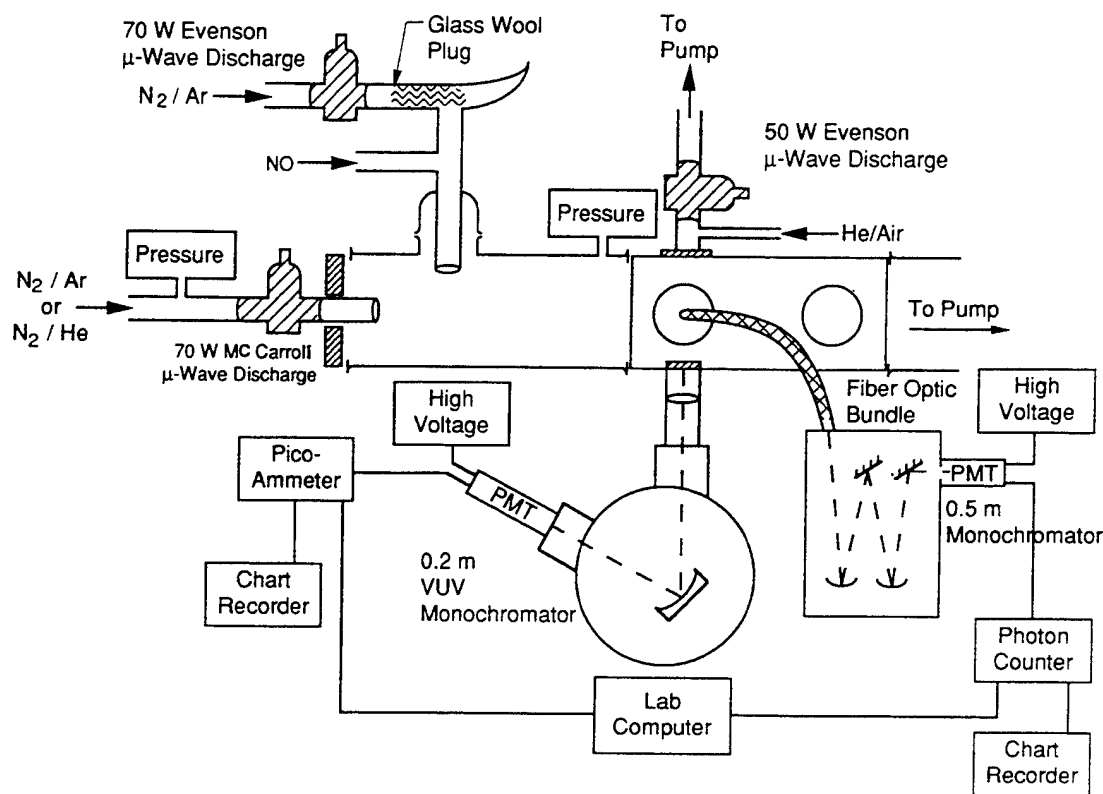
Figure 1. Schematic view of discharge-flow reactor used in the experiments.

Figure 2. Comparison of the spectrum of $N_2(C\ ^3\Pi_u - B\ ^3\Pi_g)$ emission from the lamp used in the absorption measurements with synthetic spectra generated assuming different rotational temperatures for the $N_2(C)$ emission. The best fit rotational temperature, 500 K, corresponds to the kinetic temperature in the lamp.

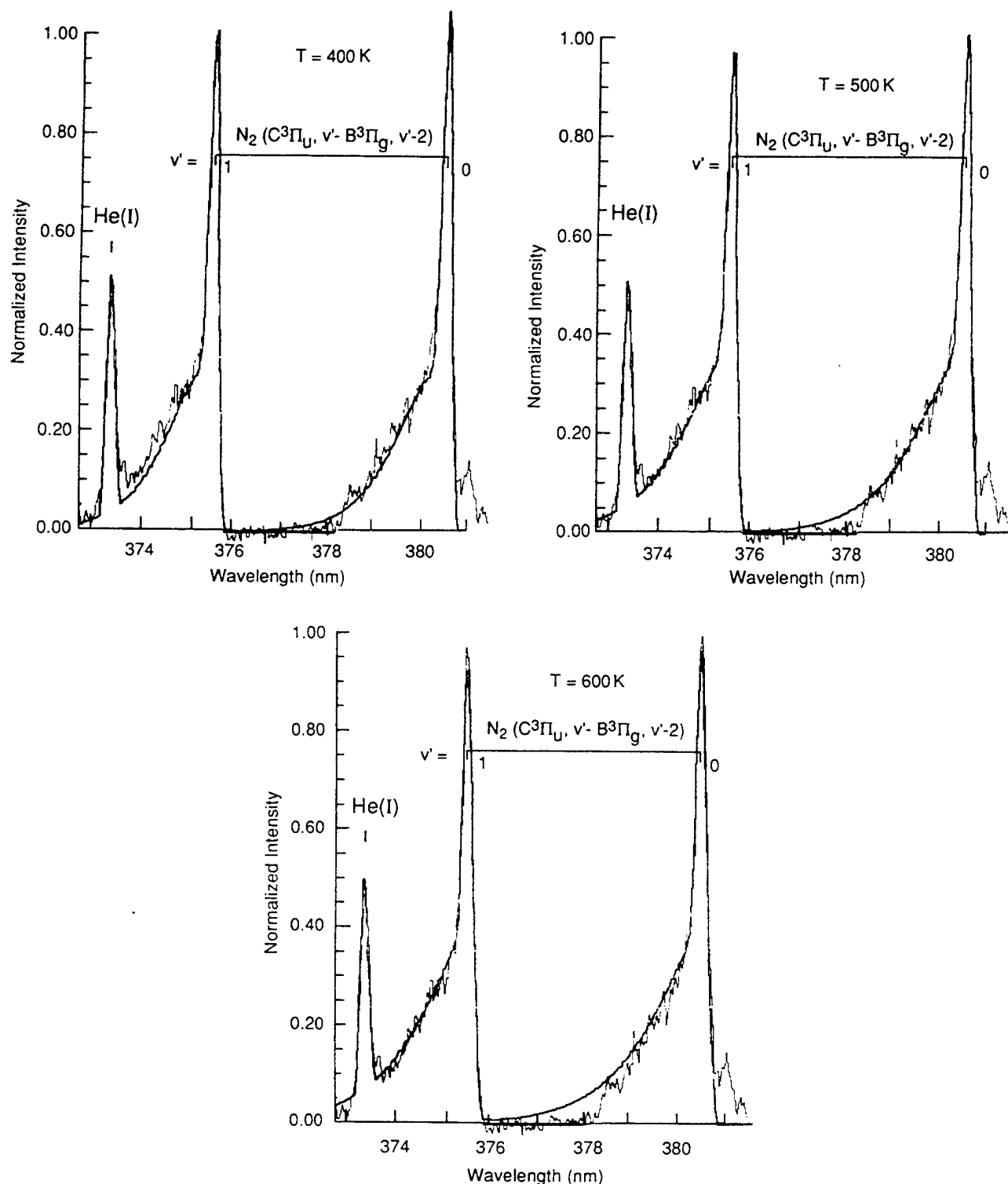
Figure 3. Typical experimental results showing the relationship between observed $N(^2P - ^4S)$ emission intensities and measured $N(^2P)$ number densities.

Table 1. Spectroscopic Data for the N($2p^3$ $^2P^o$ - $2p^2$ $3s$ 2P) Multiplet at 174 nm

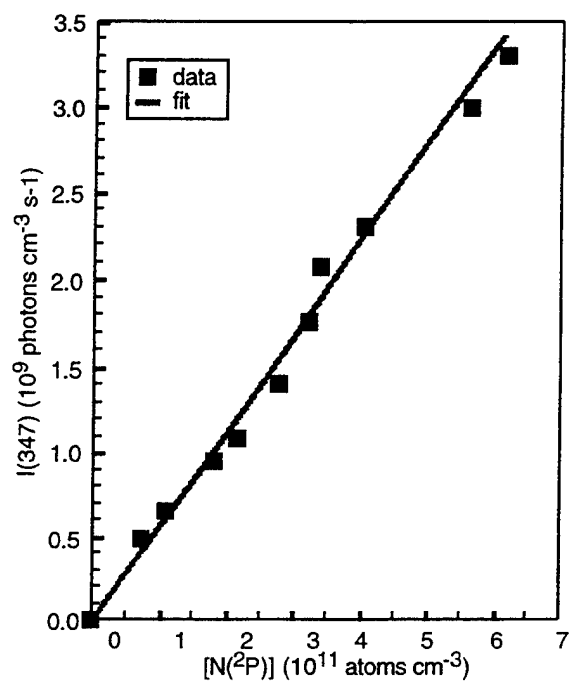
Transition (i)	Wavelength (nm)	d_l	d_u	A_{ul} (s^{-1})	C_i	k_{oi}/N_i (cm^{-2})	k_{oi}/N_{total} (cm^{-2})
1	174.272	2	4	0.247×10^8	1	0.984×10^{-13}	0.328×10^{-13}
2	174.273	4	4	1.233×10^8	5	2.455×10^{-13}	1.637×10^{-13}
3	174.525	2	2	0.987×10^8	2	1.974×10^{-13}	0.658×10^{-13}
4	174.526	4	2	0.493×10^8	1	0.493×10^{-13}	0.329×10^{-13}



L. G. Piper
 Experimental Determination of the
 Einstein Coefficient for the N(²P-⁴S) Transition
 Figure 1



L. G. Piper
Experimental Determination of the
Einstein Coefficient for the N(²P-⁴S) Transition
Figure 2



L. G. Piper
Experimental Determination of the
Einstein Coefficient for the $\text{N}(^2\text{P}-^4\text{S})$ Transition
Figure 3

APPENDIX 8

Observations on the O/NO Air Afterglow

Observations on the O/NO Air Afterglow

Lawrence G. Piper*
Physical Sciences Inc.
20 New England Business Center
Andover, MA, 01810-1077

ABSTRACT

We have reviewed the literature on the quantitative aspects of the O/NO air afterglow to reconcile conflicts and confusions in the literature. Most previous reports of the relative distribution of intensity as a function of wavelength agree reasonably well for wavelengths shorter than 700 nm. At longer wavelengths, however, consensus on the distribution is lacking. Consequently, we report new measurements of this distribution between 400 and 1750 nm. The absolute values of the O/NO emission rate coefficient have been reported in a variety formats, which renders comparison of the different measurements difficult. We have reanalyzed the previous reports and find a consensus value to be $(1.17 \pm 0.11) \times 10^{-19} \text{ cm}^3 \text{ molecule}^{-1} \text{ s}^{-1} \text{ nm}^{-1}$ at a wavelength of 580 nm and room temperature (300 K). The total rate coefficient integrated over all wavelengths out to 3500 nm is $8.9 \times 10^{-17} \text{ cm}^3 \text{ molecule}^{-1} \text{ s}^{-1}$.

Key Words: air afterglow, chemiluminescence, kinetics, photometry standards

1. INTRODUCTION

The air afterglow has been observed in discharge systems for more than a century, and has been observed in the upper atmospheric night glow for at least half that long. Kaufman¹ reviewed most of the pertinent facts related to the air afterglow about 25 years ago, and more recently, Adler-Golden proposed a model for it.^{2,3} Basically, mixtures of atomic oxygen and nitric oxide combine in an apparent two-body reaction to emit a continuum radiation which extends from about 390 nm out to beyond 3000 nm in the IR. The intensity of this emission is directly proportional to the product of the number densities of atomic oxygen and nitric oxide, and is independent of pressure of bath gas for system pressures greater than about 0.2 Torr:

$$I_{O/NO} = k_{O/NO}[O][NO]. \quad (1)$$

At lower pressures the intensity for constant number densities of O and NO drops off and plateaus to a value about one tenth the high pressure limit for pressures below about a mTorr. Although in the Torr range, the intensity is independent of pressure, it does vary to some extent with the nature of the bath gas. For example, intensities in a helium bath gas are somewhat higher than those in nitrogen; oxygen or argon, all of which are roughly comparable, and, conversely, intensities are somewhat lower in a CO₂ or SF₆ atmosphere.

Since the pioneering observations of Fontijn et al.,⁴ the air afterglow has been used as a quantitative photometric standard in discharge-flow systems, and the validity of a large number of kinetic measurements depend upon the basic accuracy of the air afterglow rate coefficient. In the 20 years subsequent to Fontijn et al.'s publication, at least seven other papers presented values for the air afterglow rate coefficient.⁵⁻¹¹ Direct comparison of the results from the various groups is difficult because the authors have chosen a variety of formats in which to present their results.

Although some have presented an absolute value tied to a particular wavelength, most have reported the integral of the intensity over some wavelength interval, one which generally differs from one paper to another. When we reduced all reported measurements to a value at a common wavelength and temperature, we found that reported values varied by a factor of two and a half. Five of the eight reports, however, are within $\pm 15\%$ of each other.

Reports of the relative intensity of the air afterglow emission as a function of wavelength are reasonably consistent at wavelengths shorter than 700 nm,^{4, 5, 7-12} but diverge considerably at longer wavelengths.^{4-6, 8, 10, 11, 13} Our observations indicate that some of the disagreement may result from systematic errors in the response calibrations of the spectral systems used for the measurements.

The purpose of the present work was to examine the literature to place all reported measurements on a common basis so as to allow us to recommend a consensus value for the air afterglow rate coefficient. In addition, we have measured the variation in the relative intensity of the air afterglow emission as a function of wavelength over the range between 400 and 1750 nm. Our measurements allow us to determine which of the previous measurements are reliable. Since the air afterglow is rather easily generated, its distribution as a function of wavelength has at times been used to provide relative response calibrations for photometric systems. Naturally using an incorrect distribution will result in invalid results. In fact it was our initial inability to obtain reasonable results for our measurements of branching ratios from common upper vibronic levels to various lower ones in the nitrogen first positive system,¹⁴ when we used an air afterglow derived spectrometer response, which prompted this investigation.

2. EXPERIMENTAL

Our measurements of the air afterglow spectral distribution used a 2-in. diameter discharge flow reactor. The apparatus was configured so that the monochromator looked through a CaF₂ window down the axis of the flow reactor without any intervening optics between the monochromator entrance slit and the flow reactor window. This procedure eliminates any distortions to the intensity distribution that might accrue as a result of chromatic aberrations in refractive optical elements. The reactants were prepared and mixed in a side arm of the reactor prior to their flowing into the observation region.

We used a variety of approaches to generate the air afterglow. All techniques involved generating at least one of the free radicals in a microwave discharge. In some instances, both free radicals were generated in the same discharge. The sources included discharging O₂ dilute in Ar or He and adding NO to the discharge effluent; discharging N₂ dilute in Ar or He and adding excess NO, so as to convert all the N atoms generated in the discharge to O atoms with some residual NO remaining; discharging mixtures of O₂ dilute in N₂ or N₂ dilute in O₂; and discharging N₂O dilute in helium.¹⁵ All sources gave the same relative spectral distribution.

The monochromator used was a 0.5 m focal length Minuteman instrument using different grating and detector combinations to cover the wavelength regions 400 to 880 nm and 650 to 1750 nm. At the shorter wavelengths, we used a 1200 g mm⁻¹ grating blazed at 250 nm and a thermoelectrically cooled HTV R-943-02 photomultiplier. Signals were processed using either a photon-counting rate meter or picoammeter. For the longer wavelength region, we used a 300 g mm⁻¹ grating blazed at 1000 nm and a liquid nitrogen cooled intrinsic germanium detector. For these measurements, light from the reactor was chopped prior to its entering the monochromator and a phase sensitive amplifier processed the signals.

The relative response of the monochromator was calibrated by scanning the output of several different radiation standards whose emission was reflected into the monochromator off a diffusely reflecting screen. For our early measurements we used an aluminum plate coated with several millimeters of BaSO₄ as the diffuse reflector, but later on used a Spectralon® target. We used three different quartz halogen lamps with spectral calibrations traceable to the National Institute of Standards and Technology, and, in addition, a 1000°C black body.

3. RESULTS

Relative Spectral Distribution

Figure 1 shows how the intensity of the air afterglow varies as a function of wavelength between 400 and 1750 nm. This distribution results from the average of a number of spectra taken over a 5-yr time period using a variety of excitation methods for generating the air afterglow. Distributions between 400 and 880 nm and 650 and 1750 nm were normalized to give common values between 700 and 850 nm. The relative agreement over this wavelength region was within 2% for the two detector systems.

In general our results for the relative intensity distribution in the visible are reasonably consistent with previous measurements. Ratios of the other distributions to ours are constant, for the most part, to better than $\pm 10\%$ over the wavelength range 450 to 750 nm, although there appear to be some systematic drifts in a few of the ratios. We have plotted these ratios in Figure 2. A completely flat line would correspond to perfect agreement with our results. Prior to making the ratios, the distributions were all normalized to have a common integral value between 450 and 750 nm. The various data sets plotted in Figure 2 have been offset from each other for clarity and error bars illustrating variations of $\pm 5\%$ have been attached to some. Most notable in

the figure is that our results agree with those of Paulsen et al.¹² (curve 2 in Figure 2) and Golomb and Brown⁷ (curve 1) to better than $\pm 2\%$ over the whole wavelength region, and with the results of Woolsey et al.⁸ (curve 3) and Bradburn and Lilenfeld¹¹ (curve 4) to about $\pm 5\%$.

Our measurements indicate the peak in the intensity distribution is shifted slightly to the red compared to some determinations. We find the peak in the distribution to be around 670 nm as compared to the 600 nm reported by Fontijn et al.⁴ (curve 8), Vanpee et al.⁵ (curve 6), Pravilov and Smirnova⁹ (curve 5), and Sutoh et al.¹⁰ (curve 7). Our findings, however, are supported by the other groups reporting this distribution.^{7, 11, 12}

Figure 3 shows the ratio of intensity at each wavelength in the IR region of the spectrum as reported by the various groups to that which we determined plotted as a function of wavelength. The distributions were again normalized to have a common integrated intensity over an appropriate wavelength interval, and have again been offset from each other for clarity. We see that the ratio of the measurements of Vanpee et al.⁵ (curve 4 in Figure 3) and of Bradburn and Lilenfeld¹¹ (curve 3) to ours are nearly constant over the complete wavelength range, showing very good agreement between the distributions determined by the three groups. The general drift downward in the curves related to the data reported by Fontijn et al.⁴ (curve 7), Sutoh et al.¹⁰ (curve 6), and Woolsey et al.⁸ (curve 5) indicate these groups all under determined the amount of radiation in this region.

To the red of 1250 nm, we plot ratios of data from Golde et al.⁶ (curve 2 in Figure 3) and Stair and Kennealy¹³ (curve 1). The fact that the two curves are essentially parallel indicates excellent agreement between the results from these two groups. Their results, however, indicate a systematic variation with respect to ours. This variation might result from some problem in calibration units. We find that if we adjust both sets of data by multiplying by wavelength, the

intensity ratios become constant to about $\pm 2\%$ over the common wavelength region. Such a correction would obtain if the actual plotted distributions had been in units of Watts rather than photon per second.

Interestingly, the data of Sutoh et al. also show this trend to the red of 900 nm. Their distribution between 450 and 900 nm is reasonably consistent with our measurements, but then begins to diverge considerably from ours in the IR. If we weight their published distribution to the red of 900 nm by wavelength, however, their distribution and ours become congruent. Such a discrepancy would be consistent with their having changed calibration units for their IR detector.

While this suggestion of a systematic error is appealing, Golde et al. are quite explicit that their results are in photon units. The distribution of Stair and Kennealy was originally reported to be units of Watts per wavenumber, and we were careful to convert to a consistent set of units. The fact that our results agree excellently with those of Vanpee et al. and with Bradburn and Lilenfeld as well as the fact that our earlier work on the transition moment variation of the nitrogen first positive band system gave reasonable results *only* when the relative monochromator response function used to derive the present data was used, indicates to us that our results are essentially correct.

Table 1 lists our recommended relative distribution as a function of wavelength over the range between 400 and 1750 nm.

Absolute Rate Coefficient

The absolute rate coefficient for the air afterglow has been reported by eight different groups. Unfortunately, inconsistencies in how the various groups reported their results, as well as differences in the conditions employed, make comparison between the various results difficult. We have analyzed each of the results to determine a consensus value for the rate coefficient at a

single wavelength. The rate coefficient at other wavelengths, then, can be determined by multiplying the value at the reference wavelength by the ratio of the intensity from the relative distribution at the desired wavelength to that at the reference wavelength. We have chosen our reference wavelength to be 580 nm. This wavelength corresponds to a peak in the nitrogen-first positive radiation when it is generated by N-atom recombination. It is one of the wavelengths most convenient to use for calibrating optical systems when using the air afterglow technique. We have described our procedures for doing this in some detail previously.¹⁵⁻¹⁷

Fontijn et al.⁴ published the first measurements on the absolute photon yield for the air afterglow reaction. They used an actinometric technique whereby light from the air afterglow was sent through a cell containing a solution of $K_3Fe(C_2O_4)_3$. The light from the reaction converted the ferric ion in solution to ferrous ion, and the final concentration of ferrous ion was subsequently determined spectrophotometrically. The quantum yield for the conversion process as a function of wavelength had been determined previously. These measurements along with their determination of the distribution of intensity of the air afterglow as a function of wavelength led them to report the total air afterglow rate coefficient, integrated over the extent of their spectral distribution, measured by them to be 385 to 1400 nm, as $6.4 \times 10^{-17} \text{ cm}^3 \text{ molecule}^{-1} \text{ s}^{-1}$. Since subsequent observations indicated that they seriously underestimated the intensity of the air afterglow emission at longer wavelengths, this number is generally considered to be low.

Their actinometric measurements were sensitive to the air afterglow only from its onset at 390 nm out to about 510 nm, where the actinometric quantum yield drops off. Thus one can expect reasonable accuracy for their value at shorter wavelengths. By multiplying their total rate coefficient by the ratio of their relative intensity in a one nanometer interval around

580 nm to the integral over the intensity distribution they published, we find that their measurements indicate a value for the air afterglow rate coefficient at 580 nm of $1.36 \times 10^{-19} \text{ cm}^3 \text{ molecule}^{-1} \text{ s}^{-1} \text{ nm}^{-1}$.

Vanpee et al.⁵ investigated the air afterglow in a free jet expansion of O and NO. They characterized the jet's physical characteristics and used a photometric system they had calibrated against several tungsten ribbon lamps. They also demonstrated that the O/NO intensity distribution extended out to at least 2000 nm. Their published result was $6.8 \times 10^{-17} \text{ cm}^3 \text{ molecule}^{-1} \text{ s}^{-1}$ over the wavelength range between 385 and 2000 nm and at a temperature of 367 K. In order to compare their results with others, one must not only correct for a different wavelength range, but also for a different temperature. Golomb and Brown⁷ report a temperature dependence which incorporates not only their own measurements but also those of several other groups. Using this value to correct Vanpee et al.'s measurements to 300 K, and further correcting the Vanpee et al. value to our reference wavelength, results in a rate coefficient at 580 nm of $1.59 \times 10^{-19} \text{ cm}^3 \text{ molecule}^{-1} \text{ s}^{-1} \text{ nm}^{-1}$.

Golde et al.⁶ investigated the air afterglow in the IR between 1280 and 3300 nm. They calibrated their optical system absolutely against a black body source and determined that the rate coefficient for the air afterglow emission at 1510 nm was $2.4 \times 10^{-20} \text{ cm}^3 \text{ molecule}^{-1} \text{ s}^{-1} \text{ nm}^{-1}$. If we multiply this value by the ratio of intensity at 580 nm to that at 1510 nm, as determined in this work, we find a value for the air afterglow rate coefficient at 580 nm of $1.16 \times 10^{-19} \text{ cm}^3 \text{ molecule}^{-1} \text{ s}^{-1} \text{ nm}^{-1}$.

Golomb and Brown⁷ conducted an extensive series of measurements on the air afterglow emission rate coefficient as a function of temperature and pressure. They used standard radiance

sources to calibrate their optical system. They reported a rate coefficient of $3.7 \times 10^{-17} \text{ cm}^3 \text{ molecule}^{-1} \text{ s}^{-1}$ over the wavelength range between 400 and 800 nm at 300 K. This translates to a value of $1.14 \times 10^{-19} \text{ cm}^3 \text{ molecule}^{-1} \text{ s}^{-1} \text{ nm}^{-1}$ at 580 nm.

Woolsey et al.⁸ developed a novel radiation calibration source which mimicked the geometry one would observe when looking along the axis of a discharge flow reactor.¹⁸ They used this to calibrate their optical system and subsequently measured rate coefficients for the air afterglow emission rate at a number of wavelengths between 530 and 1400 nm. Their results give a value of $0.72 \times 10^{-19} \text{ cm}^3 \text{ molecule}^{-1} \text{ s}^{-1} \text{ nm}^{-1}$ at 580 nm.

Pravilov and Smirnova⁹ measured the absolute air afterglow rate coefficient between 430 and 630 nm, but reported a value of $8.0 \times 10^{-17} \text{ cm}^3 \text{ molecule}^{-1} \text{ s}^{-1}$ over the wavelength range between 395 and 2000 nm at 300 K. They reported a relative intensity distribution between 400 and about 950 nm, and extended the distribution into the IR using the distribution Vanpee et al. had published. Using their composite curve, we infer a value from their data of $1.27 \times 10^{-19} \text{ cm}^3 \text{ molecule}^{-1} \text{ s}^{-1} \text{ nm}^{-1}$ at 580 nm. This measurement, however, was made in a helium buffer gas which has a slightly higher third body efficiency than does oxygen, nitrogen, or argon, all of which produce similar air afterglow intensities given comparable concentrations of O and NO in one's reactor. Kaufman's review¹ indicates an enhancement over argon as a third body of 1.21 ± 0.04 . Making this correction leads to a value for the air afterglow rate coefficient of $1.05 \times 10^{-19} \text{ cm}^3 \text{ molecule}^{-1} \text{ s}^{-1} \text{ nm}^{-1}$.

Sutoh et al.¹⁰ measured the absolute value of the air afterglow rate coefficient at 562 nm using a photometer for a detector (essentially an interference filter/photomultiplier combination with a carefully controlled field of view). They calibrated their photometer using an absolute

brightness standard. Their result was $1.07 \times 10^{-19} \text{ cm}^3 \text{ molecule}^{-1} \text{ s}^{-1} \text{ nm}^{-1}$ at 562 nm which translates to a value of $1.14 \times 10^{-19} \text{ cm}^3 \text{ molecule}^{-1} \text{ s}^{-1} \text{ nm}^{-1}$ at 580 nm.

Finally Bradburn and Lilenfeld¹¹ compared the intensity of the air afterglow emission at 1270 nm produced by known concentrations of O and NO with the intensity of emission from O₂ (a $^1\Delta_g$) when known concentrations of singlet oxygen were in their reactor. They measured the singlet oxygen via EPR for which an absolute calibration could be determined by comparing singlet oxygen signals with those produced by known concentrations of normal, ground state, triplet oxygen. Using the widely accepted value for the radiative lifetime for O₂ (a $^1\Delta_g$) of 64 min,¹⁹ they could place their fluorescence measurements on an absolute basis. Their result, $0.62 \times 10^{-19} \text{ cm}^3 \text{ molecule}^{-1} \text{ s}^{-1} \text{ nm}^{-1}$ at 1270 nm, translates to a value of $1.86 \times 10^{-19} \text{ cm}^3 \text{ molecule}^{-1} \text{ s}^{-1} \text{ nm}^{-1}$ at 580 nm. The accuracy of this value, naturally, depends upon the accuracy of the lifetime for O₂ (a $^1\Delta_g$). We discuss this issue below.

Table 2 summarizes the values for the air afterglow rate coefficient at 580 nm and room temperature we have determined from analyzing the results of each group. The data divide into roughly three ensembles. Five of the groups obtained results which are remarkably consistent, two reports are considerably higher than the bulk of the measurements, while Woolsey et al.'s determination is much lower than any of the other reported values. An average of the results of Fontijn, et al., Golde et al., Golomb and Brown, Pravilov and Smirnova, and Sutoh et al. yields a value of $(1.17 \pm 0.11) \times 10^{-19} \text{ cm}^3 \text{ molecule}^{-1} \text{ s}^{-1} \text{ nm}^{-1}$ at 580 nm, where the error bar represents one standard deviation. All of the measurements included in the average are within two standard deviations from the mean, whereas the other three values are all four or more standard deviations removed from this mean value.

4. DISCUSSION

Most of the determinations of the absolute rate coefficient for the air afterglow depend upon calibrations determined by comparison with standard lamps. Such calibrations are straightforward in principle, but are often difficult to implement in practice. The reason for this is that the geometry of the optical system is generally quite different when viewing an extended source such as the air afterglow compared to a compact filament of a standard lamp. The generally good agreement between most of the groups using such calibration procedures indicates their geometrical corrections have been handled correctly.

Of the two measurements which do not use direct comparison with a standard photometric source, one agrees well with the bulk of the observations while the other does not. Fontijn et al.'s determination was, in effect, subsequently confirmed by Fontijn and Lee²⁰ using a second chemiluminescent comparison. That is to say, they "calibrated" an optical system using the air afterglow and using the phosphorescence from the liquid luminol reaction, whose quantum yield had been established previously by several groups, and obtained calibration factors agreeing within 10%.

As we mentioned above, the determination of Bradburn and Lilenfeld depends on the validity of the Einstein coefficient for spontaneous emission from O₂ (a ¹Δ_g). For 30 years the value reported by Badger et al., $2.58 \times 10^4 \text{ s}^{-1}$, was accepted without serious question, although several estimates based on aeronomic observations tended to favor a somewhat lower value.²¹ The remeasurement of this value by Lin et al.,²² which was subsequently superceded by a more careful measurement from the same group by Hsu et al.,²³ appeared to confirm Badger et al.'s measurement. Mlynczak and Nesbitt,²¹ however, showed that Lee et al. and Hsu et al. converted their line strength data into a band Einstein coefficient incorrectly when they used the wrong

value for a degeneracy ratio between ground and excited states of the transition. When the proper degeneracy ratio is used, the Einstein coefficient inferred from Hsu et al.'s data is actually $1.47 \times 10^{-4} \text{ s}^{-1}$.

Using this corrected value for the O_2 ($a^1\Delta_g$) Einstein coefficient to analyze the measurements of Bradburn and Lilenfeld would result in a value of the air afterglow rate coefficient at 580 nm of $1.04 \times 10^{-19} \text{ cm}^3 \text{ molecule}^{-1} \text{ s}^{-1} \text{ nm}^{-1}$, in agreement with the bulk of the measurements listed in Table 1. Alternatively, if one considers the value for the air afterglow rate coefficient we propose here to be correct, then one could look upon Bradburn and Lilenfeld's work as essentially an alternative measurement of the Einstein coefficient for spontaneous radiation from O_2 ($a^1\Delta_g$). One would then derive a value of $1.65 \times 10^{-4} \text{ s}^{-1}$ for this transition probability, agreeing within 12% with the re-analyzed Hsu et al. value, and, thereby, confirming Mlynczak and Nesbitt's contention that the long accepted value of Badger et al. is indeed incorrect. This issue is still a contentious one in the aeronomic community.²⁴

The air afterglow rate coefficient integrated over the wavelength range studied here, 400 to 1750 nm, is $8.15 \times 10^{-17} \text{ cm}^3 \text{ molecule}^{-1} \text{ s}^{-1}$. If we normalize the relative distribution reported by Golde et al. to ours at 1650 nm, we can integrate the rate coefficient out to 3500 nm. This results in a total rate coefficient for emission in the recombination of O with NO of $8.9 \times 10^{-17} \text{ cm}^3 \text{ molecule}^{-1} \text{ s}^{-1}$. This value agrees excellently with the $9.4 \times 10^{-17} \text{ cm}^3 \text{ molecule}^{-1} \text{ s}^{-1}$ proposed by Golde et al. from a combination of their results in the IR with those of Fontijn et al. in the visible.

5. ACKNOWLEDGMENTS

We thank Karl Holtzclaw and Terry Rawlins for providing some much needed insight and Tom Tucker for help digitizing the various published distributions. We appreciate partial financial support from the Air Force Office of Scientific Research (Task 2310G4) and Defense Nuclear Agency (Project SA, Task SA/SDI, work unit 00175) from a contract with the Phillips Laboratory/Geophysics Directorate under contract nos. F19628-88-C-00173 and F19628-93-C-0046.

6. REFERENCES

1. F. Kaufman, in *Chemiluminescence and Bioluminescence*, M.J. Cormier, D.M. Hercules, and J. Lee, eds., New York, Plenum Publishing Corp., pp. 83-100, 1973.
2. S.M. Adler-Golden, *J. Phys. Chem.* 93 (1989) 684.
3. S.M. Adler-Golden, *J. Phys. Chem.* 93 (1989) 691.
4. A. Fontijn, C.B. Meyer, and H.I. Schiff, *J. Chem. Phys.* 40 (1964) 64.
5. M. Vanpee, K.C. Hill, and W.R. Kineyko, *AIAA J.* 9 (1971) 135.
6. M.F. Golde, A.E. Roche, and F. Kaufman, *J. Chem. Phys.* 59 (1973) 3953.
7. D. Golomb and J.H. Brown, *J. Chem. Phys.* 63 (1975) 5246.
8. G.A. Woolsey, P.H. Lee, and W.D. Slafer, *J. Chem. Phys.* 67 (1977) 1220.
9. A.M. Pravilov and L.G. Smirnova, *Kinet. Catal. (USSR)* 19 (1978) 202.
10. M. Sutoh, Y. Morioka, and M. Nakamura, *J. Chem. Phys.* 72 (1980) 20.
11. G. Bradburn and H.V. Lilienfeld, *J. Phys. Chem.* 92 (1988) 5266.
12. D.E. Paulsen, W.F. Sheridan, and R.E. Huffman, *J. Chem. Phys.* 53 (1970) 647.
13. A.T. Stair, Jr. and J.P. Kennealy, *J. de Chim. Phys.* 64 (1967) 124.

14. L.G. Piper, K.W. Holtzclaw, B.D. Green, and W.A.M. Blumberg, *J. Chem. Phys.* 90 (1989) 5337.
15. L.G. Piper and W.T. Rawlins, *J. Phys. Chem.* 90 (1986) 320.
16. L.G. Piper, G.E. Caledonia, and J.P. Kennealy, *J. Chem. Phys.* 75 (1981) 2847.
17. L.G. Piper, *J. Chem. Phys.* 88 (1988) 231.
18. P.H. Lee, G.A. Woolsey, and W.D. Slafer, *Appl. Opt.* 15 (1976) 2825.
19. R.M. Badger, A.C. Wright, and R.F. Whitlock, *J. Chem. Phys.* 43 (1965) 4345.
20. A. Fontijn and J. Lee, *J. Opt. Soc. Amer.* 62 (1972) 1095.
21. M.G. Mlynczak and D.J. Nesbitt, *Geophys. Res. Lett.* 22 (1995) 1381 and references therein.
22. L.B. Lin, Y.P. Lee, and J.F. Ogilvie, *J. Quant. Spectrosc. Radiat. Transfer* 39 (1988) 375.
23. Y.T. Hsu, Y.P. Lee, and J.F. Ogilvie, *Spectrochim. Acta* 9 (1992) 1227.
24. B.J. Sandor, R.T. Clancy, D.W. Rusch, C.E. Randall, R.S. Eckman, D.S. Siskind, and D.O. Muhleman, *J. Geophys. Res.* 102 (1997) 9013.

Table 1. Distribution of Air Afterglow Intensities as a Function of Wavelength

Wavelength (nm)	Relative Intensity	Absolute Rate Coefficient ($10^{-19} \text{ cm}^3 \text{ molecule}^{-1} \text{ s}^{-1} \text{ nm}^{-1}$)
400	1.3	0.02
410	4.1	0.05
420	7.4	0.09
430	12.6	0.15
440	17.5	0.22
450	22.5	0.28
460	29.0	0.36
470	36.5	0.45
480	44.2	0.54
490	50.1	0.62
500	56.8	0.70
510	63.1	0.78
520	70.4	0.87
530	74.4	0.92
540	80.4	0.99
550	84.5	1.04
560	88.5	1.09
570	92.0	1.13
580	95.1	1.17
590	97.8	1.20
600	100.0	1.23
610	101.9	1.25
620	103.4	1.27
630	104.6	1.29
640	105.4	1.30
650	105.9	1.30
660	106.2	1.31
670	106.2	1.31
680	105.9	1.30
690	105.4	1.30
700	104.7	1.29
710	103.8	1.28
720	102.7	1.26
730	101.5	1.25

Table 1. Distribution of Air Afterglow Intensities as a Function of Wavelength (Continued)

Wavelength (nm)	Relative Intensity	Absolute Rate Coefficient ($10^{-19} \text{ cm}^3 \text{ molecule}^{-1} \text{ s}^{-1} \text{ nm}^{-1}$)
740	100.0	1.23
750	98.6	1.21
760	96.6	1.19
770	94.6	1.16
780	92.5	1.14
790	90.4	1.11
800	88.3	1.09
810	86.1	1.06
820	84.0	1.03
830	81.9	1.01
840	79.7	0.98
850	77.6	0.95
860	75.5	0.93
870	73.4	0.90
880	72.5	0.89
890	70.9	0.87
900	69.2	0.85
950	61.7	0.76
1000	55.2	0.68
1050	49.5	0.61
1100	44.6	0.55
1150	40.3	0.50
1200	36.5	0.45
1250	33.2	0.41
1300	30.3	0.37
1350	27.6	0.34
1400	25.1	0.31
1450	22.6	0.28
1500	20.2	0.25
1550	17.7	0.22
1600	15.3	0.19
1650	14.3	0.18
1700	13.1	0.16
1750	12.2	0.15

Table 2. Determinations of the Absolute Air Afterglow Rate Coefficient
at 580 nm and 300 K

Group	Year	Absolute Rate Coefficient ($10^{-19} \text{ cm}^3 \text{ molecule}^{-1} \text{ s}^{-1} \text{ nm}^{-1}$)
Fontijn et al. ⁴	1964	1.36
Vanpee et al. ⁵	1971	1.59
Golde et al. ⁶	1973	1.16
Golomb and Brown ⁷	1975	1.14
Woolsey et al. ⁸	1977	0.72
Pravilov and Smirnova ⁹	1978	1.05
Sutoh et al. ¹⁰	1980	1.14
Bradburn and Lilienfeld ¹¹	1988	1.86

Figure Captions

1. Relative distribution of the intensity of the air afterglow as a function of wavelength.
2. Ratio of the air afterglow intensity distributions between 420 and 900 nm reported in the literature to that determined in this work. The curves have been offset from each other for clarity. The bars on some of the distributions represent variations of $\pm 5\%$ in the ratios. The numbered curves are as follows: 1 - Golomb and Brown⁷; 2 - Paulsen et al.¹²; 3 - Woolsey et al.⁸; 4 - Bradburn and Lilenfeld¹¹; 5 - Pravilov and Smirnova⁹; 6 - Vanpee et al.⁵; 7 - Sutoh et al.¹⁰; and 8 - Fontijn et al.⁴
3. Ratio of the air afterglow intensity distributions between 800 and 1800 nm reported in the literature to that determined in this work. The curves have been offset from each other for clarity. The bars on some of the distributions represent variations of $\pm 5\%$ in the ratios. The numbered curves are as follows: 1 - Stair and Kennealy¹³; 2 - Golde et al.⁶; 3 - Bradburn and Lilenfeld¹¹; 4 - Vanpee et al.⁵; 5 - Woolsey et al.⁸; 6 - Sutoh et al.¹⁰; and 7 - Fontijn et al.⁴

Figure 1

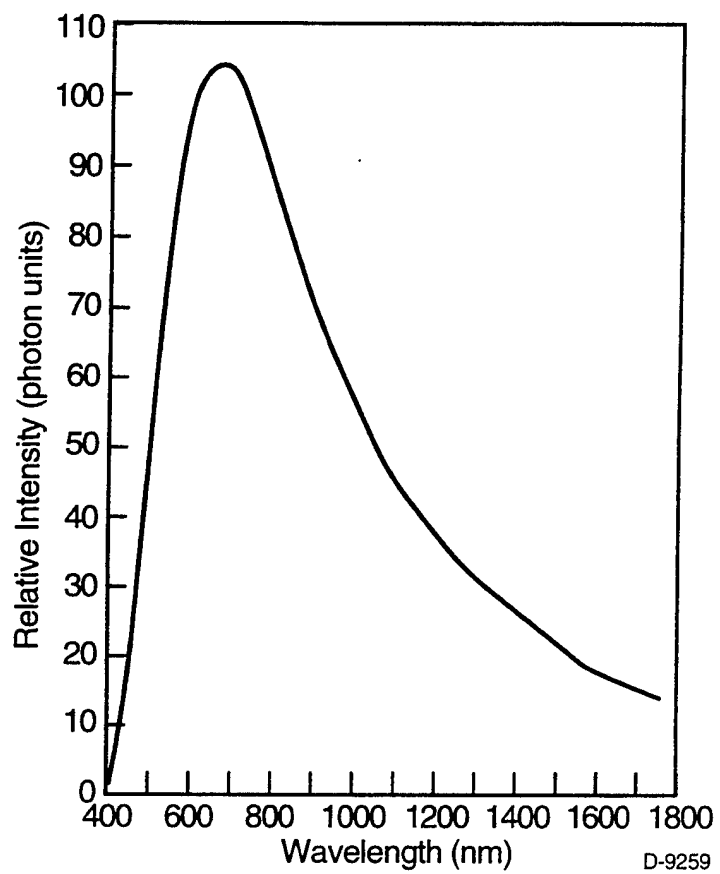


Figure 2

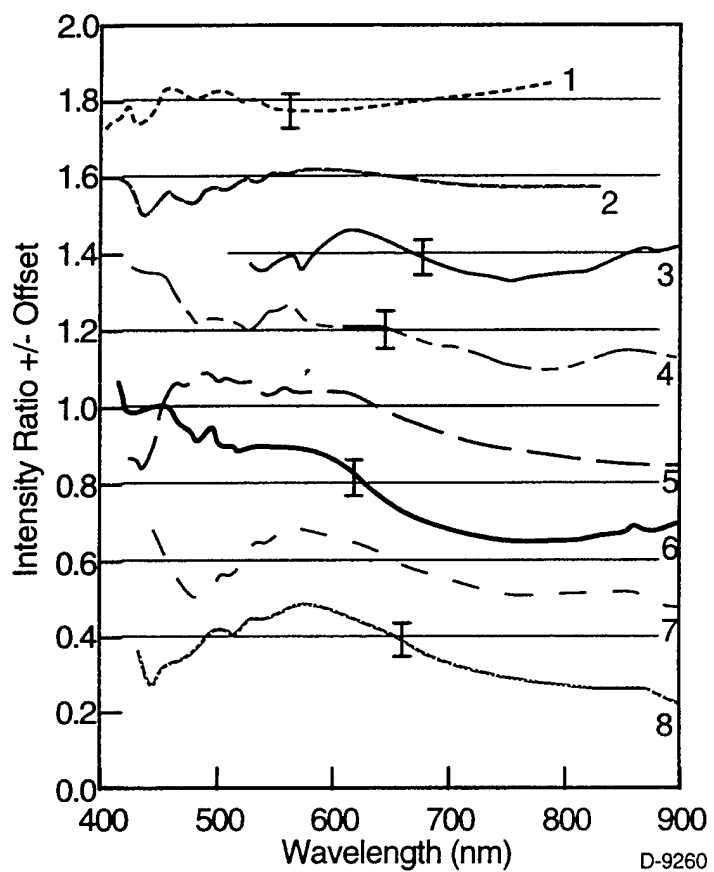
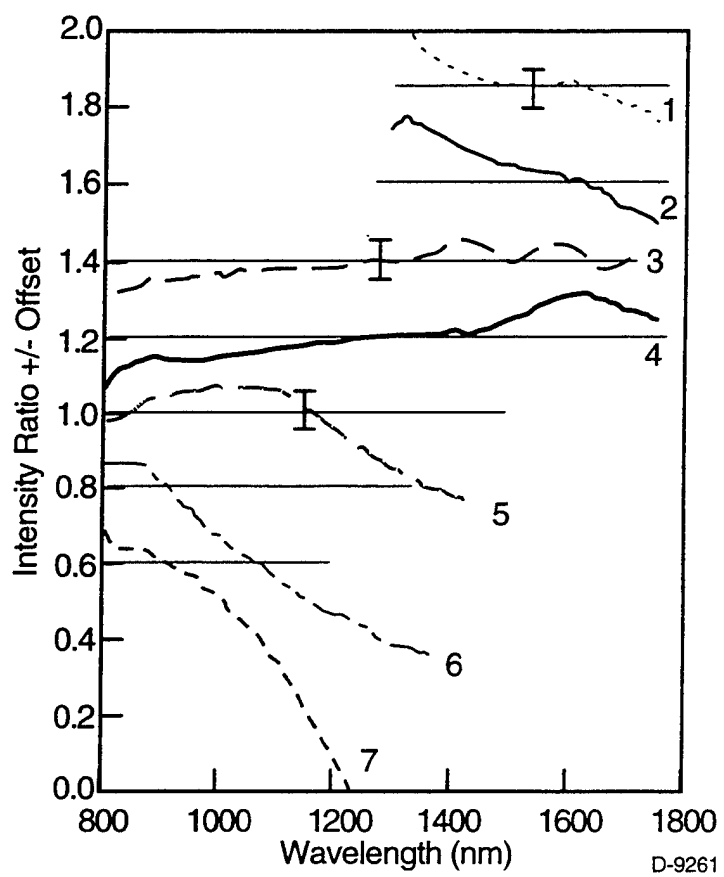


Figure 3



APPENDIX 9

CIRRIS 1A Ozone Airglow Analysis

CIRRIS 1A OZONE AIRGLOW ANALYSES

**B.D. Green and W.T. Rawlins
Physical Sciences Inc.**

CIRRIS 1A Program Review

9 September 1993

OBJECTIVES

T-17835

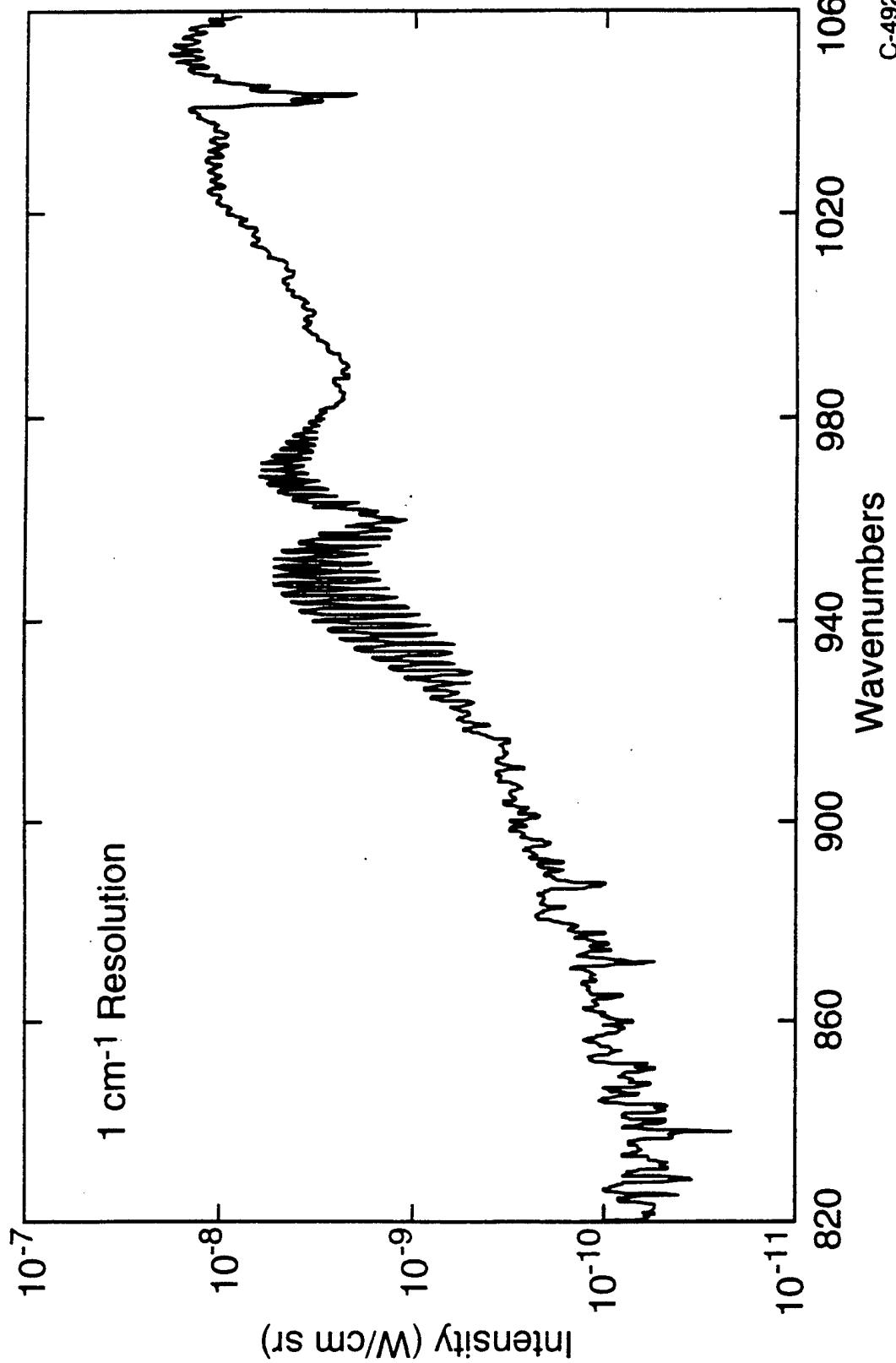
- Quantify global variability of ozone airglow and thermal radiances
 - Radiance profiles
 - Excitation mechanisms
- Determine internal vibrational energy distributions
 - Comparison to previous atmospheric measurements
- Develop adequate internal state description
- Improve profiles, distributions, and relaxation rates to permit model refinement

CURRENT STATUS

T-17836

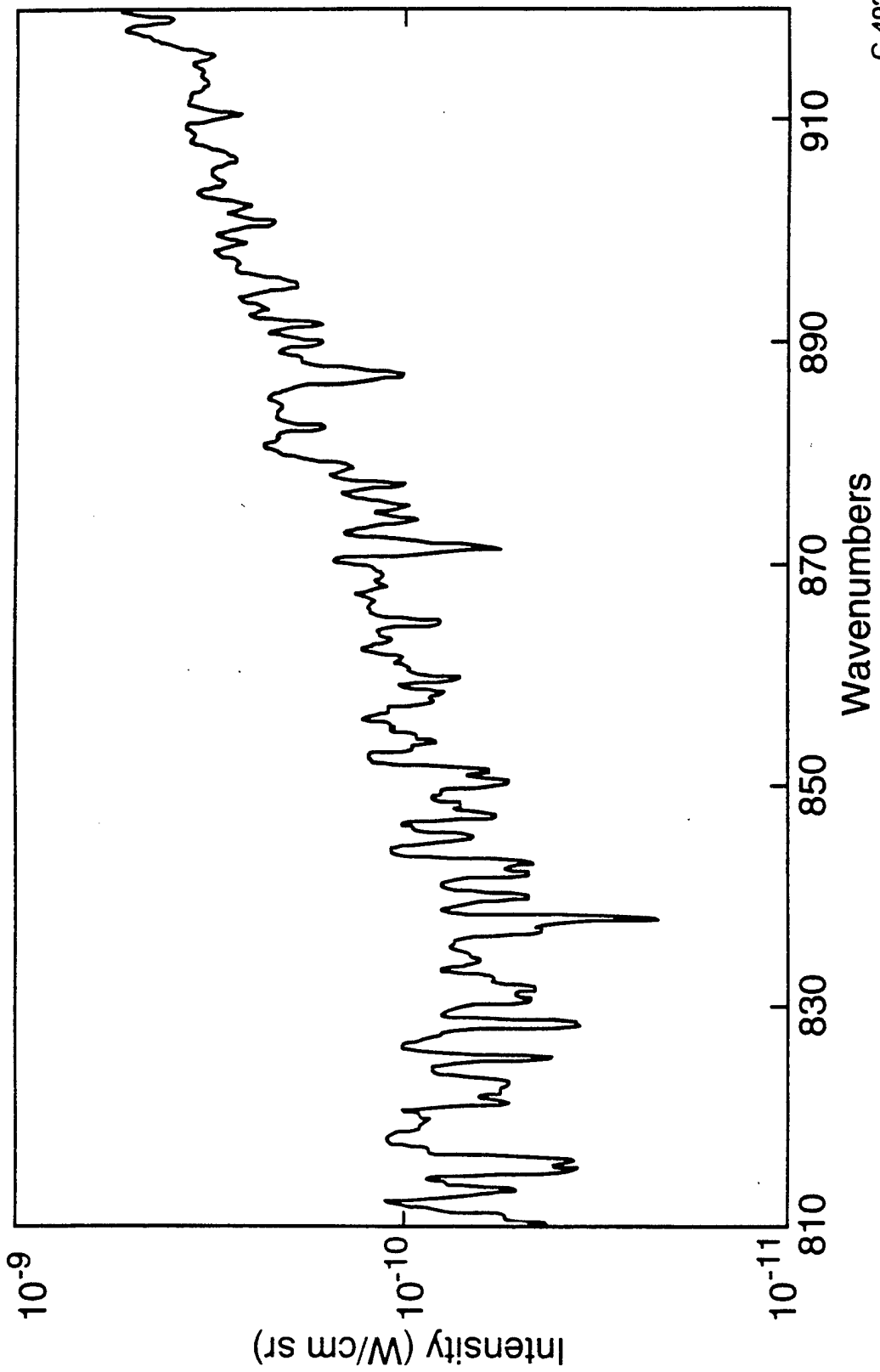
- Exercised analysis techniques on small portion of CIRRIS 1A database
 - Spectral smoothing and manipulation
 - Spectral fitting
 - Using ν_3 only (7 band)
 - Using ν_1, ν_3 coupled dyads (101,002; 102,003;,...) (7 band)
 - Using ν_1, ν_3 and ν_2, ν_3 coupled dyads (101,002; 012,111;,...) (12 band)
- Assessment of altitude and spectral range of data
- Preliminary determination of
 - Internal states populated
 - Altitude profiles
- Preliminary comparison with SPIRE and model

CIRRIS 1A SCAN 11E0239
74 km TH, 60 N, 67 SZA, 9-pt smooth

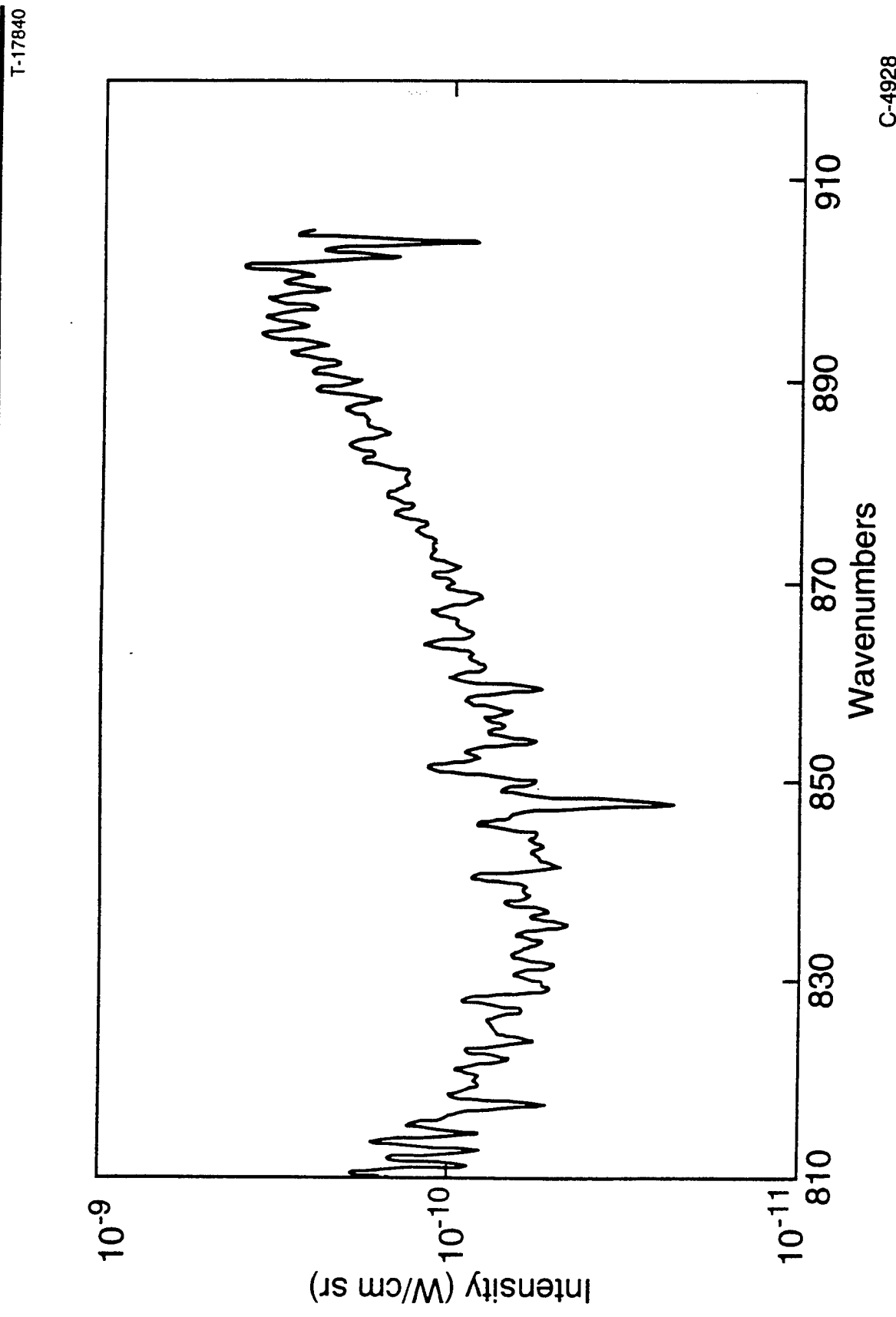


CIRRIS 1A SCAN 11E0239
74 km altitude, 9-pt smooth

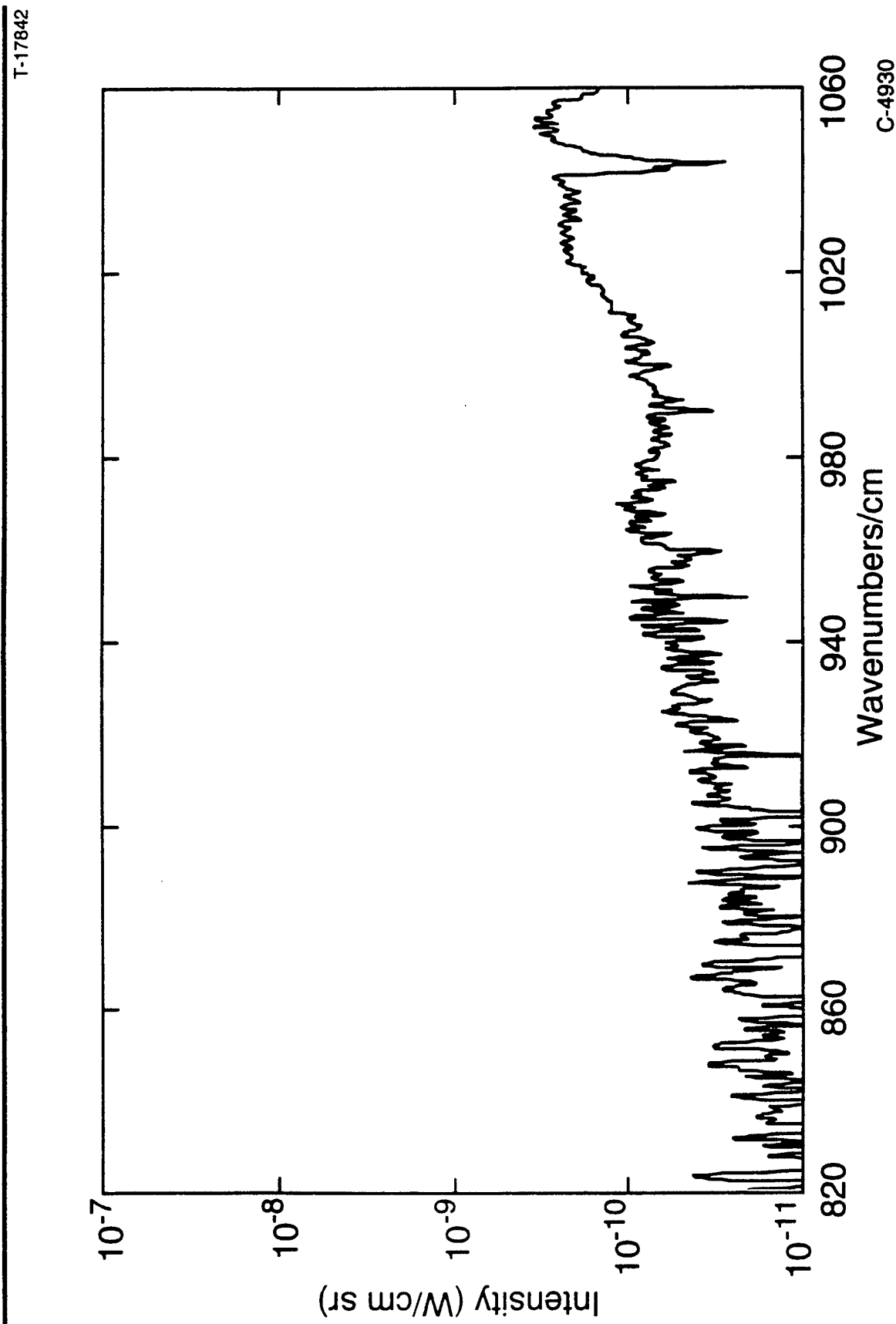
T-17839



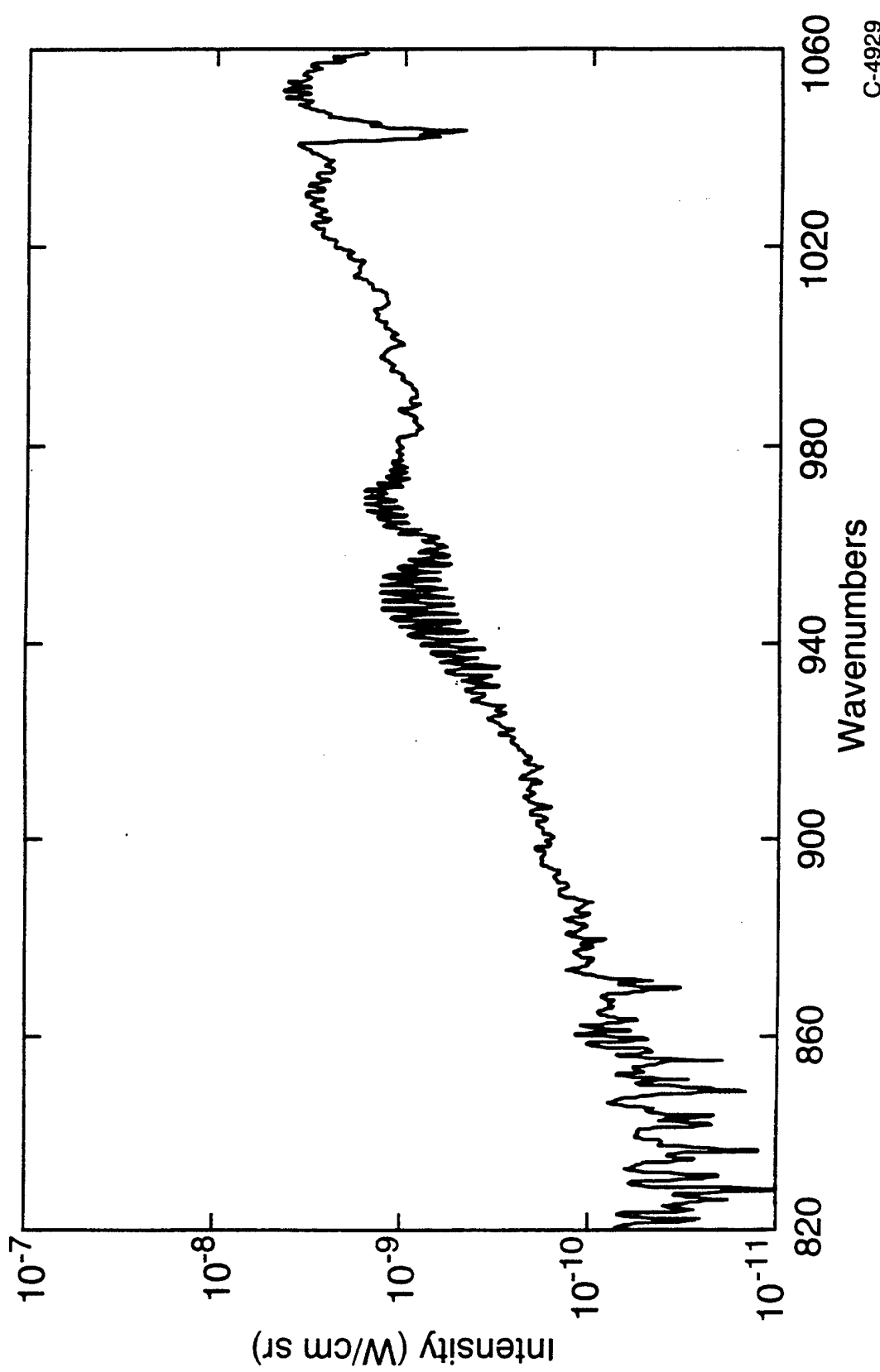
CIRRIS 1A SCAN 11F1023
71 km TH, 68 N, SZA 54, 9-pt smooth



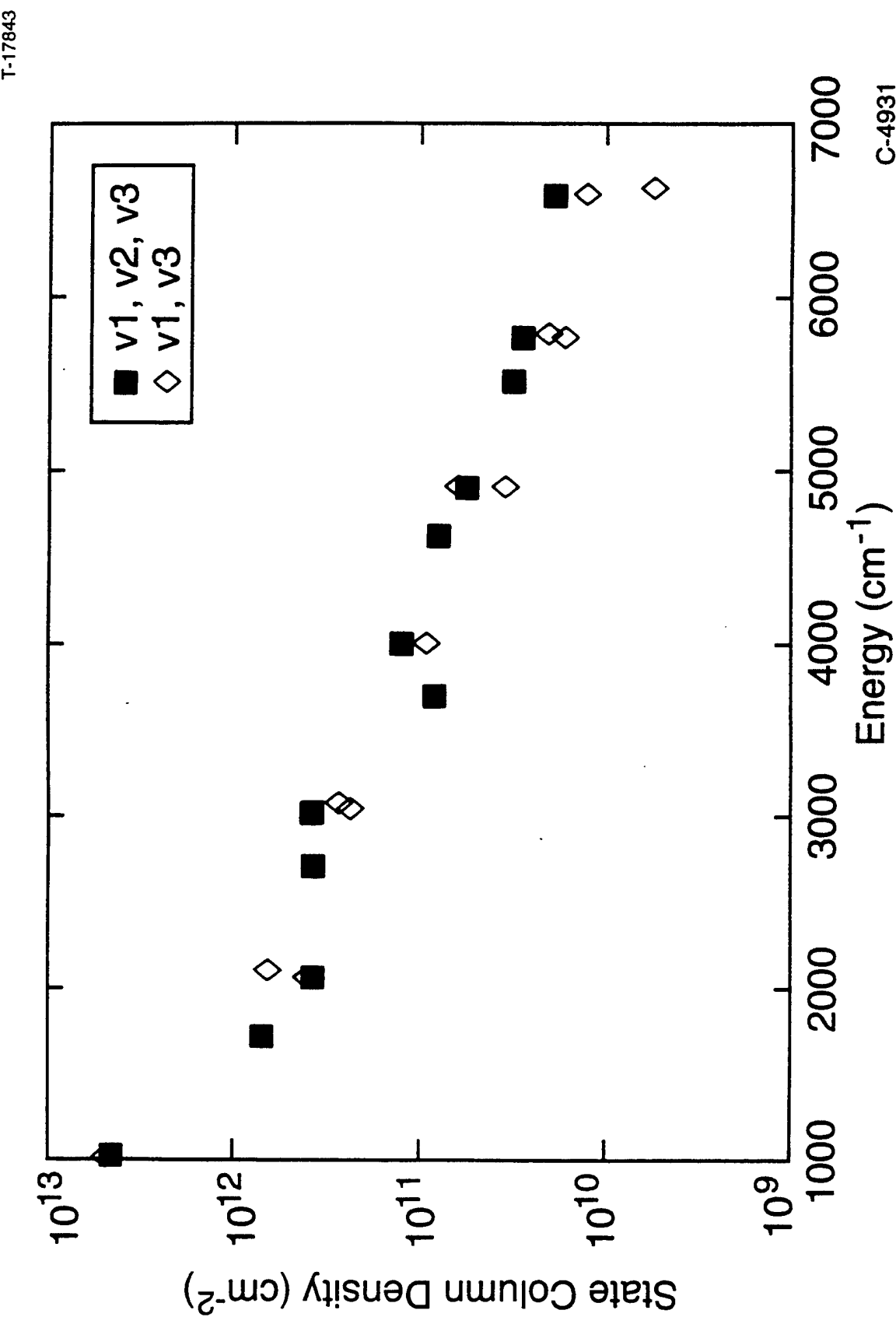
CIRRIS 1A SCAN 11E0261
97.7 km, 62 N, SZA 63, 9-pt smooth



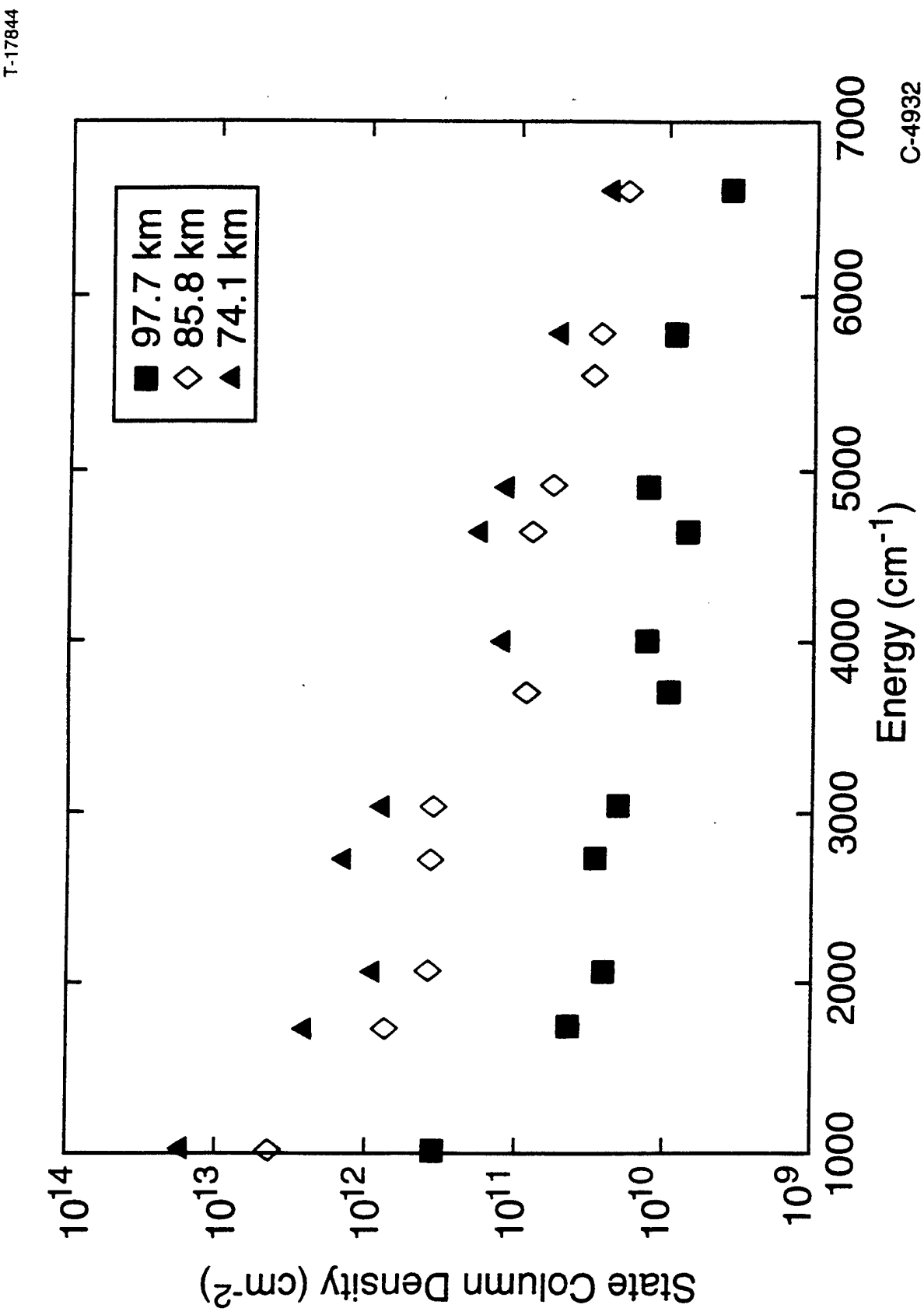
CIRRIS 1A SCAN 11E0250
86 km TH, 61 N, 65 SZA, 9-pt smooth



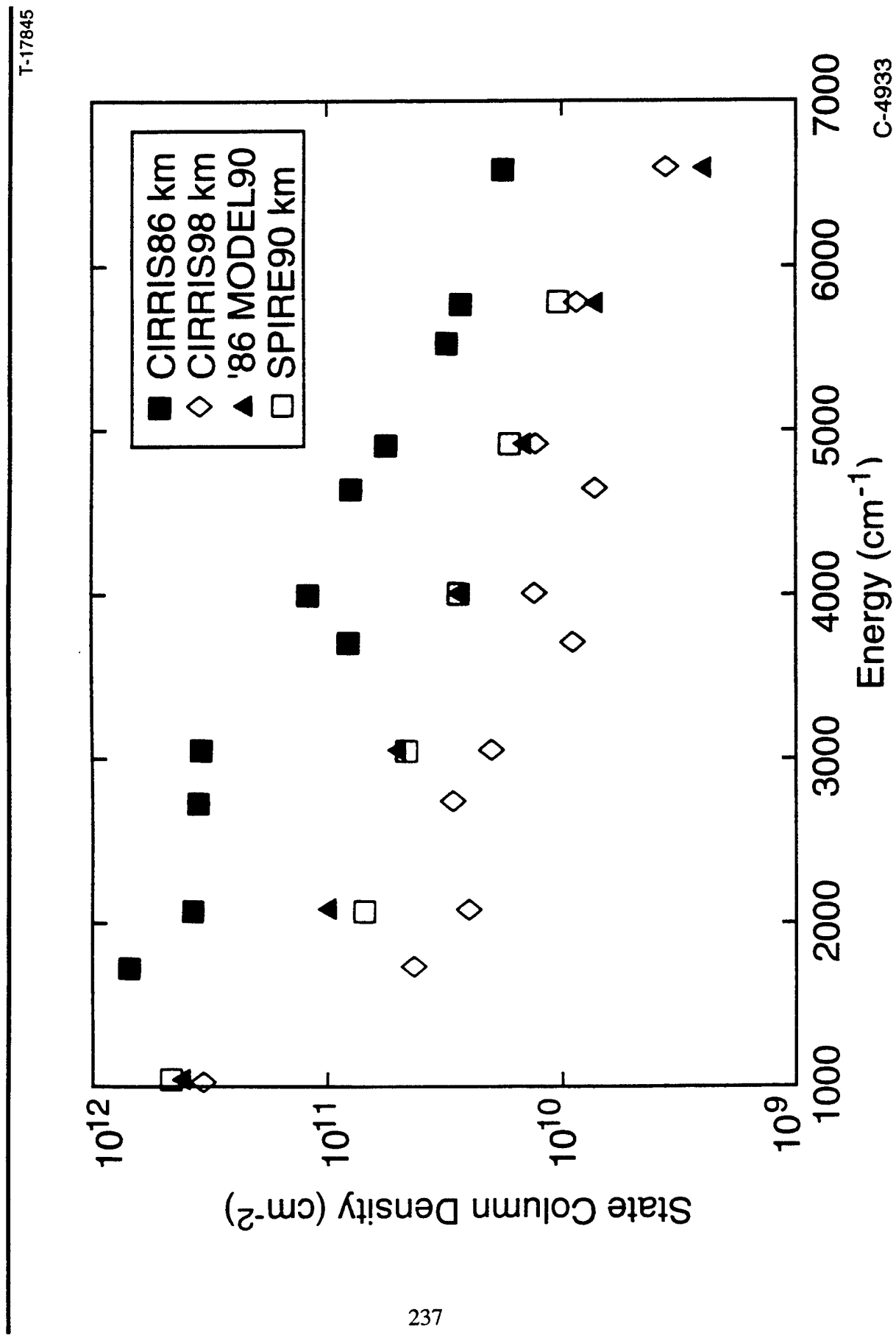
CIRRIS 1A OZONE \tilde{V}_3 DISTRIBUTIONS (86 km)



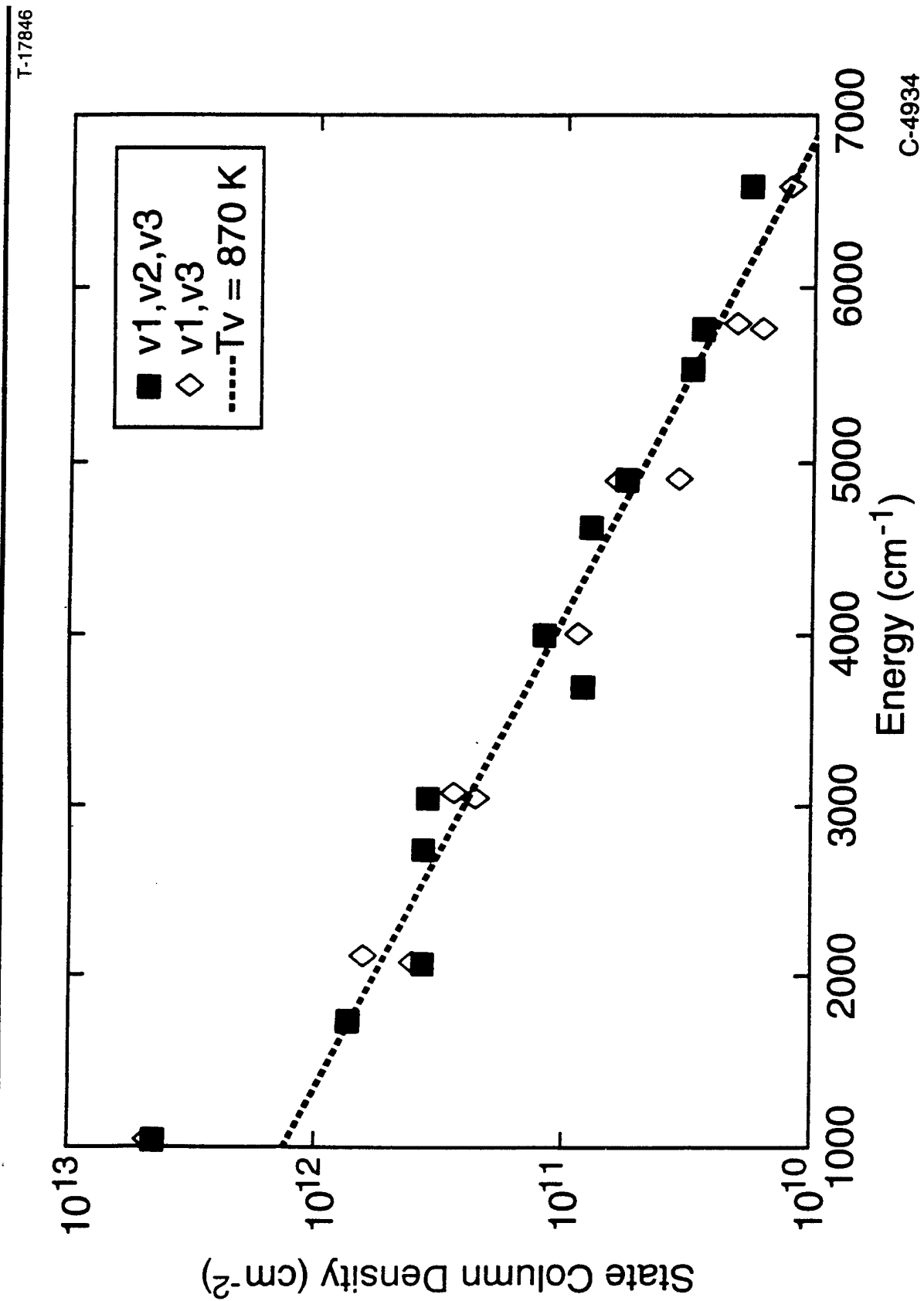
CIRRIS 1A OZONE \tilde{V}_3 DISTRIBUTIONS



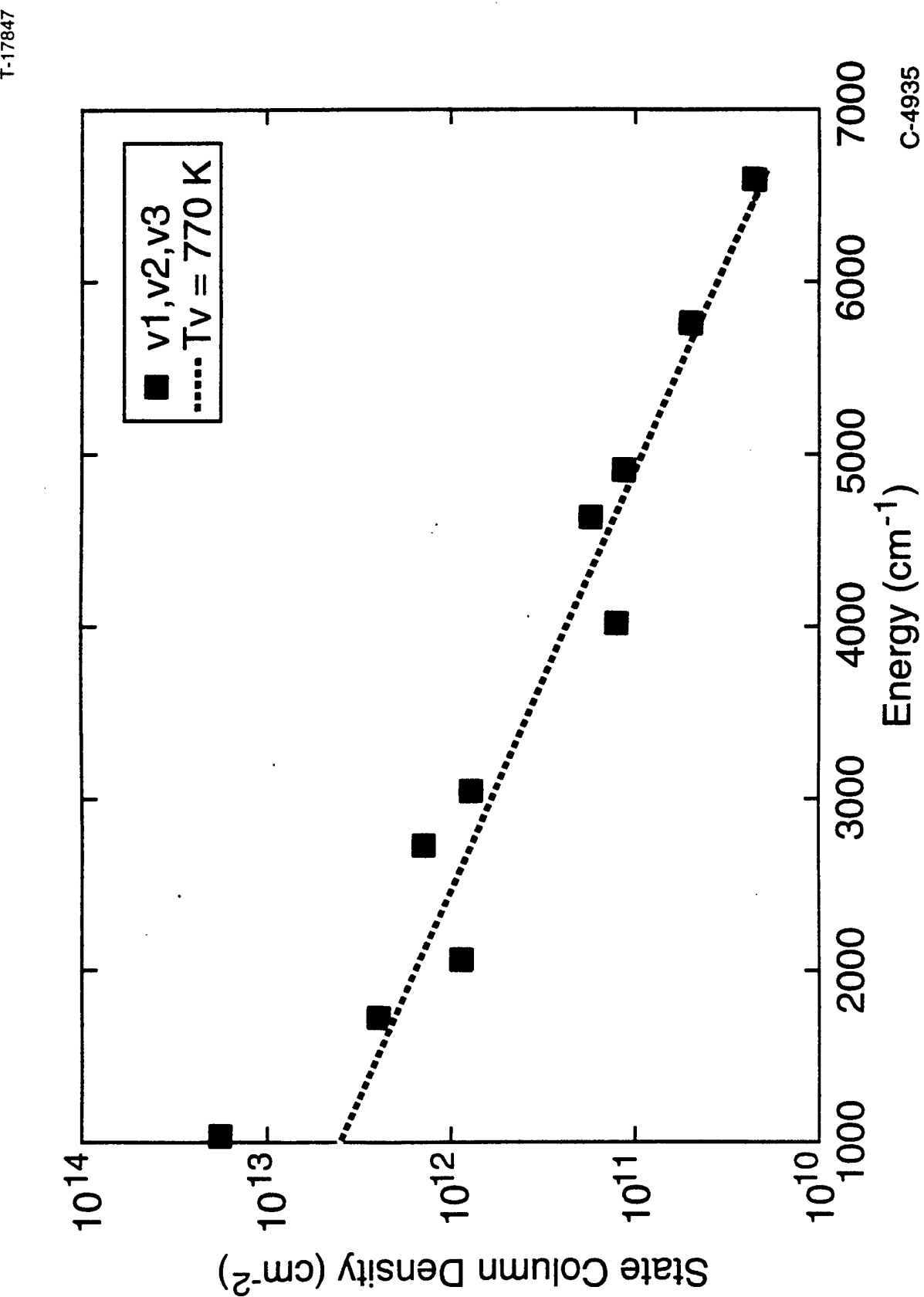
OZONE \tilde{V}_3 DISTRIBUTIONS



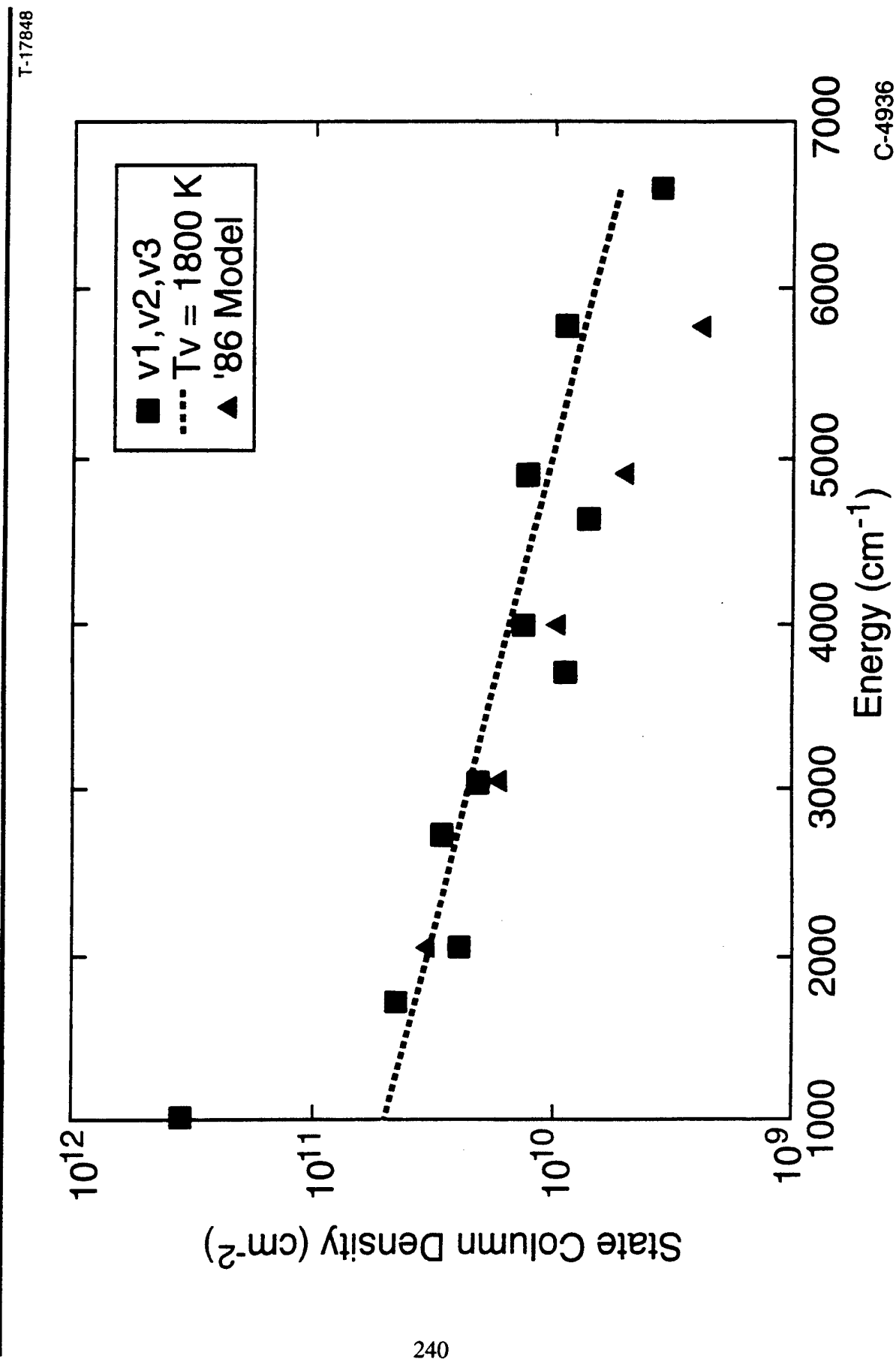
CIRRIS 1A OZONE \tilde{V}_3 DISTRIBUTIONS (86 km)



CIRRIS 1A OZONE \tilde{V}_3 DISTRIBUTIONS (74 km)

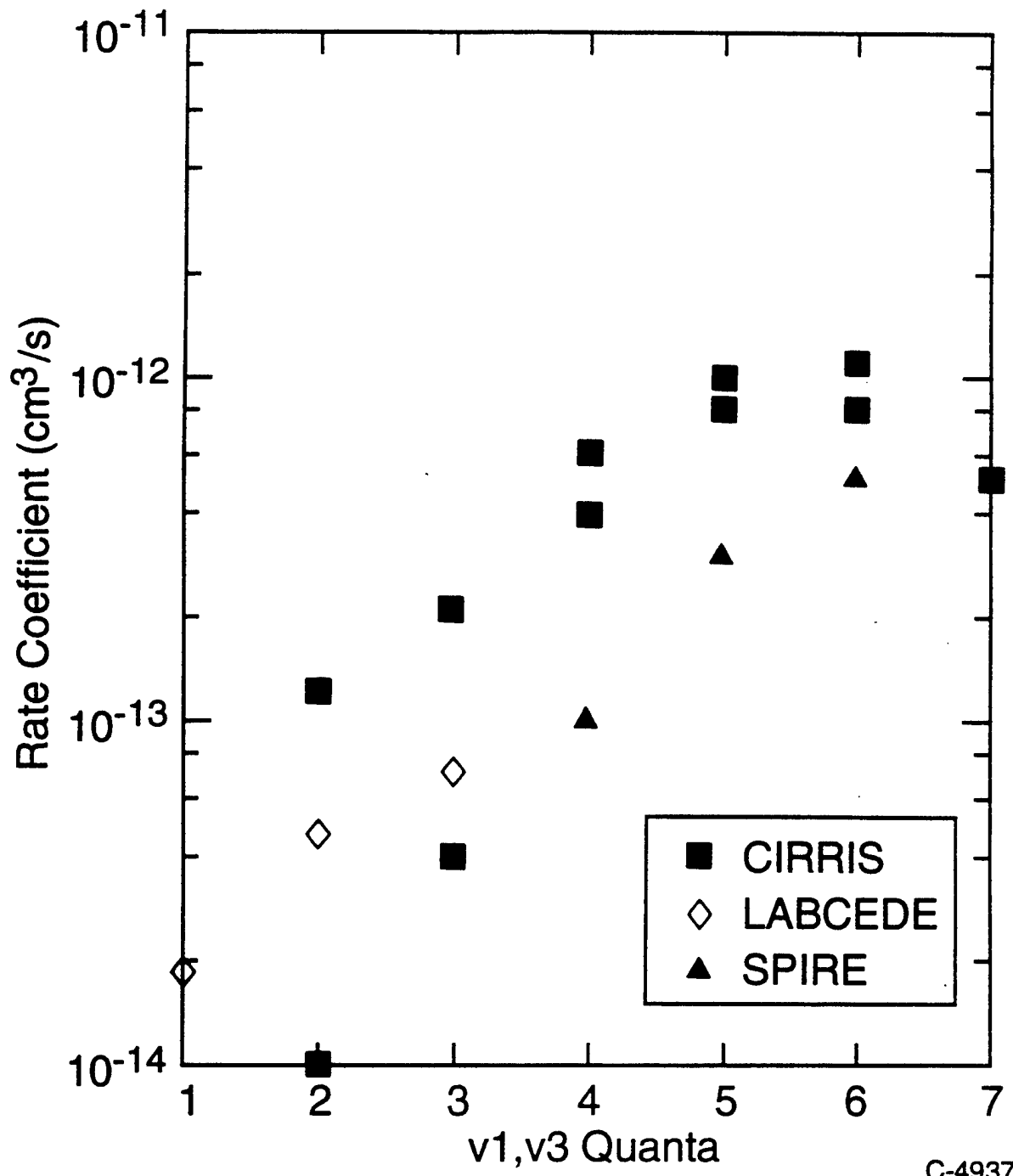


CIRRIS 1A O₃ \tilde{V}_3 DISTRIBUTIONS (98 km)



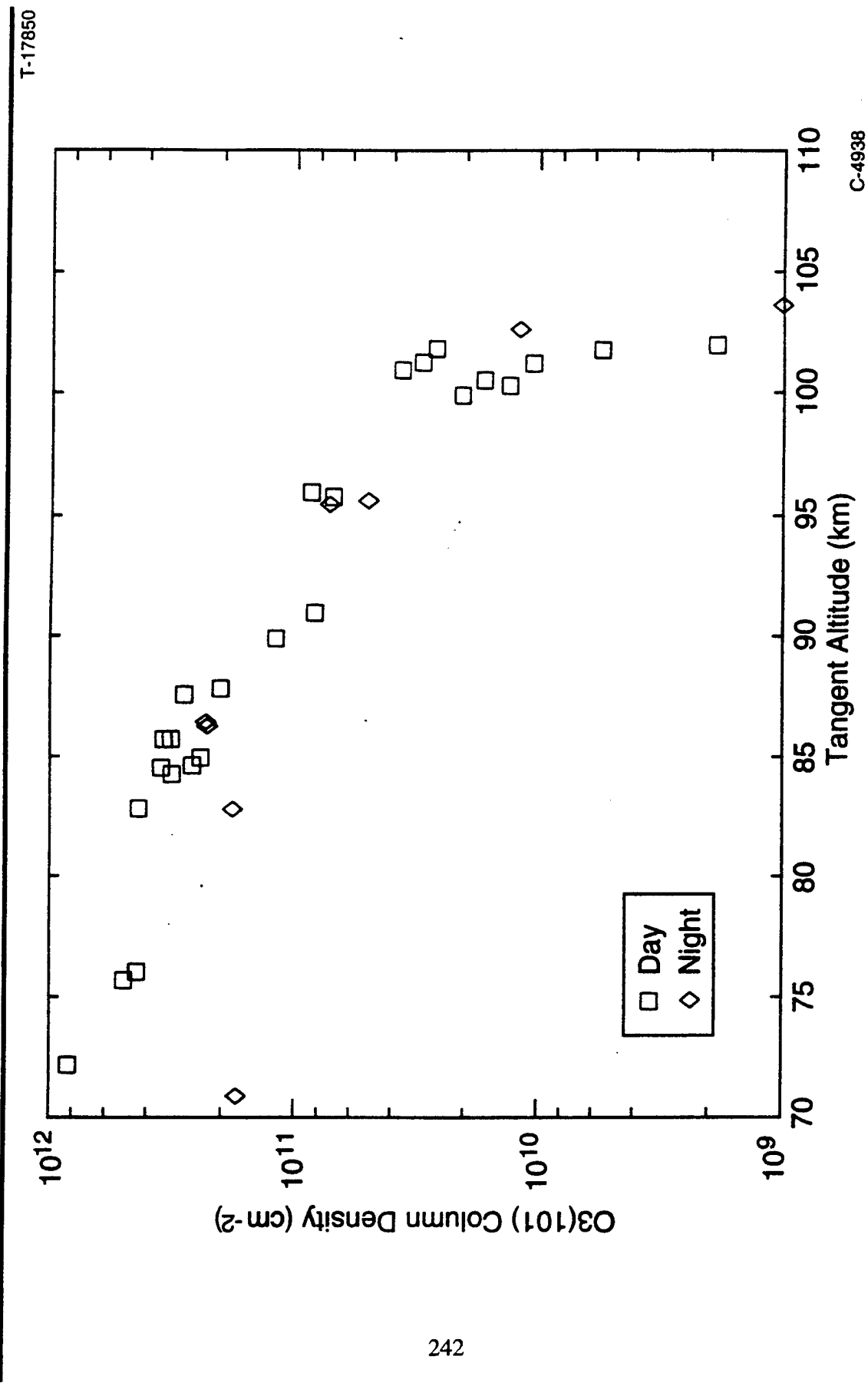
OZONE \tilde{v}_3 RELAXATION

T-17849



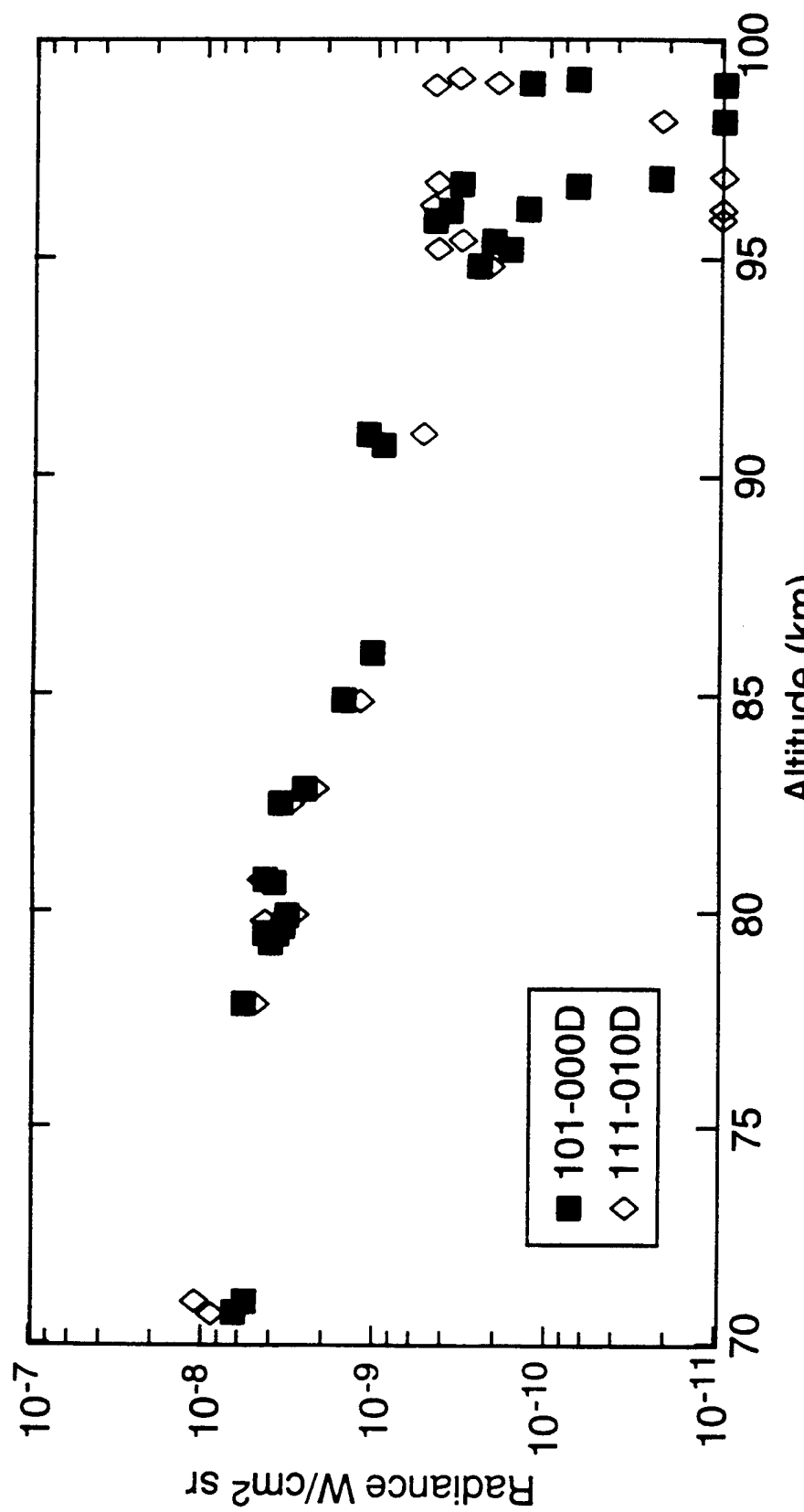
C-4937

CIRRIS 1A O₃ (101) COLUMN DENSITIES



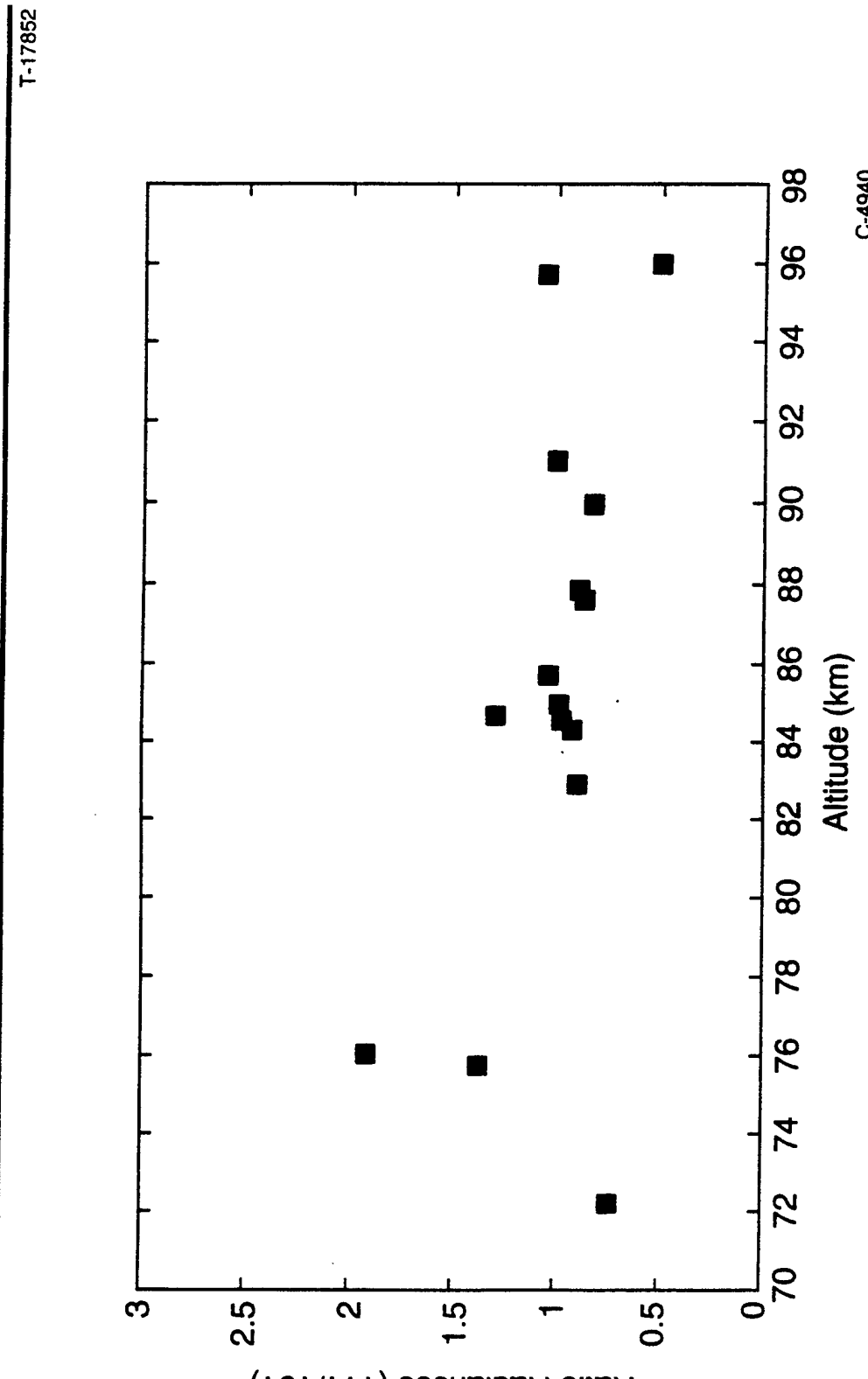
- Populations from PL fitting

CIRRIS 1A OZONE 101,111 5-Km Footprint Correction



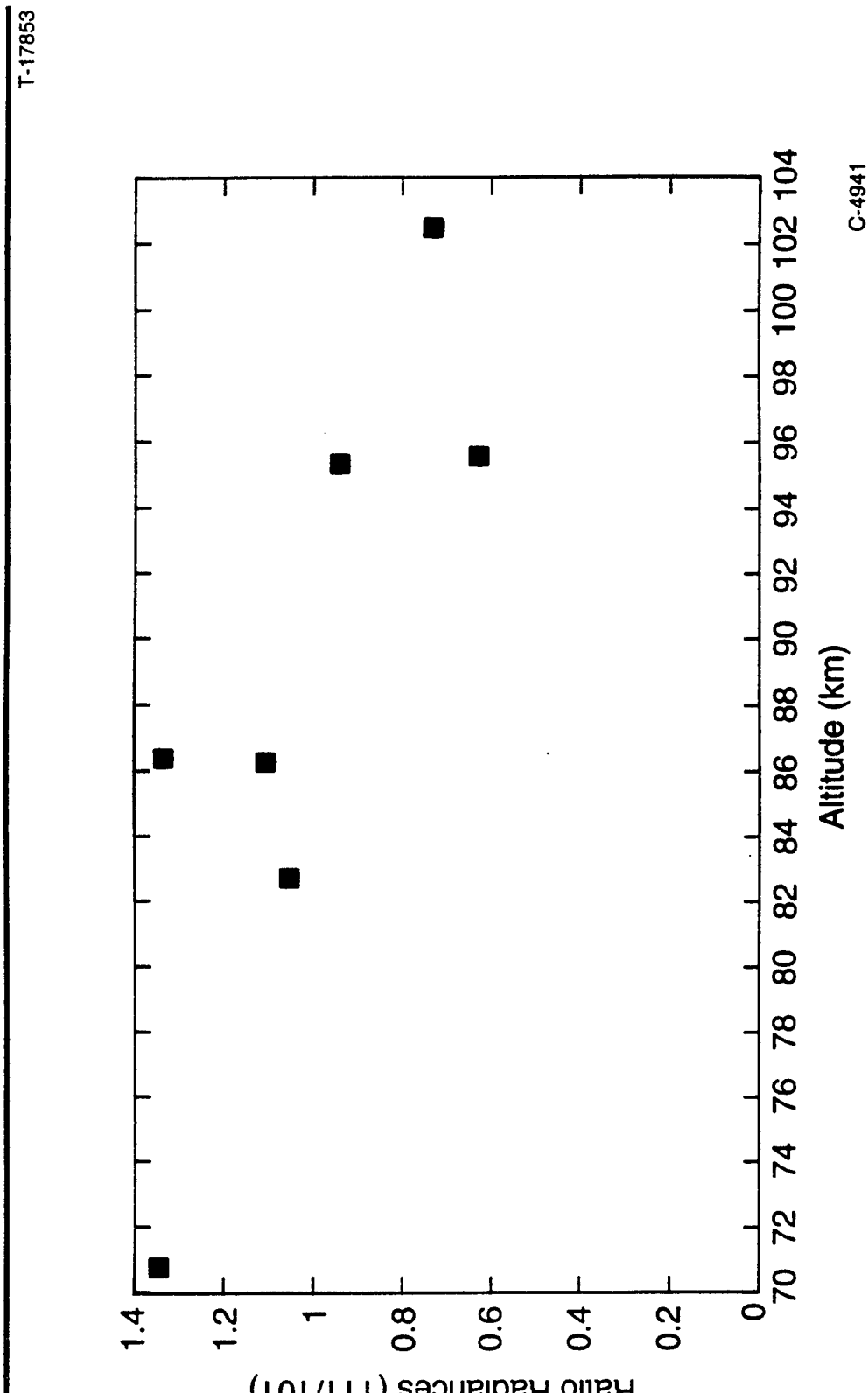
- Radiances from PL fitting

CIRRIS 1A DAY OZONE 111/101



- Populations from PL fitting

CIRRIS 1A NIGHT OZONE 111/101



- Populations from PL fitting

SUMMARY

T-17871

- Spectral signature well-described by ν_1 , ν_3 and ν_2 , ν_3 dyads
- Hot band radiance extends out to beyond 12 μm
- ν_3 population distribution compares well with SPIRE data and model
- Preliminary quenching coefficients for $\nu \leq 7$ agree with laboratory, SPIRE
- Apparent day/night effects observed in 4.8 μm band at low altitudes

CONTINUING ANALYSIS EFFORTS

T-17837

- Extract Ozone, O, relaxation rates, and radiance profiles for comparison with other databases, analyses, and models
- Analyze entire CIRRIS 1A ozone database to extract ozone variabilities
 - Hot band radiances
 - Terminator transients
 - Solar zenith angle
 - Latitude
- Provide profiles, distributions, and rates to permit predictive atmospheric radiance model refinement